

Final Report

SPARTA - Surveillance Platform for Attritable
Reconnaissance and Target Acquisition

AE3200: Design Synthesis

Group 31

Franciszek Białkowski 5736196
Domantas Grigaravičius 5745632
Piotr Moczybroda 5787505
Frank Sprangers 5034809
Wout van Vliet 5811813

Olaf Eek 5762251
Maciej Lewiński 5687632
Filip Ślesinger 5755573
Niels Verdegaal 5748321
Wisse de Vries 5550866



Final Report

SPARTA - Surveillance Platform for Attributable Reconnaissance and Target Acquisition

by

Group 31

Franciszek Białkowski	5736196	Olaf Eek	5762251
Domantas Grigaravičius	5745632	Maciej Lewiński	5687632
Piotr Moczybroda	5787505	Filip Šlesinger	5755573
Frank Sprangers	5034809	Niels Verdegaal	5748321
Wout van Vliet	5811813	Wisse de Vries	5550866

Tutor: Sam van Elsloo
Coaches: Imran Khan & George Popi
Faculty: Faculty of Aerospace Engineering, Delft

Cover: ALTIUS 600 at EDGE 22 [1]
Style: TU Delft Report Style, with modifications by Daan Zwaneveld

Contents

Nomenclature	iii		
1 Introduction	1	9 Control Surfaces Design	57
2 System Functional Analysis	2	9.1 Functional Analysis	57
3 Market Analysis	6	9.2 Requirement Analysis	58
3.1 Market Trends	6	9.3 Aileron Design	58
3.2 SWOT Analysis	7	9.4 Ruddervator Design	59
4 System Requirements	7	9.5 Sustainability & Attritability	60
5 Trade-off and Iteration Summary	9	9.6 Risk Analysis	60
5.1 Trade-off Summary	9	9.7 RAMS Analysis	61
5.2 Iteration Summary	10	9.8 Financial Analysis	61
6 Airfoil Design	12	9.9 Compliance Matrix	61
6.1 Functional Analysis	12	9.10 Recommendations	62
6.2 Requirement Analysis	12	10 Mechanical Design	62
6.3 Airfoil Selection	13	10.1 Functional Analysis	62
6.4 Final Airfoil Configuration	16	10.2 Requirement Analysis	62
6.5 Compliance Matrix	17	10.3 Rotating Wing Mechanism	63
6.6 Recommendations	17	10.4 Telescopic Wing Mechanism	65
7 Wing Structure	18	10.5 Aileron Mechanism	69
7.1 Functional Analysis	18	10.6 Rotating Tail And Ruddervator Mechanism	70
7.2 Requirement Analysis	18	10.7 Component List	70
7.3 Analysis Setup	18	10.8 Sustainability & Attritability	71
7.4 Aerodynamic Analysis	21	10.9 Risk Analysis	72
7.5 Wing Morphing	22	10.10 RAMS Analysis	72
7.6 Structural Analysis	30	10.11 Financial Analysis	73
7.7 Aeroelasticity Analysis	36	10.12 Compliance Matrix	74
7.8 Verification	40	10.13 Recommendations	74
7.9 Sustainability & Attritability	42	11 Propulsion Design	75
7.10 Risk Analysis	42	11.1 Functional Analysis	75
7.11 RAMS Analysis	42	11.2 Requirement Analysis	75
7.12 Financial Analysis	43	11.3 Trade-off Setup	76
7.13 Compliance Matrix	43	11.4 Propeller Design	76
7.14 Recommendations	43	11.5 Trade-off Results	77
8 Fuselage Structure	45	11.6 Unfolding Mechanism Design	78
8.1 Functional Analysis	46	11.7 Sustainability & Attritability	78
8.2 Requirements	46	11.8 Risk Analysis	78
8.3 Analysis	46	11.9 RAMS Analysis	79
8.4 Design	48	11.10 Financial Analysis	79
8.5 Sustainability & Attritability	55	11.11 Compliance Matrix	79
8.6 Risk Analysis	55	11.12 Recommendations	80
8.7 RAMS Analysis	56	12 Communication System	80
8.8 Financial Analysis	56	12.1 Functional Analysis	80
8.9 Compliance Matrix	56	12.2 Requirement Analysis	81
8.10 Recommendations	57	12.3 Analysis	81
		12.4 Chosen Components	82
		12.5 Sustainability & Attritability	84
		12.6 Risk Analysis	84
		12.7 RAMS Analysis	85
		12.8 Financial Analysis	85
		12.9 Compliance Matrix	85
		12.10 Recommendations	86

13 Avionics	86	16 Sustainability & Attritability	108
13.1 Functional Analysis	86	16.1 Wing, Control Surfaces and Fuselage .	108
13.2 Requirement Analysis	86	16.2 Mechanisms	108
13.3 Analysis	87	16.3 Avionics and Propulsion	109
13.4 Chosen Components	88	16.4 Flight Environment	109
13.5 Risk Analysis	89	16.5 Operations	109
13.6 Financial Analysis	89	16.6 Social Sustainability	109
13.7 RAMS Analysis	89	16.7 Life Cycle Assessment	110
13.8 Compliance Matrix	90	17 Risk Analysis	110
13.9 Recommendations	90	17.1 System Risks	110
14 Recovery	90	17.2 Risk Assessment	111
14.1 Functional Analysis	91	17.3 Risk Mitigation	112
14.2 Requirement Analysis	91	18 Financial Analysis	113
14.3 Trade-off	91	18.1 Cost Breakdown	113
14.4 Sustainability & Attritability	93	18.2 Return of Investment	115
14.5 Risk Analysis	93	18.3 Compliance Matrix	116
14.6 RAMS Analysis	93	19 Project Design and Development Logic	116
14.7 Financial Analysis	94	19.1 Stage I: Design Synthesis	116
14.8 Compliance Matrix	94	19.2 Stage II: Detailed Engineering Design	117
14.9 Recommendations	94	19.3 Stage III: Manufacturing, Assembly & Integration	119
15 System Overview	95	19.4 Stage IV: Testing	123
15.1 Architecture	95	19.5 Stage V: Production	124
15.2 Resource Allocation	97	19.6 Stage VI: Operations	125
15.3 Signature Assessment	99	19.7 Project Gantt Chart	130
15.4 Dynamic Stability Analysis	103	20 Conclusion	131
15.5 Sensitivity Analysis	106	Bibliography	132
15.6 Performance Changes	108		
15.7 Model Verification	108		

Nomenclature

Abbreviations

Abbreviation	Definition	Abbreviation	Definition
ABS	Acrylonitrile Butadiene Styrene	O&S	Operations & Support
AHP	Analytical Hierarchy Process	ODE	Ordinary Differential Equation
BIT	Build-In Test	PC	Polycarbonate
CAD	Computer-Aided Design	PEEK	Polyether Ether Ketone
CFD	Computational Fluid Dynamics	PEI	Polyether Imide
CFRO	Carbon Fibre Reinforced Plastics	PET	Polyethylene Terephthalate
CG	Centre of Gravity	PESCO	Permanent Structured Cooperation
DASML	Delft Aerospace Structures and Materials Laboratory	PIPS	Power Isolation & Protection System
DOF	Degree Of Freedom	PLA	Polylactic Acid
DOT	Design Option Tree	QA	Quality Assurance
DSE	Design Synthesis Exercise	QC	Quality Control
EM	Elector-Magnetic	QFD	Quality Function Deployment
EoM	Equation of Motion	RAM	Radar-Absorbent Materials
EOL	End-of-Life	RAMS	Reliability, Availability, Maintainability, Safety
ESC	Electronic Speed Controller	RCS	Radar Cross Section
EU-OSHA	European Agency for Safety and Health at Work	RNLAF	Royal Netherlands Air Force
FBS	Functional Breakdown Structure	R&D	Research & Development
FFD	Functional Flow Diagram	ROI	Return on Investment
FEM	Finite Element Method	RMS	Root Mean Square
FHSS	Frequency Hopping Spread Spectrum	SAM	Surface to Air Missile
FPS	Frames Per Second	SHORAD	Short Range Air Defence
GNSS	Global Navigation Satellite System	SIL	Simulation-In-the-Loop
GPS	Global Positioning System	SM	Stability Margin
HD	High Definition	SMART	Specific, Measurable, Achievable, Relevant & Time-Bound
HEVC	High Efficiency Video Coding	SPARTA	Surveillance Platform for Attributable Reconnaissance and Target Acquisition
IAS	Indicated Air Speed	STANAG	Standardization Agreement
IMU	Inertial Measurement Unit	SWOT	Strengths, Weaknesses, Opportunities & Threats
IR	Infrared	TBD	To Be Determined
ISA	International Standard Atmosphere	UAS	Unmanned Aerial System
ISTAR	Intelligence, Surveillance, Target Acquisition and Reconnaissance	UAV	Unmanned Aerial Vehicle
KPI	Key Performance Indicators	USA	United States of America
MAC	Mean Aerodynamic Chord	US	United States
NATO	North Atlantic Treaty Organization	USB	Universal Serial Bus
NDI	Non-Destructive Inspection	UV	Ultra Violet
NIST	National Institute of Standards and Technology	VNS	Visual Navigation System

Symbols

Symbol	Definition	Unit	Symbol	Definition	Unit
a	Acceleration	m/s ²	A_0	Time fraction in which system is available	-
a	Control positional parameter	-	B	Boom area	m ²
A	Aspect ratio	-	B	Number of blades	-
A	Area	m ²	B	Input matrix	-
A	System matrix	-	B	Aerodynamic mass matrix	-
A	Structural mass matrix	-	b	Distance between adjacent booms	m
A_m	Enclosed area	m ²	b	Wingspan	m
A_t	Tail aspect ratio	-			

Symbol	Definition	Unit	Symbol	Definition	Unit
b_t	Tail span	m	C_{l_r}	Rolling moment derivative with respect to yaw rate	-
b_f	Fuselage width	m	$C_{l_{\delta_a}}$	Rolling moment derivative with respect to aileron deflection	-
c	Chord length	m	$C_{l_{\delta_r}}$	Rolling moment derivative with respect to rudder deflection	-
\mathbf{C}	Structural damping matrix	-	$C_{L_{\delta_a}}$	Change in lift coefficient due to aileron deflection	-
c_h	Pitch axis positional parameter	-	C_{X_u}	Axial force derivative with respect to forward velocity	-
c_n	Chord length of a section	m	C_{X_α}	Axial force derivative with respect to angle of attack	-
c_r	Root chord	m	C_{X_q}	Axial force derivative with respect to pitch rate	-
c_t	Tip chord	m	$C_{X_{\delta_e}}$	Axial force derivative with respect to elevator deflection	-
c_{tail}	Tail chord	m	C_{Y_β}	Side force derivative with respect to sideslip angle	-
C	Constant based on boundary conditions	-	$C_{Y_{\dot{\beta}}}$	Side force derivative with respect to sideslip rate	-
C_h	Structural damping of plunge	kg/s ²	C_{Y_p}	Side force derivative with respect to roll rate	-
C_α	Structural damping of plunge	kg/s ²	C_{Y_r}	Side force derivative with respect to yaw rate	-
C_β	Structural damping of plunge	kg/s ²	$C_{Y_{\delta_a}}$	Side force derivative with respect to aileron deflection	-
$C(k)$	Theodorsen function	-	$C_{Y_{\delta_r}}$	Side force derivative with respect to rudder deflection	-
C_D	Drag coefficient	-	$C_{Z_{\delta_e}}$	Normal force derivative with respect to elevator deflection	-
C_{D_0}	Zero-lift drag coefficient	-	\mathbf{D}	Aerodynamic damping matrix	-
C_{D_e}	Endurance drag coefficient	-	D_m	Mean coil diameter	m
C_{D_r}	Range drag coefficient	-	D_P	Diameter pitch	1/m
$C_{D_{cruise}}$	Cruise drag coefficient	-	D_w	Wire diameter	m
C_L	Lift coefficient	-	e	Oswald efficiency factor	-
C_{L_0}	Zero-angle-of-attack lift coefficient	-	E	Endurance	h
C_{L_e}	Endurance lift coefficient	-	E	Irradiance	W/m ²
C_{L_r}	Range lift coefficient	-	\mathbf{E}	Structural stiffness matrix	-
$C_{L_{cruise}}$	Cruise lift coefficient	-	F	Force	N
C_{L_w}	Wing lift coefficient	-	\vec{F}	Vector of external forces	N
C_{L_t}	Tail lift coefficient	-	\mathbf{F}	Aerodynamic stiffness matrix	-
C_{L_α}	Lift curve slope	1/rad	F_b	Flatness of airfoil bottom	-
$C_{L_{\alpha,w}}$	Wing lift curve slope	1/rad	F_w	Face width of a spur gear	m
$C_{L_{\alpha,t}}$	Tail lift curve slope	1/rad	F_{cr}	Critical column buckling load	N
$C_{L_{design}}$	Design lift coefficient	-	$F_{friction}$	Friction force	N
$C_{l_{max}}$	Maximum 2D lift coefficient	-	\vec{F}_i	Aerodynamic force at i wing section	N
$C_{L_{max}}$	Maximum 3D lift coefficient	-	h	Plunge, vertical movement of a wing section	m
C_m	Moment coefficient	-	h_f	Fuselage height	m
$C_{m_{ac}}$	Moment coefficient around the aerodynamic centre	-	\vec{H}_b	Angular momentum vector around the body mass	kg m ² /s
$C_{M_{\delta_a}}$	Change in moment coefficient due to aileron deflection	-	I_α	Mass moment of inertia of wing about pitch axis	kg m ²
C_{m_u}	Pitching moment derivative with respect to forward velocity	-	$I_{\alpha\beta}$	Product of inertia of I_α and I_β	kg m ²
C_{m_α}	Pitching moment derivative with respect to angle of attack	-	I_β	Mass moment of inertia of control surface around hinge axis	kg m ²
$C_{m_{\dot{\alpha}}}$	Pitching moment derivative with respect to angle of attack rate	-	I_i	Inertia tensor of the UAS component	kg m ²
C_{m_q}	Pitching moment derivative with respect to pitch rate	-	I_{wing}^b	Inertia tensor of wing in body frame	kg m ²
$C_{m_{\delta_e}}$	Pitching moment derivative with respect to elevator deflection	-	\dot{I}	Inertia tensor derivative	kg m ² /s
C_{n_β}	Yawing moment derivative with respect to sideslip angle	-	I_{wing}^b	Inertia tensor derivative of the wing in the body frame	kg m ² /s
$C_{n_{\dot{\beta}}}$	Yawing moment derivative with respect to sideslip rate	-	I_{XXP}	Area moment of inertia about pitch axis	m ⁴
C_{n_p}	Yawing moment derivative with respect to roll rate	-	I_{xx}	Product of inertia around x-axis	kg/m ²
C_{n_r}	Yawing moment derivative with respect to yaw rate	-			
$C_{n_{\delta_a}}$	Yawing moment derivative with respect to aileron deflection	-			
$C_{n_{\delta_r}}$	Yawing moment derivative with respect to rudder deflection	-			
C_{l_β}	Rolling moment derivative with respect to sideslip angle	-			
C_{l_p}	Rolling moment derivative with respect to roll rate	-			

Symbol	Definition	Unit	Symbol	Definition	Unit
I_{xz}	Product of inertia around x- and z-axes	kg/m ²	P_h	Absorbed Power	W
I_{yy}	Product of inertia around y-axis	kg/m ²	P_{in}	Input Power	W
I_{zz}	Product of inertia around z-axis	kg/m ²	P_{int}	Internal Power	W
I_α	Moment of inertia about α axis	kg m ²	P_{min}	Minimum Detectable Power	W
J	Geometry factor for spur gears	-	P_t	Transmitted Power	W
JO_P	Polar moment of inertia about pitch axis	m ⁴	P_r	Power Required	W
$J_{mB}(x)$	Bessel function of order mB at argument x	-	q	Pitch rate	rad/s
K_X^2	Non-dimensional product of inertia around x-axis	-	q	Shear flow	N/m
K_Y^2	Non-dimensional product of inertia around y-axis	-	Q	State coefficient matrix	-
K_Z^2	Non-dimensional product of inertia around z-axis	-	q_b	Shear flow due to bending	N/m
K_α	Torsional stiffness	Nm/rad	q_{s0}	Basic shear flow	N/m
K_h	Bending stiffness	N/m	Q_{gen}	Heat generation	W
K_β	Rotational stiffness	Nm/rad	R	Radius	m
k	Spring stiffness	N/m	R	Range	m
k	Thermal conductivity	W/mK	R	Input coefficient matrix	-
l_t	Distance between wing and tail aerodynamic centres	m	R_{max}	Maximum radar detection range	m
l_f	Fuselage length	m	Re	Reynolds number	-
$l(t)$	Dynamic lift	N	RoC	Rate of climb	m/s
L	Position of the wing from the root	m	\vec{R}_i	Vector between the wing section and the body mass	m
L/D	Lift-to-drag ratio	-	$\vec{r}_{i/b}$	Position vector of the UAS component with respect to the body frame	m
L_e	Effective length	m	$\vec{r}_{section_i/b}$	Vector between the wing i section and the body mass	m
m	Total mass	kg	$\vec{r}_{section_i/i}$	Vector between the wing i section and the hinge	m
m	Mass per unit length	kg/m	S	Wing area	m ²
m	Harmonic order	-	S	Distance from prop hub to observer	m
M	Mass matrix	-	S_t	Tail surface area	m ²
m_i	Mass of the UAS component	kg	s	Distance travelled	m
$m_{avionics}$	Avionics mass	kg	\vec{S}_{ac}	Static moment of the whole UAS	kg m
m_{batt}	Battery mass	kg	$\dot{\vec{S}}_{ac}$	Static moment derivative of the whole UAS	kg m/s
m_{comms}	Communications mass	kg	$\ddot{\vec{S}}_{ac}$	Static moment second derivative of the whole UAS	kg m/s ²
m_{engine}	Engine mass	kg	$[S_{ib}]_x$	Skew symmetric matrix of the UAS component	kg m
m_{fuse}	Fuselage mass	kg	\vec{S}_{ib}	Static moment of the UAS component	kg m
$m_{payload}$	Payload mass	kg	$\dot{\vec{S}}_{ib}$	Static moment derivative of the UAS component	kg m/s
$m_{payload,1}$	Payload 1 mass	kg	$\ddot{\vec{S}}_{ib}$	Static moment second derivative of the UAS component	kg m/s ²
$m_{payload,2}$	Payload 2 mass	kg	t	Thickness	m
m_{prop}	Propulsion mass	kg	t	Time	s
m_{tail}	Tail mass	kg	$t_{charging}$	Charging time	s
$m_{thermal}$	Thermal mass	kg	t_{launch}	Launch time	s
$m_{transformers}$	Transformers mass	kg	$t_{operation}$	Operational time	s
m_{wing}	Wing mass	kg	$t_{preparation}$	Preparation time	s
$m_{x_f}(t)$	Dynamic moment around hinge axis	Nm	$t_{refurbishment}$	Refurbishment time	s
$m_{x_h}(t)$	Dynamic moment around pitch axis	Nm	$(t/c)_t$	Tail thickness-to-chord ratio	-
\vec{M}	External moments moments	Nm	t/c	Thickness-to-chord ratio	-
\vec{M}_i	Airfoil moment vector at i wing section	Nm	T	Thrust	N
M_t	Tip Mach number	-	T	Temperature	K
N	Normal force	N	T_{amb}	Ambient temperature	K
N_{crit}	Turbulence model	-	$T_{b/h}$	Transformation from hinge to body frame	-
n	Empirical exponent for crippling	-	$T_{b/h}^T$	Transpose of the transformation from hinge to body frame	-
n_{max}	Max load factor	-	T_n	Theodorsen constant (n=1,2,...,14)	-
n_{min}	Min load factor	-	T_u	Wing and tail unfolding period	s
$n_{ult,max}$	Ultimate max load factor	-	u	Flow speed	m/s
$n_{ult,min}$	Ultimate min load factor	-	u	Control input vector	-
p	Roll rate	rad/s			
P	Descriptor matrix	-			
$\vec{p}_{b/I}$	Linear momentum of body with respect to the inertial frame	kg m/s			
P_d	Pitch diameter	m			
P_{fail}	Change of not surviving a mission	-			
p_m	RMS sound pressure level	dyne/m ²			

Symbol	Definition	Unit	Symbol	Definition	Unit
T_u	Unfolding period	s	W	Aerodynamic state influence matrix	-
\hat{u}	Non-dimensional velocity	-	W_n	Aerodynamic state equation matrices (n=1,2)	-
$\vec{V}_{i/I}$	Velocity vector of the UAS component with respect to the inertial frame	m/s	W/P	Power loading	N/W
$\vec{V}_{b/I}$	Velocity vector of the UAS body mass with respect to the inertial frame	m/s	W/S	Wing loading	N/m ²
$\dot{\vec{V}}_{b/I}$	Acceleration vector of the UAS body mass with respect to the inertial frame	m/s	W_i	Transmitted load	N
\vec{V}_{loc}	Local velocity vector at the wing i section	m/s	w_e	Stiffened width of panel	m
v	Velocity	m/s	x	State vector	-
v''	Deflection	m	$\dot{\mathbf{x}}$	Time derivative of the state vector	-
$v_{c,max}$	Maximum operating speed	m/s	x_f	Pitch axis location	m
v_{cruise}	Cruise velocity	m/s	x_h	Aileron hinge position	m
v_{dive}	Dive speed	m/s	$x_{avionics}$	Avionics position	m
v_d	Divergence speed	m/s	$x_{battery}$	Battery position	m
v_d	Design speed	m/s	x_{comms}	Comms position	m
v_e	Endurance speed	m/s	x_{engine}	Engine position	m
v_{max}	Maximum speed	m/s	$x_{payload,1}$	Payload 1 position	m
v_r	Range speed	m/s	$x_{payload,2}$	Payload 2 position	m
v_{stall}	Stall speed	m/s	x_{tail}	Tail position	m
v_{∞}	Free stream velocity	m/s	$x_{thermal}$	Thermal position	m
V_x	Shear force in the x-direction	N	$x_{transformers}$	Transformers position	m
V_z	Shear force in the z-direction	N	x_{wing}	Wing position	m
w	Airfoil downwash	-	x_{ac}	Aerodynamic centre location	m
w_n	Aerodynamic states (n=1,2,...,6)	-	\bar{x}_{ac}	Aerodynamic centre location normalized with \bar{c}	-
W	Weight	N	x_{cg}	CG location	m
α	Angle of attack	deg	\bar{x}_{cg}	CG location normalized with \bar{c}	-
α	Empirical constant for crippling	-	Y	Lewis factor	-
α_{ind}	Induced angle of attack	deg	z_{cg}	CG location in z-direction	m
β	Sideslip angle	deg	ρ	Radius of gyration	m
β	Control surface angle	rad	ρ_m	Battery mass density	Wh/kg
ΔV	Velocity increment delivered by the launch tube	m/s	ρV	Battery volume density	Wh/L
Δt	Wing morphing simulation timestep	s	σ	Radar cross section	m ²
δ_a	Deflection angle of the aileron	rad	σ	Stefan-boltzmann constant	W/m ² K ⁴
δ_e	Deflection angle of the elevator	rad	σ	Stress	Pa
δ_r	Deflection angle of the rudder	rad	σ_{cc}	Crippling stress	Pa
ϵ_n	Exponent part of Wagner function approximation (n=1,2)	-	σ_{cr}	Critical Euler buckling stress	Pa
$\dot{\alpha}$	Angle of attack rate	deg/s	$\sigma_{fuselage}$	Radar cross section of fuselage	m ²
$\dot{\beta}$	Sideslip rate	deg/s	$\sigma_{specular}$	Radar cross section in specular case	m ²
ϵ	Emissivity	-	σ_{tail}	Radar cross section of tail	m ²
η	Efficiency	-	σ_{wing}	Radar cross section of wing	m ²
η_p	Propeller efficiency	-	σ_y	Yield stress	Pa
$\frac{d\theta}{dy}$	Rate of twist per unit length	rad/m	τ	Shear stress	Pa
Γ	Circulation	m ² /s	θ	Angle of neutral axis	deg
Γ	Dihedral angle	deg	θ	Observer angle relative to prop	deg
Γ_t	Tail dihedral angle	deg	θ	Pitch angle	deg
λ	Wavelength	m	θ	Wing or tail unfolding angle	rad
λ_i	i-th eigenvalue	-	φ	Roll angle	deg
Λ	Sweep angle	deg	$\Phi(t)$	Wagner function	-
Λ_t	Tail sweep angle	deg	ψ_n	Wagner function approximation multiplier (n=1,2)	-
μ	Dynamic viscosity of fluid	m ² /s	ω_h	Natural frequency plunge	Hz
μ	Friction coefficient	-	ω_{n_i}	Frequency of i eigenvalue	Hz
μ	Parameter of c_h	-	ω_{α}	Natural frequency pitch	Hz
μ_b	Non-dimensional mass (normalised with b)	-	$\vec{\omega}_{b/I}$	Angular velocity of the UAS body mass with respect to the inertial frame	rad/s
μ_c	Non-dimensional mass (normalised with \bar{c})	-	$\dot{\vec{\omega}}_{b/I}$	Angular acceleration of the UAS body mass with respect to the inertial frame	rad/s ²
ν	Poisson's ratio	-	$\vec{\omega}_{i/b}$	Unfolding angular velocity of the component	rad/s
ξ_i	Damping of i eigenvalue	-	$\dot{\vec{\omega}}_{i/b}$	Unfolding angular acceleration of the component	rad/s ²
Φ	Radiated power	W	$[\omega_{i/b}]_{\times}$	Skew symmetric matrix of the unfolding angular velocity of the component	rad/s
ϕ	Dihedral angle	rad	$\vec{\omega}_{i/I}$	Angular velocity of the UAS component with respect to the inertial frame	rad/s
ρ	Density	kg/m ³			

Executive Summary

With an ever more unpredictable global political situation and increasing tensions, Europe finds itself in a precarious position. With uncertain security guarantees and an aggressor to the east, it needs to play catch-up to fend for itself. SPARTA (Surveillance Platform for Attributable Reconnaissance and Target Acquisition) aims to provide the European community with a response to these technological advancements.

Mission Need Statement:

Europe needs a domestic attritable tube-launched unmanned reusable system capable of ISTAR (Intelligence, Surveillance, Target Acquisition and Reconnaissance), made from purely European components with replaceable payloads.

Project Objective Statement:

Design an attritable tube-launched Unmanned Aerial System (UAS) for general purpose surveillance and reconnaissance within 10 weeks, with 10 students.

Market analysis

The market analysis for the SPARTA project goes deep into the external factors influencing its potential success, particularly the current economic and geopolitical trends, which are prominently highlighted by the European ReArm program. This initiative is set to reshape defence strategies and procurement across Europe, bolstered by a substantial increase in defence budgets and a preference for European-based solutions, as presented in Figure 1.

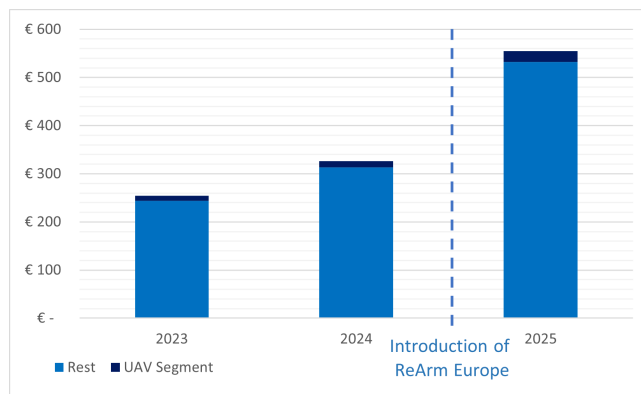


Figure 1: European Military Spending in billions of €

The market trends show a growing demand for cost-effective solutions like UAVs, which is fuelled by the heightened defence spending in the post-Ukraine crisis world and the now proven proficiency of drones in the Ukraine-Russia conflict. Given this, the European UAV market is poised to grow substantially, presenting a lucrative opportunity for SPARTA. By conducting a SWOT (Strengths, Weaknesses, Opportunities, Threats) analysis, the key strengths, such as wide operational capabilities and European manufacturing that SPARTA brings to the table, are revealed. Alongside identifying weaknesses like high unit costs and design limitations that must be mitigated. Opportunities include growing defence expenditures and geopolitical alignments as discussed previously, while threats encompass potential budget cuts, new geopolitical shifts and supply chain vulnerabilities.

Requirments SPARTA

SPARTA Requirements The requirements that make SPARTA unique and thus drive the design more than average are listed here.

- **REQ-SYS-01** The UAS shall have a range of at least 500 km.

- **REQ-SYS-02** The UAS shall have an endurance of at least 5 h.
- **REQ-SYS-08** The UAS shall stream full HD video in real time to a ground station within 100 km.
- **REQ-SYS-10** The UAS shall be launchable from an Airbus A400M at Indicated Air Speed (IAS) ≥ 190 kts in steady flight.
- **REQ-SYS-11** The UAS shall be launchable from an Apache helicopter in hover.
- **REQ-SYS-12** The UAS shall be launchable from a tube launcher on the ground.
- **REQ-SYS-22** In stowed configuration, the UAS shall fit in a size A sonobuoy (123.9 mm \times 914.4 mm)..
- **REQ-SYS-31** No components shall originate from outside European Political Community.

Trade-off

In the previous design phase, a trade-off between various design options was performed. In this section, the resulting starting parameters will be presented. These are created by running the optimisation code created during the previous phase with the new airfoil selected specifically for this design. The results of these iterations are presented in Table 2.

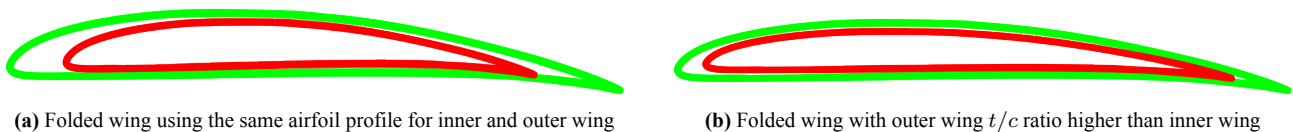
Table 2: Most important design parameters

Unit	Description	Value
v_{cruise} [m/s]	Cruise speed	40.332
S [m ²]	Wing surface area	0.148
b [m]	Wingspan	1.980
A [-]	Aspect ratio	26.4
m [kg]	Total mass	14.288
m_{batt} [kg]	Battery mass	4.136

Airfoil Design

During the preliminary design phase, the NACA 2412 airfoil was selected for the aircraft. However, this choice was made somewhat arbitrarily and without fully considering the specific needs of the design. To address this, an airfoil trade-off study is performed, which results in the SG6043 being chosen due to its high effectiveness in maximising endurance.

To maximise space for the telescoping mechanism, the outer wing profile is slightly modified. Using XFOIL, this modification is found to have no significant impact on performance. This comparison is shown in Figure 2.



(a) Folded wing using the same airfoil profile for inner and outer wing

(b) Folded wing with outer wing t/c ratio higher than inner wing

Figure 2: Comparison of folded wing cross sections: (a) identical airfoils vs. (b) adjusted t/c ratios for inner and outer wing.

Wing Structure

In this section, the design of the wing structure is discussed. First, a sophisticated coupled model is developed for obtaining the loads on the wing structure during launch. A schematic representation of the model is provided in Figure 3.

First, the aerodynamic analysis is created, which takes into account 3D downwash effects to give an accurate estimation of the lift created by the wing. Then in order to analyse the launch performance, a varying geometry flight dynamics is created. Then the three different launch sequences from the Apache, Airbus A400M, and the ground to determine both the stability on launch and the loads during the launch sequence.

Using these results, the wing structure is designed, and a material is selected for it by means of a trade-off. Finally, an aeroelastic analysis is performed, which verifies the wing during launch and cruise conditions.

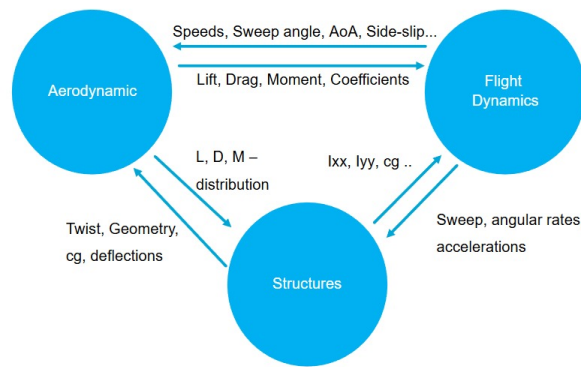


Figure 3: Created coupled model

Fuselage Structure

This section details the fuselage structure designed for SPARTA, using an extension of the same model discussed in the previous section. The design process considers both yielding and buckling to ensure structural integrity. To improve overall strength and stiffness, stiffeners and frames are incorporated throughout the fuselage.

A material trade-off is conducted to determine the most suitable skin material. Aluminium is ultimately selected due to its good balance of environmental and impact resistance, specific modulus, cost, and recyclability. One key advantage of the chosen design is the ease with which skin panels can be removed, enabling convenient access to internal components for maintenance and inspection.

The final design of the fuselage structure is shown in Figure 4, highlighting the arrangement of key structural elements such as frames, stringers, and skin panels.

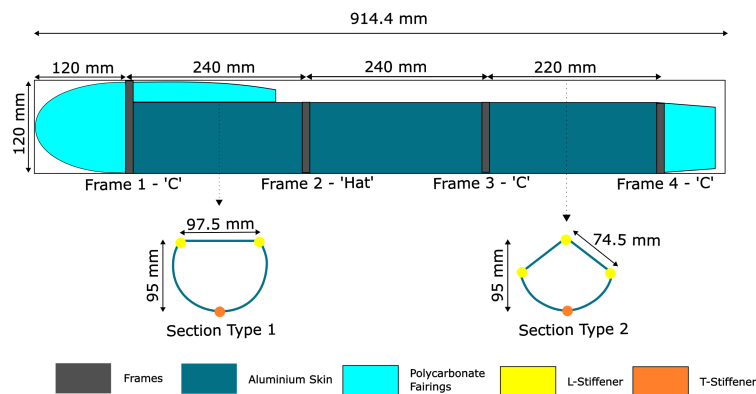


Figure 4: Fuselage structure diagram

Control Surfaces Design

The control surfaces for SPARTA are designed to provide effective manoeuvrability and stability, incorporating both ailerons and ruddervators (combined rudder and elevator). The ailerons are positioned on the outer telescopic sections of the wing, with actuators housed in the wing tips to minimise linkage complexity. For pitch and yaw control, a full moving inverted V-tail configuration is implemented. This design choice maximises control authority of the UAV, improving SPARTA’s operability.

Mechanism Design

This section describes the mechanisms designed for unfolding the wings and tail of SPARTA. For the rotational component of the unfolding process, a worm gear mechanism is selected due to its high attritability and decent serviceability, as shown in Figure 5. For the telescopic section of the main wing unfolding mechanism, a spring-loaded design is chosen following a trade-off analysis, which highlights its fast deployment speed and relatively

low risk; this is illustrated in Figure 6. The tail unfolding mechanism employs a similar rotational mechanism to that used for the main wings, depicted in Figure 7.

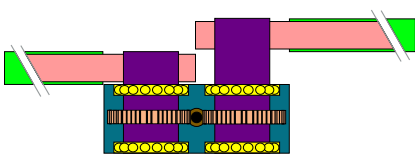


Figure 5: Worm gear mechanism for rotational wing unfolding

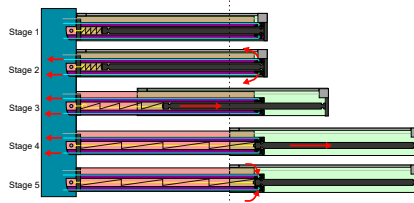


Figure 6: Spring-loaded telescopic wing unfolding mechanism

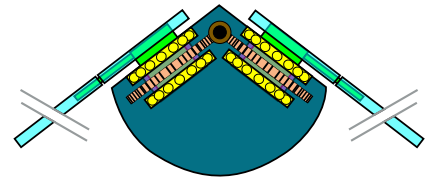


Figure 7: Rotational hinge mechanism for the tail unfolding mechanism

Propulsion Design

For the propulsion system, the Orbit 1 engine from Plettenberg is selected, paired with a compatible electronic speed controller to ensure motor control. The propeller is chosen from a dataset provided by the American company APC. Following a trade-off analysis considering performance, efficiency, and compatibility with the motor, a propeller with a diameter of 229 mm and a pitch of 254 mm is determined to be the most suitable choice for this initial design, due to its high suitability to modification for folding and good efficiency.

Communication System

A communication system is designed to fulfil the requirement of full HD video streaming from 100 km away. The XVTR transmitter is chosen in combination with the XBOOST24G8W video booster, which is an all-in-one solution for encoding, encryption and transmission. The system is developed by Digital Micro Devices, a company specialised in UAV communication systems, based in Spain. To accompany the chosen transmitter, a ground control and launch vehicle control receiver and interface are selected. For the ground station, the data is received by the SATPROV2 and for a vehicle-born operator, the compact RXLRS receiver is used. These components in combination meet all communication requirements.

Avionics

A set of Avionics components is selected in order to fulfil the required level of autonomy. The selected components are: an integrated autopilot, the Spanish Veronte 1X, which also features 3 IMUs, 3 Magnetometers, a Pitot-tube and 2 Barometers. A Spanish-made visual navigation system to navigate in GNSS-denied environments. And finally, a Belgian GNSS receiver, the Septentrio Mosaic-G5 P3H. These components are shown in Figures 8, 9, 10. Note that they are not presented to scale.



Figure 8: Veronte autopilot
[2]

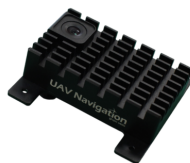


Figure 9: VNS01 Visual Navigation System
[3]

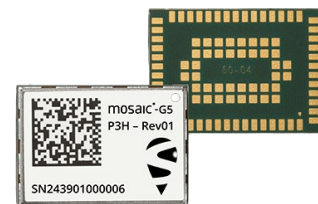


Figure 10: Mosaic-G5 P3H
[4]

Recovery

In this section, the chosen recovery method is discussed. First, a trade-off is performed between the following options: Landing gear, parachute, net catch, wire catch and belly landing. Due to its low size and complexity

drone-side, the net recovery is deemed to be the most feasible.

System overview

In this section, an overview is presented of the performance changes caused by the changes made to the design in this initial design phase. These values are presented in Table 3.

Table 3: Parameters obtained after new iteration

Parameter	Old Value	New Value
v_{stall} [m/s]	31.02	31.02
v_{cruise} [m/s]	40.33	40.33
b_t [m]	0.56	0.56
m [kg]	14.29	13.12
m_{batt} [kg]	4.14	4.14
R [km]	725.97	788.43
E [h]	5	5.43

Then suggestions are made regarding reducing the size of the batteries to increase the available space for still missing components, like the thermal control system and detailed design of the electrical subsystem.

Financial analysis

The results of the financial analysis are presented in this section. This analysis took the estimated costs of each subsystem and added manufacturing costs to produce an estimate of the unit price of SPARTA at €54,928. Subsequently, a return on investment analysis is performed to estimate the initial cost at which SPARTA should be sold at €150,000.

Future design

In this section, the future of the SPARTA design is discussed. First, the future detailed design phase is discussed, which is estimated to take about six months. This mainly focuses on covering off the parts of the design that were omitted during the preliminary design and verifying all the user requirements for which compliance have not yet been proven. In addition, a detailed verification and validation table is presented with plans to prove each requirement.

Afterwards, time is taken to describe a detailed manufacturing and assembly plan for the initial prototyping of SPARTA. This shows how to integrate the various shelf products that make up the design with the custom-made components designed specifically for SPARTA. Then, a test campaign is outlined in order to make sure that the prototypes work as intended.

Subsequently, the production and operations of SPARTA are outlined. This covers the setup of production facilities, quality control procedures, and the production ramp-up plan. Then, a RAMS (Reliability, Availability, Maintainability, Safety) analysis is performed to give a better view of the system’s characteristics. Using the results of this RAMS, a concept of operations is developed, which covers how the operator would operate, maintain and dispose the system. Specifically, the launch sequence is analysed since that is a unique part of SPARTA. A flow chart showcasing the system’s launch sequence is shown in Figure 11.

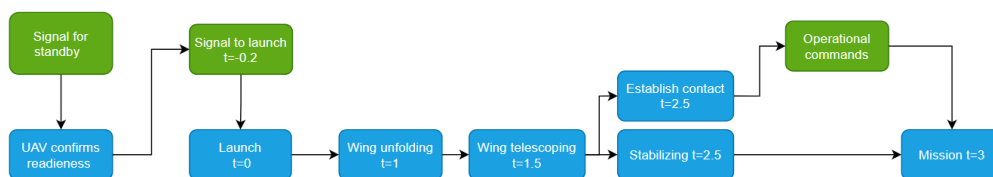


Figure 11: Launch operation

Conclusion

The SPARTA system is a high-wing morphing drone with an inverted V-tail. It can be launched from an Airbus A400m aircraft, an Apache helicopter or from the ground. The system operator just needs to press a button, and it will launch automatically from the tube and provide an HD video feed to the system operator over the mission area. It can fly to targets at 725 km away or loiter for 5 hours around the target at speeds between 31 m/s and 55 m/s. After the mission, it can be recovered by catching SPARTA in a net. When the system is back on the ground, it can be inspected, maintained and folded to fit inside the tube within four hours, so it to fly again.

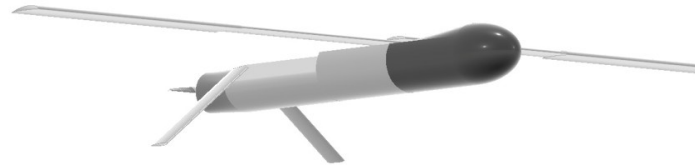


Figure 12: Design configuration of SPARTA

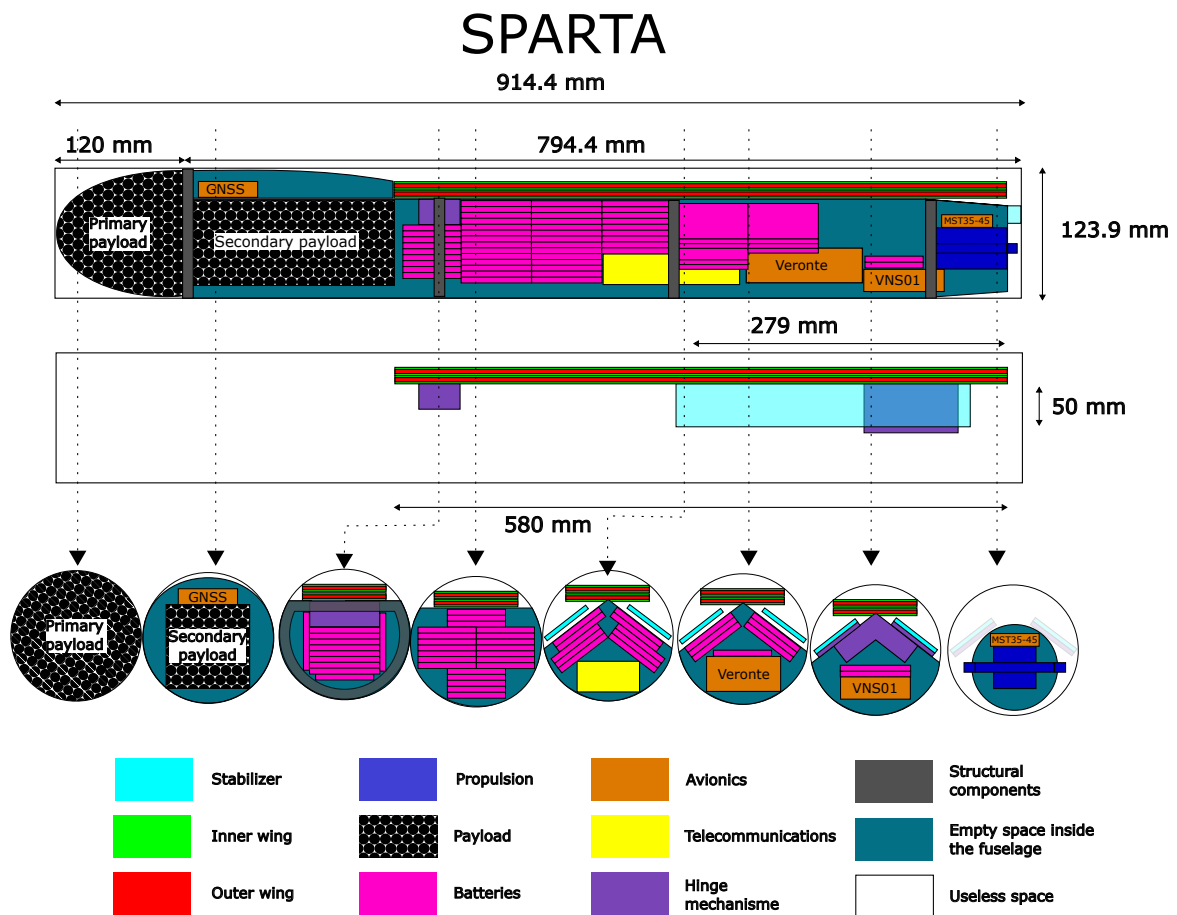


Figure 13: Internal lay-out of SPARTA

1. Introduction

With an ever more unpredictable global political situation and increasing tensions, Europe finds itself in a precarious position. With uncertain security guarantees and an aggressor to the east, it needs to play catch-up to fend for itself. This is where SPARTA comes in, an all-European attritable unmanned aerial system to be ready by 2027. SPARTA aims to provide the European Political Community¹ with a response to these new technological advances. It is to be designed as a system capable of delivering high-quality Intelligence, Surveillance, Target Acquisition and Reconnaissance (ISTAR) data live from beyond enemy lines, with sufficient range and endurance to make it home safe and fly again. Being modular, it will allow it to perform a wide variety of missions, both military and civilian. Furthermore, its form factor allows it to be tube-launched from a standard sonobuoy tube, meaning it can be deployed from an aircraft, helicopter, or the ground. SPARTA will be able to communicate and collaborate with its mothership and other unmanned systems for ultimate mission effectiveness. It is aiming to achieve all of this while adhering to European sustainability ideals. And most importantly, being made entirely in Europe, it is helping build a stronger, self-sufficient Union. The mission need statement and the project objective statement for SPARTA are given by:

Mission Need Statement:

Europe needs a domestic attritable tube-launched unmanned reusable system capable of ISTAR, made from purely European components with replaceable payloads.

Project Objective Statement:

Design an attritable tube-launched Unmanned Aerial System (UAS) for general purpose surveillance and reconnaissance within 10 weeks, with 10 students.

This report represents the fourth and final report detailing the design of SPARTA during the 2025 Design Synthesis Exercise (DSE). It follows the planning done in the Project Plan [5], the system exploration and definition of the Baseline Report [6], and the system concept evaluation and selection of the Midterm Report [7]. In this report, the main focus is on designing some of the most crucial and defining subsystems of SPARTA, evaluating the performance and feasibility of the system, and laying the groundwork for making SPARTA a real and functioning system beyond the scope of the DSE.

The structure of the report is as follows: Chapter 2 and 3 cover the functional and market analysis for SPARTA, respectively. Based on these, system requirements are presented in Chapter 4. Next, a trade-off and iteration summary is provided in Chapter 5, defining the configuration of SPARTA. After that, the detailed design of subsystems starts. Chapter 6 and Chapter 7 present the airfoil and wing structure. Chapter 8 then designs the fuselage structure, followed by the design of control surfaces in Chapter 9, mechanical design in Chapter 10 and propulsion design in Chapter 11. Next, the communications and avionics are presented in Chapter 12 and 13 respectively. Recovery of SPARTA is discussed in Chapter 14. After that, system analysis is presented. Firstly, a system overview is presented in Chapter 15. Sustainability, risk and financial analysis are performed in Chapter 16, 17 and 18. The project design and development logic are presented in Chapter 19, outlining the next steps for SPARTA. To conclude, Chapter 20 will highlight the main findings of the report.

¹URL: <https://www.consilium.europa.eu/en/meetings/international-summit/2022/10/06/> [cited 23 June 2025]

2. System Functional Analysis

The system functional analysis serves a crucial role in describing what the system is capable of doing without necessarily diving into how or how well, which remains the domain of requirements. It was first visited during the Baseline Report [6] where it was developed at a high level without implying any design solutions so as not to influence the concept selection from said report. Now that the concept is set in stone and being actively developed, the functional analysis in this report focuses on modifying it to reflect all the decisions made until this point in the design, with some of the functionalities being developed in further detail. Later in this report, in the individual subsystem design chapters, the system functions are used to create subsystem functions and from them, subsystem requirements. Further in this chapter, the top-level functions and the structure of the diagrams are described.

The functional analysis compiles the functions of all mission elements of the system. In the case of SPARTA, these are: the Unmanned Aerial Vehicle (UAV), operators, designers and the manufacturers. While the prime focus of the design is on the SPARTA UAV itself, the functions of the other segments are reflected as well, albeit at a lower resolution.

Main Functionalities

The main functionalities of the system need to be determined to have an overview of what the system is capable of accomplishing. Firstly, the system needs to be designed, after which it can be manufactured. Now, it can be readied for its mission. When assigned to a mission, preparation is needed before launching the aerial system. This involves installing the payloads and morphing the system within the launch tube. Then, the system can be launched. During this stage, the system morphs from the folded configuration to the flight configuration and assumes active control of its state. Next, the cruise conditions can be reached, and the mission location shall be approached. Once the right location is reached, the assigned mission can be executed. This involves both the main design mission (ISTAR) and various civilian missions, for which only two examples are included. After completing the mission, the system navigates towards recovery. There it shall be caught using a net, or if recovery is not possible, belly land at a safe location. After recovery, the system is either maintained, stored or disassembled in case of End-of-Life (EOL).

During the entire flight, parallel to most in-flight functions, some general operations are conducted only partially, due to the requirement for autonomous flight. Since commands can adjust the flight plan at any given moment, communication and changes in the flight plan should always be possible. Furthermore, there is a constant need to scan the surroundings, measure and evaluate its state and act accordingly.

Diagrams

The top-level functions described in the previous subsection are summarised in the Functional Flow Diagram (FFD) as top-level functions (in blue). Note that parallel functions in the top level are unusual; however, **FUN-SYS-4** happens simultaneously as **FUN-SYS-5 - FUN-SYS-6**, as described in the previous section as well. These actions may include stability, communications and system checks, since the aerial system flies autonomously. This has been done to prevent having to repeat those steps on every level, since they can be performed during the entire flight. Additionally, the FFD is a continuous loop itself, outside of the manufacturing function **FUN-SYS-1** and the branch in **FUN-SYS-8** in case the EOL is reached **FUN-SYS-8.5**. Whenever the system should be reused, it loops back from **FUN-SYS-8** to **FUN-SYS-2**. The FFD can be found in Figures 2.1 and 2.2.

While the FFD is sequential, a Functional Breakdown Structure (FBS) is presented to show the relationships between functions in an 'AND' tree format. In this diagram, some functions are developed one level deeper to add more detail where possible. The FBS can be seen in Figure 2.3.

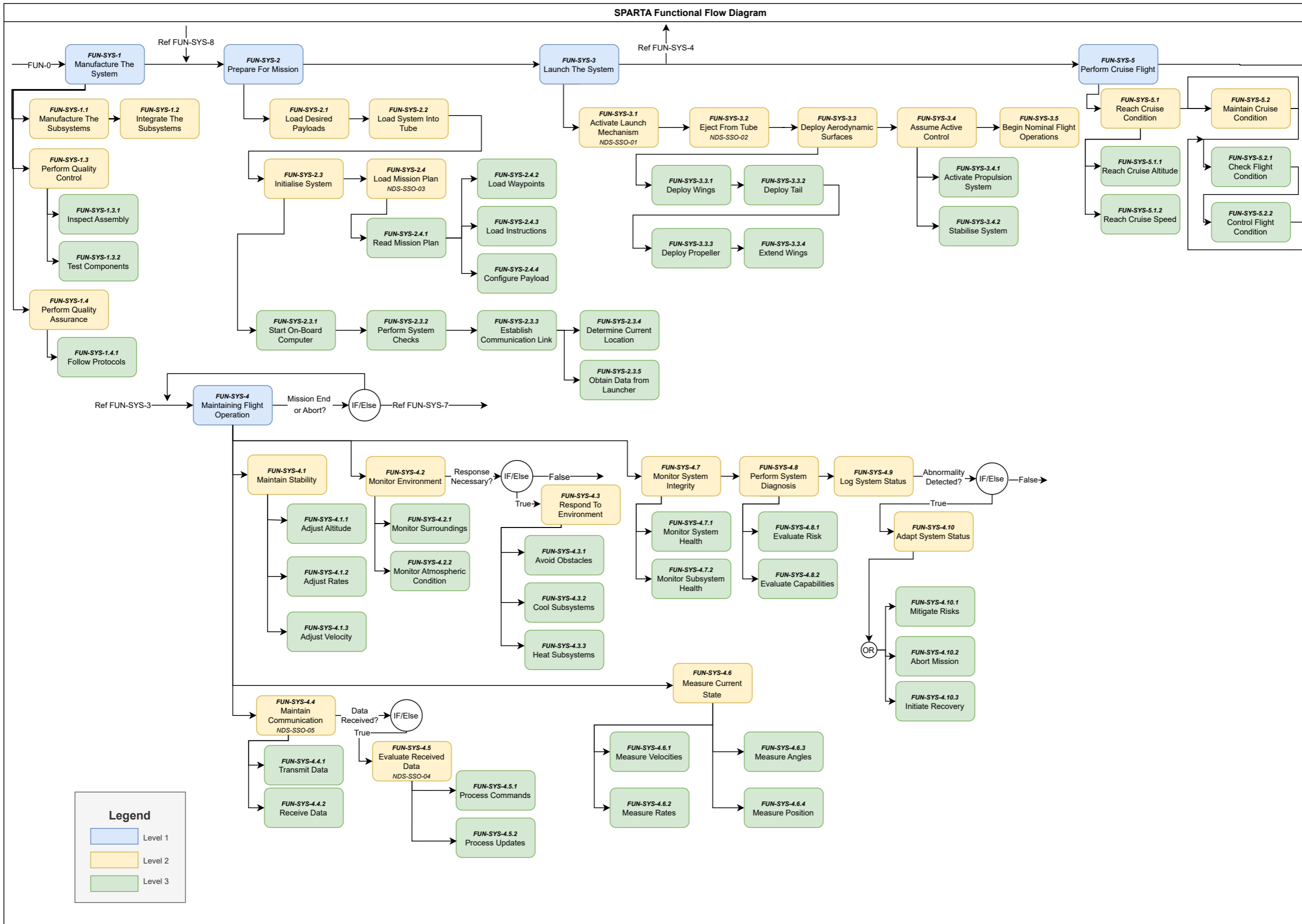


Figure 2.1: Functional Flow Diagram (part 1)

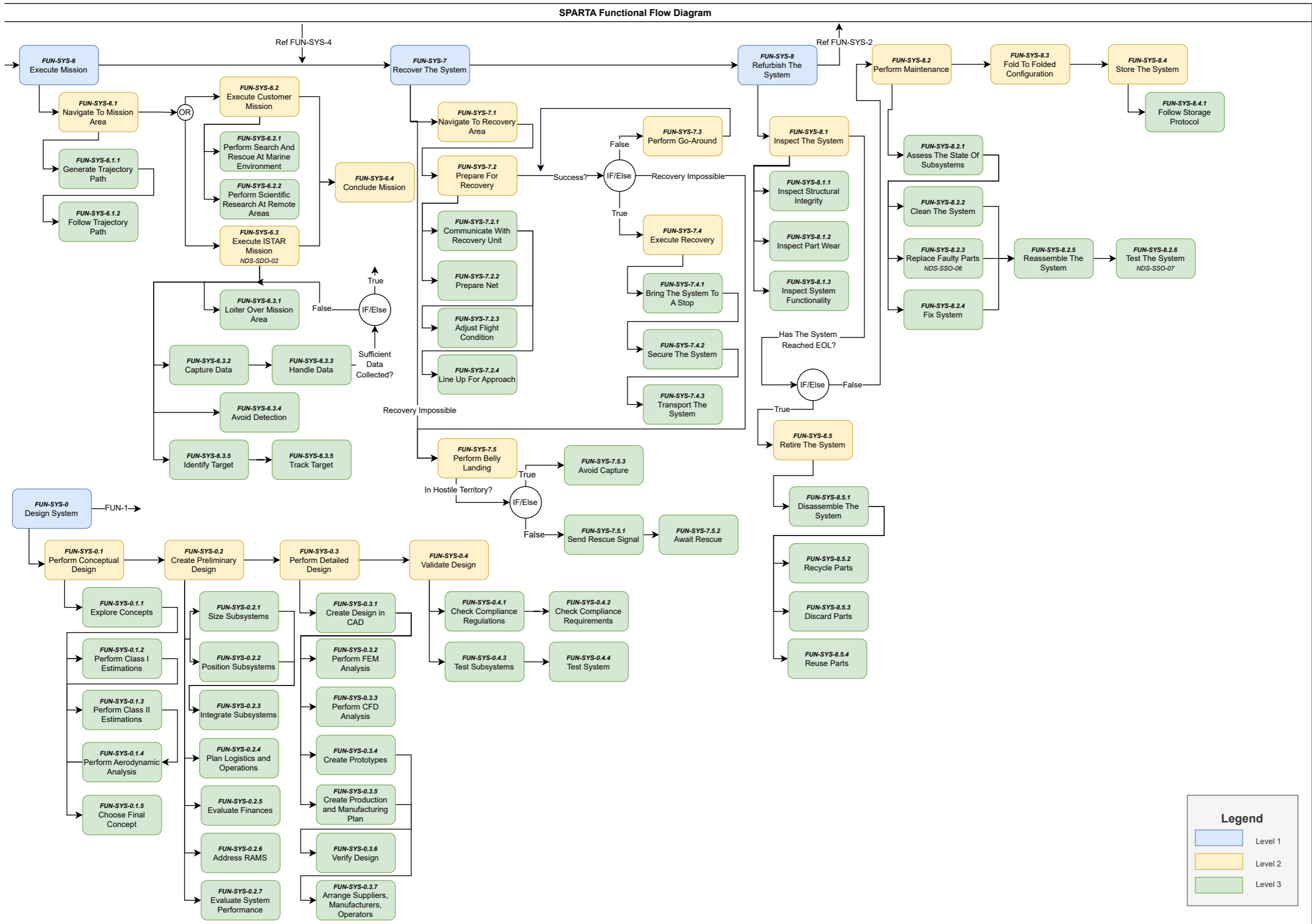


Figure 2.2: Functional Flow Diagram (part 2)

SPARTA Functional Breakdown Structure

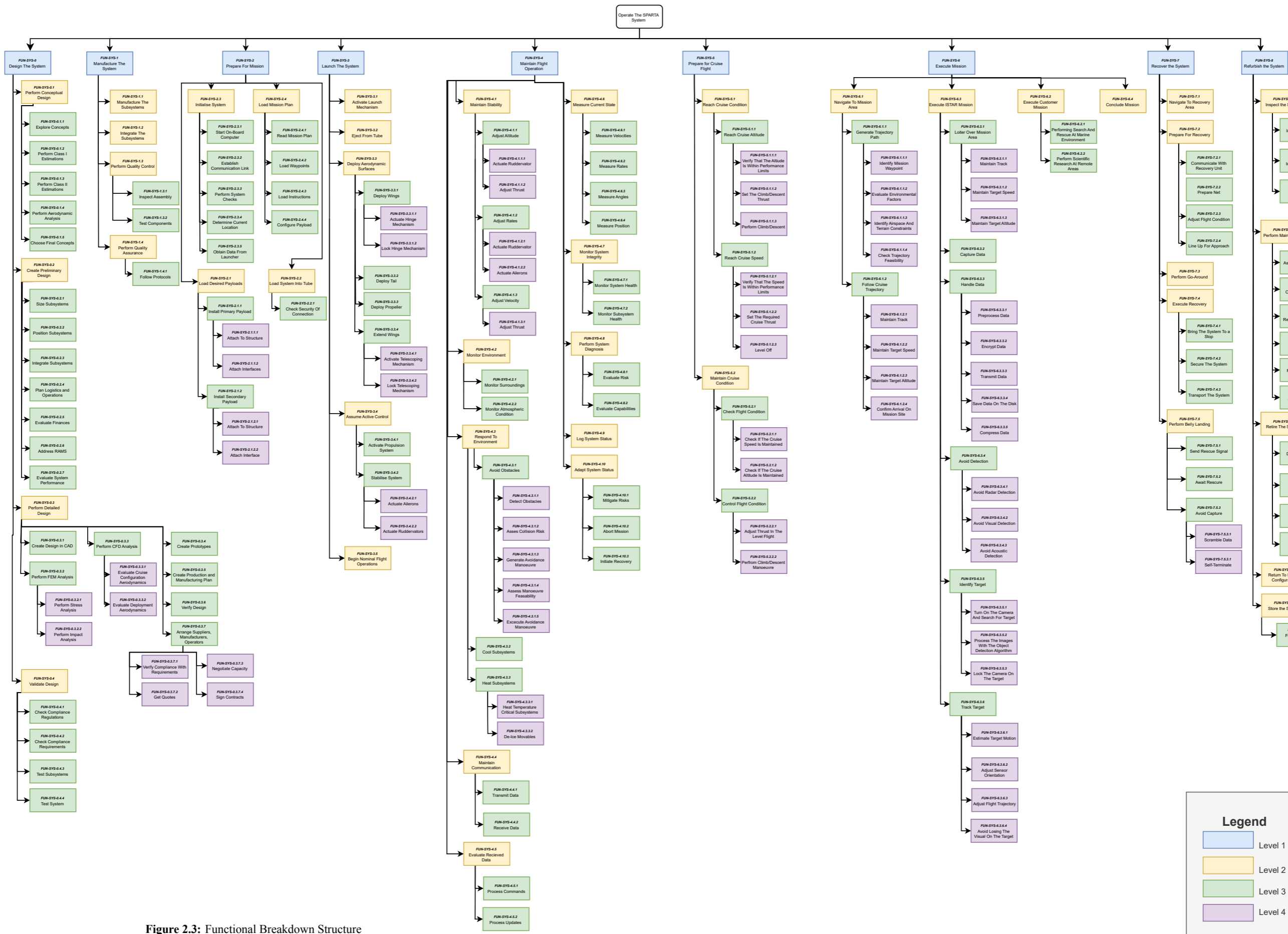


Figure 2.3: Functional Breakdown Structure

3. Market Analysis

This chapter evaluates the external factors that may impact the success of the SPARTA project, with a particular focus on current economic and geopolitical trends. A central focus is placed on the European ReArm program, which is expected to introduce new defence strategies, funding, and procurement across Europe. Understanding its influence is crucial for selecting proper strategies aligned with future market trends and demands, which is done in Section 3.1. Additionally, the analysis in Section 3.2 includes a Strengths, Weaknesses, Opportunities and Threats (SWOT) assessment. These insights will help define the system requirements.

3.1. Market Trends

SPARTA will enter a competitive yet rapidly expanding market. European defence budgets now focus on cost-effective companies within Europe, which will drive demand for innovative solutions and new designs. Additionally, there is an increasing demand for UAVs, as they offer significantly lower cost compared to larger military fighter jets, both in procurement and maintenance. This growth in demand is primarily driven by increased defence spending following the Ukraine crisis. Additionally, the latest ReArm Europe Plan will introduce a substantial increase in the budgets of European countries while restricting contracts to European-based companies.

In 2023, the European defence budget was specified at €254 billion, with predictions to increase to €326 billion in 2024 [8]. Project ReArm Europe aims to allocate up to €800 billion for urgent and significant defence investments through joint purchases [9]. This prominent project plans to allocate more than double the current budget's resources.

In recent years, the US (United States) Department of Defence has allocated between 3% and 5% of its total budget to drones¹. Assuming a similar expenditure on UAVs in Europe, therefore using an estimate of 4% of its budget would suggest a 2024 expense of around €13 billion, along with an additional future funding of €32 billion through the ReArm Europe Project. Ultimately, the future European UAV market can be estimated at approximately €40 to €50 billion, offering a significant opportunity for the SPARTA project.

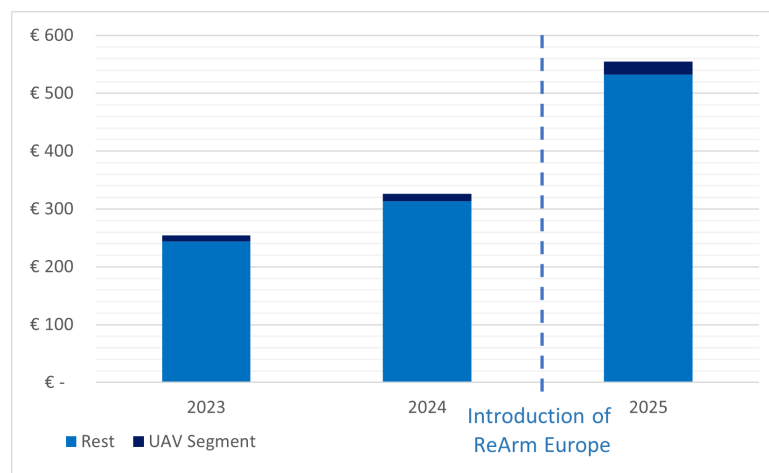


Figure 3.1: European Military Spending in billions of €

Figure 3.1 compares the European military defence budget for the years 2023 to 2025. It uses the previously mentioned estimate of 4% growth for drones, as well as an assumption of similar growth rates between 2025 and 2024 as between 2024 and 2023.

¹URL: <https://thegunzone.com/how-much-of-u-s-military-spending-is-on-drones/> [Cited 20 June 2025]

Competitor Analysis

Although there are multiple established companies in the market, such as Leonardo and Safran, none of them offer the unique tube-launched characteristics except for the US-based company Anduril with its Altius-600 series². This gap in the market presents an opportunity that the project aims to fulfil and benefit from.

This tube-launch solution provides a unique advantage for rapid deployment in hostile or denied airspace. It allows immediate mission execution without the need for nearby runways or launch pads. Furthermore, when an aircraft or helicopter launches the UAV at a specific altitude and speed, it significantly extends the UAV's operational range by conserving battery capacity for the actual mission rather than for the transit period.

Given the current trend in European-based solutions [10], there is a unique opportunity for SPARTA to enter the European market as a medium-cost option that offers versatility and rapid development while maintaining good performance in both endurance and range.

3.2. SWOT Analysis

A SWOT analysis was performed to properly categorise the market conditions and the potential advantages and disadvantages of the design. A full overview of the SWOT is presented in Table 3.1.

Table 3.1: SWOT Analysis

Strengths	Weaknesses
European-based manufacturing (S_1)	Higher manufacturing costs due to European production (W_1)
Rapid deployment time (S_2)	Low cruise speed (W_2)
Long operational range (S_3)	Limited communication range relative to unit cost (W_3)
High-resolution video capability (S_4)	Deployment method adds additional cost (W_4)
Modular payload system (S_5)	Lengthy installation process (W_5)
Multiple available launch methods (S_6)	Potentially high unit cost compared to competing systems (W_6)
Wide operational temperature range (S_7)	
Opportunities	Threats
Significant projected market growth (O_1)	De-escalation of conflict in Ukraine (T_1)
Increased defence spending in Europe (O_2)	Shortage of raw materials (T_2)
Non-American alternative system offering (O_3)	High level of market competition (T_3)
Geopolitical divergence between Europe and the US (O_4)	Potential decrease in European defence budgets (T_4)
Favourable current geopolitical trends (O_5)	Strengthening of US-European defence cooperation (T_5)
Growing frequency of extreme weather events (O_6)	Evolving military tactics and requirements (T_6)

The analysis identifies several key strengths, including European-based manufacturing, modular payload capabilities, and flexible launch methods, which provide clear market advantages. However, it also highlights weaknesses such as the relatively high unit cost and limited cruise speed that need to be addressed through design optimisation.

Additionally, there are opportunities for growth in the European defence sector, influenced by the political relations with the United States of America (USA) and the increasing demand for autonomous systems. These aspects present opportunities for market expansion. On the other hand, threats such as a decrease in military spending and material shortages demand new design requirements to mitigate or reduce these risks.

4. System Requirements

This chapter outlines the requirements that were established to provide a foundation for the design of SPARTA. All requirements were established and validated based on the needs of all stakeholders of the system. Systems requirements are divided into different categories based on their scope. The compliance and verification methods for these requirements are presented in Chapter 19.

²URL: <https://customer.janes.com/display/JUAVB108-JUAV> [cited 29 April 2025]

Table 4.1: System requirements of SPARTA

Code	Description
Performance Requirements	
REQ-SYS-01	The UAS shall have a range of at least 500 km.
REQ-SYS-02	The UAS shall have an endurance of at least 5 h.
REQ-SYS-03	The UAS shall have a cruise speed of at least 25 m/s.
REQ-SYS-36-17	The ISA sea level rate of climb at Maximum Take Off Weight (MTOW) shall be at least 1.5 m/s [11].
REQ-SYS-04	The autonomy of the UAS shall be at least level 4 in Clough's Autonomy Control Level Framework [12].
REQ-SYS-05	The UAS shall accommodate a primary payload (semi-spherical, 110 mm diameter, 120 mm length, 1.5 kg).
REQ-SYS-06	The UAS shall accommodate a secondary payload (90 x 90 x 200 mm, 2 kg).
REQ-SYS-07	Payloads shall be replaceable post-manufacturing within 60 min.
REQ-SYS-08	The UAS shall stream full High Definition (HD) video in real time to a carrier aircraft within 100 km.
REQ-SYS-09	The UAS shall stream full HD video in real time to a ground station within 100 km.
REQ-SYS-10	The UAS shall be launchable from an Airbus A400M at Indicated Air Speed (IAS) \geq 190 kts in steady flight.
REQ-SYS-11	The UAS shall be launchable from an Apache helicopter in hover.
REQ-SYS-12	The UAS shall be launchable from a tube launcher on the ground.
REQ-SYS-45	SPARTA shall be repairable.
REQ-SYS-52	The UAS shall be able to be transported outside of the launch tube.
REQ-SYS-53	The UAS shall maintain structural integrity during flight.
REQ-SYS-38	The system shall be equipped with a communication system.
Safety and Reliability Requirements	
REQ-SYS-13	The UAS shall have a failure rate of $< 1\%$ for its first 20 missions.
REQ-SYS-14	The UAS shall include a flight manual with launch envelopes for all launch configurations.
REQ-SYS-15	Collision probability with carrier aircraft or rotorcraft shall be $< 0.001\%$.
REQ-SYS-16	The UAS shall have an allowable storage temperature between $-70\text{ }^{\circ}\text{C}$ and $+70\text{ }^{\circ}\text{C}$.
REQ-SYS-17	The UAS shall have an operational temperature between $-70\text{ }^{\circ}\text{C}$ and $+50\text{ }^{\circ}\text{C}$.
REQ-SYS-18	The UAS shall operate in harsh environments.
REQ-SYS-34	The UAS shall be refurbishable within four hours.
REQ-SYS-34-01	The system shall be refurbished with tools that can be carried by a system operator.
REQ-SYS-34-02	The system shall, after refurbishment, be able to be stowed in the tube by a system operator.
Sustainability Requirements	
REQ-SYS-19	A lifecycle assessment of the system shall be performed.
REQ-SYS-20	Signature assessment (exhaust, noise, radar, infrared) shall be performed.
REQ-SYS-21	At least 90% of the UAS structure shall be recyclable.
Engineering Budget Requirements	
REQ-SYS-22	In stowed configuration, the UAS shall fit in a size A sonobuoy (123.9 mm \times 914.4 mm).
REQ-SYS-23	The UAS mass shall not exceed 25 kg.
Financial Requirements	
REQ-SYS-24	Development cost for the first 50 UASs shall not exceed €300 million (FY2025).
REQ-SYS-25	Cost price beyond 50 UASs shall not exceed €300,000 (FY2025).
REQ-SYS-26	Maintenance cost per mission shall not exceed €5,000 (FY2025).
Timeline and Resource Requirements	
REQ-SYS-27	First UAS shall be operational by the end of 2027.
REQ-SYS-28	Remaining 49 UASs shall be operational by the end of 2028.
REQ-SYS-29	From 2029, up to 50 UASs per month shall be manufacturable and deliverable.
REQ-SYS-30	From 2029, system lead time shall be < 6 weeks.
REQ-SYS-31	No components shall originate from outside European Political Community.
REQ-SYS-32	The system shall not use any materials from outside European Political Community, except for the raw materials needed for batteries and electronics.
REQ-SYS-33	The use of materials from outside of European Political Community shall not exceed 5%.
REQ-SYS-41	The shelf life of the system leading to initial performance shall be at least 10 years.
REQ-SYS-54	The system shall be capable of ramping up production in case of conflict.
Regulatory Requirements	
REQ-SYS-35	The UAS shall follow the rules for European defence projects as outlined by Permanent Structured Cooperation (PESCO) [13].

Code	Description
REQ-SYS-36	The system shall follow the NATO STANAG (North Atlantic Treaty Organisation Standardisation Agreement) 4703 standard [11].
REQ-SYS-43	The system shall not be made of materials that would be labelled hazardous under European Agency for Safety and Health at Work (EU-OSHA) regulations.
REQ-SYS-47	SPARTA shall comply with Regulation (EU) 2021/821 of the European Parliament and of the Council of 20 May 2021 [14].

5. Trade-off and Iteration Summary

In this chapter, a summary is given on the trade-off of design options, and the iteration results used throughout the subsystem design, presented in Section 5.1 and 5.2 respectively.

5.1. Trade-off Summary

Based on the system requirements established in Chapter 4, a Design Option Tree (DOT) was created, which generated five possible design options shown in Table 5.1. A trade-off is performed on these to determine the best design fit for SPARTA. The trade-off is based on six criteria, established based on their relevance and their assigned weight using Quality Function Deployment (QFD). These are summarised in Table 5.2.

Table 5.1: Summary of the design options for SPARTA

Design	Wing-Configuration	Tail-Configuration
1	Conventional	Canard
2	Conventional	V-Tail
3	Tandem	-
4	X-Wing	X-Tail
5	Conventional	Inverted V-Tail

Table 5.2: Summary of the chosen trade criteria and weights

Criteria	Parameter	Weight
Leftover Volume	V_{left}	20%
Component Accessibility		20%
Sustainability	Battery Mass	15%
Design Complexity		15%
Risk	Unacceptable Risks	20%
Stability Margin	Stability Margin	10%

To analyse the performance of the design options, a model is created. This model starts with class I weight estimation, after which wing and power loading, and performance diagrams are generated, establishing the basic dimensions of the UAS. After that, the propulsion, airframe, and wing subsystems are further analysed. This results in the creation of the V-n diagram and a class II weight estimation, which is used to approximate the Centre of Gravity (CG) locations of subsystems and the system, then used to size the tail. The model is used iteratively with XFLR5 for aerodynamic design.

The technical parameters of the trade-off are found with the model. Further analysis on the Risk and Design Complexity of each design is done to finalise the trade-off table, with its results presented in Table 5.3. A sensitivity analysis confirmed that 95% of the time, Design 5 wins; therefore considered the best fit to SPARTA.

Table 5.3: Completed trade-off table. Criteria are given in the top row, and design options are in the first column. The number of points scored is given. The colour is related to the number of points. The white circles, top right of the coloured cell, indicate the colour: G for green, B for blue, Y for yellow, R for red, and X for black.

	Leftover Volume	Component Accessibility	Sustainability	Design Complexity	Risk	Stability Margin	Final Score
Weight	20%	20%	15%	15%	20%	10%	100%
Design 1	0.36 B	0.66 B	0.67 G	0.33 Y	0.33 Y	1.00 G	0.56
Design 2	0.59 B	0.66 B	1.00 G	0.33 Y	0.33 Y	0.00 R	0.50
Design 3	Negative X	0.66 B	0.00 R	0.00 R	0.66 B	0.53 B	-
Design 4	Negative X	0.33 Y	0.00 R	0.33 Y	1.00 G	0.03 R	-
Design 5	1.00 G	1.00 G	0.21 Y	0.66 B	0.66 B	0.28 Y	0.69

5.2. Iteration Summary

After the trade-off was completed and Design 5 was chosen as the final design, certain changes to the model were made.

Firstly, the wing is assumed to use the maximum allowed wing geometry throughout the iterations, with the stall speed being now a free variable. This decision was made due to the stall speed being too high, and the reduction in wing size was not of utmost importance.

Secondly, the cruise speed has been set to 1.3 times the stall speed instead of being equal to the maximum endurance speed. This decision was made because the cruise speed was dangerously close to the stall speed, which could lead to a failure of the UAS.

Thirdly, more accurate estimations of mass values for certain components have been made available, leading to the replacement of their respective Class II Weight Estimation formulas. Additionally, the margin has been removed because miscellaneous parts have already been accounted for in the specific parts' masses.

Fourthly, now, if the battery mass increases during the iteration, it is added behind, such that the CG location of the battery is moved aft. This decision was made due to space constraints.

Lastly, now, the size of the tail is selected based on a scissor plot. This has been changed due to the questionable feasibility of the previous method, and the additional advantage of this method providing a clear view of the CG range for static stability. As this is the most significant change in the model, it is explained in more detail below.

After implementing those changes, the model iteration was performed once again, outputting the values (shown in Table 5.4) that are used for all of the following stages of the design procedure. For the future, it is recommended to

Table 5.4: Summary of parameters for the UAS

Parameter	Description	Value	Parameter	Description	Value
Battery Density			Masses		
ρ_m [Wh/kg]	Mass density	450	m [kg]	Total mass	14.288
ρ_V [Wh/L]	Volume density	1000	m_{engine} [kg]	Engine mass	0.260
Speeds			m_{fus} [kg]	Fuselage mass	1.386
v_{stall} [m/s]	Stall speed	31.024	m_{wing} [kg]	Wing mass	2.556
v_{cruise} [m/s]	Cruise speed	40.332	m_{tail} [kg]	Tail mass	0.799
v_{max} [m/s]	Max cruise speed	55.567	m_{avionics} [kg]	Avionics mass	0.350
v_e [m/s]	Max endurance speed	33.919	m_{comms} [kg]	Communications mass	0.450
v_r [m/s]	Max range speed	36.970	m_{prop} [kg]	Propulsion mass	0.510
v_{dive} [m/s]	Dive speed	61.742	m_{batt} [kg]	Battery mass	4.136
Aerodynamics			$m_{\text{payload,1}}$ [kg]	Payload 1 mass	1.500
$C_{L_{\text{max}}}$ [-] ¹	Maximum C_L	1.602	$m_{\text{payload,2}}$ [kg]	Payload 2 mass	2.000
C_{D_0} [-]	Zero-lift C_D	0.022	m_{trans} [kg]	Transformers mass	0.200
C_{L_0} [-]	Zero-angle-of-attack C_L	0.644	m_{thermal} [kg]	Thermal mass	0.400
C_{L_α} [1/rad]	Lift curve slope	6.192	Locations (from nose)		
C_{L_e} [-]	Endurance C_L	1.340	x_{wing} [m]	Wing location	0.360
C_{D_e} [-]	Endurance C_D	0.040	x_{tail} [m]	Tail location	0.820
C_{L_r} [-]	Range C_L	1.128	x_{engine} [m]	Engine location	0.840
C_{D_r} [-]	Range C_D	0.033	x_{comms} [m]	Comms location	0.500
$C_{L_{\text{cruise}}}$ [-]	Cruise C_L	0.948	$x_{\text{payload,1}}$ [m]	Payload 1 location	0.060
$C_{D_{\text{cruise}}}$ [-]	Cruise C_D	0.028	$x_{\text{payload,2}}$ [m]	Payload 2 location	0.220
C_{L_w} [-]	Wing C_L	1.047	x_{battery} [m]	Battery location	0.474
C_{L_t} [-]	Tail C_L	0.620	x_{avionics} [m]	Avionics location	0.500
$C_{L_{\alpha,w}}$ [1/rad]	Wing lift curve slope	5.642	x_{trans} [m]	Transformers location	0.500
$C_{L_{\alpha,t}}$ [1/rad]	Tail lift curve slope	3.188	x_{thermal} [m]	Thermal location	0.590
Wing Geometry			x_{cg} [m]	CG location	0.404

¹Obtained by taking the maximum lift coefficient from the results of an XFRL5 simulation.

Parameter	Description	Value	Parameter	Description	Value
S [m ²]	Wing surface area	0.148	z_{cg} [m]	CG location (from bottom of the fuselage)	0.051
b [m]	Wing span	1.980	x_{ac} [m]	Aerodynamic centre location	0.379
c_r [m]	Root chord	0.069	Performance		
c_t [m]	Tip chord	0.080	W/S [N/m ²]	Wing loading	944.3
A [-]	Aspect ratio	26.40	W/P [N/W]	Power loading	0.298
Λ [deg]	Sweep angle	0	η_p [-]	Propeller efficiency	0.800
Γ [deg]	Dihedral angle	0	RoC [m/s]	Rate of climb	1.500
t/c [-]	Thickness-to-chord ratio	0.100	R [km]	Range	726
Tail Geometry			E [h]	Endurance	5
S_t [m ²]	Tail surface area	0.028	L/D [-]	Lift-to-drag ratio	33.4
b_t [m]	Tail span	0.563	n_{max} [-]	Max load factor	3.80
c_{tail} [m]	Tail chord	0.050	n_{min} [-]	Min load factor	-1.50
A_t [-]	Tail aspect ratio	11.27	$n_{ult,max}$ [-]	Ultimate max load factor	4.94
Λ_t [deg]	Tail sweep angle	0	$n_{ult,min}$ [-]	Ultimate min load factor	-1.95
Γ_t [deg]	Tail dihedral angle	37.50			
$(t/c)_t$ [-]	Tail thickness-to-chord ratio	0.120			

Tail Sizing

As explained above, the tail is sized using a scissor plot. Figure 5.1 shows the scissor plot for the Design 5 UAS. The stability curve can be expressed as,

$$\frac{S_t}{S} = \left(\frac{1}{\frac{C_{L_{\alpha,t}} l_t}{C_{L_{\alpha,w}} \bar{c}}} \bar{x}_{cg} - \frac{\bar{x}_{ac} - SM}{\frac{C_{L_{\alpha,t}} l_t}{C_{L_{\alpha,w}} \bar{c}}} \right) \cos \Gamma_t, \quad (5.1)$$

with the effects of downwash excluded, l_t being the distance from wing aerodynamic centre to the tail aerodynamic centre, \bar{x}_{cg} being the CG location in x-direction normalized with \bar{c} , \bar{x}_{ac} being the wing aerodynamic centre location in x-direction normalized with \bar{c} , and $SM = 5\%$ being the stability margin [15]. Note that Equation (5.1) includes the V-tail adjustment in the form of multiplication by $\cos \Gamma_t$, with Γ_t being the tail dihedral angle.

The control curve can be expressed as,

$$\frac{S_t}{S} = \left(\frac{1}{\frac{C_{L_t} l_t}{C_{L_w} \bar{c}}} \bar{x}_{cg} + \frac{\frac{C_{m_{ac}}}{C_{L_w}} - \bar{x}_{ac}}{\frac{C_{L_t} l_t}{C_{L_w} \bar{c}}} \right) \cos \Gamma_t, \quad (5.2)$$

with the effects of downwash excluded, C_{L_t} being obtained using Equation (5.3), and $C_{m_{ac}}$ being the moment coefficient around wing aerodynamic centre obtained using Equation (5.4), with b_f being the fuselage width, l_f being the fuselage length, and h_f being the fuselage height [16]. Note that, again, Equation (5.2) includes the V-tail adjustment in the form of multiplication by $\cos \Gamma_t$.

$$C_{L_t} = -0.35A_t^{1/3} \quad (5.3)$$

$$C_{m_{ac}} = C_{m_{airfoil}} \left(\frac{A \cos^2 \Lambda}{A + 2 \cos \Lambda} \right) - 1.8 \left(1 - \frac{2.5b_f}{l_f} \right) \frac{\pi b_f h_f l_f C_{L_0}}{4S\bar{c} C_{L_w}} \quad (5.4)$$

Now, coming back to Figure 5.1, it is important to note that its horizontal axis is normalised to the mean aerodynamic chord (\bar{c}), and that it starts from the leading edge of the wing. Another thing to note is that the purple line is created by plotting the maximum tail-surface-to-wing-surface ratio $\left(\frac{S_t}{S}\right)_{max}$, with $S_{t_{max}} = 0.030 \text{ m}^2$ (constrained by space and explained further in Section 15.2) and $S = 0.148 \text{ m}^2$. That means for static stability,

the \bar{x}_{cg} cannot be aft of the vertical purple line. To size the tail for the UAS, two extreme CG locations were considered:

1. $\bar{x}_{cg, \max \text{ front}}$ represents a case where the entire secondary payload mass is positioned at the front of the secondary payload,
2. $\bar{x}_{cg, \max \text{ aft}}$ represents a case where secondary payload mass is equal to 0 kg.

These cases were chosen due to the secondary payload being the only potential cause of change in the CG location. The maximum possible aft CG turned out to be the definitive case, and it yielded $\frac{S_t}{S} = 0.190$, which made $S_t = 0.028 \text{ m}^2$ (as seen in Table 5.4). To conclude, the UAS is statically stable, even for the extreme CG location cases.

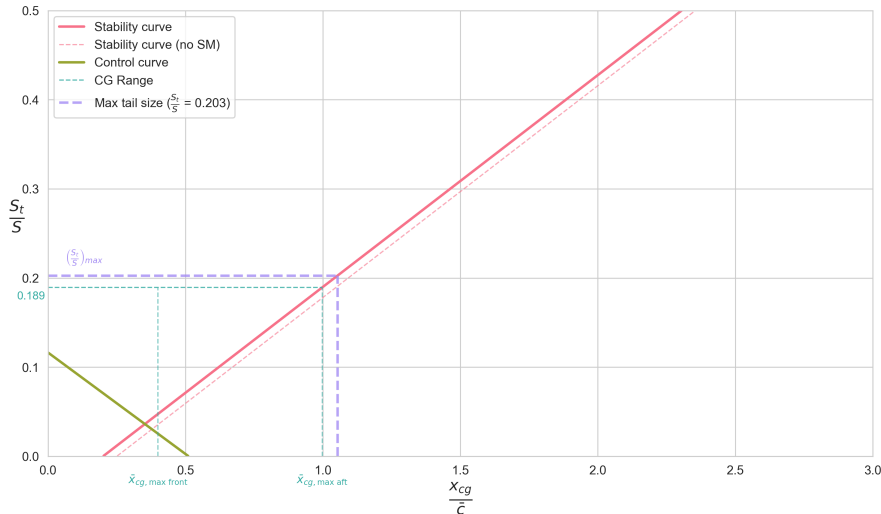


Figure 5.1: Scissor plot

6. Airfoil Design

In the trade-off shown in Chapter 5, iterations used the standard NACA 2412 airfoil, from the National Advisory Committee for Aeronautics (NACA). However, this remains open for further optimisation to the specific mission. This is covered in this chapter; Section 6.1 and Section 6.2 cover the functional and requirement analysis, respectively. Section 6.3 selects an airfoil shape, which is then used to obtain a final configuration in Section 6.4. Next, Section 6.5 checks compliance with requirements. Finally, Section 6.6 gives recommendations for future development.

6.1. Functional Analysis

Below in Table 6.1, the functions of the airfoil are addressed.

Table 6.1: Functions relevant for the airfoil design

Code	Description	Origin
FUN-AIR-01	Adjust the altitude of the system.	FUN-SYS-4.1.1
FUN-AIR-02	House the telescoping mechanism.	REQ-SYS-22

6.2. Requirement Analysis

Having obtained the required functions, they can be combined with existing system and subsystem requirements to derive a list of requirements for the airfoil to comply with and guide its design. They can be found in Table

6.2. On these requirements, a contingency factor must be applied at this stage of the design. A size contingency of 10% was given for the preliminary design stage of the lifting device. For the final design phase, this is 2%.

Table 6.2: Requirements relevant for the airfoil design

Code	Description	Origin
REQ-AIR-01	The lifting system shall provide lift.	FUN-AIR-01
REQ-AIR-02	The maximum lift coefficient of the airfoil shall be at least 10% greater than the design lift coefficient.	FUN-AIR-01
REQ-AIR-03	The chord length of the wing shall be at most 0.08 m.	REQ-SYS-22
REQ-AIR-04	The thickness of the wing cross section shall be at most 0.011 m.	REQ-SYS-22
REQ-AIR-05	The thickness of the wing cross section shall be at least 0.006 m.	FUN-AIR-02
REQ-AIR-06	Signature assessment shall be performed.	REQ-SYS-20

6.3. Airfoil Selection

To select the airfoil properly, a trade-off is performed. Firstly, the criteria and weights are addressed, after which an analysis obtains the required parameters. Finally, the trade-off is done, and a final airfoil is selected. Note that for this selection, it is assumed that both the inner and outer section of the wing use the same airfoil profile, and the analysis is done on the iteration results obtained in the trade-off between the design concepts; it is not up-to-date with the iteration results from Chapter 5 and will use a 10% contingency factor.

6.3.1. Trade-Off Criteria & Weights

Firstly, trade-off criteria are established based on the flight characteristics and properties of the design resulting from the trade-off. Next, weights are established using the Analytical Hierarchy Process (AHP) method [17] which compares the importance of individual criterion against each other in a pairwise comparison matrix from importance one to five, seen in Table 6.3, after which the outcome is normalised to obtain percentages.

From the iterations, it is observed that the cruise speed was relatively close to the stall speed, endangering the system when manoeuvring. Therefore, both the cruise speed can be increased and the stall speed can be decreased. To decrease the stall speed, a higher maximum lift coefficient is required. With a design lift coefficient ($C_{L_{\text{design}}}$) equal to 1.09 (using Equation (6.1)), a minimum required maximum airfoil lift coefficient ($C_{l_{\text{max}}}$) of 1.20 is needed according to **REQ-AIR-02**. Since stall can lead to loss of control and can potentially endanger SPARTA, achieving a high $C_{l_{\text{max}}}$ is essential.

$$C_{L_{\text{design}}} = \frac{1.1W}{\frac{1}{2}\rho v_{\text{cruise}}^2 S} \quad (6.1)$$

Here, W is the total weight of the system. Furthermore, for the given mission, the Reynolds number is only 150,000, for which viscous forces significantly influence the boundary layer behaviour and flow separation [18]. Therefore, a sharp drop in lift at stall shall be avoided [19]. A more gradual flow separation can be obtained by increasing the thickness-to-chord ratio (t/c), which also decreases the structural weight of the wing [20]. However, a higher t/c increases the amount of friction drag of the wing since the wetted surface area increases. The minimum and maximum t/c can be found from **REQ-AIR-03**, **REQ-AIR-04** and **REQ-AIR-05**, including the contingency factor, equal to 0.091 and 0.138, respectively. This criterion is slightly less important than $C_{l_{\text{max}}}$, since it gives benefits in weight and stall characteristics, but doesn't prevent it, and adds additional drag.

Next, endurance is a driving performance requirement for SPARTA (**REQ-SYS-02**). To optimise flight for this, the ratio of C_L^3/C_D^2 can be maximised. Compared to $C_{l_{\text{max}}}$, it is less important, however it can significantly increase endurance performance and improve overall aerodynamic efficiency of SPARTA. It is therefore seen as equally important as the t/c ratio.

Furthermore, the iteration results showed that the system is slightly unstable. The airfoil choice can slightly improve this via its moment coefficient (C_m) in case it is negative. However, since a UAV can be slightly statically unstable, this criterion is not deemed as important as the others.

Finally, due to the military nature of SPARTA, radar stealth is considered in the airfoil design (**REQ-AIR-06**). A flatter bottom of the airfoil can reduce the radar cross section of the wing structure, since a flatter bottom

reduce the probability that the specular reflection of incoming radar waves is reflected back to its origin. More details on this are covered in Section 15.3.1. Furthermore, the structure of the wing is influenced by the flatness of the bottom side of the wing. Since the wing is telescopic, the inner wing needs to fit in the outer wing, where a flatter bottom allows for easier fitting. This parameter is less straightforward to calculate; a linear regression can be performed on the bottom side of the wing, and the Root Mean Square (RMS) multiplied by 100 used. This parameter is called F_b . The relevance of this criterion is relatively high; a highly curved airfoil might not allow for telescoping mechanism, and storing the inner and outer wing can be hard. Since it also covers stealth, it encompasses a large range of constraints for SPARTA, and is therefore deemed more important than all other criteria, except for $C_{l_{\max}}$.

The above discussed influences form the trade-off criteria. Note that cost and risk differ very little between the designs and are therefore not considered in the trade-off. Sustainability is partially covered with C_L^3/C_D^2 ; higher values ensure more efficient flight, improving sustainability. The importance of the criteria are plugged into Table 6.3, with a summarising trade-off table presented in Table 6.4.

Table 6.3: AHP pairwise comparison values and their resulting normalised weights

Criteria	$C_{l_{\max}}$	C_L^3/C_D^2	C_m	t/c	F_b	Total	Normalised Weight
$C_{l_{\max}}$	1.00	2.00	5.00	2.00	1.50	11.50	0.32
C_L^3/C_D^2	0.50	1.00	4.00	1.00	0.75	7.25	0.20
C_m	0.20	0.25	1.00	0.25	0.25	1.95	0.05
t/c	0.50	1.00	4.00	1.00	0.75	7.25	0.20
F_b	0.67	1.33	4.00	1.33	1.00	8.33	0.23

Table 6.4: Trade-off criteria and their respective weights

Criteria	Parameter	To be	Bottom Line	Weight
Maximum lift coefficient of the airfoil.	$C_{l_{\max}}$	Maximised	1.20	30%
Endurance performance of the airfoil.	C_L^3/C_D^2	Maximised	75% of Best Design	20%
Stability of the airfoil.	C_m	Minimised	0.0	5%
Thickness of the airfoil.	t/c	Maximised	0.091	20%
Flatness of the bottom of the airfoil.	F_b	Minimised	Worst Design	25%

The parameters are scaled linearly from zero to one, with the bottom line representing zero points. The bottom line is formed by the requirements or established based on other design options. The colours are assigned based on the amount of points given, shown in Table 6.5.

Table 6.5: Colouring scale. The white circles, top right of the coloured cell, indicate the colour: G for green, B for blue, Y for yellow and R for red.

Scale	Points	Scale	Points
Excellent (G)	0.67-1	Neutral (Y)	0.01-0.34
Good (B)	0.34-0.66	Bad (R)	0

6.3.2. Airfoil Analysis

To perform the trade-off, the first step is to find candidates that fit the mission description of SPARTA. After that, a model is created that determines the given parameters for each airfoil, after which the model is verified and validated.

Airfoil Options

Possible candidates fitting the mission of SPARTA are obtained firstly. It is important that these candidates cover a wide range of airfoil characteristics, to see potential strengths and flaws. Furthermore, the airfoils need to work at low Reynolds number and relative high C_L .

Firstly, two standard airfoils are selected, forming the baseline for performance to compare the chosen airfoils. The first required airfoil is a symmetrical airfoil, the NACA 0012. Secondly, a commonly used cambered airfoil is the NACA 4412 [21] forming the baseline in comparison to high lift airfoils. With these two baselines established, airfoils fulfilling the requirements can be selected, obtained via several sources [22–25]. The airfoils selected were minimised in similarities; multiple airfoils having the same shape won't show differences in the trade-off. Figure 6.1 shows the final candidates for the trade-off, with the images obtained via `Airfoil Tools`¹.

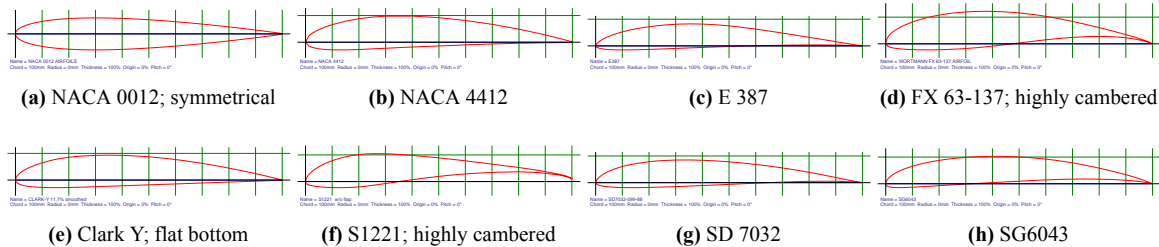


Figure 6.1: Airfoils selected for the trade-off

Simulation

To analyse the performance of the airfoils, existing software can be used such as XFOIL. Using the library `aerosandbox`, XFOIL can be integrated into python. It requires a ".dat" file in Selig format and three inputs; Mach number M , Re and N_{crit} . Here N_{crit} is the amplification factor that describes how easily the flow transitions from laminar to turbulent². As a conservative estimate, N_{crit} is set to 5; at low Reynolds numbers, transition is sensitive to disturbances [18]. The simulation then obtains all of the performance characteristics for the given flight conditions and required $C_{L_{design}}$.

Finally, the flatness of the bottom is estimated. For this, linear regression from the library `sklearn` is used. The error is quantified RMS, which penalises large errors more, identifying high curvature.

Verification & Validation

To verify that the simulation performs as supposed, it is verified and validated. Since the simulation uses already validated software, not much testing is required. Unit tests are conducted and system tests plot graphs for the airfoil polars, which are compared to polars constructed in `Airfoil Tools`¹ and show similar results for different values of N_{crit} and Re . Furthermore, the values for F_b are verified visually.

6.3.3. Trade-Off Results

Based on the analysis performed in the previous section, all values for the trade-off are obtained. The results are shown in Table 6.6.

The trade-off shows that for the given weights and criteria, high lift airfoils with high negative C_m fit well to SPARTA, even though they score worse in F_b . From the last column in this table, it can be seen that the winning airfoil choice is the SG6043 [25], scoring excellent in the endurance criterion compared to the others.

6.3.4. Sensitivity Analysis

To validate the outcome of the trade-off, a sensitivity analysis is performed, in which 60.4% of the times, the SG6043 wins, with the closest competitor being the FX 63-137, winning 16.3% of the times.

To further analyse the sensitivity of the trade-off, the input parameter Re and N_{crit} can be modified, and the endurance requirement can be changed to the range requirement (C_L/C_D), since getting behind enemy lines is deemed more important than flying for a long time³. The results of these modifications are shown in Table 6.7.

As can be seen from Table 6.7, changing N_{crit} does not change the outcome of the trade-off. Increasing Re and the criterion does however give different winning airfoils. Note however that they win by a margin of only 0.01. Combining this with the sensitivity analysis on the weights, the SG6043 is selected as the winning airfoil, and the trade-off is deemed valid for the given flight conditions.

¹URL: <http://airfoiltools.com/> [cited 23 June 2025]

²URL: https://web.mit.edu/aeroutil_v1.0/xfoil_doc.txt [cited 12 June 2025]

³From discussion of S. van Elsloo with M. Voskuil

Table 6.6: Completed trade-off table. Criteria are given in the top row, and design options are in the first column. The actual values for the parameters are given. The colour is related to the amount of points. The white circles, top right of the coloured cell, indicate the colour; G for green, B for blue, Y for yellow and R for red.

Criteria	$C_{l_{\max}}$	C_L^3/C_D^2	C_m	t/c	F_b	Score
Weight	30%	20%	5%	20%	25%	100%
NACA 0012	1.05 (R)	718.92 (R)	0.04 (R)	0.12 (B)	0.78 (B)	0.23
NACA 4412	1.34 (Y)	5015.29 (R)	-0.09 (B)	0.12 (B)	0.15 (G)	0.45
E387	1.26 (Y)	5839.63 (B)	-0.07 (B)	0.091 (R)	0.27 (G)	0.35
FX 63-137	1.63 (B)	5135.09 (Y)	-0.20 (G)	0.137 (G)	1.12 (Y)	0.49
Clark-Y	1.28 (Y)	3874.16 (R)	-0.06 (Y)	0.117 (B)	0.09 (G)	0.41
S1221	1.87 (G)	3855.72 (R)	-0.16 (G)	0.121 (B)	1.3 (R)	0.47
SD 7032	1.42 (B)	4898.51 (R)	-0.08 (B)	0.10 (Y)	0.31 (G)	0.36
SG6043	1.55 (B)	6794.36 (G)	-0.16 (G)	0.10 (Y)	0.72 (B)	0.56

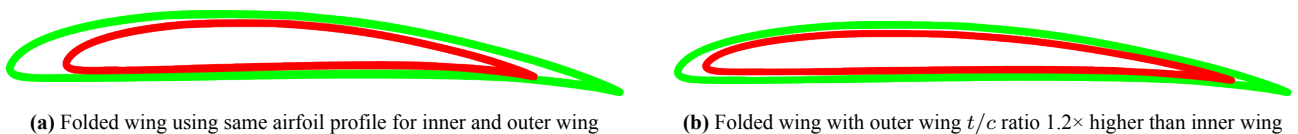
Table 6.7: Sensitivity study on trade-off outcome for airfoil selection.

Parameter	Original Value	New Value	Effect
Re	1.5E5	2E5	SG6043 wins with 0.57, by a margin of 0.08
	1.5E5	1E5	NACA4412, FX 63-137 score equally good at 0.55 points, with the SG6043 following at 0.54 points
N_{crit}	5	4	SG6043 wins with 0.57, by a margin of 0.07
	5	6	SG6043 wins with 0.56, by a margin of 0.06
Criterion	C_L^3/C_D^2	C_L/C_D	FX 63-137 wins by a margin of 0.01 from the SG6043

6.4. Final Airfoil Configuration

The airfoil profile selected in the previous section is used to generate the final set of iterations results presented in Chapter 5. At this point, the analysis can be performed on the up-to-date iteration results, entering the final design phase using contingency of 2%. With the new iteration results, the airfoil selected still requires some further analysis towards the telescoping nature of the wing, which is performed in this section.

For the currently selected airfoil, assuming both the inner and outer wing use the profile, the cross section of the folded configuration is as shown in Figure 6.2a. As can be seen, the storing efficiency is low, and there is a gap between the leading edges of the inner and outer wing. To tackle this issue, further analysis is done on the sizing of the wing. The outcome of this analysis is to adjust the t/c ratio for the inner and outer wing; optimally the outer wing has a t/c that is 1.2 times bigger than the t/c of the inner wing. For this configuration, the folded cross section is as shown in Figure 6.2b.



(a) Folded wing using same airfoil profile for inner and outer wing

(b) Folded wing with outer wing t/c ratio 1.2× higher than inner wing

Figure 6.2: Comparison of folded wing cross sections: (a) identical airfoils vs. (b) adjusted t/c ratios for inner and outer wing.

It can be seen that for the new cross section, the gap between the leading edges of the inner and outer wing has become smaller, as is the gap at the trailing edge. Therefore, the aim is to select two airfoils with a t/c difference of 20%. The SG6043 profile is modified to new t/c ratios by scaling the y -coordinates of the airfoil data points. The trade-off from last section is performed again, with the results shown in Table 6.8. Note that with the new contingency, the bottom line for t/c has become 7.5%. Furthermore, the new iteration results require a $C_{L_{\text{design}}}$ of 1.20, resulting in a bottom line $C_{l_{\max}}$ of 1.32.

Table 6.8: Completed trade-off table. Criteria are given in the top row, and design options are in the first column. The actual values for the parameters are given. The colour is related to the amount of points. The white circles, top right of the coloured cell, indicate the colour; G for green, B for blue, Y for yellow and R for red.

	$C_{l_{max}}$	C_L^3/C_D^2	C_m	t/c	F_b	Score
Weight	30%	20%	5%	20%	25%	100%
SG6043 8	1.48 (B)	5237.66 (R)	-0.12 (B)	0.083 (Y)	0.6 (G)	0.44
SG6043 9	1.52 (B)	7541.1 (B)	-0.14 (G)	0.091 (Y)	0.66 (G)	0.60
SG6043 10	1.57 (G)	8262.99 (G)	-0.16 (G)	0.10 (B)	0.72 (B)	0.70
SG6043 11	1.61 (G)	7809.59 (G)	-0.17 (G)	0.11 (B)	0.79 (B)	0.68
SG6043 12	1.65 (G)	6936.18 (B)	-0.18 (G)	0.12 (G)	0.87 (Y)	0.60
SG6043 13	1.68 (G)	6207.5 (R)	-0.19 (G)	0.13 (G)	0.93 (R)	0.55

Table 6.8 shows that the SG6043 profile with a t/c of ten or eleven percent perform almost equally good. The profiles with a t/c nine and twelve percent follow closely, scoring slightly worse in the endurance criterion. Airfoils smaller than nine or bigger than twelve have significant performance loss with respect to endurance. Summing up the scores results in a winning combination of ten and twelve, winning marginally from nine and eleven. Aerodynamically, the difference between the combinations is small, however for sizing, more internal space imposes less strict sizing constraints for the telescoping mechanism and aileron mechanisms, which still have to be designed at this point in the design stage. The polars of the final airfoil configuration can be seen in Figure 6.3.

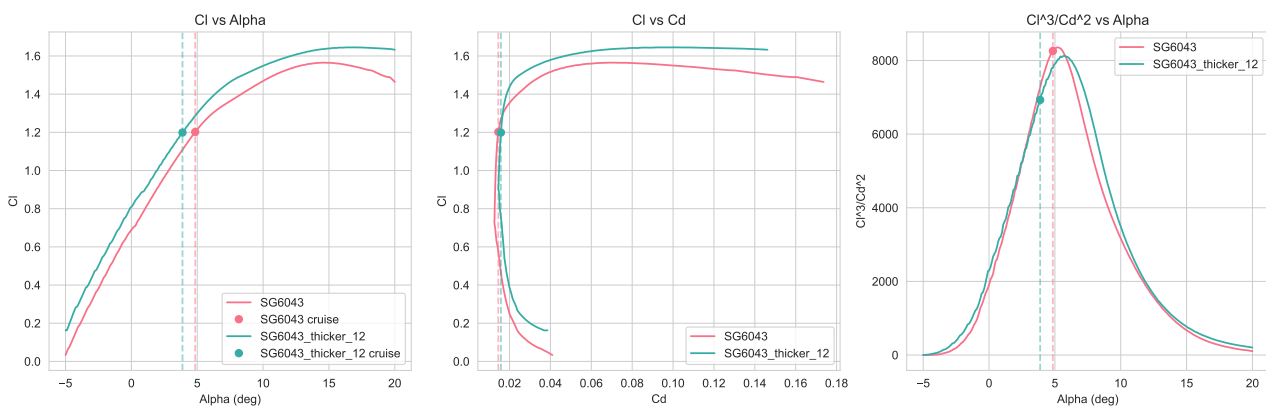


Figure 6.3: Polars for the two selected airfoils for the final wing configuration

6.5. Compliance Matrix

For the requirements presented in Section 6.1, it shall be confirmed that they are actually met. This can be done using a compliance matrix, shown in Table 6.9. It can be seen that all requirements are met for the airfoil selection.

Table 6.9: Requirement compliance matrix for the airfoil selection

Code	Compliance	Code	Compliance
REQ-AIR-01	(G)	REQ-AIR-04	(G)
REQ-AIR-02	(G)	REQ-AIR-05	(G)
REQ-AIR-03	(G)	REQ-AIR-06	(G)

6.6. Recommendations

For future development on the airfoils, firstly the input parameters Re and N_{crit} must be approximated better, since the outcome of the airfoil selection depends on it. Furthermore, adjustment of t/c ratios of the SG6043 to decimal points can be done in the final configuration section to find the most optimal configuration. This

can further optimise the wing configuration. If time allows, it is also possible to create a self-made airfoil. By analysing more airfoils and taking the ones performing excellent, interpolation can be done to get the most optimal airfoil design.

7. Wing Structure

This chapter designs the wing structure of the UAS using a coupled model. It discusses the different functions of the wing design in Section 7.1. In 7.2, the requirements are outlined to fulfil the functions. To provide reasoning behind the design, Section 7.3 discusses the analysis of the structure. The aerodynamic properties of the wing are analysed in Section 7.4 and Section 7.5 will analyse the performance during the deployment out of the tube. Following in Section 7.6, the structural properties of the wing are shown. Next, Section 7.7 analyses the effects of aeroelasticity on the UAS. Section 7.6.1 presents the verification tests for the wing analysis model. Furthermore, Section 7.9 the sustainability is discussed, Section 7.10 highlights the risks of the wing, in Section 7.11 the Reliability, Availability, Maintainability and Safety (RAMS) analysis is performed, in Section 7.12 the financial analysis of the wing is performed, Section 7.13 highlights the compliance matrix, and lastly Section 7.14 highlights the recommendations for further research.

7.1. Functional Analysis

This section presents the functional analysis of the wing structure in Table 7.1.

Table 7.1: Functions relevant for the wing design

Code	Description	Origin
FUN-WING-01	Provide lift	FUN-SYS-5
FUN-WING-02	Withstand loads	FUN-SYS-5
FUN-WING-03	Enable morphing	FUN-SYS-3.3
FUN-WING-04	Enable extension	FUN-SYS-3.3
FUN-WING-05	Accommodate ailerons	FUN-SYS-3.5

7.2. Requirement Analysis

This section presents the requirement analysis of the wing structure in Table 7.2.

Table 7.2: Requirements relevant for the wing design

Code	Description	Origin
REQ-WING-01	The wing shall maintain structural integrity during flight	REQ-SYS-53
REQ-WING-02	The wing shall be able to operate in harsh environments	REQ-SYS-18
REQ-WING-03	The wing shall fit inside the fuselage	REQ-SYS-22
REQ-WING-04	The wing shall be able to unfold and extend during the launch procedure	REQ-SYS-22
REQ-WING-05	SPARTA shall be repairable.	REQ-SYS-45
REQ-WING-06	The wing shall be fully recyclable	REQ-SYS-21
REQ-WING-07	The UAS mass shall not exceed 25 kg.	REQ-SYS-23
REQ-WING-08	The wing shall withstand the loads prescribed by STANAG [11]	REQ-SYS-36

7.3. Analysis Setup

This section discusses the tools developed for the wing. With Subsection 7.3.1 showing the model that connects the different disciplines, Subsection 7.3.2 presents the mesh that is used to combine the aerodynamic, structural and flight dynamics analyses.

Assumptions

Table 7.3: Assumptions used in the simulation model

Code	Description	Validity
Materials		
AS-MAT-01	The materials are homogeneous and isotropic.	For aluminium and steel, this is a reasonable approximation due to their polycrystalline nature, under planar loading. However, composites can be inherently anisotropic; this assumption can only be made under in-plane loading [26].
Structures		
AS-STR-01	The system is linear elastic, ignoring non-linear effects and plasticity.	This assumption holds if deformation is exclusively in the elastic region and does not exceed the yield stress of the material (with 0.2% offset) [26].
AS-STR-02	The wing is a cantilever beam with a constant cross-section and it is fixed at the root, free at the tip. Therefore, standard bending equations can be used.	Valid for preliminary design stages where simple stress approximations have to be made [27].
AS-STR-03	The telescopic and hinge mechanisms are ignored. This reduces the complexity, making the wing a single rigid structure, ignoring moving parts.	Valid for preliminary design stages where simple stress approximations have to be made [27].
AS-STR-04	Lift and drag act at the centre of pressure only. This simplifies moment calculations, ignoring distributed loads across the wing span.	Valid for preliminary design stages where simple stress approximations have to be made [27].
AS-STR-05	Centre of pressure is located at half the height of the airfoil. This simplifies load application by assuming a fixed vertical position, which reduces complexity in moment arm and stress calculations.	Acceptable for symmetric or simple airfoil shapes in preliminary conceptual design stages [27].
AS-STR-06	The structure is idealised. This simplifies the geometry and material properties and ignores real-world complexities like joints, fasteners, and local details.	Valid in preliminary design stages where simple approximations have to be made [27].
AS-STR-07	Inertial acceleration forces are neglected.	Valid as the magnitude of these forces is far below the aerodynamic forces.
Aerodynamics		
AS-AERO-01	The analysis does not simulate the stall behaviour.	The model is intended for pre-stall, linear aerodynamic analysis.
AS-AERO-02	The analysis does not consider the effects of aeroelasticity and structural influence.	Common simplification in early aerodynamic models.
AS-AERO-03	The analysis does not consider the effects of aeroelasticity and structural influence.	For small UAVs at low Mach numbers, this assumption can be a roughly justifiable simplification in early-stage analysis, especially if the wing has low taper and minimal spanwise flow variation.
Flight Dynamics		
AS-FD-01	The telescopic extension of the wings is not considered in this simulation	The modelling of the extending wing is beyond the scope of this project
AS-FD-01	Downwash is not considered for the launch from the Apache helicopter and Airbus A400M	The aerodynamic modelling of this effect is beyond the scope of this problem.

7.3.1. Coupled Analysis Model

Systems, by definition, are groupings of interconnected elements. The links represent the flows of not just resources but also forces, stresses and dynamics. Analysis of individual components cannot be performed without considering all of their dependencies; thus, it was decided to integrate the used models in the analysis and design of the system.

The model comprises three parts: the structural, aerodynamic and flight dynamics models, hence the name Triangle Model. The structural model contains all aspects of geometry, stress, buckling and deflection analysis, as well as being responsible for creating the wing discretisation mesh for the other two models. The aerodynamic model investigates the forces and moments on the mesh, as well as considering aeroelasticity of the structure. Finally, the flight dynamics model can simulate and evaluate the flight in both steady cruise and during the complex launch phase. The data flows between the models can also be seen in Figure 7.1.

The main advantage of this model is that it can be used in a looping simulation with little human intervention. So, structures generate the mesh and provide moments of inertia, aerodynamics provide forces, flight dynamics evaluate motions and speed, and structures find deflections and repeat. This architecture is especially beneficial to simulate unsteady flight regimes, such as the moments right after launch and during the unfolding procedure.

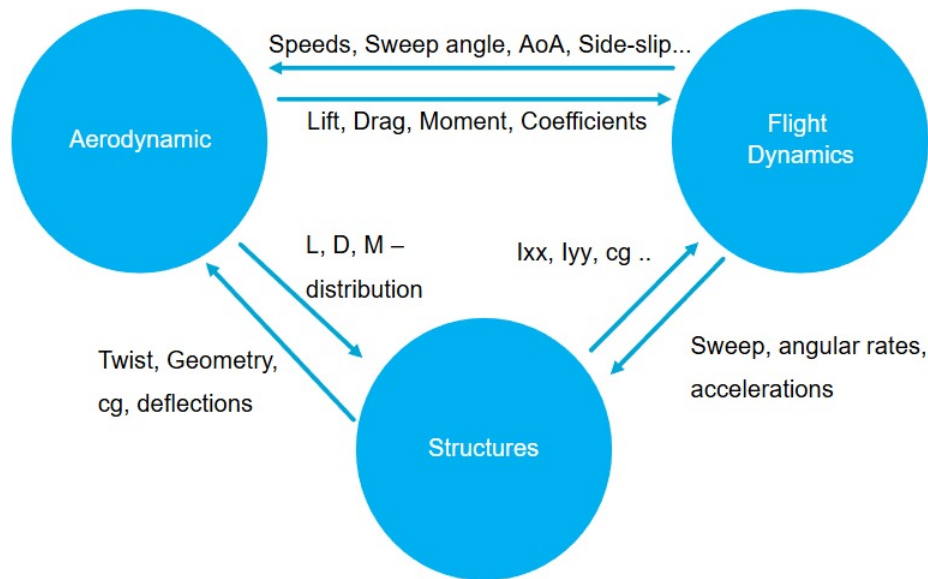


Figure 7.1: Coupled model illustration

7.3.2. Mesh

To facilitate the aerodynamic, structural and flight dynamics analyses, a unified mesh for the wing needs to be developed. While the meshing falls under the purview of the structural department and model, it stands quite separate and is presented as such. The goal of the mesh is to provide an array of the quarter-chord points of discrete wing slices in an aircraft-fixed coordinate system while also supporting rotation and extension of the wings.

Implementation

A Mesh class is created to handle the creation and updating of the wing mesh and easy implementation with other parts of the model. Initially, two coordinate systems are defined, each aligned with the leading edge of the wing as depicted in Figure 7.3.

The wing is then split into the desired number of sections defined by the leading edge point in the middle of each slice, its chord length and airfoil profile, all in the wing-fixed coordinate system. Each slice, with the exception of two, is the same size. These two leftover slices stem from the nature of the extending wing and make it possible to only have one chord length per section.

The partial section at the transition between the inner and outer wing also facilitates the modelling of the extension process. The extension is characterised by a parameter e ranging from zero to one. As the parameter increases, the slice at the transition grows until it reaches the same size as the rest of the slices. At that point, a new partial slice is created, and the process repeats. Finally, the modelling of the rotation is incorporated in the transformation of the wing coordinate system into the aircraft-fixed coordinate system by rotating around the z-axis by the deployment angle.

The outputs of the mesh are points at the quarter-chord, widths of the slices and coordinates of cross-section profiles, all in the aircraft-fixed coordinate system. These are then handed over to other models to work with before being instructed to proceed with the morphing procedure.

7.4. Aerodynamic Analysis

This Section focuses on analysing the aerodynamic forces acting on the wing to calculate sectional lift, drag, and moment. It will start with Subsection 7.4.1, which will explain the implementation of the mesh from Section 7.3.2. In Subsections 7.4.2 and Subsection 7.4.3, the theoretical basis for these calculations will be presented, while Section 7.8 outlines the verification of the aerodynamics model. Finally, Subsection 7.14.2 will provide a discussion and recommendations for future improvements. This analysis determines the forces and moments acting on the aircraft, which will further be used in assessing its stability, structural integrity, and sustaining flight.

7.4.1. Mesh Implementation

When outputting the mesh described in Section 7.3.2, an array of coordinates is generated for the right and left wings, with convention from the root to the tip chord of each wing. However, for aerodynamic analysis, a continuous wing model is needed, which begins with the tip chord of the left wing and goes through the midpoint of the right wing until the tip chord of the right wing. To meet this requirement, the code implements a function that restructures the mesh, which is essential for the calculation of downwash effects, further explained in this section

Additionally, the mesh code divides both the left and right wings into an equal number of points, resulting in an even total number of points. However, since the analysis uses a numerical integration technique, namely Simpson's rule, it requires an odd number of points. Therefore, an additional point has been added at the midpoint to ensure that the total number of points becomes odd.

7.4.2. 2D Airfoil Data Interpolation

After selecting the airfoils in Chapter 6, the first step was to calculate the appropriate Reynolds number, which will be used for the data derivation.

Given the Reynolds number, it is possible to run an airfoil analysis in the XFOIL software, with angles of attack varying from -10° to $+20^\circ$ with increments of 0.1° . At each discrete point, the software calculated the sectional lift coefficient, drag coefficient, and moment coefficient. The resulting tables of $C_L(\alpha)$, $C_D(\alpha)$, and $C_m(\alpha)$ work as the base data for the aerodynamic code.

The flight model often requires aerodynamic coefficients at angles of attack that lie between the grid points generated in XFOIL. To address this situation, the code finds the two nearest points and computes each coefficient using linear interpolation.

Beyond an angle of attack of 20° , the airfoil begins to stall, thus loses lift, a phenomenon that is not accurately simulated by software. As a result, a hard upper limit of 20° has been established. When the code attempts to use an angle of attack that goes beyond these bounds, the model assumes that lift production collapses, setting the lift coefficient to zero. In this scenario, the simulation does not attempt to calculate drag or moment either, as these values are undefined for this model in a fully stalled regime.

Similarly, at the lower end with angles below -10° also lack reliable data. Therefore, the solver sets the coefficients to 0. Although these assumptions establish a clear operational envelope, they do introduce errors in extreme post-stall conditions. For future code improvements, it is crucial to address this issue more effectively, which is explained in Subsection 7.14.2.

7.4.3. Extending to 3D: Downwash Effects

While two-dimensional airfoil data gives a good basis for initial force predictions, it does not consider the aerodynamic losses that occur when a wing has a finite span. In real-world conditions, the wing tips allow air to mix between the upper and lower surfaces of the wing, creating trailing vortices and a downward velocity component in the flow field behind the wing. This downwash influences the effective angle of attack experienced by each point along the wing, effectively reducing the total lift. To account for the effects of finite wing a numerical lifting-line model has been employed inside.

The approach is based on the non-linear numerical lifting-line theory described in Anderson [18]. This method provides an iterative model for solving the spanwise circulation distribution along a finite wing by considering

the induced velocities generated by the wing.

Since the wing has already been discretised in previous steps, the process begins with an initial guess for the spanwise circulation distribution, assuming an elliptical lift distribution. Using this initial distribution, the code computes the induced angle of attack at each point by summation of the downwash contributions from other sections of the wing. This is done by applying numerical integration techniques, namely Simpson's rule, as can be seen in Equation 7.1.

$$\alpha_i(y_n) = \frac{1}{4\pi V_\infty} \frac{\Delta y}{3} \sum_{j=2,4,6}^k \frac{(d\Gamma/dy)_{j-1}}{y_n - y_{j-1}} + 4 \frac{(d\Gamma/dy)_j}{y_n - y_j} + \frac{(d\Gamma/dy)_{j+1}}{y_n - y_{j+1}} \quad (7.1)$$

Once the induced angle of attack (α_{ind}) is calculated, the effective angle of attack is determined at each control point.

Having the effective angle of attack, the new C_L is obtained by interpolation from previously derived 2D airfoil data. This is then used to recalculate a new sectional circulation value (Γ) using Equation (7.2).

$$\Gamma = \frac{1}{2} v_\infty c_n (c_l)_n \quad (7.2)$$

Here, v_∞ is the free stream velocity, c_n represents the chord length of the section, and $(c_l)_n$ is the lift coefficient for that specific section. These updated circulation values replace the initial guesses, and the process is iterated. This iteration repeated until the spanwise circulation distribution converges, effectively recalculating the circulation values, induced and effective angles of attack.

After the iteration is complete, the final output of this method consists of an improved distribution of the induced angle of attack across the wing. These results enable the model to account for the loss of lift and the additional drag caused by finite-wing effects. They also serve as the foundation for calculating the total aerodynamic forces and moments experienced by the aircraft. A result of this method can be visualised with the lift distribution per section along the span, as presented in Figure 7.2.

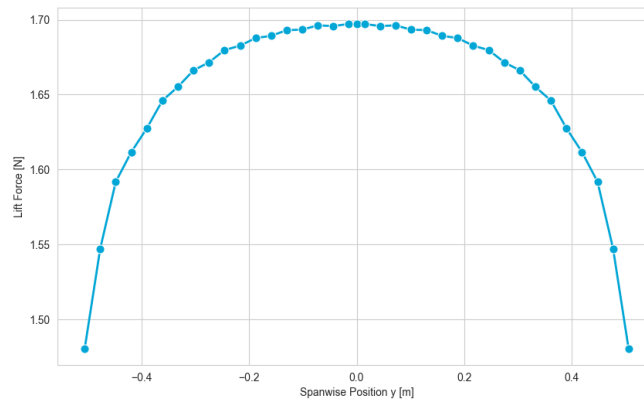


Figure 7.2: Lift distribution along the wing

7.5. Wing Morphing

In this section, the launch from the tube is analysed. This is a critical function that the UAS needs to perform, therefore, it requires a thorough investigation to determine the structural loads as well as the overall stability of the UAS during launch. Since the wing and tail have to be foldable, and the right wing is mounted above the left one, it induces internal moments that are coupled with the aerodynamic forces, yielding a non-standard response that needs to be analysed.

Firstly, the reference frames and transformations between them are discussed to ensure the dynamics are modelled properly. It is then followed by the explanation of equations of motion that govern the response of the

aircraft. To calculate the response of the UAS, both static moments and inertia tensors of all components are necessary. Their calculation is discussed in the following section. Finally, the flight dynamics model is integrated with the aerodynamic model developed in Section 7.4 and eventually, the results are shown and discussed.

7.5.1. Reference Frames & Transformations

The application of equations of motion, described in Subsection 7.5.2, requires properly setting up reference frames and transformations between them. Since the distance travelled by the UAS is small compared to the Earth's radius, and the speed is relatively low compared to the Earth's rotational velocity, the Earth frame coordinate system is considered to be an inertial frame in which the equations of motion are evaluated [28].

The primary reference frame, which is used to assess the motion of the UAS, is the body frame positioned at the centre of the body mass of the aircraft. The body mass contains the mass of all aircraft components except the wings and tail. This distinction has to be made since both the tail and the wings are rotated along the hinges, and their centre of mass shifts as they unfold. The body mass, on the other hand, is fixed, and its position does not change. Thus, it is appropriate to fix the body frame at this position. The x-axis is pointing forward, the y-axis is pointing to the right, and the z-axis is pointing downwards.

As the wings and tail rotate around the hinges, it is appropriate to set a hinge reference at that point with the same x, y, and z-axis orientation as for the body frame. Since there are four hinges, there are four reference frames accordingly. Lastly, the wing and tail frame is used, which is fixed at the leading edge of the wing. The frames are shown from the top view in Figure 7.3. When the wings are fully deployed, all hinge and wing/tail frames are aligned with the body frame. In Figure 7.3, the dihedral angle is not accounted for to simplify the drawing. Table 7.4 contains the positions of all reference frames with respect to each other.

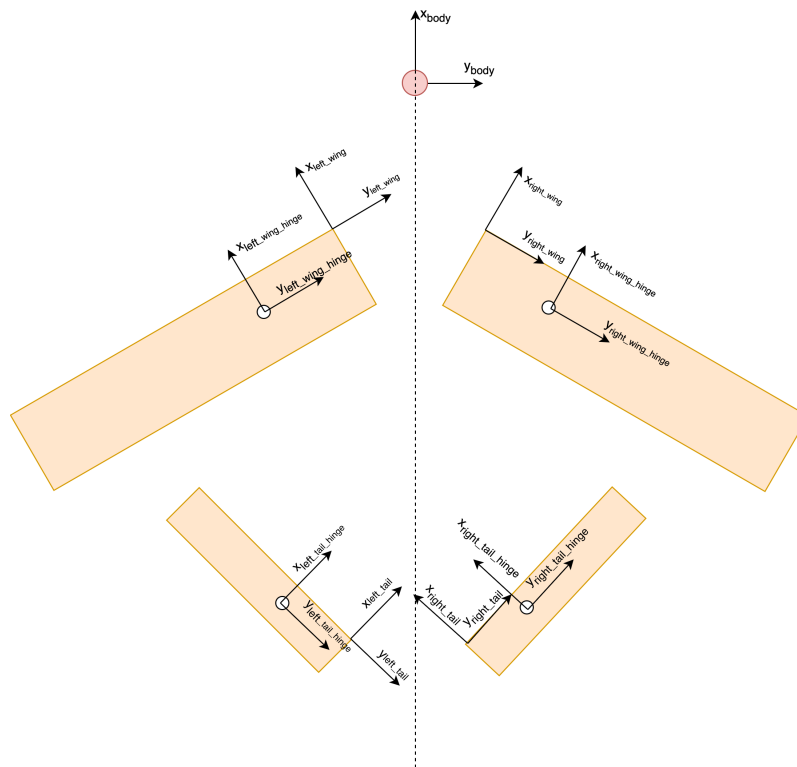


Figure 7.3: UAS top view with the reference frames

The coordinates are rotated by angle θ with respect to each other. Angle θ is defined from the body x-axis to the hinge x-axis. Therefore, a clockwise rotation is considered positive. To clarify, the right wing rotates from the stowed position of $+90^\circ$ to deployed 0° , whereas the left wing rotates from -90° to 0° . The unfolding motion is described in greater detail in Subsection (7.5.4). Finally, a vector in a hinge frame can be expressed in the

body frame by multiplying it with a transformation matrix given in Equation (7.3). Firstly, the wing or tail is rotated by a dihedral angle ϕ and then by angle θ . The UAS is designed without any dihedral on the main wing; thus, the transformation with ϕ equal to 0 is used. The inverted V-tail, however, has a dihedral angle equal to 37.5° , as shown in Table 5.4.

$$T_{b/h} = \begin{bmatrix} \cos -\theta & \sin -\theta & 0 \\ -\sin -\theta & \cos -\theta & 0 \\ 0 & 0 & 1 \end{bmatrix} \begin{bmatrix} 1 & 0 & 0 \\ 0 & \cos -\phi & \sin -\phi \\ 0 & -\sin -\phi & \cos -\phi \end{bmatrix} \quad (7.3)$$

Table 7.4: Reference frame positions and simulation parameters

Parameter	Value
Body frame position with respect to the nose in the x-direction [mm]	-382.3
Body frame position with respect to the nose in the y-direction [mm]	0.0
Body frame position with respect to the nose in the z-direction [mm]	3.0
Right wing hinge frame in body frame x-direction [mm]	-355.0
Right wing hinge frame in body frame y-direction [mm]	19.0
Right wing hinge frame in body frame z-direction [mm]	-44.0
Left wing hinge frame in body frame x-direction [mm]	-355.0
Left wing hinge frame in body frame y-direction [mm]	-19.0
Left wing hinge frame in body frame z-direction [mm]	-36.0
Right tail hinge frame in body frame x-direction [mm]	-839.0
Right tail hinge frame in body frame y-direction [mm]	38.0
Right tail hinge frame in body frame z-direction [mm]	-11.0
Left tail hinge frame in body frame x-direction [mm]	-839.0
Left tail hinge frame in body frame y-direction [mm]	-38.0
Left tail hinge frame in body frame z-direction [mm]	-11.0
Right wing hinge frame in right wing frame x-direction [mm]	-20.0
Right wing hinge frame in right wing frame y-direction [mm]	20.0
Right wing hinge frame in right wing frame z-direction [mm]	0.0
Left wing hinge frame in left wing frame x-direction [mm]	-20.0
Left wing hinge frame in left wing frame y-direction [mm]	-20.0
Left wing hinge frame in left wing frame z-direction [mm]	0.0
Right tail hinge frame in left wing frame x-direction [mm]	-25.0
Right tail hinge frame in left wing frame y-direction [mm]	25.0
Right tail hinge frame in left wing frame z-direction [mm]	0.0
Left tail hinge frame in left wing frame x-direction [mm]	-25.0
Left tail hinge frame in left wing frame y-direction [mm]	-25.0
Left tail hinge frame in left wing frame z-direction [mm]	0.0

7.5.2. Equations of Motion

The equations of motion of the UAS can be derived from the conservation of linear and angular momentum, yielding six scalar equations that form a system of equations that can be solved for linear and angular acceleration vectors. If no external forces and moments are considered, and the UAS is considered a system, its momentum has to be conserved. Therefore, the movement of the wings and tail induces internal forces and moments that affect the UAS. Additionally, external forces, such as aerodynamic forces and gravity, are acting on the system, which further affects motion. Propulsion is not considered in this model. Since the dynamics model is sophisticated, it is derived directly from the principle of conservation of linear and angular momentum.

Firstly, the linear acceleration is derived from Equation (7.4), which begins with expressing the linear momentum of all points belonging to the body that have mass m_i and velocity $\vec{V}_{i/I}$ with respect to the inertial frame

of reference. The velocity of each component with respect to the inertial frame can be expressed in the body frame, as shown in Equation (7.5).

$$\vec{p}_{b/I} = \sum m_i \vec{V}_{i/I} \quad (7.4)$$

$$\vec{V}_{i/I} = \vec{V}_{b/I} + \frac{\dot{\vec{S}}_{ib} + \vec{\omega}_{b/I} \times \vec{S}_{ib}}{m_i} \quad (7.5)$$

Finally, Equation (7.5) can be inserted into Equation (7.4). The force expressed in the body frame can be calculated by taking the derivative of the linear momentum. The static moments and their derivatives can be summed up for all the components - fuselage, right and left wing and tail, which results in Equation (7.6) that contains the unknown state variables on the left-hand side. The final equation is identical to the one derived in the article by Yue [29].

$$m \dot{\vec{V}}_{b/I} + \sum_i \vec{\omega}_{b/I} \times \vec{S}_{ac} = \vec{F} - \ddot{\vec{S}}_{ac} - 2\vec{\omega}_{b/I} \times \dot{\vec{S}}_{ac} - \vec{\omega}_{b/I} \times (\vec{\omega}_{b/I} \times \vec{S}_{ac}) \quad (7.6)$$

Next, the angular momentum is analysed. The derivation of the state variables for rotational motion is much more sophisticated than for linear momentum. The derivation begins with expressing the angular momentum around the body mass centre of mass \vec{H}_b , which is the sum of the angular momentum of all the aircraft components, such as the body, wings and tail. Equation (7.8) [30], expresses the angular momentum around the centre of body mass, where $\vec{\omega}_{i/I}$, given by Equation (7.7) is a sum of angular rotation of point b around the inertial frame and the component's angular rotation around point b . In the case of UAS, $\vec{\omega}_{i/b}$ is the angular velocity of the unfolding wing or tail.

$$\vec{\omega}_{i/I} = \vec{\omega}_{b/I} + \vec{\omega}_{i/b} \quad (7.7)$$

$$\vec{H}_b = \sum_i \left[\vec{r}_{i/b} \times m_i \vec{V}_{i/I} + m_i \vec{r}_{i/b} \times (\vec{\omega}_{i/I} \times \vec{r}_{i/b}) \right] \quad (7.8)$$

Equation (7.8) can be rewritten, according to Hibbeler [30], resulting in the inclusion of the inertia tensor of each component. Furthermore, static moment terms can be included instead of velocities and position vectors, and Equation (7.7) can be inserted, which results in Equation (7.9).

$$\vec{H}_b = \vec{S}_{ac} \times \vec{V}_{b/I} + \sum_i \left[I_i \vec{\omega}_{b/I} + I_i \vec{\omega}_{i/b} + \frac{\vec{S}_{ib}}{m_i} \times (\dot{\vec{S}}_{ib} + \vec{\omega}_{b/I} \times \vec{S}_{ib}) \right] \quad (7.9)$$

Finally, the moment can be calculated by taking the derivative of the angular momentum. After tedious mathematical operations, the final equation, where state variables are on the left-hand side, is given by Equation (7.10)

$$\begin{aligned} \vec{S}_{ac} \times \dot{\vec{V}}_{b/I} + \left(\sum_i \left[I_i - \frac{1}{m_i} [S_{i/b}]_{\times} [S_{i/b}]_{\times} \right] \right) \dot{\vec{\omega}}_{b/I} &= \vec{M} - \vec{\omega}_{b/I} \times (\vec{S}_b \times \vec{V}_{b/I}) \\ - \sum_i \left[\dot{I}_i \vec{\omega}_{b/I} + \vec{\omega}_{b/I} \times (I_i \vec{\omega}_{b/I}) + \dot{I}_i \vec{\omega}_{i/b} + I_i \dot{\vec{\omega}}_{i/b} + \vec{\omega}_{b/I} \times (I_i \vec{\omega}_{i/b}) \right] \\ - \sum_i \left[\frac{1}{m_i} (\vec{S}_{ib} \times \ddot{\vec{S}}_{ib} + \vec{\omega}_{i/b} \times (\vec{S}_{ib} \times \dot{\vec{S}}_{ib})) \right] \\ - \sum_i \left[\frac{1}{m_i} (\dot{\vec{S}}_{ib} \times (\vec{\omega}_{b/I} \times \vec{S}_{ib}) + \vec{S}_{ib} \times (\vec{\omega}_{b/I} \times \dot{\vec{S}}_{ib}) + \vec{\omega}_{b/I} \times (\vec{S}_{ib} \times (\vec{\omega}_{b/I} \times \vec{S}_{ib}))) \right] \end{aligned} \quad (7.10)$$

Equation (7.6) and (7.10) result in six scalar equations that can be solved for two state vectors $\vec{V}_{b/I}$ and $\vec{\omega}_{b/I}$. Common linear algebra methods can be used to solve this matrix-vector equation. The only missing components to solve the system are $\vec{V}_{b/I}$ and $\vec{\omega}_{b/I}$, static moments and moments of inertia.

The first two components can be obtained by applying a forward Euler scheme with a short time step Δt as shown in Equations (7.11) and (7.12). The forward Euler scheme is an iterative scheme that can be applied to solve the linear and angular velocities in the following iteration steps. The derivation of static moments and moments of inertia is treated in the following Subsection 7.5.3.

$$\vec{V}_{b/I}(t + \Delta t) = \vec{V}_{b/I}(t) + \Delta t \dot{\vec{V}}_{b/I}(t) \quad (7.11)$$

$$\vec{\omega}_{b/I}(t + \Delta t) = \vec{\omega}_{b/I}(t) + \Delta t \dot{\vec{\omega}}_{b/I}(t) \quad (7.12)$$

7.5.3. UAS Static Moments & Moments of Inertia

The static moment, Equation 7.13, is defined as a product of the component's mass and distance between the body centre of mass and the centre of mass of one of the UAS components expressed in the body frame. To calculate the first derivative, the rotating motion of the hinge has to be considered by taking into account the unfolding angular velocity $\vec{\omega}_{i/b}$ and the wing/tail centre of gravity position $\vec{r}_{i/b}$. Since that position is expressed in the wing or hinge reference frame, a transformation has to be applied to convert the vector into the desired body frame. Since the telescopic extension of the wing is not accounted for at this stage and the hinge frame does not move with respect to the body, the expression for the static moment derivative can be simplified, Equation (7.14). Similarly, the expression for the second derivative of the static moment can be simplified by applying the same assumptions, Equation (7.15).

$$\vec{S}_{ib} = m_i \vec{r}_{i/b} \quad (7.13)$$

$$\dot{\vec{S}}_{ib} = m_i (\vec{\omega}_{i/b} \times \vec{r}_{i/b}) \quad (7.14)$$

$$\ddot{\vec{S}}_{ib} = m_i (\dot{\vec{\omega}}_{i/b} \times \vec{r}_{i/b} + \vec{\omega}_{i/b} \times (\vec{\omega}_{i/b} \times \vec{r}_{i/b})) \quad (7.15)$$

The inertia tensor has to be calculated for all of the aircraft components. The results are provided in Table 7.7. However, when calculated, they are given in the reference frame of the wing/tail. Since the equations of motion are expressed in the body frame, they need to be transformed into the body frame. Given that the wing/tail frame and hinge frame are not rotated between each other and the inertia tensor was initially calculated in the wing/tail frame, the transformation from hinge to body frame can be used for both the tail and the wing, Equation 7.16. The derivative of the inertia tensor, as it changes with time when the wings and tail unfold, is given by Equation 7.17¹.

$$I_{\text{wing}}^b = T_{b/h} I_{\text{wing}}^w T_{b/h}^T \quad (7.16)$$

$$\dot{I}_{\text{wing}}^b = [\omega_{i/b}]_{\times} I_{\text{wing}}^b - I_{\text{wing}}^b [\omega_{i/b}]_{\times} \quad (7.17)$$

7.5.4. Wing & Tail Unfolding Profile

The wings and tail have the same unfolding motion, which differs only in the initial and final angular position and the direction of unfolding. A cosine profile was chosen for both the tail and wings because it has smooth derivatives that do not generate impulses. The unfolding angle is angle θ , introduced in Subsection 7.5.1, between the x-axis in the body frame and the x-axis in the hinge frame. An example is given in Equation 7.18 for the right wing, where T_u is the unfolding period, and the function range is from 90° to 0° . The derivatives can

¹URL: <https://www.steelmetind.com/7075-aluminum-sheet-plate.html> [cited 22 June 2025]

be simply taken to compute angular velocity and acceleration of the unfolding components, $\vec{\omega}_{i/b}$ and $\dot{\vec{\omega}}_{i/b}$ that is required for the computation of the static moments and their derivatives.

$$\theta(t) = \frac{\pi}{4} + \frac{\pi}{4} \cos\left(\frac{\pi}{T_u}t\right) \quad (7.18)$$

7.5.5. Integration with the Aerodynamic Model

The above-described flight dynamics model is integrated with the aerodynamic model to provide a robust tool that can analyse the UAS behaviour during the launch phase. The outputs of the aerodynamic code are the forces and moments in the wing frame that have to be transformed into the body frame using the transformation provided in Subsection 7.5.1. On top of that, the gravitational force has to be included by applying the transformation from Earth to the body frame. The total external forces and moments around the centre of body mass can be summed by applying Equations 7.19 and 7.20.

$$\vec{F} = \sum_i \left[\vec{F}_i + m_i \vec{g} \right] \quad (7.19)$$

$$\vec{M} = \sum_i \left[\vec{r}_{section_i/b} \times \vec{F}_i + \vec{r}_{i/b} \times m_i \vec{g} \right] \quad (7.20)$$

The inputs required for the aerodynamic code from the flight dynamics are local velocities at each wing section. They are calculated with Equation 7.21, which includes the effects of aircraft rotational motion as well as wing or tail unfolding motion. $(\vec{r}_{section_i/i} + \vec{r}_{i/b})$ is the sum between the distance from the body frame to the hinge, and the distance from the hinge to the wing section's quarter chord point. Eventually, the equation is transformed into a hinge frame and projected onto the x-z plane of the hinge.

$$\vec{V}_{loc} = \vec{V}_{b/I} + \vec{\omega}_{b/I} \times (\vec{r}_{section_i/i} + \vec{r}_{i/b}) + \vec{\omega}_{i/b} \times \vec{r}_{section_i/i} \quad (7.21)$$

7.5.6. Results

The launch was analysed for three different cases as specified by the requirements, from the hovering Apache helicopter (**REQ-SYS-11**), from the ground (**REQ-SYS-12**) and the Airbus A400M (**REQ-SYS-10**). The ΔV delivered by the tube is designed and constrained at 40 m/s, as explained in Chapter 8. The initial Euler angles, angular acceleration and velocity are assumed to be equal to zero to simplify the analysis and discard the deviations. The unfolding of the wings and tail takes 0.5 s, and the chosen timestep is 0.01s. In this simulation, the effect of the propeller is not considered, and the wings are not telescopically extended after unfolding.

The initial phase of the flight, when the wing and tail unfold, is similar for all the cases. It is driven by the changing centre of gravity of the UAS in the first 0.5 s. Since the right wing is mounted above the left wing, the movement of its centre of gravity induces a negative roll on the body to conserve the angular momentum. A slight pitch-up moment is induced due to the movement of the wings' mass to the front. However, since the wings are not fully extended and lift is significantly lower when compared to cruise, the UAS eventually tends to pitch down after the wings and tail are deployed.

The structural analysis was performed for all the above-mentioned launch cases, in Section 7.6, to determine whether the wings are capable of withstanding significant aerodynamic and inertial loading during the unfolding period. The analysis yielded a positive result proving that all the launch cases are feasible from the structural point of view. In the following paragraphs, the stability and feasibility during launch is assessed.

Helicopter Launch

As stated by **REQ-SYS-11**, the UAS shall be capable of being launched from the Apache helicopter in hover. In the simulation, the launch is performed at 1000 m above sea level. The simulation is run at the initial airspeed of 40 m/s, when the helicopter hovers above the ground. The results are shown in Figure 7.4, where it can be observed, that the UAS tend to roll and yaw in the negative direction. It indicates that the UAS show spiral instability when the wings are not fully extended. Most importantly, however, the roll angle is not too excessive

during the unfolding period and can be mitigated during the later stages by either extending the wing or applying control surface input. This indicates that even with the wings that are not yet telescopically extended, the UAS can survive the launch without showing any aggressive attitude variations.

However, there are a few shortcomings of this simulation not captured by the model. The Apache helicopter that hovers above the ground produces significant downwash and vortices that can not be modelled by the aerodynamic model used for the simulation. It is thus recommended to validate the results with a Computational Fluid Dynamics (CFD) simulation that captures these effects.

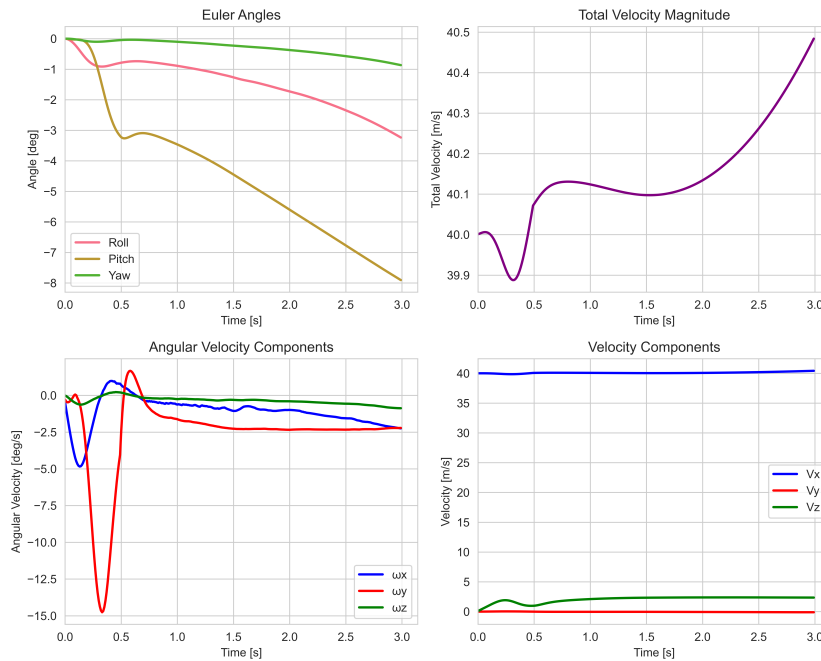


Figure 7.4: Helicopter launch at 40 m/s at an altitude of 1000 m.

Ground Launch

The ground launch is performed at an initial speed of 40 m/s at an angle of 45° . This combination of values was chosen to ensure that the UAS is launched at the maximum available launch speed from a stationary tube and has enough vertical velocity to not hit the ground after launch. The results are shown in Figure 7.5, where it can be observed that the pattern of roll and yaw is similar to the behaviour observed when launched from the helicopter. However, the aircraft stalls at around 22 m/s, where spikes in angular rate can be observed, which makes this launch unfeasible.

The actual stall speed of the aircraft is much lower than the one shown in Table 5.4 because during the iterative design, the lift of the tail was not accounted for. Since the inverted V-tail has a non-negligible surface area it is expected that the actual stall speed in the simulation is lower than initially calculated.

Since the launch tube is designed for only ΔV of 40 m/s, it could be mounted on a moving vehicle to deliver higher initial airspeed. Alternatively, the stationary tube could be placed on a structure above the ground letting the launch angle be reduced. If either of these alterations are incorporated this launch case can be deemed as feasible.

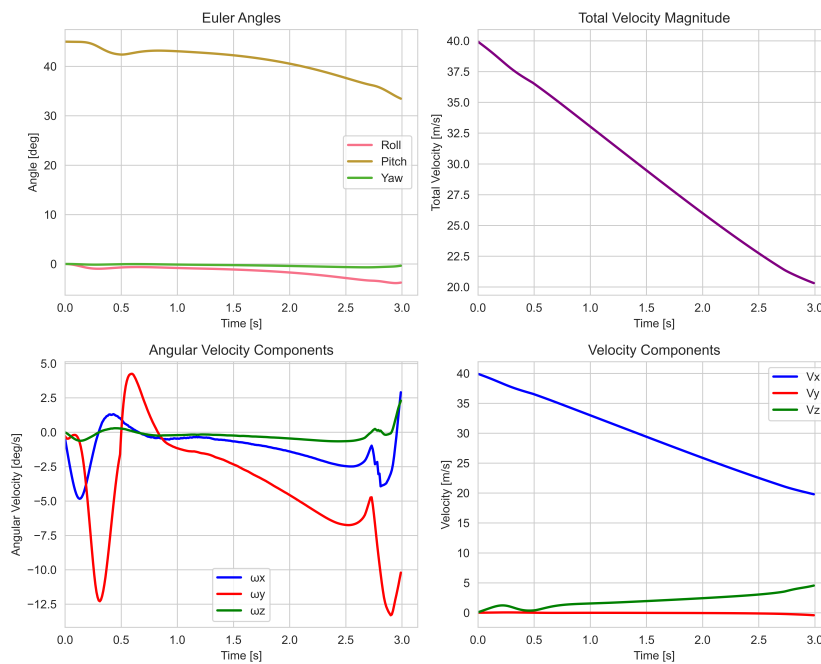


Figure 7.5: Ground launch at 40 m/s.

Airbus A400M Launch

As stated by the requirements, the UAS needs to be launched from an A400M at a speed of 190 knots (**REQ-SYS-10**), which is approximately equivalent to 100 m/s. To avoid the aircraft's wake, the UAS is launched forward in the direction of the flight. However, the UAS needs to be launched at a velocity higher than the aircraft to avoid collision. Therefore, a ΔV of 20 m/s was chosen, which leads to an initial airspeed of 120 m/s when the airspeed of Airbus is accounted for. The results of the launch carried out at an altitude of 3000 m are shown in Figure 7.6.

As can be observed, during the wing and tail unfoldment period, the induced roll and yaw are much lower when compared with the helicopter launch. The rolling motion is caused by the increasing gravity moment created in the direction of the roll. Since the wings are not fully extended, the lift force is too small to counteract this moment. However, when launched at a higher velocity, the aerodynamic forces are much higher and the roll motion is reduced. The biggest difference, however, between the A400M and Apache launch is the aggressive pitch-up moment, which results in quite a fast speed reduction. This pitch-up moment is too aggressive, so applying an elevator input of -13° per second is recommended. The necessary pitch rate input can be read from Figure 7.6.

The major concern of this launch case is the very high initial velocity, which is far from the operational range. In Section 7.6, it is assessed that the wing structure is able to withstand the loading at high-speed conditions. This is a positive outcome, although it is recommended to delay the main wing unfolding during this launch to let the UAS slow down and not cause an aggressive pitch-up reaction.

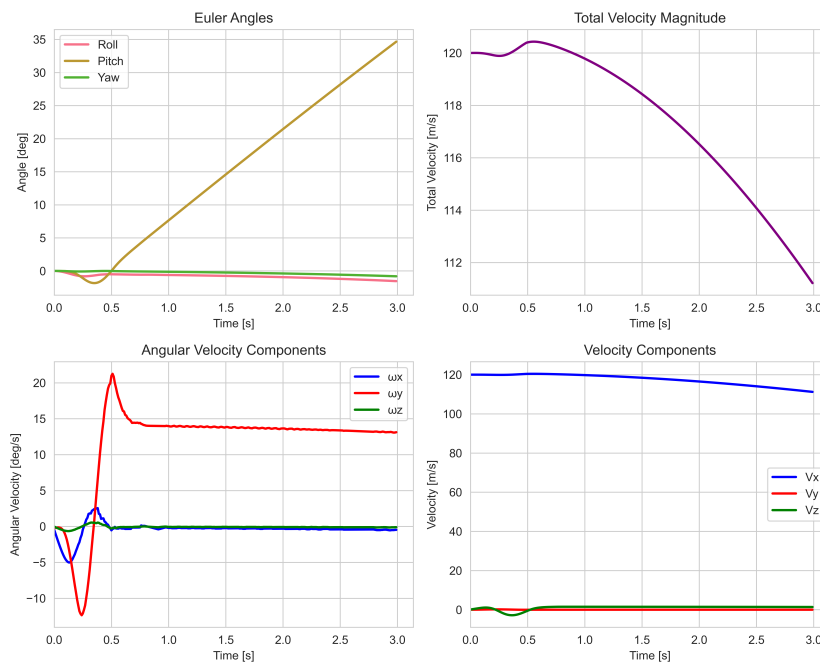


Figure 7.6: Airbus launch at 120 at an altitude of 3000 m

7.6. Structural Analysis

The design of the SPARTA wing structure is discussed in this section.

7.6.1. Structural Model

The second piece of the model is evaluating structures. The main aim is to provide deflections and deformations, and moments of area and inertia to the other models. While achieving this, internal forces and stresses are calculated, and with the addition of buckling analysis, it also informs the design and sizing of structural components of the UAS.

Coordinate System

The foundation of any mechanics-based analysis is a coordinate system. Any right-handed system can be selected. However, to stay in accordance with the rest of the models, the chosen coordinate system will have the x-axis oriented towards the nose of the UAS, the z-axis directed downwards, and the y-axis towards the right wing, completing the right-handed system. This is summarised in Figure 7.7.

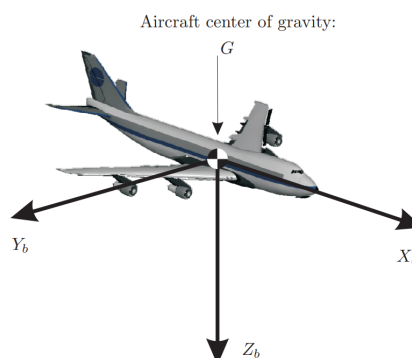


Figure 7.7: The reference frame of SPARTA

Loads

The initial step in determining the stresses and deflections of the structure is identifying the critical loads. These are the normal and tangential forces and moments of the wing, tail and fuselage, the thrust and the weights of all

components. The loads are amplified by the limit load factor as specified by **REQ-SYS-36-14** or **REQ-SYS-36-15** and a safety factor of 1.3 as specified by **REQ-SYS-53-01**.

The loads can be converted into internal force and moment diagrams along the CG or centroidal axes of the wing, fuselage and tail. The normal and shear force, the torsional and bending moment diagrams can be constructed. The torque and normal force diagrams can be assembled independently, with the moment being the integral of the shear. The standard method, as described by Megson [20], is used.

Boom Areas

To analyse the structures using a computer without Finite Element Method (FEM), it is useful to simplify them into idealised forms using booms. Non-ideal structures would require a more complex analysis using a continuous skin. Therefore, to begin the idealisation process, the boom positions need to be chosen; for this, it was chosen to take the coordinates defining the shape of a cross-section, with distances between points being approximated as straight lines. Granted that everything works correctly, increasing the density of points should converge to an accurate description of the situation.

The boom area determination process is an iterative one as to find the boom areas, one needs to know the ratio of stress between neighbouring points. To find these, one needs the centroid, which in turn requires the boom areas again. To start the analysis, an appropriate area must be assumed to avoid divide-by-zero errors. From this area, the centroid can be determined using Equation (7.22), and the coordinates can be adjusted relative to it.

$$\bar{x} = \frac{\sum_{i=0}^n x_i B_i}{\sum_{i=0}^n B_i} \quad (7.22)$$

Here, \bar{x} is the centroid, x_i is x-coordinate of element i and B_i is the boom area of the i -th element. Afterwards, the different moments of inertia (I_{xx} , I_{zz} and I_{xz}) can be calculated using Equation (7.23).

$$I_{xx} = \sum B z^2, \quad (7.23)$$

With the moments of inertia and location of the booms known, the stresses are calculated using Equation (7.24)

$$\sigma_y = \frac{(M_x I_{zz} - M_z I_{xz}) \cdot z + (M_z I_{xx} - M_x I_{xz}) \cdot x}{I_{xx} I_{zz} - I_{xz}^2} \quad (7.24)$$

Here, σ_y is the yield stress, and M_x , M_y and M_z are the moments about the x, y and z-axis, respectively. Now that all the characteristics are known, the boom areas can be identified using Equation (7.25).

$$B_i = \frac{t_{skin} b}{6} \left(2 + \frac{\sigma_{i+1}}{\sigma_i} \right), \quad (7.25)$$

Here, t_{skin} is the thickness of the skin, b is the distance between adjacent booms and σ_i is the stress at the i -th boom. With the new boom areas identified, the process can be repeated until the differences are within a margin that's less than 1%. The areas can now be used to simplify stress and shear flow calculations.

Shear Flow

To obtain the full shear flow, it must be divided into two parts: the basic shear flow and the complementary shear flow. First, the difference in shear flow (Δq) over a boom is determined. This is done using Equation (7.26).

$$\Delta q_i = -\frac{V_z I_{zz} - V_x I_{xz}}{I_{xx} I_{zz} - I_{xz}^2} (B_i z_i) - \frac{V_x I_{xx} - V_z I_{xz}}{I_{xx} I_{zz} - I_{xz}^2} (B_i x_i), \quad (7.26)$$

Here, V_x , V_y and V_z are the shear forces about the x, y and z-axis, respectively, and I_{xz} is the product moment of inertia. Now that the differences caused by the booms are identified, the basic shear flow can be determined by cutting the structure at an arbitrary point. The over-the-boom change is then taken counter-clockwise across the outline. To verify that the Δq was calculated correctly, it was checked that the total sum equalled zero. Since the basic shear flow is known at this stage, the complementary shear flow can be determined using moment equivalence. To determine the moment around the trailing edge, the shear flows must be multiplied by their respective lengths derived from the boom and the moment arm. The moment can be taken around an arbitrary

point. Now that all the moments are known, the only variable left to determine is the area of the enclosed region. The enclosed area (A_m) can be obtained using the following equation²:

$$A_m = \frac{1}{2} \sum_{i=0}^{n-1} (x_i z_{i+1} - z_i x_{i+1}), \quad (7.27)$$

With all the variables obtained, the complementary shear flow (q_{s0}) is obtained using Equation (7.28), which can be added to the basic shear flow (q_b) to obtain the total shear force.

$$q_{s0} = \frac{(V_x \Delta z + V_z \Delta x) - \sum_{i=0}^n q_{bi} l_i d_i}{2A_m}, \quad (7.28)$$

The previous only applies if the shear force is applied through the shear centre, the point where a force creates no torque and only shear. This point is non-trivial to determine for asymmetrical sections, i.e. airfoils. Therefore, the following method is used to determine the shear centre.

First, an arbitrary force has to be chosen in a direction; here, it was chosen to start in the z-direction. From this force, the basic shear flow can be obtained, as mentioned before, using Equation (7.26). The complementary shear flow can be obtained using Equation (7.29).

$$q_{s0} = -\frac{\oint q_b ds}{\oint t ds} \quad (7.29)$$

Now that the full shear flow is known for the cross section, the position of the shear centre perpendicular to the z-direction can be found using moment equilibrium, which can be found by rewriting Equation (7.28) to Equation 7.30.

$$V_z \Delta x = \sum_{i=0}^n q_i l_i d_i \quad (7.30)$$

Now that the direction along the x-axis is known to obtain the full shear centre, the same procedure has to be done by an arbitrary force in a different direction. For convenience, this force was chosen to act in the x-direction. From this, the z-distance is known, and its intersection is the shear centre for the cross section.

Knowing the shear flows, the shear stress (τ) in each section can be calculated using Equation (7.31). The stress depends on the thickness of the segment and can thus be used to design the required thickness.

$$\tau = \frac{q}{t} \quad (7.31)$$

Bending Stresses and Deflection

With the forces and geometry defined, the bending stress about the y-axis can be easily calculated. The stresses can be determined using the following equation:

$$\sigma_y = \frac{(M_x I_{zz} - M_z I_{xz}) \cdot z + (M_z I_{xx} - M_x I_{xz}) \cdot x}{I_{xx} I_{zz} - I_{xz}^2}, \quad (7.32)$$

In every structure, there is a neutral axis where the stress due to bending is zero. The angle of this neutral axis (θ) can be calculated using:

$$\theta = -\frac{M_z I_{xx} - M_x I_{xz}}{M_x I_{zz} - M_z I_{xz}} \quad (7.33)$$

²URL: <https://www.101computing.net/the-shoelace-algorithm/> [cited 21 May 2025]

The bending stresses are determined based on the bending forces outlined in Subsection 7.6.3. The maximum bending stresses are presented in Table 7.8.

For the deflection (v''), it is important to note that these values stay within manageable margins, so the deflection is determined using Equation (7.34), where E is the Young's Modulus. This formula needs to be double-integrated over the entire span to obtain the deflection function.

$$v'' = -\frac{M_x}{EI_{xx}} \quad (7.34)$$

Axial Stress

Besides bending, normal stress is also created in the structure by axial forces. These create a uniform normal stress within the cross-section of the structure, which can simply be superimposed on the stress caused by bending. Equation (7.35) describes the relationship between force (F), area (A) and stress (σ). For the area, the actual cross-section can be used or the boom simplification.

$$\sigma = \frac{F}{A} \quad (7.35)$$

Normal stresses is expanded up in the fuselage structure design in Chapter 8 in connection to buckling and crippling.

Mass Moment of Inertia

To later determine how the aircraft performed during flight, the flight dynamics require some main characteristics. The main ones are the mass moment of inertia and the mass of the wing itself. In Subsection 7.6.1, the area moments of inertia were defined. For the mass moments of inertia, the boom method is not valid anymore, as the ratio of stresses in 3D is different and introduces extra material that is not present in the wing.

For this, a different approach will be taken; the wing will be discretised into its components for each section in the same way the area moment of inertia is discretised. As the points are known, the distance between the points is multiplied by the thickness to obtain the sectional area. These areas are multiplied by half the length of each adjacent panel. This gives the full volume of the material required.

Now that the masses are known and their locations, the centre of mass can be obtained as this is the same as the centroid, as the wing has a constant density. With the masses and centroid known, the mass moment of inertia can be obtained. These will be found for the left and right wings, respectively, in their centroid location. To convert this to the whole wing, the parallel axis theorem is applied for both sides of the wing to the centre line. Both wings are symmetric, leading to no cross terms in the y direction.

Torsion

The angle of attack is a major aspect of SPARTA as it is flying close to stall speed for maximum endurance. In these cases it the wing has to maintain its orientation to avoid stalling during flight. Therefore, the wing has to resist the torsional forces to accommodate this phenomenon. Now, to obtain the twist angle for the entire wing, first, the twist difference ($d\theta/dy$) for each section of the wing has to be obtained. This is done by using Equation 7.36.

$$\frac{d\theta}{dy} = \frac{T}{4A_m^2 G} \oint \frac{1}{t} ds \quad (7.36)$$

Where G is the shear modulus, and the torque (T) is the resultant internal torque that is obtained by integrating all the applied torques over the wing. Integrating the different twist angles over the span, with zero twist at the root as the wing is fixed there, gives the total twist, where the maximum value is obtained at the tip.

Verification

To ensure that all the functions function correctly, several unit and system tests have been implemented. Therefore, it can be assumed that these functions function without error. The system tests used are shown in Table 7.11.

Skin

The primary design philosophy is having a load-bearing skin that can effectively support the loads generated by the wing. This approach simplifies the design process, as the extended portion of the wing must be accommodated outside of the inner wing. As a result, this imposes limitations on the sizing of the extension mechanism, which means there is no possibility for spars.

However, a challenge associated with the load-bearing skin is its increased thickness, which restricts the available space for the inner wing. This thickness must be carefully considered to ensure that the design remains efficient while accommodating the necessary mechanisms and loads.

7.6.2. Material Selection

As the skin has a load-bearing characteristic, a suitable material needs to be chosen. For this, a trade-off will be performed.

Trade-off Setup

First, given that the skin is exposed to external conditions, it must endure a wide range of temperatures and harsh environments. Evaluating the environmental parameters is essential for this purpose. This evaluation will be conducted qualitatively, where a score of one indicates no design changes are required, 0.66 suggests minor adjustments are necessary, 0.33 represents the need for additional coatings or materials, and a score of zero indicates a complete redesign is essential.

Second, the wing constitutes a significant portion of the system's weight, making density an important factor to assess. A linear scale will be utilised for this evaluation, where the lowest density receives a score of one and the highest a score of zero.

Third, a primary challenge associated with long, slender wings is bending stress and deflection. To minimise this issue, Young's modulus will be examined, as it indicates how much a material deforms under applied load. This will also be evaluated on a linear scale, with a score of one for the highest values and zero for the lowest. Since this measurement directly influences the deflection and stresses on the wing, it is an important criterion.

Next, considering the need for the wing's materials to be recyclable to aid attritability, a qualitative scale will be employed. A score of zero is awarded to non-recyclable materials, 0.33 to those that are difficult to recycle, 0.66 to materials that are not economically viable to recycle, and a score of one for commonly recycled materials.

Finally, to keep SPARTA economically competitive, the costs of the materials have to be kept as low as possible. The price per kilogram will be used as a benchmark, as a lower density typically results in a larger volume, making mass comparisons viable across different designs. Now to obtain the weights, AHP-method is used and visualised in Table 7.5.

Table 7.5: AHP pairwise comparison values and their resulting normalised weights for skin trade-off

Criteria	Env. Resistance	Density	Young's Modulus	Recyclability	Cost	Computed Weight
Environmental Resistance	1.00	0.50	0.40	0.50	0.25	0.08
Density	2.00	1.00	1.00	2.00	4.00	0.30
Young's Modulus	2.50	1.00	1.00	3.00	0.80	0.25
Recyclability	2.00	0.50	0.33	1.00	0.75	0.14
Cost	4.00	0.25	1.25	1.33	1.00	0.23

Material Choices

For the wing, several materials were evaluated. The first is Al7075-T6^{3,4}, chosen for its optimal balance between density and Young's modulus. The second material, Ti6Al4V^{5,6}, offers similar properties to Al7075-T6 but has a

³URL: <https://asm.matweb.com/search/specificmaterial.asp?bassnum=ma7075t6> [cited 14 June 2025]

⁴URL: <https://www.steelmetind.com/7075-aluminum-sheet-plate.html> [cited 14 June 2025]

⁵URL: <http://www.metalspiping.com/titanium-alloy-ti-6al-4v.html> [cited 18 June 2025]

⁶URL: <https://asm.matweb.com/search/specificmaterial.asp?bassnum=mtp641> [cited 18 June 2025]

higher density and modulus. The third option is Carbon Fibre Reinforced Plastic (CFRP)^{7,8}, which boasts a low density that allows for a significantly lighter wing; however, it comes at the expense of being non-recyclable. Lastly, AM-350⁹ is considered for its high strength, although it entails a greater density and cost.

Trade-off Results

With the final weight and criteria defined, the trade-off is performed in Table 7.6. As can be seen, Al7075-T6 wins the trade-off not by a large margin. Thus, a sensitivity study was performed, indicating this result is the best in 60% of the cases, with AM-350 winning the rest. This is not a sizable margin, however, it was deemed sufficient with the possibility to use AM-350 in areas where extra reinforcement is required.

Table 7.6: Completed trade-off table. Criteria are given in the top row, and design options are in the first column. The actual values for the parameters are given. The colour is related to the number of points. The white circles, top right of the coloured cell, indicate the colour; G for green, B for blue, Y for yellow and R for red.

	Env. tance	Resis-	Density [kg/m ³]	Young's Modulus [GPa]	Recyclability	Cost [€/kg]	Score
Weight	8%	30%	25%	14%	23%	100%	
Al7075-T6	1.00 (G)	2810 (Y)	71.9 (R)	1.00 (G)	3.5 (G)	0.59	
CFRP	0.66 (B)	1600 (G)	70 (G)	0.00 (R)	87 (Y)	0.35	
Ti6Al4V	1.00 (G)	4430 (R)	115 (Y)	0.66 (B)	20.85 (G)	0.50	
AM-350	1.00 (G)	7810 (R)	200 (G)	1.00 (G)	50 (Y)	0.57	

7.6.3. Design

The design has gone through several iterations, being updated in tandem with the aerodynamics to maintain structural integrity. All while still staying in the region where the product can be produced. To start, the loads were obtained from the aerodynamic analysis of the wing. These loads were then transformed to get the limit loads by multiplying by 3.8, and the safety factor of 1.3 was applied. These diagrams are visualised in Figure 7.8.

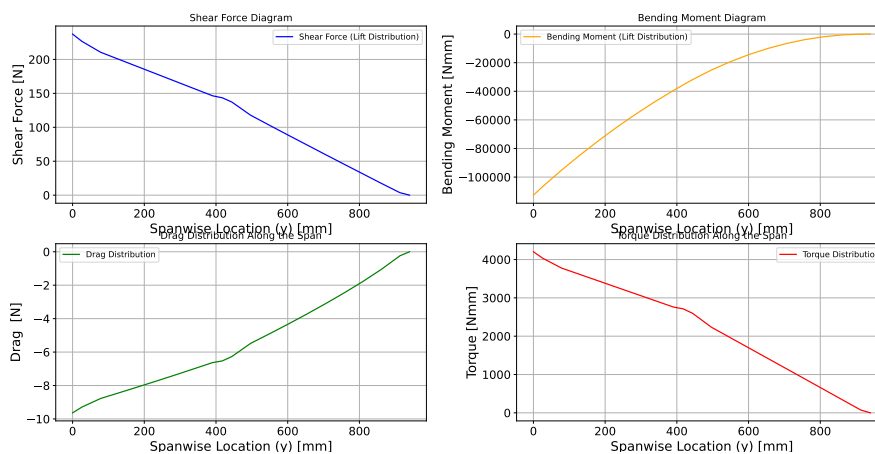


Figure 7.8: Force diagrams for cruise conditions with a load factor of 3.8

It can be identified that the most critical cross-section is shown to be at the root of the wing, which is expected as the forces only increase along the span. For this section, the stress distributions are shown for the different loading cases in Table 7.8. The most noteworthy is that the normal stress in the cross section reaches up to 492

⁷URL: https://www.matweb.com/search/datasheet_print.aspx?matguid=39e40851fc164b6c9bda29d798bf3726 [cited 14 June 2025]

⁸URL: <https://www.easycposites.eu/double-sided-high-strength-carbon-fibre-sheet> [cited 14 June 2025]

⁹URL: <https://www.hightempmetals.com/techdata/hitempAM350data.php> [cited 18 June 2025]

MPa, while the shear stress is much less, reaching a maximum of 28.5 MPa. For the shear, this is well below the shear strength, while the normal force needs some managing as it is very close to the yield strength of 502 MPa.

The last parts that are evaluated are the twist and deflection of the wing. These values are shown in Table 7.8, with as a result a maximum twist of 17.3° and a deflection of 298.1 mm, which is quite a large deflection that requires further analysis what the effect on the aerodynamics of the UAS.

For the final scenario, the loads are analysed for the morphing scenario. These loads are evaluated at every timestamp to ensure that the wing unfolds properly. These simulations were run for every type of launch condition to ensure proper functionality of the system. The most critical forces and deflections, for the morphing procedure, are shown in Table 7.8.

The geometric results derived from the analysis are summarised in Table 7.7. These findings encompass both cruise and maximum load conditions. The cruise load characteristics contribute to the aerodynamic analysis, while the maximum load conditions are essential for verifying the structural integrity of the system.

Table 7.7: Summary of the geometry of the wing

Parameter	Right Wing	Whole Wing	Retracted Right Wing	Tail
Centroid in x-direction [mm]	-34.31	-34.31	-34.31	-24.5
Centroid in y-direction [mm]	486.9	0	275	141
Centroid in z-direction [mm]	-2.62	-2.62	-2.62	0
I_{xx} [gmm ²]	93.29E6	7.92E8	32.34E6	8.52E6
I_{yy} [gmm ²]	1.13E6	3.74E6	5.34E5	2.85E5
I_{zz} [gmm ²]	94.39E6	7.96E8	32.86E6	8.78E6
I_{xy} [gmm ²]	-5.71E6	0	0	0
I_{xz} [gmm ²]	-1.59E6	0	-2.37E6	0
I_{yz} [gmm ²]	-5.89E5	-3.3E6	0	0
Skin Thickness [mm]	1	1	1	1
Mass [g]	440	880	440	84

Table 7.8: Summary of the structural loads of the wing

Parameter	Value Cruise	Value Limit Load	Value Morphing
Shear Force in the x-direction [N]	2.54	9.65	11.43
Shear Force in the z-direction [N]	62.4	217	333.31
Torque [Nmm]	1106	3862	5279
Maximum Bending Stress [MPa]	115.59	439.12	313.4
Maximum Shear Stress [MPa]	5.48	20.89	32.87
Safety Margin Bending	4.34	1.14	1.60
Safety Margin Shear	60.37	15.88	10.31
Tip Angle Wing [deg]	4.32	16.4	7.56
Tip Deflection Wing [mm]	61.13	232.29	58.12
Twist at Tip [deg]	0.325	1.23	0.867

7.7. Aeroelasticity Analysis

Aeroelastic effects, when unmitigated, could cause the structural failure of the system. Therefore, a thorough analysis is necessary. Because of the stringent time constraint, the analyses chosen had to be simple to implement, but also give relevant results. Additionally, because it was developed in parallel with the coupled physics model, the said model could not be used here. In this section, the main relevant parameters will be explained, a brief overview of the method explained and the results shown.

7.7.1. Parameter Acquisition

For all analyses, an equivalent cross-section suspended with springs was set up, and eigenvalues were analysed to monitor the divergent behaviour. To successfully utilise them, stiffnesses for said springs and the location of the pitch axis have to be correctly chosen.

To make the calculations simpler, the aerodynamic properties and mass moments of inertia (\mathbf{A} in Equation 7.55) were obtained by estimating the airfoil as a thin plate. This assumption enabled the flutter analysis, as otherwise those figures, especially control surface parameters, could not be obtained.

As the section moves around pitch and hinge axes, moment of inertia parameters used were around them. I_{xx_P} and J_{O_P} were, for example, gotten by using the Section 7.6 data and moving it via parallel axis theorem. Others are further defined in Table 7.9.

The stiffnesses, however, were based on the wing properties. The system has discontinuous wings; therefore, it was approximated as a simple wing with averaged stiffnesses. For the modes analysed in the rest of the chapter, a section located at three quarters of wing length, measuring from the wing root [31], is taken. The torsional and bending stiffness are obtained from Equations (7.37) and (7.38), and are 2794 Nm/rad and 779 N/m, respectively, using the values from Table 7.9.

$$K_\alpha = \frac{GJ_{O_P}}{L} \quad (7.37)$$

$$K_h = \frac{3EI_{xx_P}}{L^3} \quad (7.38)$$

Table 7.9: Parameters used for aeroelasticity

Parameter	Value	Description
ρ	1.225	Air density [kg m^{-3}]
m	0.424	Mass per unit length [kg m^{-1}]
S	0.148	Wing area [m^2]
C_{L_α}	7.8	airfoil lift slope [rad^{-1}]
E	70E9	Elastic modulus [Pa]
G	26.7E9	Shear modulus [Pa]
L	0.75	Position of representative cross-section of the wing counting from the root [m]
c	0.075	Chord length [m]
x_f	$0.31 \cdot c$	Pitch axis location from the nose of the airfoil (chosen to be the shear centre) [m]
x_{ac}	$0.25 \cdot c$	Airfoil aerodynamic centre [m]
x_h	$0.9 \cdot c$	Aileron hinge position from the nose of the airfoil [m]
A	141.7E-6	Area of the airfoil cross section [m^2]
I_{xx_P}	1.082E-9	Area moment of inertia around the pitch axis [m^4]
J_{O_P}	1.074E-7	Polar moment of inertia around the pitch axis [m^4]
b	$\frac{c}{2}$	Half chord [m]
a	$\frac{x_f}{b} - 1$	Control positional parameter
c_h	$\frac{x_h}{b} - 1$	Pitch axis positional parameter
μ	$\cos^{-1}(c_h)$	
S	$m \left(\frac{c}{2} - x_f \right)$	Static mass moment of wing around pitch axis(plate)[kg m]
I_α	$\frac{m}{3} (c^2 - 3cx_f + 3x_f^2)$	Mass moment of inertia of wing around pitch axis(plate)[kg m ²]
S_β	$\frac{(c-x_h)^2}{2c}$	Static mass moment of control surface around hinge axis(plate)[kg m]
I_β	$\frac{(c-x_h)^3}{3c}$	Mass moment of inertia of control surface around hinge axis(plate)[kg m ²]
$I_{\alpha\beta}$	$I_\beta + (x_h - x_f)S_\beta$	Product of inertia(plate)[kg m ²]
T_1	$-\frac{1}{3}\sqrt{1-c_h^2} (2+c_h^2) + c_h\mu$	
T_2	$c_h(1-c_h^2) - \sqrt{1-c_h^2} (1+c_h^2)\mu + c_h\mu^2$	
T_3	$-\left(\frac{1}{8}+c_h^2\right)\mu^2 + \frac{1}{4}c_h\sqrt{1-c_h^2}\mu(7+2c_h^2) - \frac{1}{8}(1-c_h^2)(5c_h^2+4)$	
T_4	$-\mu + c_h\sqrt{1-c_h^2}$	
T_5	$-(1-c_h^2) - \mu^2 + 2c_h\sqrt{1-c_h^2}\mu$	
T_6	T_2	
T_7	$-\left(\frac{1}{8}+c_h^2\right)\mu + \frac{1}{8}c_h\sqrt{1-c_h^2}(7+2c_h^2)$	
T_8	$-\frac{1}{3}\sqrt{1-c_h^2} (2c_h^2+1) + c_h\mu$	
T_9	$\frac{1}{2} \left(\frac{1}{3}\sqrt{1-c_h^2}^3 + aT_4 \right)$	
T_{10}	$\sqrt{1-c_h^2} + \mu$	
T_{11}	$\mu(1-2c_h) + \sqrt{1-c_h^2} (2-c_h)$	
T_{12}	$\sqrt{1-c_h^2} (2+c_h) - \mu(2c_h+1)$	
T_{13}	$\frac{1}{2} (-T_7 - (c_h - a)T_1)$	
T_{14}	$\frac{1}{16} + \frac{1}{2}ac_h$	
Ψ_1	0.165	First multiplier part of Wagner function approximation
Ψ_2	0.335	Second multiplier part of Wagner function approximation
ϵ_1	0.0455	First exponent part of Wagner function approximation
ϵ_2	0.3	Second exponent part of Wagner function approximation

7.7.2. Static Effects

Static effects are the ones that show up using analysis with steady aerodynamic response. The main considerations here are the torsion divergence and the aileron reversal.

Torsion divergence is an effect where the twist of the wing grows exponentially due to an increase in the angle of attack the wing provides. It can be found by setting up an airfoil suspended with a torsion spring at its pitch axis. The final system is reduced to Equation 7.39, where v_d is the divergence speed, and is equal to 907 m/s.

$$v_d = \sqrt{\frac{2K_\alpha}{\rho S(x_f - x_{ac})C_{L_\alpha}}} \quad (7.39)$$

The result is unsurprising because the flexural axis is very close to the aerodynamic centre and because of the high torsional stiffness of the wing.

Additionally, due to high torsional stiffness and low operational speed, the aileron reversal was assumed not to be a problem. This assumption will be revisited in Subsection 9.3.2.

7.7.3. Dynamic Effects

Dynamic effects require more involved methods to determine correctly. Many different flutter effects, such as transonic buzz or stall flutter, mainly occur at high Mach speeds [32], and as the system flies in the incompressible regime, they are left for future analyses. Here, only classical flutter will be assessed. It is usually caused by inter-coupling between coupling of the different motions of the wing, in this case between horizontal movement of the wing, the rotation of it and the rotation of the control surface.

Before the system is defined, it is important to mention that the structural natural frequencies (ω_h and ω_α) are calculated using Equations (7.40) and (7.41), and equal to 6.8 Hz and 450 Hz, respectively.

$$\omega_h = \sqrt{\frac{K_h}{m}} \quad (7.40) \quad \omega_\alpha = \sqrt{\frac{K_\alpha}{I_\alpha}} \quad (7.41)$$

Frequencies are of a different order of magnitude, therefore, these motions are unlikely to couple. Because of that, a two-degree-of-freedom model (pitch-plunge) would not be enough to analyse flutter.

A representative 3-Degree-Of-Freedom (DOF) (pitch-plunge-control) linear system with unsteady aerodynamics is chosen as the most reasonable system to represent it. The method is used with example data to verify it. The data can be found in "Introduction to Nonlinear Aeroelasticity"[32].

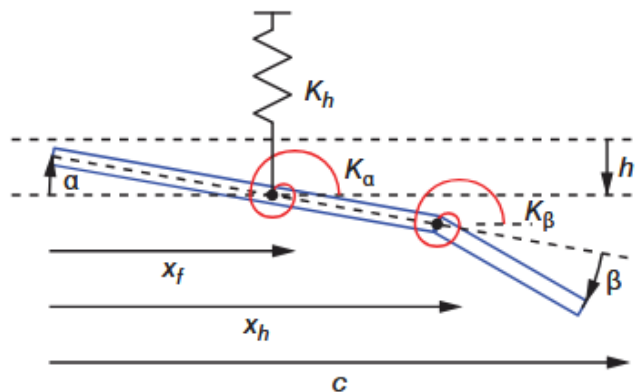


Figure 7.9: Pitch-plunge-control system cross section [32]

The system can be represented as a second-order differential equation:

$$\begin{bmatrix} m & S & S\beta \\ S & I_\alpha & I_{\alpha\beta} \\ S\beta & I_{\alpha\beta} & I_\beta \end{bmatrix} \begin{bmatrix} \ddot{h} \\ \ddot{\alpha} \\ \ddot{\beta} \end{bmatrix} + \begin{bmatrix} C_h & 0 & 0 \\ 0 & C_\alpha & 0 \\ 0 & 0 & C_\beta \end{bmatrix} \begin{bmatrix} \dot{h} \\ \dot{\alpha} \\ \dot{\beta} \end{bmatrix} + \begin{bmatrix} K & 0 & 0 \\ 0 & K_\alpha & 0 \\ 0 & 0 & K_\beta \end{bmatrix} \begin{bmatrix} h \\ \alpha \\ \beta \end{bmatrix} = \begin{bmatrix} -l \\ m_{x_f} \\ m_{x_h} \end{bmatrix} \quad (7.42)$$

First matrix is **A**, second **C** and third **E**. The aerodynamic forcing¹⁰ is [31]:

$$l(t) = \rho b^2 \left(U\pi\dot{\alpha} + \pi\ddot{h} - \pi ba\ddot{\alpha} - UT_4\dot{\beta} - T_1b\ddot{\beta} \right) + 2\pi\rho bUC(k)w \quad (7.43)$$

$$m_{x_f}(t) = -\rho b^2 \left[-a\pi b\ddot{h} + \pi b^2 \left(\frac{1}{8} + a^2 \right) \ddot{\alpha} - (T_7 + (c_h - a)T_1) b^2 \ddot{\beta} + \pi \left(\frac{1}{2} - a \right) Ub\dot{\alpha} \right] \\ - \rho b^2 \left[(T_1 - T_8 - (c_h - a)T_4 + T_{11}) Ub\dot{\beta}(T_4 + T_{10})U^2\beta \right] + 2\rho Ub^2\pi \left(a + \frac{1}{2} \right) C(k)w \quad (7.44)$$

$$m_{x_h}(t) = -\rho b^2 \left[-T_1b\ddot{h} + 2T_{13}b^2\ddot{\alpha} - \frac{1}{\pi}T_3b^2\ddot{\beta} \left(-2T_9 - T_1 + T_4 \left(a - \frac{1}{2} \right) \right) Ub\dot{\alpha} - \frac{1}{2\pi}UbT_4T_{11}\dot{\beta} \right] \\ - \rho b^2 U^2 \frac{1}{\pi} (T_5 - T_4T_{10})\beta - \rho b^2 UT_{12}C(k)w \quad (7.45)$$

$C(k)$ is the Theodorsen function, T_n are constants, and w is the downwash:

$$w = U\alpha + \dot{h} + b \left(\frac{1}{2} - a \right) \dot{\alpha} + \frac{T_{10}}{\pi} U\beta + b \frac{T_{11}}{2\pi} \dot{\beta} \quad (7.46)$$

Because these equations involve both time derivatives and reduced frequency $k = \frac{\omega b}{v}$, they need to be reduced. $C(k)\omega$ can be found by first applying Wagner theory (assumes attached flow), which gives an expression of lift as a purely time function, equating it to Equation 7.44. Then $C(k)\omega$ can be expressed. The result and a good Wagner function Φ approximation are:

$$C(k)w = \Phi(0)w(t) - \int_0^t \frac{\partial\Phi(t-t_0)}{\partial t_0} w(t_0)dt_0 \quad (7.47) \quad \Phi(t) = 1 - \Psi_1 e^{-\epsilon_1 Ut/b} - \Psi_2 e^{-\epsilon_2 Ut/b} \quad (7.48)$$

To make it easier to solve aerodynamic forcing, six states w_n can be established, for all combinations of h, α, β and both ϵ . For example, w_1 is, and its derivative (Leibniz's rule) are:

$$w_1(t) = \int_0^t e^{-\epsilon_1 v(t-t_0)/b} h(t_0)dt_0 \quad (7.49) \quad \dot{w}_1(t) = h(t) - \frac{\epsilon_1 v}{b} w_1(t) \quad (7.50)$$

w_2 is with plunge and ϵ_2 , w_3 - with pitch and ϵ_1 and so on.

With them, equations of motion, assuming no forcing, can be written in the form:

$$(\mathbf{A} + \rho\mathbf{B})\ddot{\vec{y}} + (\mathbf{C} + \rho v\mathbf{D})\dot{\vec{y}} + (\mathbf{E} + \rho v^2\mathbf{F})\vec{y} + \rho v^3\mathbf{W}\vec{w} = \vec{0} \quad (7.51)$$

$$\dot{\vec{w}} - \mathbf{W}_1\vec{y} - v\mathbf{W}_2\vec{w} = \vec{0} \quad (7.52)$$

This system was represented as a matrix of first-order Ordinary Differential Equations (ODE), and the eigenvalues λ were extracted. This was done for a range of speeds, tracking the eigenvalues that represent structural modes, until one of them shows divergence ($\Re(\lambda) \geq 0$).

$$\dot{\vec{x}} = \mathbf{Q} \cdot \vec{x} \quad (7.53)$$

$$\mathbf{Q} = \begin{bmatrix} -\mathbf{M}^{-1}(\mathbf{C} + \rho v\mathbf{D}) & -\mathbf{M}^{-1}(\mathbf{E} + \rho v^2\mathbf{F}) & -\rho v^3\mathbf{M}^{-1}\mathbf{W} \\ \mathbf{I}_{3 \times 3} & \mathbf{0}_{3 \times 3} & \mathbf{0}_{3 \times 6} \\ \mathbf{0}_{6 \times 3} & \mathbf{W}_1 & v\mathbf{W}_2 \end{bmatrix} \quad (7.54)$$

$$\mathbf{M} = \mathbf{A} + \rho\mathbf{B} \quad (7.55)$$

A, **C** and **E** are structural mass, damping and stiffness matrices and **B**, **D**, **F** are the aerodynamic counterparts of structural matrices. W_1 , W_2 and W are aerodynamic state equation and influence matrices. The full matrices

¹⁰Assumptions: ideal, attached flow conditions, disturbances were assumed small and the wake is assumed to move with the free stream. It cannot capture stall or leading edge separation, but for the initial flutter check, it is enough.

for this equation can be found in the book [32].

All of them can be constructed with the assumptions set in Subsection 7.7.1, except the structural damping matrix \mathbf{C} . The exact values of it are difficult to estimate and will vary with the frequency of respective motions. It is clear, however, that the smaller the damping, the sooner the flutter occurs. However, with no damping present, the system displays undesirable behaviour, such as flutter at speed close to zero or decreasing flutter speed for increased (control) stiffness. The lowest setting where this did not occur was $\mathbf{C} = 0.00005 \cdot \mathbf{I}_{3 \times 3}$. The plunge and pitch DOF certainly have a larger effect, as purely viscous damping ratio for aluminium is $0.5E-4$ ¹¹, and the critical frequency is bigger than 1 rad/s. As for control, this damping is also achievable, as MathWorks default for small actuators is twice as big¹².

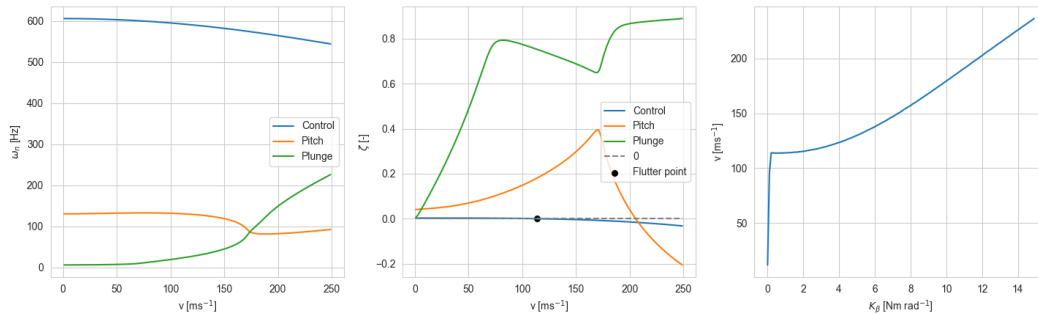


Figure 7.10: 1 and 2: Natural frequency $\omega_{n_i} = |\lambda_i|$ and damping $\zeta_i = -\frac{\Re(\lambda_i)}{\omega_{n_i}}$ at a given speed for $K_\beta = 0.5$. 3: Flutter speed based on control stiffness

As can be seen in Figure 7.10, flutter is not an issue for almost any K_β . And when it does appear, it first manifests in the control surfaces, and much later in pitch DOF. The main way to delay it would be to dampen and stiffen the control surfaces, but even with the conservative assumptions, it does not appear within the flight envelope.

7.7.4. Sensitivity

The K_β is set to 0.5 Nm/rad and the model is tested by varying different inputs by -10% to 10%. Axis parameter increase means that the axis is moved further aft.

Table 7.10: Sensitivity analysis of flutter analysis

Parameter	K_α, J_{oP}	$K_h, C_h, C_\alpha, I_{xxP}$	C_β	x_f	x_h
Effect on flutter speed (m/s for +1% change)	0.4	no effect	0.3	-0.4	high effect

The pitch parameters having a moderate impact, while the plunge having almost none, make sense, as the flutter in this case is caused by pitch-control interaction. For structural damping, only the control one having any impact also makes sense, as they are orthogonal, and flutter manifests first in the control DOF. Moving x_f makes the control surface smaller, decreasing the mass moments of inertia for it and expediting flutter.

Only the effect of x_h is nonlinear. A slight increase in it makes flutter speed much higher and vice versa. This makes sense, as all the moments are calculated around it. It is so well known that even the act of moving it has a name - mass balancing.

7.8. Verification

Testing was performed on the code implementation. Unit tests were first conducted on the class and all of its functions, mostly focusing on ensuring correct outputs and functioning of individual parts. Subsequently,

¹¹URL: https://help.solidworks.com/2016/English/SolidWorks/cworks/r_viscous_damping_ratios.htm, Cited on 22 June, 2025

¹²URL: <https://www.mathworks.com/help/sps/ref/femparameterizedrotaryactuator.html>, Cited on 22 June, 2025

several system tests for each of the parts of the flight model were conducted and can be seen in Table 7.11.

Table 7.11: System tests for the wing structural model

Test	Action	Expected Outcome	Result
Mesh			
TST-WING-01	Vary deployment angle from 0° to 90° .	Mesh starts parallel to x-axis and ends parallel to y-axis.	Passed
TST-WING-02	Vary extension from 0 to 1.	Length begins at the length of the inner wing and ends at half span. New mesh points are created.	Passed
Structures			
TST-WING-03	Vary load to test changes in shear centre.	Shear centre is independent.	Passed
TST-WING-04	Calculate the bending stresses in a known case.	The stresses match.	Passed
TST-WING-05	Insert a cylindrical shape to calculate the twist.	Hand calculated value matches the total twist.	Passed
TST-WING-06	Test the shear flow calculations by integrating the forces in the horizontal and vertical direction	Integrated values match the shear forces applied	Passed
TST-WING-07	Test moment calculation for shear by calculating the moment caused by the full shear flow and that of the applied shear forces	Both moments match	Passed
TST-WING-08	Test the slope angle of a wing with $M_x = 1 \text{ Nmm}$, $y = 3 \text{ mm}$, $E = 71.7 \text{ GPa}$, $I_{xx} = 666 \text{ mm}^4$	Expected slope of $-6.28\text{E-}08 \text{ rad}$	Passed
TST-WING-09	Test mass for a cylinder of cord of 100 mm and height of 500 mm	Mass is 883 grams	Passed
TST-WING-10	Test I_{xx} for a cylinder of cord of 100 mm and height of 500 mm	I_{xx} is $2.28\text{E}7 \text{ mm}^4$	Passed
Aerodynamics			
TST-WING-11	The inner wing and outer wing feature different airfoil designs. This test verifies whether the extension is applied correctly, identifying the inner and outer wing lengths and assigning the appropriate airfoil data to both the inner and outer wings.	The correct airfoil is assigned based on various telescopic parameter values.	Passed
TST-WING-12	Test the wing assembly function to confirm it correctly inputs the mesh and restructures it.	Returns a wing mesh from tip to tip, with the correct dimensions of widths, chords, and points.	Passed
TST-WING-13	Test how the function derives data and interpolates aerodynamic coefficients	The code uses interpolation to estimate unknown data points and produces reasonable values both in magnitude and sign.	Passed
TST-WING-14	Test how the function approximated the circulation in the first iteration.	The first approximation for the circulation should follow an elliptical distribution along the span.	Passed
TST-WING-15	Test whether the twist from the structural analysis is correctly applied to each point along the discretised wing.	the twist has been correctly applied and influences the local angle of attack in the correct direction.	Passed
Wing Morphing			
TST-WING-16	Wings are symmetric around the body's x-axis.	Static moments symmetric around the x-axis.	Passed
TST-WING-17	Wings symmetric around the body x-axis; launch from a helicopter.	No variation in roll and yaw observed.	Passed
TST-WING-18	Launch from a helicopter; all degrees of freedom constrained except roll; initial roll rate applied.	UAS rolls in the direction of the initial roll rate until it approaches an asymptote where the roll rate decays to zero.	Passed
TST-WING-19	Launch from a helicopter; roll and yaw degrees of freedom constrained; initial pitch rate applied.	UAS shows a phugoid motion.	Passed
Aeroelasticity			
TST-WING-20	Input example values (Example 5.1 [32])	The eigenvalues match with the book ones	Passed

Test	Action	Expected Outcome	Result
TST-WING-21	Vary parameters and check the response	The model behaves as expected (Subsection 7.7.4)	Passed

7.9. Sustainability & Attritability

Here, the sustainability related to the structure of the wing is discussed. First, it was made to get the most performance with the minimal amount of material. The wing itself is made purely out of aluminium, and in case of damage, the damaged parts can be recycled.

In terms of attritability, the wing manufacturing process is based on bending and forming aluminium sheets into shape. Excluding the setup, this process is cheap and produces parts quickly. Therefore, the wing is optimised for attrition.

7.10. Risk Analysis

In this section, the sustainability related to the wing structure is discussed.

RSK-WING-01: Failure of wing unfolding mechanism

One of the most critical risks is the wing's inability to unfold during the launch process. If this situation occurs, the system loses its ability to generate lift and will fall, thus being unable to complete the mission. One way to avoid this catastrophic issue is to perform rigorous pre-flight testing and simulations. This would validate that the unfolding mechanism can be relied upon to perform as intended.

RSK-WING-02: Failure due to extreme cases

One of the structural risks is the unexpected structural overload leading to a catastrophic failure. This can be caused by severe turbulence and emergency manoeuvres. Mitigation techniques should include a proper design phase to ensure that the yield strength exceeds the loads encountered during flight in extreme conditions.

RSK-WING-03: Failure of the telescopic extension mechanism

Failing to fully extend the wing significantly impacts risk management. Although it is not as critical as a failure of the unfolding mechanism, it still interferes with the system's performance. Without the ability to fully extend the wing, the aircraft will be limited to flying with only half of its wing span. While the UAS can still generate lift and remain in the air, it lacks the necessary surface area for optimal performance. As a result, it will be in a descending flight with very limited range and endurance. Mitigation techniques could include a procedure that, in case of extension failure, would abort the mission and redirect the aircraft back to the base.

RSK-WING-04: Plastic deformation of the wing

Another structural risk involves the deformation of the wing. When subjected to excessive stresses, the wing may begin to experience permanent deformation. This not only increases the risk of structural failure but also poses a requirement for additional maintenance, as the wings will no longer be able to fold back due to experienced deformation. To keep the wing within the elastic range during all loading conditions, it is recommended to conduct static load tests on the structure.

7.11. RAMS Analysis

This subsection investigates the reliability, accessibility, maintainability and safety of the wing of SPARTA.

Reliability

Thermal cycles can induce cracks in the material due to the operational range of -70 to 50 °C, and while material fatigue could lead to failure, this is not a significant concern since the UAS is only required to perform 20 missions.

Availability

The wing is constructed from pure Al7075-T6, which is recyclable and widely available within Europe¹³. This ensures a high availability of replacement parts, enabling quick recovery in the event of damage. Additionally, the wing's simple design allows for fast inspections and easy identification of any issues.

¹³URL: <https://european-aluminium.eu/about-aluminium/aluminium-industry/> [cited 18 June 2025]

Maintainability

The wing experiences the most damage during cruise operations, necessitating ongoing monitoring and maintenance. This is addressed through several design choices. The utilisation of thin sheet wings ensures that components are simple and convenient to replace. Regular visual inspections will be conducted to detect any significant structural damage early on. Additional inspections will also focus on corrosion, especially since the system is designed to operate in potentially harsh environmental conditions.

Safety

There is the risk that the system could experience resonance during gusts, which might lead to wing failure and compromise the system's integrity. Additionally, control system malfunctions in such scenarios could severely limit manoeuvrability. To mitigate these risks, an emergency recovery protocol has been established.

7.12. Financial Analysis

The cost of the wing comprises two main components that contribute to the overall expense. These components include the constant costs incurred during the production of SPARTA, which consist of the material costs for the wing and the costs of labour. The material costs of Al7075-T6 are \$3.50 per kg¹⁴, this is negligible. The labour costs are considered for performing pressing¹⁵, milling¹⁶ and welding [33]. As this process will take about 7 hours to manufacture. Altogether, these factors result in a total cost of €2,500 per wing. Thus, a total of €5,000 will be spent on the manufacturing of both wings as a whole. Additionally, recurring costs primarily consist of labour expenses, which amount to approximately €200 per mission, representing roughly one-third of the total system inspection costs.

7.13. Compliance Matrix

In this section, the requirements presented in Section 7.2 are checked for their compliance, shown in Table 7.12.

Table 7.12: Wing design compliance matrix

Code	Compliance
REQ-WING-01	G
REQ-WING-02	G
REQ-WING-03	G
REQ-WING-04	G

7.14. Recommendations

Here lie the recommendations gathered from all the analyses of the wing. They appear here in the order they were in this chapter.

7.14.1. Structures

This subsection discusses the recommendations for the structural analysis.

Thin Walled Approximation

Run the analysis of the wing while not using a thin-wall approximation, as the thickness-to-cord ratio is such that the thin-walled approximation is starting to deviate from the real value, as it starts to overestimate the stresses.

Buckling

During the design, the main focus was put on shear and buckling. The failure due to buckling has been underdeveloped and thus requires extra attention. As with preliminary calculations done the structure requires additional stringers and stiffeners to accommodate the buckling stress.

¹⁴URL: <https://www.steelmetind.com/7075-aluminum-sheet-plate.html> [cited 17 June 2025]

¹⁵URL: <https://testbook.com/mechanical-engineering> [cited 18 June 2025]

¹⁶URL: <https://richconn.com/cnc-milling-cost/> [cited 20 June 2025]

7.14.2. Aerodynamics

This subsection presents recommendations for the aerodynamic analysis. They should be considered for future improvements to improve the code performance and accuracy.

Stall Angle Limitations

The current aerodynamic model is based on two-dimensional data generated by XFOIL software. This data is limited to angles of attack ranging from -10 to +20 degrees. Outside of this range, there is no available aerodynamic data. Therefore, the model assumes a complete loss of lift for angles of attack greater than +20 degrees and less than -10 degrees. This simplification leads to discontinuities and inaccuracies.

To improve this model, future versions should consider extending the range of angles of attack. Such improvements could be done by either using experimental data obtained from wind tunnel tests or flight data, which would provide a more accurate representation of post-stall aerodynamic behaviour. If such data is unavailable, this limitation can be addressed by using stall behaviour approximation models. These models could estimate lift, drag, and moment beyond stall conditions based on trends from known data. Both approaches would enhance the model's ability to handle non-linear stall behaviour.

Correction at the Wing Midpoint

During testing, it was observed that the computed lift distribution exhibited an elliptical-like pattern across the span, as expected. However, the lift value at the midpoint of the wing was significantly lower, approximately 30 to 40% lower than the values near that point.

Due to time constraints, this issue was not fully addressed. As a temporary solution, the lift at the midpoint was altered to match the average of the two neighbouring spanwise sections. This adjustment was considered reasonable, as an elliptical-like distribution should have nearly constant lift in the central region of the wing. Additionally, since the fuselage was not modelled, the centre section was treated only as part of the lifting surface, without any interference or discontinuity.

However, this correction with overwriting the data should be regarded as a short-term fix. Future work should focus on the investigation of the root cause and ensuring that the model generates results that do not require special adjustments.

Efficient Mesh Distribution for Aerodynamics

Currently, the wing is divided into spanwise sections using a uniform distribution, where all control points are placed equally across the span. While this method is simple to implement, it is not the most accurate for the aerodynamic behaviour of finite wings. The variation in lift and downwash is most important near the wing tips, while the middle sections of the wing typically experience smooth and more uniform conditions.

A recommended improvement is to switch to cosine or non-uniform spacing, where the points would be denser near the wing tips and sparser in the centre. This approach would enhance numerical accuracy without increasing the total number of points, keeping the computational power and time the same as the basic mesh. It allows for better handling of the sharp gradients and induced angles near the tips. Thus, it will lead to a more precise estimation of the aerodynamic coefficients.

Helicopter Launch Downwash Effects

The current model assumes isolated deployment and does not take into account external disruptions that occur during the tube launch from a helicopter. This scenario includes complex flow phenomena, like downwash, turbulence, and potential wake interactions, which are not considered in the existing aerodynamic model.

It is recommended that future versions of the model include a simulation or approximation of these effects for helicopter launch. This could involve CFD simulations or wind tunnel experiments. It is crucial to assess these effects and their influence on stability and controllability for a safe deployment.

Structural Influences and Aeroelasticity

The current aerodynamic model assumes a rigid wing. However, in real-world conditions, the wing experiences elastic deformations. These deformations can influence the local angle of attack, changing the distribution of aerodynamic forces.

The model is designed to account for the key structural effect, namely torsional twist. The code includes a function that adjusts the effective angle of attack at each discrete point based on the torsional deformation. Although the code has this capability, it was not integrated into the final implementation due to time constraints.

For future development, it is recommended to fully integrate this torsion-induced twist effect. Additionally, the model should be expanded to include more aeroelastic effects, like bending deflections and their interaction with aerodynamics. This extension would allow the simulation to more accurately reflect the behaviour of elastic wings.

Flight Conditions

The current aerodynamic model relies on two-dimensional airfoil data, which was derived with a Reynolds number of 150,000. This number was calculated for standard atmospheric conditions at a fixed altitude in operation. However, parameters like air density and air viscosity change during different deployment procedures or in varying atmospheric conditions, thus modifying the Reynolds number. Different Reynolds number further influences the aerodynamic coefficients. To make sure that the model is authentic, future versions should include airfoil data across a range of Reynolds numbers. Such improvement would guarantee that aerodynamic predictions remain valid under changing flight conditions.

7.14.3. Wing Morphing

In this subsection, the recommendations for the wing morphing analysis are presented. Since the launch simulation incorporates the aerodynamics model, the shortcomings of that model are present during the wing morphing phase as well.

Wing Extension

The telescopic extension of the wing is not accounted for in the launch situation due to the lack of time to fully implement it. It would require adjusting the dynamics model to consider the varying inertia tensor of the extending wing and translating wing centre of gravity.

Ground Launch Reevaluated

The simulation was performed for the launch at 45° and 40 m/s and it resulted in a stall occurring a few seconds after launch. Therefore, it is recommended to redesign the fuselage to withstand launch at a higher speed. Alternatively, the launch from a moving vehicle can be simulated to verify that indeed the launch is feasible.

Airbus A400M Launch

The aggressive pitch-up moment is observed when the UAS is launched from the aircraft. It is recommended to simulate first the tail unfoldment and delay the wing unfoldment until the airspeed is reduced. Since the tail creates a negative pitching moment, it is likely to compensate for the pitch-up behaviour.

7.14.4. Aeroelasticity

The aeroelasticity model could still be improved to eliminate the uncertainty that is still lingering.

First thing to assess would be the gust response. The current analysis can only determine the steady state response; therefore, it is unclear if deflection due to input would not be too large.

Second would be the stall and compressible flow effects. Incorporating them would allow for analysis of more complex flutter types, such as stall flutter.

The last major effect to include is the structural non-linearities of the wing. It is composed of two sections, which have similar polar moment of inertia, but considerably different moments of inertia about the horizontal axis. Because of telescoping, it will also inevitably have free-play between the sections.

The first point could be addressed by adding forcing to the model and analysing the time response. The second would require implementation of a much more complex, semi-empirical aerodynamics model, which needs to be tuned with experimental results. The last one necessarily requires a 3D model, and the easiest way to achieve it would be to incorporate the existing multi-physics model.

8. Fuselage Structure

In this chapter, the fuselage structure subsystem is discussed. The entire design process is walked through from functional and requirements analysis in Sections 8.1 and 8.2. Then the tools and design are presented in Sections 8.3 and 8.4. Subsystem analysis of sustainability, risks, RAMS and financials is performed in Sections 8.5-8.8. To conclude, a compliance matrix and recommendations are provided in Sections 8.9 and 8.10.

8.1. Functional Analysis

The fuselage structure serves two primary roles: load carrying and protection. Below in Table 8.1, the functions of the fuselage structure subsystem are addressed.

Table 8.1: Functions of the fuselage structure

Code	Description	Origin
FUN-FUS-01	Transmit flight, launch and recovery loads without failing.	FUN-SYS-3, FUN-SYS-5, FUN-SYS-7
FUN-FUS-02	Protect internal components.	FUN-SYS-4
FUN-FUS-03	Facilitate easy access to internal components.	FUN-SYS-8
FUN-FUS-04	Provide satisfactory housing to components and payloads.	FUN-SYS-1.2

8.2. Requirements

Having obtained the required functions, they can be combined with existing system and subsystem requirements to derive a list of requirements for the fuselage structure to comply with and guide its design. They can be found in Table 8.2.

Table 8.2: Fuselage structure requirements

Code	Description	Origin
REQ-FUS-01	The fuselage shall accommodate the primary payload.	FUN-FUS-04,
REQ-FUS-02	The fuselage shall accommodate the secondary payload.	REQ-SYS-05,
REQ-FUS-03	The fuselage shall have a storage temperature between -70 and +70.	FUN-FUS-04,
REQ-FUS-04	The fuselage shall have a service temperature between -70 and +50.	REQ-SYS-06,
REQ-FUS-05	The fuselage shall protect the internal components.	REQ-SYS-16
REQ-FUS-06	The fuselage shall provide at least 8.5 litres (excluding contingency) of internal volume.	REQ-SYS-17
REQ-FUS-07	The fuselage shall have maximum cylindrical dimensions of 123.9 mm × 914.4 mm.	FUN-FUS-02,
REQ-FUS-08	The fuselage structure shall provide direct access to all internal components.	REQ-SYS-18-03
REQ-FUS-09	The fuselage shall provide the primary payload with a clear view of its surroundings.	FUN-FUS-04,
REQ-FUS-10	The fuselage shall be capable of withstanding the loads associated with a limit load factor of 3.8g.	Chapter 5
REQ-FUS-11	The fuselage shall withstand the loads associated with each allowable point on the launch envelope.	REQ-SYS-22
REQ-FUS-12	A safety factor of 1.3 shall be applied to all loads.	FUN-FUS-03
REQ-FUS-13	The fuselage structure shall be easily manufacturable.	FUN-FUS-04
REQ-FUS-14	The fuselage structure shall only use European materials.	REQ-SYS-36
REQ-FUS-15	The fuselage shall be recyclable.	REQ-SYS-36
REQ-FUS-16	The fuselage structure shall have a mass lower than 1.16 kg (excluding contingency).	REQ-SYS-30
REQ-FUS-17	The fuselage structure shall have a volume of less than 0.38 L (excluding contingency)	REQ-SYS-32
		REQ-SYS-21
		From budgets in Section 15.2
		From budgets in Section 15.2

8.3. Analysis

Below, the details of the analysis model used in sizing the fuselage structure will be outlined. First, new assumptions will be summarised, followed by the model description and ending with model verification.

Assumptions

As an extension of the model from Chapter 7, all assumptions have been inherited, with this subsection presenting assumptions that are added. They can be found in Table 8.3.

Table 8.3: Assumptions used in the fuselage model

Code	Description	Validity
AS-FUS-01	The fuselage is only significantly loaded in the longitudinal plane.	Torque and side forces are significantly lower than lift and wing moments, and the cross-section geometry favours stiffness in that direction.
AS-FUS-02	All assumptions of Euler buckling theory hold.	Applicable to slender beams of uniform cross-section and material, such as stiffeners and thin panels. Gives an initial estimate without FEA.
AS-FUS-03	Launch inertial loads are quasi-static and applied at the CG.	Conservative, as the real inertial loads would be more gently distributed along the length.
AS-FUS-04	Fuselage weight is distributed uniformly along its load-carrying length.	Necessary assumption without specific weight distributions. Conservative as real weight would likely be more concentrated at the most highly loaded point, reducing the absolute maximum bending loads there.

Model

The analysis procedure used in designing the fuselage structure closely parallels the structural analysis of the wing structure as outlined in Chapter 7. The loads acting parallel to the longitudinal plane of the aircraft are first transformed into internal force and moment diagrams. Each of the cross-sections of the fuselage is then discretised into booms, and the most critical internal loads per section are analysed. Furthermore, as brief periods of high acceleration are expected during launch, the fuselage will be axially loaded by extreme inertial loads. This naturally introduces the danger of buckling of skin and stiffener elements, as well as column buckling of the entire structure.

The first type of buckling considered and the foundation of all of the subsequent, is Euler buckling. It is described by Equation (8.1):

$$\sigma_{cr} = \frac{\pi^2 E}{(L_e/\rho)^2}, \quad (8.1)$$

where σ_{cr} is the critical buckling stress, E represents the modulus of the material, L_e the effective length of the beam, based on boundary conditions, and ρ is the radius of gyration. Stiffeners shall be considered fixed on either side due to their connection to frames, so their effective length is equal to half of their real length [20]. For column buckling of the entire structure, which has two different cross-sections, a useful relation is derived by Wang [34], who presents the modified Equation (8.2) for which m can be obtained by numerically solving Equation (8.3):

$$F_{cr} = \frac{m^2 E I_2}{L^2}, \quad (8.2) \quad \tan \left(m \sqrt{\frac{L_1^2 I_2}{L^2 I_1}} \right) \tan \left(m \left(1 - \frac{L_1}{L} \right) \right) = \sqrt{\frac{I_2}{I_1}}. \quad (8.3)$$

The previous equations assume a fixed-free beam made of two cross-sections of the same material, with the bottom (fixed) section designated as 2 and the top (free) as 1. F_{cr} is the critical load, I represents the moment of inertia of the cross-section and L the length of the section.

Euler buckling can be modified to represent that of a thin plate, which concerns the skin panels and contributes to stiffener crippling calculations. It can be described by Equation (8.4), which can describe both normal and shear buckling,

$$\sigma_{cr} = C \frac{\pi^2 E}{12(1 - \nu^2)} \left(\frac{t}{b} \right)^2. \quad (8.4)$$

In this equation, ν is the Poisson's ratio, t the thickness of the plate and b its width perpendicular to loading.

Constant C can be chosen based on boundary conditions and the aspect ratio of the plate. Skin panels will be assumed to be simply supported on all sides, whereas stiffener elements will be simply supported if surrounded by other elements and free on one side if not. To obtain the constants for flat plates, one can consult Megson [20]. For curved panels, which are less likely to buckle, refer to Gerard and Becker [35].

Building on thin plate buckling, one can assess the crippling of stiffeners which represents the behaviour of the flanges buckling while corners are still carrying load. This can be described by Equations (8.5) and (8.6).

$$\frac{\sigma_{cc,i}}{\sigma_y} = \alpha \left(\frac{C}{\sigma_y} \frac{\pi^2 E}{12(1-\nu^2)} \left(\frac{t}{b} \right)^2 \right)^{1-n} \quad (8.5) \quad \sigma_{cc} = \frac{\sum \sigma_{cc,i} A_i}{\sum A_i} \quad (8.6)$$

Equation (8.5) refers to crippling of individual stringer elements with α and n being empirical material constants. After computing, they can be averaged based on areas using Equation (8.6), where the area in the denominator includes any corners. The failure condition that will be the most critical for a stiffener can be obtained from the Johnson-Euler curve using its slenderness ratio. This curve is defined by the Johnson parabola, Equation (8.7), the Euler curve, Equation (8.1), and the critical value where Euler buckling takes over from crippling, described by their tangency point. The curves are additionally bounded by the yield stress.

$$\sigma_{cr} = \sigma_{cc} \left(1 - \frac{\sigma_{cc}(L_e/\rho)^2}{4\pi^2 E} \right) \quad (8.7)$$

Finally, one can evaluate the actual buckling strength of stiffened panels. A portion of the skin of a stiffened panel located under the stiffener will fail with the stiffener instead of the plate. This leads to the effective panel width being decreased. After recomputing the new buckling stress of the panel, the critical stress of the entire stiffened assembly can be computed by averaging using Equation (8.6). The stiffened width w_e of the panel can be computed using Equation (8.8),

$$w_e = \frac{t}{2} \sqrt{\frac{C\pi^2}{12(1-\nu^2)}} \sqrt{\frac{E}{\sigma_{cc,\text{stiffener}}}}. \quad (8.8)$$

To be conservative, the $\sigma_{cc,\text{stiffener}}$ used is the actual failure stress of the stiffener as per the Johnson-Euler curve.

Verification

The model is unit and system tested to ensure correct functioning and implementation. It is assumed that the base of the model verified in Chapter 7 functions correctly. The system test used can be seen in Table 8.4.

Table 8.4: System tests for the fuselage structural model

Test	Action	Expected Outcome	Result
TST-FUS-1	Vary load to test changes in critical buckling stress.	Buckling stress is independent.	Passed
TST-FUS-2	Set length of stringer to 0 m.	Crippling stress is equal to critical stress.	Passed
TST-FUS-3	Test crippling of L-stiffener of dimensions 10x10x1 mm made of AL7075-T6.	Hand calculation expected value is 328.7 MPa.	Passed
TST-FUS-4	Test crippling of 100x100x1 mm thin panel of AL7075-T6 bounded by L-stringers from TST-FUS-4	Hand calculation expected value is 193.9 MPa	Passed
TST-FUS-5	Test column buckling for beam of $L_1 = 2$ m, $L_2 = 1$ m, $I_1 = 10$ m ⁴ , $I_2 = 1$ m ⁴ and $E = 71.9$ GPa	Expected buckling force of 29.24 GN	Passed

8.4. Design

The design of the SPARTA fuselage structure is discussed in this section. The topology, elements, materials and loads are addressed.

Topology

The concept for the fuselage structure is that of a semi-monocoque structure. The UAV is built around a load-bearing backbone consisting of transverse frames and longitudinal stiffeners to which the skin, internal non-load-bearing structure and components can be attached. Owing to this configuration, skin panels can be easily removed or swapped without the UAV losing its shape and having a large portion of its load-bearing capacity compromised (**REQ-FUS-08**).

To maintain commonality, simplify procurement and utilise its useful properties, the internal backbone shall also be made of this Al7075-T6, following wing structural design in Chapter 7. On the other hand, the choice of skin material is performed separately, as the requirements for it differ from the more loaded parts of the structure.

Stiffeners

The bulk of the longitudinal strength and shape retention comes from stiffeners. They are rigidly connected to the frames to provide the required load paths and to break them up into smaller sections to resist buckling. Following the accessibility requirement (**REQ-FUS-08**), they need to allow easy switching of smaller panels while also providing enough space between them to allow installation of large components, such as the secondary payload (**REQ-FUS-02**). The final placements in the two load-bearing cross-sections can be seen in Figure 8.1.

As they need to connect the skin panels, the most appropriate shape for them is an angle, such as an L-stiffener or inverted T-stiffener, with angles between flanges depending on the exact corner they need to fit. These are common shapes which can easily be purchased off-the-shelf¹ or have custom made using bending (only L), extrusion or milling for relatively cheap. The T-stiffener comes with an additional advantage of allowing internal components to be attached to its flange. Small stiffeners, 10 mm flange and 1 mm thickness, are used due to space constraints and expected loads.

Frames

The frames serve to hold the structure together circumferentially [36]. In total, four comprise the structure of SPARTA's fuselage, and their placement can be seen in Figure 8.1. Frame 1 is the only fully circular frame that serves to attach the primary semi-spherical payload and begin the load-bearing structure. Frame 2 follows the outline of its section of the fuselage and is integrally joined with the housing for the wing hinge mechanisms, from which it also transfers loads. Frame 3 is located before the transition to the second type of cross-section, and its main purpose is to terminate the stiffeners of the first section and change to the arrangement of the second. Finally, frame 4 caps off the fuselage structure by transferring propulsive and tail loads.

Besides having to provide a continuous load path, the cross-section of the frames needs to facilitate easy connection to the skin and internal components. For this reason, two commonly available and easily manufacturable cross-sections with flat horizontal elements on the inside are chosen: the C-shape and the hat shape. Both of these shapes can be easily bent, extruded or milled and will be welded shut at the end. In the case of frame 2, integration is needed with the hinge housing, requiring either integral milling or welding. Frames 1, 2 and 4 will have the C-cross-section and frame 4, being the most loaded, will be given the symmetrical hat cross-section to avoid torsion of the frame. They need to be larger than the stiffeners, as they need to be joined, and the top part of the C could interfere. The size of these is a flange (each straight element) of 12 mm and a thickness of 1 mm.

Skin

Due to the selected structural topology, the skin is mostly relegated to shear carrying and interior protection. Thus, the needs for its material are quite different to the main structure and the skin material warrants having a trade-off.

Trade-off Setup

First, the design is required to operate over a wide range of temperatures and in harsh environments (**REQ-FUS-04**), because of this, environmental resistance is a crucial parameter to evaluate. As it covers a wide range of

¹URL: https://www.rvs-products.nl/aluminium-hoekprofiel-100-x-100-x-10-mm-aw-6060/?eyk_source=google&eyk_campaign=22250759756&eyk_content=733369404396&gad_source=1&gad_campaignid=22250759756&gbraid=0AAAAACv80Pzfx0jR00tmMD0dt1pLpAOA&gclid=Cj0KCQjwjdTCBhCLARIsAEu8bpLBdYptGek1GqY6ynB-94m76rm-d1Q0Lo6fvivUIF8NzCABix3o20saApiZEALw_wcB [cited 14 June 2025]

properties from Ultra Violet (UV) resistance to moisture and corrosion resistance, it is graded on a qualitative scale from zero to one with steps of 0.33. One signifies perfect performance, 0.66 acceptable deficiencies, 0.33 unacceptable deficiencies, which can be addressed through coatings or modifications and zero unacceptable performance. As exceeding the requirements is not necessarily the goal, this is not as important as other criteria.

Second, the skin will be facing the impact loads associated with recovery, so its impact resistance should be high. Usually, the Izod or Charpy test would be used to evaluate impact resistance; however, these are unsuitable to compare different material classes, as Izod is for plastics and Charpy for metals. A qualitative scale from zero to one will be used again. This time, zero will indicate the worst candidate and one the best, with the ones in between being given 0.33 or 0.66 based on whether they are closer to the best or the worst. Since the chosen method of recovery is the relatively gentle net, Chapter 14, the importance of this parameter is diminished.

Next, the system needs to be recyclable (**REQ-FUS-15**) and, by extension, so do its materials. This is the last qualitative factor, once again on a scale from zero to one. This time, zero represents non-recyclable, 0.33 down-cyclable or theoretically recyclable, 0.66 uncommonly recycled, and one means easy and common recycling. This criterion is important to adhere to European ideals.

Looking at the buckling relations of Section 8.3, an important factor in preventing buckling is having a high modulus and/or thickness. When combined with the mass budget requirement, it can be concluded that a material with a high specific modulus is beneficial to the design. This is a quantitative parameter for which a linear scale from the best to the worst design will be used. Due to the high compressive loads of launch, this is considered a more important parameter than the resistances and recycling.

Finally, the design needs to be attritable, therefore, its cost should be minimised. The price per kilogram of material can then be used to compare the candidates. Once again, a linear scale shall be used from the best to the worst design. Due to the nature of SPARTA's mission, this is the most important parameter. The weights for these criteria were obtained using AHP and can be seen in Table 8.5.

Table 8.5: AHP pairwise comparison values and their resulting normalised weights for skin trade-off

Criteria	Env. Resistance	Impact Resistance	Specific Modulus	Recyclability	Cost	Computed Weight	Rounded Weight
Environmental Resistance	1.00	0.75	0.25	0.5	0.25	0.08	0.10
Impact Resistance	1.33	1.00	0.5	0.75	0.25	0.12	0.10
Specific Modulus	4.00	2.00	1.00	1.25	1.00	0.28	0.25
Recyclability	2.00	1.33	0.80	1.00	0.75	0.18	0.20
Cost	4.00	4.00	1.00	1.33	1.00	0.34	0.35

Material Choices

The first material entering the trade-off is the same aluminium as the structure Al7075-T6^{2,3}, a high-performance aerospace-grade alloy. Second, there are CFRP^{4,5}, which combine high-performance with light weight but at the cost of price and resistance. Third comes Polyether Ether Ketone (PEEK)^{6,7}, a high-performance aerospace polymer with high environmental resistance but a high price tag. It is followed by Polyether Imide (PEI)^{8,9},

²URL: <https://asm.matweb.com/search/specificmaterial.asp?bassnum=ma7075t6> [cited 14 June 2025]

³URL: <https://www.steelmetind.com/7075-aluminum-sheet-plate.html> [cited 14 June 2025]

⁴URL: https://www.matweb.com/search/datasheet_print.aspx?matguid=39e40851fc164b6c9bda29d798bf3726 [cited 14 June 2025]

⁵URL: <https://www.easycposites.eu/double-sided-high-strength-carbon-fibre-sheet> [cited 14 June 2025]

⁶URL: https://www.matweb.com/search/datasheet_print.aspx?matguid=2164cacabcde4391a596640d553b2ebe [cited 14 June 2025]

⁷URL: <https://www.steelofabrica.com/polyether-ether-ketone-price/> [cited 14 June 2025]

⁸URL: https://www.matweb.com/search/datasheet_print.aspx?matguid=d2c5e6d867344ea38d286d202d36b6ee [cited 14 June 2025]

⁹URL: https://filament2print.com/en/peek-pekk-pei/1317-6627-pei-cf-ultem1010-pellets.html#/237-colour-black/834-format-1_kg [cited 14 June 2025]

which represents a lower-performance but cheaper version of PEEK. Finally, Polycarbonate (PC)^{10,11}, a common plastic used in everyday applications such as roofing, with good resistance and a cheap price but poor strength.

Unfortunately, cheap, commercially available and light-weight plastics such as Polyethylene Terephthalate (PET), Acrylonitrile Butadiene Styrene (ABS) or Polylactic Acid (PLA)¹² do not meet the temperature requirements (**REQ-FUS-03**). However, they could prove quite competitive if there were a lower-performance version of SPARTA in the future.

Trade-off

Table 8.6 presents the results of the trade-off. As can be seen, Al7075-T6 wins the trade-off and shall be used as skin material. A sensitivity study based on varying the weights around the base value confirms this result in 99.7 % of cases.

Table 8.6: Completed trade-off table. Criteria are given in the top row, and design options are in the first column. The actual values for the parameters are given. The colour is related to the number of points. The white circles, top right of the coloured cell, indicate the colour; G for green, B for blue, Y for yellow and R for red.

	Env. tance	Resis-	Impact Resis-	Specific Modulus [MPam ³ kg ⁻¹]	Recyclability	Cost D/kg]	[US-	Score
Weight	10%	10%	10%	25%	20%	35%		100%
Al7075-T6	1.00 (G)	0.66 (B)	0.66 (B)	25.59 (Y)	1.00 (G)	3.5 (G)		0.85
CFRP	0.66 (B)	0.33 (Y)	0.33 (Y)	43.75 (G)	0.00 (R)	87 (Y)		0.53
PEEK	1.00 (G)	1.00 (G)	1.00 (G)	2.83 (R)	0.33 (Y)	175 (R)		0.27
PEI	0.66 (B)	0.66 (B)	0.66 (B)	4.69 (R)	0.33 (Y)	118 (Y)		0.33
PC	0.66 (B)	0.66 (B)	0.66 (B)	2.66 (R)	0.66 (B)	2.8 (G)		0.61

Considering the high strength and modulus of this aluminium alloy, a thin sheet of 1 mm shall be used for the skin panels, as later analysis will show, it is the minimum sheet thickness that is feasible to avoid any buckling. It will be attached to the backbone of the structure with M3 phillips screws for easy removal.

Fairings

The design features three aerodynamic fairings: one over the primary payload, another covering the transition from the initial circular cross-section, and the last tapering toward the propeller. These will be made of 2 mm-thick PC plastic, which came second in the trade-off. Its weakness and low modulus are not an issue for these non-load-bearing sections. Additionally, it can be made transparent to provide the primary payload with a clear view (**REQ-FUS-09**), and it is transparent to Electro Magnetic (EM) waves, allowing for the installation of communications and Global Navigation Satellite System (GNSS) antennas in the top fairing. A summary of all chosen components can be found in Table 8.7.

¹⁰URL: <https://businessanalytiq.com/procurementanalytics/index/polycarbonate-price-index/> [cited 14 June 2025]

¹¹URL: <https://designerdata.nl/materials/plastics/thermo-plastics/polycarbonate> [cited 14 June 2025]

¹²Even biodegradable.

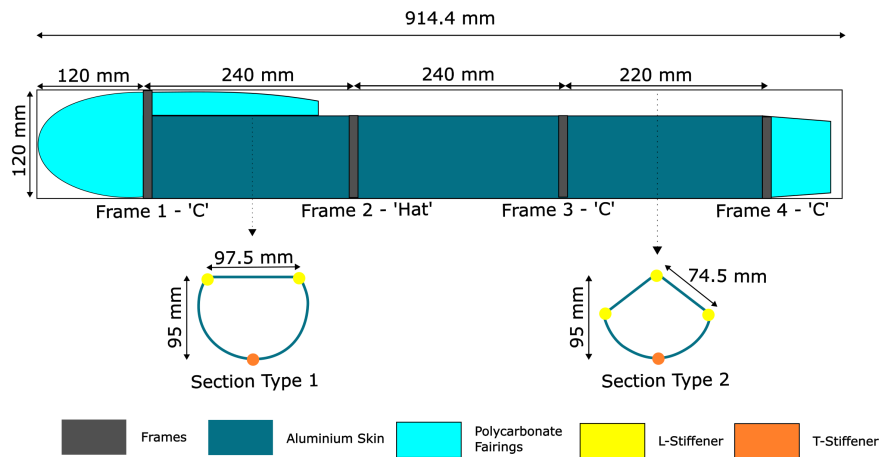


Figure 8.1: Structural topology of the fuselage

Table 8.7: Summary of chosen components

Component	Description	Material	Manufacturing Method	Total mass [kg]
Skin	9x 1 mm thickness panel	Al7075-T6	Cold rolled	0.65733
Fairings	3x 2 mm thickness	PC	Injection moulded	0.189
Stiffeners	7x L-stiffener 10x10x1 mm	Al7075-T6	Bent/extruded	0.095
	3x T-stiffener 20x10x1 mm	Al7075-T6	Extruded	0.0627
Frames	3x C-cross-section 12x12x1 mm	Al7075-T6	Bent/extruded + welded	0.1172
	1x hat-cross-section 36x12x1mm (equal segment lengths)	Al7075-T6	Bent/extruded + welded	0.06677

Design Evaluation

The components and their dimensions, as outlined in the previous subsections, are obtained using an iterative procedure that minimises weight and prevents failure while remaining within the realm of manufacturability. First, weights and loads were converted to internal forces for the maximum load factor of 3.8 with a safety factor of 1.3 applied. The Free Body Diagram (FBD) of the SPARTA can be seen in Figure 8.2 and the internal loads in Figure 8.3. In the FBD, all forces have been translated to the centreline and, where relevant, replaced by equivalent couple moments.

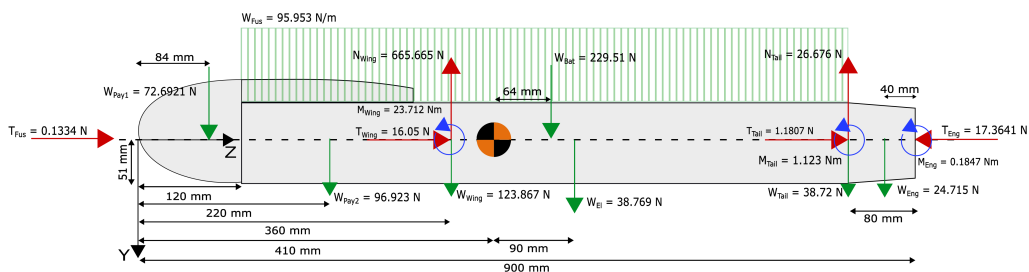


Figure 8.2: Free body Diagram of SPARTA

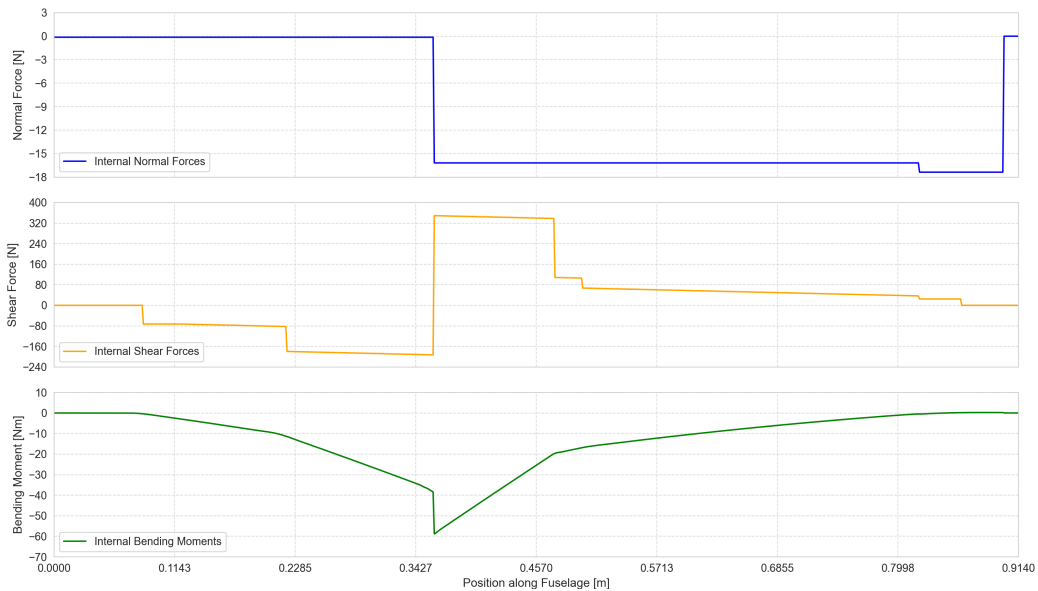


Figure 8.3: Internal loads along the length of the fuselage

The most critical cross-sections during nominal flight are identified at 0.36 m and 0.6 m from the nose, corresponding to the two types of cross-sectional area. The stress distributions within the cross-sections for the nominal flight condition can be seen in Figure 8.4. It can be observed that stresses are quite low, with maximum normal stresses around 5.5 MPa and shear of 2.13 MPa.

For the launch scenario, standard launch ΔV of 40 m/s is assumed, which, assuming uniform acceleration over the length of the tube, gives 89g of acceleration or 116g with safety factors. Assuming this load to be quasi-static and applying it at the CG (**AS-FUS-03**) yields a compressive internal force of 16.26 kN. Translating this to stresses, the first cross-section experiences 38.9 MPa of compressive stress and the second 41.43 MPa, if only for a brief period. These are still well below the yield strength of aluminium 7075-T6 of 502 MPa.

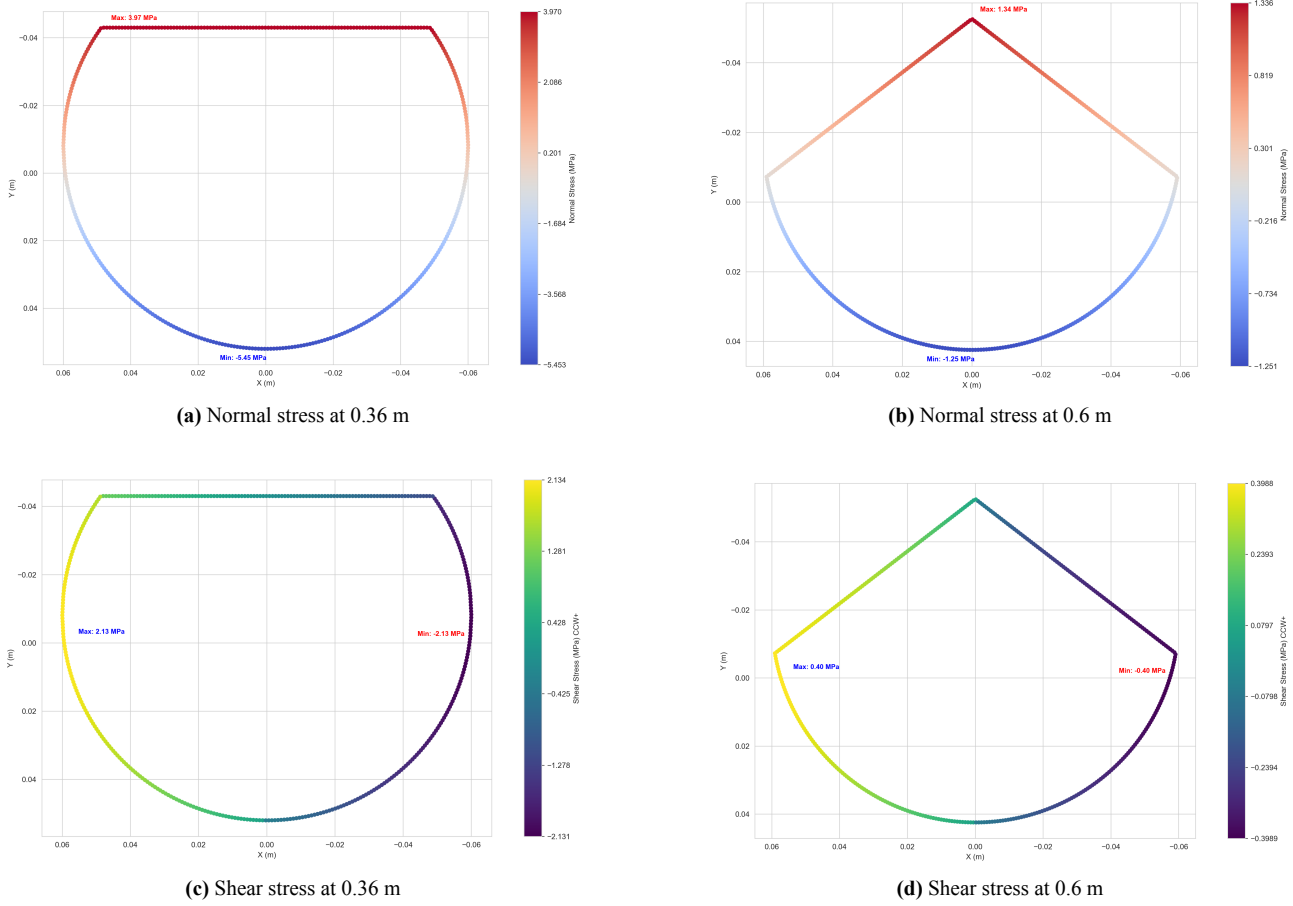


Figure 8.4: Stress distributions at 0.36 m and 0.6 m

The final thing to check is the buckling critical stress of each element of the critical sections. The critical stresses are evaluated within the bay, which contains the most loaded section. The values can be found in Table 8.8. It can be observed that buckling does not occur at any point with a good margin, neither during nominal flight nor launch. The closest are the top flat panels of the first section when not considering stiffeners. Yet they still meet the requirements, including a safety margin. An interesting observation can be made with regard to the stiffened curved panels. Due to their high buckling resistance, the addition of stringers barely changes the failure stress due to the averaging effect of Equation (8.6). The physicality of this is dubious and warrants further investigation.

Table 8.8: Critical buckling values of elements of the most loaded sections of the fuselage

Parameter	Value Cross-Section 1	Value Cross-Section 2
Load-bearing area [mm ²]	417.53	392.44
Second moment of area I_{xx} [mm ⁴]	59.3E4	38.6E4
Second moment of area I_{yy} [mm ⁴]	74.3E4	57.1E4
Critical stress L-stiffeners [MPa]	253.378	253.37
Critical stress T-stiffeners [MPa]	270.43	270.43
Normal buckling stress flat panel [MPa]	44.95	65.22
Shear buckling stress flat panel [MPa]	41.85	68.29
Normal crippling stress stiffened flat panel [MPa]	183.24	235.47
Normal buckling stress curved Panel [MPa]	284.61	305.94
Shear buckling stress curved panel [MPa]	215.21	283.08
Normal crippling stress stiffened curved panel [MPa]	284.79	297.02
Cylinder column buckling stress (about x) [MPa]	661.85	704.16
Cylinder column buckling stress (about y) [MPa]	968.79	1030.72

Sensitivity Analysis

In this section, a sensitivity analysis on the design is performed in Table 8.9. Discretisation, thickness of panels and size of stiffeners are varied to determine the robustness of the design.

Table 8.9: Sensitivity analysis of fuselage analysis

Parameter	Original value	Percentage change	Effect
Boom discretisation	400	+10%	No effect
	400	-10%	No effect
Plate thickness	1 mm	+5%	Weight increases by 4%, most critical buckling stress increases by 7%
	1 mm	-5%	Weight decreases by 4%, most critical buckling stress decreases by 7%
Linear dimension of stiffener	10 mm	+5%	No significant change in weight, normal stress decreases by 1.5 %
	10 mm	-5%	No significant change in weight, normal stress increases by 1 %

8.5. Sustainability & Attritability

In this section, the sustainability and attritability of the fuselage structure are briefly discussed. The entirety of the fuselage structure is made of recyclable materials, aluminium and polycarbonate, which, if damaged or retired, can be returned into the feedstock or downcycled. The easy removability of skin panels facilitates easy repair, increasing the system's potential lifespan, while the selection of durable and impact-resistant materials will reduce the need for replacements in the first place.

Both materials used are commonplace and very affordable, with aluminium parts only utilising easily sourceable methods and shapes, while polycarbonate might require specially tailored moulds, but its production infrastructure is already in place. This benefits attritability greatly, as in the case of a conflict, capacity can easily be increased by using existing production lines, and the loss of each unit is financially and resource-wise acceptable. Finally, both materials can be sourced in Europe, polycarbonate, for example, from Covestro¹³, and aluminium from MCB¹⁴.

8.6. Risk Analysis

Below, the most critical risks associated with the fuselage structure are outlined, and mitigations are proposed.

RSK-FUS-01: Thermal expansion mismatch

Due to the large temperature range, thermal expansion mismatch between the backbone and fairings could cause significant stresses and potentially cracking in the polycarbonate fairings. This could expose the internal components and reduce aerodynamic performance. As the polycarbonate structures are not load-bearing, floating joints or compliant interfaces should be implemented to mitigate the risk.

RSK-FUS-02: Manufacturing defects

Manufacturing defects, especially if assembled by less skilled technicians during a conflict situation, can occur in the welds and fasteners, potentially impacting performance or lifespan. Strict protocols for assembly and Quality Control (QC) and Quality Assurance (QA) need to be ensured to mitigate this risk. This could include Non-Destructive Inspection (NDI) methods, such as X-ray and ultrasound inspections, and through-sample testing of assemblies.

RSK-FUS-03: Vibrations from propeller compromise structure

Due to the high rotational speed of the propeller, vibrations could, over time, loosen fasteners or fatigue damage the structure. To mitigate this risk, detailed simulations of the interactions should be performed to evaluate whether it could be an issue over the lifespan of about 20 flights. If so, vibration-damping joints could be implemented or fasteners checked and retightened after several flights.

¹³URL: <https://solutions.covestro.com/en/brands/makrolon> [cited 15 June]

¹⁴URL: <https://www.mcb.eu/en/> [cited 15 June]

8.7. RAMS Analysis

The RAMS analysis for the fuselage structure is discussed in this section.

Reliability

The reliability of the structure is expected to be high, as most failure modes in normal operation, such as fatigue and material degradation, are unlikely to manifest over a regular lifespan of 20 missions. Additionally, the skin and fairings that are directly exposed to the environment, recovery loads and are closer to their performance limit than the backbone, can be easily inspected and replaced after every mission if needed, aiding reliability.

Availability

The fuselage structure is unlikely to have a large impact on the availability of the entire system. This is because all of the skin panels and fairing are designed to be removable within about 10 minutes by a competent operator, with regular post-flight inspections taking about 15 minutes and scheduled maintenance taking 2 hours. In total, about 35 man-minutes are necessary per flight, fitting well into the four hours for refurbishment as stated by **REQ-SYS-34**.

Maintainability

The use of standard geometries and easily procurable materials, and fasteners allows for the structure to be maintained without special procedures. The design of the backbone structure and skin allows every joint to be inspected after the skin is removed, even in the field. The welds would require specialised NDI equipment, and their inspection and maintenance would have to be done in a workshop. The structure can be visually inspected after every mission, with a more detailed inspection in a workshop recommended after every 20 missions.

Safety

The structure uses non-harmful common materials that will not endanger personnel. However, it is important to consider that 1 mm-thick aluminium sheets can be quite sharp. The margins on the structural strength of the subsystem make in-flight breakup under operating conditions unlikely.

8.8. Financial Analysis

This section aims to estimate the cost per SPARTA unit of the fuselage structure. What is considered are PC injection moulding¹⁵, aluminium extrusion [37] and welding [33], and assembly costs¹⁶. The costs are obtained from various sources, some based in the US, so a European labour cost factor of 1.33¹⁷ is added to estimated labour costs. Costs were adjusted for inflation if not from 2025. The cost of injection moulded parts includes the cost of the mould for a production run of 5000¹⁸, but aluminium parts are assumed to be standard. It is assumed that the assembly process itself takes 5 hours, including preparation, assembly and QC. The breakdown of the cost can be seen in Table 8.10.

Table 8.10: Costs of different aspects of the fuselage structure per production unit of SPARTA in 2025 EUR

Item	Material	Recurring	Non-Recurring	Total
Polymer Parts	0.46	5.21	1.57	7.24
Aluminium Parts	3.02	1.43	-	4.88
Assembly	-	174.40	-	174.40
Total	-	-	-	186.52

8.9. Compliance Matrix

In this section, one can find the compliance matrix of the fuselage structure subsystem along with its compliance with budgets. The compliance matrix can be found in Table 8.11. The budget compliance can be seen in Table

¹⁵URL: <https://formlabs.com/eu/blog/injection-molding-cost/?srsltid=AfmB0oowwQ0DgCnZGNxwP19pU9k2D1jNKLOj8icGojSqMB8f6cJZm6WY> [cited 15 June]

¹⁶URL: https://ec.europa.eu/eurostat/statistics-explained/index.php?title=Hourly_labour_costs [cited 15 June]

¹⁷URL: <https://tradingeconomics.com/united-states/wages-in-manufacturing> [cited 15 June]

¹⁸Assumes peacetime medium-scale production. Wartime production could use more durable and expensive moulds.

8.12. Preliminary mass and volume values contain a contingency of 20%, with actual values using the final design contingencies of 10% and 5%, respectively. While remaining in the mass budget, the structure exceeded its volume budget slightly, which will need to be considered during internal sizing. Considering the decrease in the volume of other subsystems, the non-compliance with the budget outlined in **REQ-FUS-17** is considered acceptable.

Table 8.11: Fuselage structure compliance matrix

Code	Compliance	Code	Compliance
REQ-FUS-01	G	REQ-FUS-09	G
REQ-FUS-02	G	REQ-FUS-10	G
REQ-FUS-03	G	REQ-FUS-11	G
REQ-FUS-04	G	REQ-FUS-12	G
REQ-FUS-05	G	REQ-FUS-13	G
REQ-FUS-06	G	REQ-FUS-14	G
REQ-FUS-07	G	REQ-FUS-15	G
REQ-FUS-08	G	REQ-FUS-16	G
REQ-FUS-17	Y	-	-

Table 8.12: Fuselage structure margin adherence

Budget	Preliminary Value	Actual Value
Mass	1.39 kg	1.19 kg
Volume	0.46 L	0.49 L

8.10. Recommendations

For future development of the fuselage structure subsystem, it is recommended that an accurate CAD model is created and FEM analysis performed to among other aspects investigate the buckling of the stiffened curved panels. A lower-performance version of SPARTA with lower temperature range requirements should be considered to expand the range of attritable materials that could be used.

Additionally, the effect of brief shock accelerations and impacts on the structure should be investigated by performing impact simulations. This would be useful to evaluate both the acceleration effect of launch and recovery. A full non-linear analysis with the digitalised geometry should be performed, so that the risk of non-elastic buckling and deformation can be analysed for various launch speeds, net recovery loads and for the case of a belly landing. To make this analysis useful, accurate mass and stiffness distributions have to be included along with analysing the extremes of the launch, flight and recovery envelope.

9. Control Surfaces Design

This chapter covers the design of the control surfaces. Firstly, a functional and requirement analysis are performed in Section 9.1 and 9.2 respectively. Next, the ailerons are designed in Section 9.3, and the ruddervators in Section 9.4. Following the design, a sustainability, risk, RAMS and financial analysis are performed in Sections 9.5 through 9.8. Compliance with requirements is then checked in Section 9.9. Finally, recommendations are discussed in Section 9.10.

9.1. Functional Analysis

Below in Table 9.1, the functions of the control surfaces are addressed.

Table 9.1: Functions relevant for the control surfaces design

Code	Description	Origin
FUN-CON-01	Stabilise the system.	FUN-SYS-3.4.2, FUN-SYS-4.1
FUN-CON-02	Reach cruise conditions.	FUN-SYS-5.1
FUN-CON-03	Maintain cruise conditions.	FUN-SYS-4.2
FUN-CON-04	Perform manoeuvres.	FUN-SYS-6.1.2, FUN-SYS-6.3.1, FUN-SYS-7.2.3, FUN-SYS-7.3

9.2. Requirement Analysis

Having obtained the required functions, they can be combined with existing system and subsystem requirements to derive a list of requirements for the airfoil to comply with and guide its design. They can be found in Table 9.2.

Table 9.2: Requirements relevant for the control surface design

Code	Description	Origin
REQ-CON-02	The control surfaces shall provide pitch control.	FUN-CON-01-04
REQ-CON-03	The control surfaces shall provide roll control.	FUN-CON-01-04
REQ-CON-04	The control surfaces shall provide yaw control.	FUN-CON-01-04
REQ-CON-05	The chord length of the tail shall be 0.05 m.	REQ-SYS-22
REQ-CON-06	The span of the tail shall be 0.558 m.	REQ-SYS-22

9.3. Aileron Design

To provide roll controllability to SPARTA (**REQ-CON-03**), ailerons can be designed. These are preferred over spoilers, since spoilers have very nonlinear response characteristics and are thus difficult to implement for roll control [38]. Since NATO STANAG 4703 [11] does not specify any requirements on roll control, the ailerons can be designed with only one constraint; the available space. This is covered in this section.

9.3.1. Aileron Sizing

The ailerons will be positioned on the outer wing. Firstly, the chord length of the aileron can be established based on the wing cross section, established in Chapter 6. At the trailing edge, it is approximated that about 7 mm of space is available for the aileron, which is at 91% of the outer wing chord. Because of this small size, the span of the ailerons is maximised on the outer wing, with a 5% margin on both sides, since at the tips, the control effectiveness is little due to vortex flow [38]. This results in an aileron spanned 0.468 m to 0.962 m from the root.

Next, the aileron characteristics can be determined. For SPARTA, differential ailerons are used with a ratio equal to 0.75, since they counteract adverse yaw [28]. Their maximum deflection is estimated at about 10 degrees, to prevent stall on the wing. To accurately estimate this, future detailed design with more expensive software can be performed, since XFLR5 gives questionable results regarding drag.

The final component that must be considered is the hinge mechanism for the ailerons, considering the telescopic nature of the wing. In the folded configuration, there is some space left between the inner and outer wing tip. This space can house the aileron mechanism, which is further discussed in the next chapter, Section 10.5.

9.3.2. Aileron Performance

For the given aileron dimensions, aileron reversal, roll rates and derivatives can be calculated.

Firstly, aileron reversal can be analysed. Equation (9.1) [20] approximates the aileron reversal speed v_{ar} . Here, $C_{L_{\delta a}}$ and $C_{M_{\delta a}}$ are the change in lift coefficient and moment coefficient due to an aileron deflection, and are obtained via XFLR5. J_{OP} and G are already established in Section 7.7. For the given configuration, the most conservative estimate of v_{ar} is equal to 700 m/s. This indicates no issue, which makes sense for the low cruise speed.

$$v_{ar} = \sqrt{\frac{-J_{OP} G C_{L\delta_a}}{\frac{1}{2} \rho S c C_{M\delta_a} C_{L\alpha}}} \quad (9.1)$$

Next, in Section 15.4, aileron derivatives are required; $C_{l_{\delta_a}}$, $C_{n_{\delta_a}}$ and $C_{Y_{\delta_a}}$, which are the rolling moment, yawing moment and side force derivatives with respect to the aileron deflection. XFLR5 is used, where both the wing and empennage are added to the model. Two simulations are run; one with no aileron deflection, and one with a deflection of +3.75 and -5 degrees for the right and left aileron respectively, with positive pointing downward. This keeps the analysis within the linear regime. From the difference between the two and the given angle, the derivatives are obtained. The results are reasonable; $C_{n_{\delta_a}}$ and $C_{Y_{\delta_a}}$ are both approximately zero, and $C_{l_{\delta_a}}$ has reasonable magnitude compared to for example the Cessna Citation [28], for which accurate data is accessible (0.32 and 0.23 respectively).

Finally, the roll rate can be calculated to get an idea of the capabilities of the ailerons. Equation (9.2) can be used, where C_{l_p} is the rolling moment derivative with respect to roll rate, equal to -1.12, which will be further addressed in Section 15.4. δ_a is the maximum average aileron deflection. With an upward deflection of 10°, and downward deflection of 7.5°, the average is equal to 8.75°. Plugging in all numbers results in a roll rate of 101 deg/s. This value is relatively high, due to the relatively high v_{cruise} over b ratio compared to for example the Cessna Citation. Furthermore, there could potentially be flaws in the results of the $C_{l_{\delta_a}}$ and C_{l_p} .

$$P = -\frac{C_{l_{\delta_a}}}{C_{l_p}} \delta_a \left(\frac{2v_{cruise}}{b} \right) \quad (9.2)$$

9.3.3. Sensitivity Analysis

In this section, some parameters of the aileron will be adjusted to analyse aileron performance. The results are presented in Table 9.3. From this table, it can be seen that reducing the aileron span by 20% reduces all

Table 9.3: Sensitivity study on the aileron performance.

Parameter	Original Value	New Value	$C_{l_{\delta_a}}$	$C_{n_{\delta_a}}$	$C_{Y_{\delta_a}}$
Original	-	-	-0.322	7.86E-4	-3.69E-3
Inner aileron position (20%)	0.468 m	0.567 m	-0.271	4.19E-4	-1.99E-3
Non-differential	$\delta_R = 3.75^\circ$	$\delta_R = 5^\circ$	-0.323	7.79E-4	-3.70E-3

derivatives. $C_{l_{\delta_a}}$ reduces slightly less than 20%, whereas the other derivatives are approximately halved. For a non-differential aileron, the results are almost equal. For $C_{l_{\delta_a}}$ and $C_{Y_{\delta_a}}$, this is logical, however an increase in magnitude of $C_{n_{\delta_a}}$ is expected. If the right aileron deflects downward, it generates more lift, but also more drag, which would induce a yaw to the left, since the left wing is expected to generate less drag [28]. This is not reflected in the results from XFLR5, again questioning the reliability of the results.

9.4. Ruddervator Design

To provide pitch and yaw controllability to SPARTA (**REQ-CON-02**, **REQ-CON-04**), ruddervators can be designed. Since NATO STANAG 4703 [11] does not specify any requirements on yaw or pitch control, the ruddervators can be designed with only one constraint; the available space. This is covered in this section.

9.4.1. Ruddervator Sizing

The ruddervators are maximised in size for SPARTA to improve the controllability of the UAV. Therefore, a full moving tail is used, except for the part touching the fuselage, which is about 0.075 m from the tail root. The ruddervators must move independently; for pitch control, both deflect in the same direction to cancel out the lateral force, but for yaw control, they deflect in opposite direction to cancel out the longitudinal force.

Next, the maximum deflection can be discussed. The NACA 0012 airfoil is used, which is symmetrical and

thus provides balanced aerodynamic forces for both positive and negative deflections. It reaches $C_{l_{\max}}$ at 12.85 degrees. With a cruise angle of attack equal to 2.6 degrees, the maximum ruddervator deflection is set to 7.5 degrees, to avoid stall on the tail surfaces and leaving margin. The hinge mechanism that can accomplish this is further discussed in Section 10.6.

9.4.2. Ruddervator Performance

In Section 15.4, rudder derivatives are required; $C_{l_{\delta_r}}$, $C_{n_{\delta_r}}$ and $C_{Y_{\delta_r}}$, which are the rolling moment, yawing moment and side force derivatives with respect to the rudder deflection. XFLR5 is used, where both the wing and empennage are added to the model. Two simulations are run; one with no ruddervator deflection, and one with a deflection of +5 and -5 degrees for the right and left ruddervator respectively, with positive pointing downward. This keeps the analysis within the linear regime. From the difference between the two and the given angle, the derivatives are obtained. The outcomes are logical and relatively close in magnitude to the Cessna Citation.

Secondly, elevator derivatives are required; $C_{X_{\delta_e}}$, $C_{Z_{\delta_e}}$ and $C_{m_{\delta_e}}$, which are the axial force, normal force and pitching moment derivative with respect to elevator deflection. The same XFLR5 model is used, now deflecting both surfaces +5 degrees. They are approximated as the change in C_D , C_L and C_m respectively at the angle of attack in cruise conditions. The outcomes are logical and relatively close in magnitude to the Cessna Citation.

9.5. Sustainability & Attritability

In this section, the sustainability and attritability of the control surfaces is briefly discussed. The materials of the control surfaces are made from the same material as the wing - aluminium. If damaged or retired, it can be fully recycled. The recyclability of the mechanisms will be addressed in Chapter 10.

Furthermore, aluminium is commonly used and very affordable, with a production infrastructure already in place in Europe, beneficial for attrition warfare. It allows for easy increase in capacity without significant cost increase.

9.6. Risk Analysis

This section covers the most critical risks associated with the control surfaces and mitigation strategies for these. It covers both development and operational risks.

RSK-CON-01: Manufacturing defects

Manufacturing defects can have critical consequences. Firstly, incorrect dimensions of the control surfaces can increase or reduce the rotational rates. Secondly, asymmetric tail control surfaces can cause asymmetry in the control rates, requiring constant adjustments. The likelihood of this risk is moderate. To mitigate this risk, strict manufacturing protocols need to be assured, and accurate calibration is needed after manufacturing to reduce the severity and likelihood of manufacturing defects.

RSK-CON-02: The actuators of the ruddervator fail

Failure of the ruddervators can have catastrophic impact on SPARTA, although it is unlikely to happen since servos are used (further discussed in Section 10.6). Due to the nature of the tail, it results in loss of both pitch and yaw control. Pitch control can be partially recovered if the ailerons can be deflected independently and symmetrically. Yaw can not be accurately recovered; the bank-to-turn strategy can not be used due to the lack of precise pitch control, however adverse yaw can be used if the ailerons can be deflected symmetrically in opposite direction. To better mitigate this risk, pre-flight checks need to be done confirming proper working control surfaces, reducing the likelihood of failure.

RSK-CON-03: The actuators of the aileron fail

Failure of the ailerons can have critical impact on the flight envelope and manoeuvring capabilities of SPARTA, since most roll control is lost. While ruddervators can provide some roll control, this introduces coupling between pitch, roll and yaw, which complicates flight behaviour and can potentially result in unstable flight dynamics. To better mitigate this risk, pre-flight checks need to be done, reducing the likelihood of the failure.

RSK-CON-04: The actuators of both control surfaces fails

In case of failure of both control surfaces, SPARTA has a complete loss in pitch, roll and yaw control, having

catastrophic impact, although being unlikely. In flight, this failure mode can not be mitigated; SPARTA needs to land as quickly as possible within its flight envelope. The risk can be mitigated on the ground by performing pre-flight checks on the control surfaces, reducing the likelihood of failure in-flight.

The mitigation strategies discussed for the risks above result in new requirements for SPARTA. They are listed in Table 9.4.

Table 9.4: Requirements stemming from risk mitigation of control surfaces

Code	Description	Origin
REQ-CON-07	The manufacturing process of the control surfaces shall strictly follow protocols.	RSK-CON-01
REQ-CON-08	The control surfaces shall be calibrated after manufacturing.	RSK-CON-01
REQ-CON-09	The control surfaces shall be checked pre-flight.	RSK-CON-02, RSK-CON-03, RSK-CON-04

9.7. RAMS Analysis

This section covers the RAMS analysis for the control surfaces.

Reliability

With the use of servos, the mechanisms of the control surfaces are reliable. However, no redundancy can be added for them due to the sizing constraints. To further improve reliability and avoid failure as much as possible, pre-flight checks and regular inspection can be done. This is already established in **REQ-CON-09**.

Availability

The control surfaces do not have large impact on the availability of the system. Since they are positioned on the outside, they can be accessed by unfolding the wing, allowing for easy inspection. Furthermore, the materials and components used are commonly used in the aerospace industry and widely available.

Maintainability

Visual inspection of the control surfaces can be done by only unfolding the wings. To access them, the wings have to be unfolded. For the aileron mechanisms, the wing tip can be removed, allowing access without special procedures. For the ruddervator mechanisms, it is more difficult to assess, since the structure of the tail is not yet established. It is expected that more complex tools are needed, which requires a workshop.

Safety

The servos used can potentially harm personnel during maintenance or disassembly. Therefore, it is important to wear safety gloves and safety glasses at all times whilst working on the control surfaces.

9.8. Financial Analysis

This section estimates the cost per SPARTA unit for the control surfaces. The material cost is low; a tail weight of 0.799 is established in Chapter 5, however including all mechanisms, and ailerons add minor weight. Considering a price of about \$3.50 per kg¹, this cost is negligible. Next, it is assumed that assembly process itself takes about 6 hours, including preparation, assembly and calibration. An uncertainty factor of 10% is added in the end. The approximated labour cost is the same as from previous chapter, resulting in a cost of about €230,-. Finally, the mechanisms is covered in Chapter 10.

9.9. Compliance Matrix

This section covers the requirement compliance for the control surfaces, shown in Table 9.5. The last three requirements are not yet met; they are covered in Section 19.3 and Section 19.6.

¹URL: <https://www.steelmetind.com/7075-aluminum-sheet-plate.html> [cited 17 June 2025]

Table 9.5: Control surfaces compliance matrix

Code	Compliance	Code	Compliance	Code	Compliance
REQ-CON-01	G	REQ-CON-04	G	REQ-CON-07	Y
REQ-CON-02	G	REQ-CON-05	G	REQ-CON-08	Y
REQ-CON-03	G	REQ-CON-06	G	REQ-CON-09	Y

9.10. Recommendations

For future development of the control surfaces, it is recommended to use more accurate and expensive software like CFD. This can better approximate the capabilities of the control surfaces, and give more accurate results for the derivatives and maximum deflection angle for the ailerons. Additionally, the structure of the control surfaces can be analysed to confirm that the chosen design configuration can withstand all the loads on them. Finally, SPARTA can be simulated during **RSK-CON-02-04** to approximate its capabilities during these failure modes.

10. Mechanical Design

This chapter covers the design of the mechanisms. Firstly, functional and requirement analyses are performed in Section 10.1 and 10.2 respectively. Next, the rotating wing mechanism, telescopic wing mechanism, aileron, and rotating tail and ruddervator mechanism are designed in Section 10.3, 10.4, 10.5 and 10.6 respectively. To summarise, a full component list is given in Section 10.7. Following the design, a sustainability, risk, RAMS and financial analysis are performed in Sections 10.8 through 10.11. Compliance with requirements is then checked in Section 10.12. Finally, recommendations are discussed in Section 10.13.

10.1. Functional Analysis

The mechanisms needs to convert the system from a slender drone that fits inside a tube to a fully deployed drone that is able to fly. The functional analysis of all the mechanisms can be found in Table 10.1

Table 10.1: Functions of the mechanisms

Code	Description	Origin
FUN-MEC-01	Provide morphing capabilities	FUN-3.3, FUN-7.2.3, FUN-7.5
FUN-MEC-02	Facilitate easy access to mechanisms.	FUN-8

10.2. Requirement Analysis

The mechanisms needs to perform certain function within certain constrains. These requirements can be found in Table 10.2.

Table 10.2: Mechanisms requirements

Code	Description	Origin
REQ-MEC-01	The mechanism shall not fail more than 1% of the time for its first 20 missions	REQ-SYS-13
REQ-MEC-02	The mechanisms shall have a storage temperature between -70° C and $+70^{\circ}$ C.	REQ-SYS-16
REQ-MEC-03	The mechanisms shall have a service temperature between -70° C and $+50^{\circ}$ C.	REQ-SYS-17
REQ-MEC-04	The mechanisms shall be housed such that no dust, water or dust can impede the motion and rotation of the mechanisms.	REQ-SYS-17-02, REQ-SYS-18-01, REQ-SYS-18-02, REQ-SYS-18-03
REQ-MEC-05	The mechanism shall be made from recyclable materials.	REQ-SYS-21
REQ-MEC-06	The mechanism shall be made from components and materials from Europe, except for the batteries and electronics.	REQ-SYS-31, REQ-SYS-32. REQ-SYS-33
REQ-MEC-07	The mechanism shall morph so the structure fits during stowage.	REQ-SYS-22-01, REQ-SYS-22-02

Code	Description	Origin
REQ-MEC-08	The mechanisms shall not use hazardous materials.	REQ-SYS-43
REQ-MEC-09	The mechanisms shall be able to go back to a stowed configuration with simple tools carried by a system operator.	REQ-SYS-34-01, REQ-SYS-34-02
REQ-MEC-10	The mechanism shall be storable for at least 10 years.	REQ-SYS-41
REQ-MEC-11	The limit loads shall be 1.25 times the maximum operational loads.	REQ-SYS-36-02
REQ-MEC-12	The ultimate loads shall be 1.35 times the maximum operational loads.	REQ-SYS-36-03
REQ-MEC-13	A safety factor of 2.0 shall be applied to castings.	REQ-SYS-36-04
REQ-MEC-14	A safety factor of 1.15 shall be applied to fittings.	REQ-SYS-36-05
REQ-MEC-15	A safety factor of 2.0 shall be applied to bearings subjected to rotation.	REQ-SYS-36-06
REQ-MEC-16	A safety factor of 4.45 shall be applied to control surface hinge-bearing loads.	REQ-SYS-36-07
REQ-MEC-17	A safety factor of 2.2 shall be applied to push-pull control system joints.	REQ-SYS-36-08
REQ-MEC-18	A factor of 1.2 shall be applied for moisture conditions.	REQ-SYS-36-09
REQ-MEC-19	A factor of 1.5 shall be applied for moisture and extreme temperature conditions.	REQ-SYS-36-10
REQ-MEC-20	A factor of 1.5 shall be applied for frequently assembled and disassembled structural parts.	REQ-SYS-36-11
REQ-MEC-21	The mechanisms shall not plastically deform when limit loads are applied.	REQ-SYS-36-12
REQ-MEC-22	The mechanisms shall not rupture when ultimate loads are applied.	REQ-SYS-36-13
REQ-MEC-23	The mechanisms shall withstand at least 3.8g during symmetric limit manoeuvring.	REQ-SYS-36-14
REQ-MEC-24	The mechanisms shall withstand at least -1.5g during symmetric limit manoeuvring.	REQ-SYS-36-15
REQ-MEC-25	The mechanism will have a fail-safe when loaded inside the launcher tube.	REQ-SYS-39
REQ-MEC-26	The mechanism shall not be damaged when transported outside the launch tube.	REQ-SYS-52
REQ-MEC-27	The mechanism will maintain structural integrity during flight.	REQ-SYS-53

10.3. Rotating Wing Mechanism

As the system needs to be stored inside a tube, the wings need to be morphed from a folded to an unfolded state. This is done with a simple planar hinge.

10.3.1. Concept generation

Different rotational mechanisms have been considered. Inspiration is gathered from both aerospace and non-aerospace examples. They are presented in Table 10.3.

Table 10.3: Concept generation for the rotating hinge mechanism

Concept	Inspiration	Explanation	Outcome
Torsion spring	Bicycle rack at Delft station	A torsion spring is loaded during storage. When the locking mechanism is deactivated, the spring rotates the wings to the correct angle.	Failed in the trade-off
Worm gear	Altius 600	A worm gear is connected to a gear, which is directly connected to the wing.	Chosen mechanism
Geneva gear	Movie projectors	A Geneva gear and a servo are used to lock and rotate the wing into place.	Failed in the trade-off
Pneumatic cylinder	Aircraft control surfaces	A pneumatic cylinder installed at a distance from the axle is used to push the wing out.	Unfeasible, too big
Linkage mechanism	Lazy chairs	A complicated linkage system that converts translation to rotation.	Unfeasible, too big
Direct drive	Hobby drones	A servo is mounted directly to the wing and resists the wing's motion during flight.	Unfeasible, too high continuous power consumption

10.3.2. Trade-off

As can be seen from Table 10.3, multiple designs are possible. To determine which is the best, a trade-off is conducted. The criteria used for the trade-off are:

- **Volume**, how much volume will the mechanism need inside the fuselage? (**REQ-SYS-22**)
- **Serviceability**, how easy is it to perform maintenance on the mechanism? (**REQ-SYS-45**)
- **Risk**, how probable is it that the mechanism breaks down? (**REQ-SYS-53**)
- **Attritability**, how easy is it to refurbish the system? (**REQ-SYS-34**)

Based on these criteria, the scores and weights can be established. The volume criterion is the most important as it influences the range and endurance of the vehicle. Risk also has a high weight as a failure of the mechanism to rotate can give catastrophic consequences. Serviceability and attritability were given a lesser weight as the system will not have a long service life due to its attritable nature.

After the trade-off is set up, the score could be determined. The results can be found in Table 10.5. It is important to note the subjectivity of this trade-off. Due to time and resource constraints, none of the trade-off designs could be worked out enough to make the scores quantitative. The scores can be found in Table 10.4.

Table 10.4: The score justification for the rotation wing mechanism trade-off

	Volume	Serviceability	Risk	Attritability
Torsion spring	The design can be put around the axles, minimising space	The design can only be accessed by removing the entire wing assembly	There are only a few parts that can break, but the torsion spring is a weak point	The design can't reset itself
Worm gear	The design needs space for the worm gear to be placed between the axles	The design can be accessed without removing the axles	There are many parts, but most are off the shelf	The design can reset itself
Geneva gear	The design needs two motors and two gear assemblies	The design can be accessed without removing the axles	The design uses two gear assemblies and two motors	The design can reset itself

Table 10.5: Completed trade-off table. Criteria are given in the top row, and design options are in the first column. The actual values for the parameters are given. The colour is related to the number of points. The white circles, top right of the coloured cell, indicate the colour; G for green, B for blue, Y for yellow and R for red.

	Volume	Serviceability	Risk	Attritability	Score
Weight	43%	14%	29%	14%	
Torsion spring	1 (G)	0.33 (Y)	0.66 (B)	0 (R)	0.66
Worm gear	0.66 (B)	0.66 (B)	0.66 (B)	1 (G)	0.71
Geneva gear	0.33 (Y)	0.66 (B)	0.33 (Y)	1 (G)	0.47

10.3.3. Design Overview

After the general design concept has been selected, a more detailed design can be made. The design is presented with different rotation angles in Figure 10.1. The rotation sequence can be described as the following:

- **Stage 1**, The wing is in a folded position with the mechanism locked.
- **Stage 2**, The stepper motor operating the mechanism is given a signal from the flight computer to rotate. The motor rotates the worm wheel, which rotates the two spur gears that are connected to the inner wing.
- **Stage 3**, The wing is in its final unfolded position and the engine stops rotating. The worm gear will prevent any rotational movement.

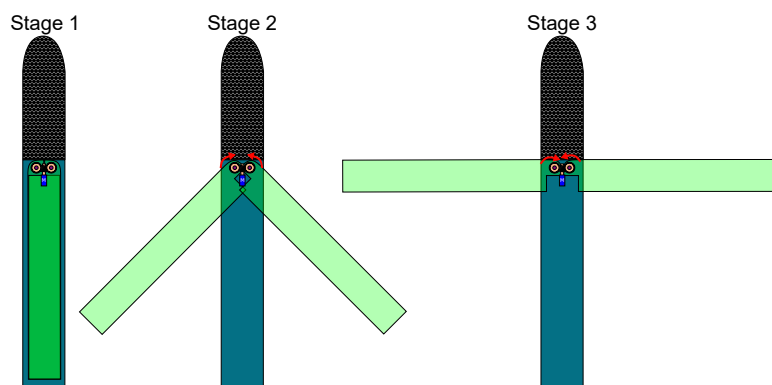


Figure 10.1: A top view of the fuselage with the rotating hinge mechanism in different rotational stages

10.3.4. Detailed Design

The rotational hinge design consists of five parts. The spur gear, the worm gear, the electric engine, the ball bearings and the rotation axle. The ball bearings are chosen as they provide freedom in one rotational direction, but restrict movement and rotation in the other five directions. The ball bearing drawn in Figure 10.2 are based on "SKF W 61704-2RS1" bearings¹. These Swedish stainless steel deep groove ball bearings with integral sealing are strong enough to cope with the load the mechanism will experience, but small enough to fit inside the system. The rotational axle is a stainless steel AM-350 axle with a diameter of 20 mm. This axle is designed so that it can cope with all the loads experienced during launch, flight and recovery. The spur gears are connected to a worm gear that is connected to a stepper engine, which can be, for example, the "NEMA17" stepper engine².

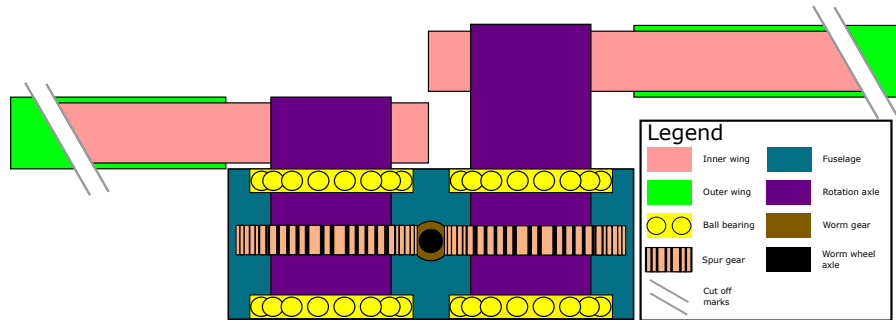


Figure 10.2: A front view of the rotational mechanism

A spur gear has many parameters that can be modified to achieve the required performance. Some of these parameters are defined based practicalities, like the face width or the number of teeth; others are defined with graphs and equations. All parameters can be found in Table 10.6.

$$\sigma_t = \frac{W_t P_d}{F_w J} \quad (10.1)$$

Table 10.6: Spur gear properties

Gear properties	Value	Unit	Justification
Number of teeth	20	-	Chosen to be compatible with the worm gear
Pressure angle	20	deg	Common pressure angle
Pitch line velocity	0.025	m/s	Defined as a quarter rotation per second
Face width (F_w)	0.01	m	Calculated using Equation 10.1
Pitch diameter (D_P)	0.03	m	Half the distance between the two rotational axis
Diameter pitch (P_d)	666.67	1/m	Calculated by taking the number of teeth and dividing it by the pitch diameter
Lewis Factor (Y)	0.32	-	From From Figure 1 from ³
Geometry factor (J)	0.24	-	From Figure 9-15 from [39]
Transmitted load (W_t)	5000	N	Force the gear tooth needs to resist

10.4. Telescopic Wing Mechanism

As the current wing area can't fit inside the tube, the wing needs to be folded. The most volume-efficient way to achieve this, is to divide the wing into two parts. One of the wings can then be stored inside the other wing. This means that the wings need to extend telescopically, and a mechanism needs to be designed.

¹URL: <https://www.skf.com/group/products/rolling-bearings/ball-bearings/deep-groove-ball-bearings/productid-W%2061704-2RS1> [cited 13 June 2025]

²URL: <https://www.123-3d.nl/123-3D-NEMA17-stappenmotor-1-8-graden-per-stap-48-mm-lang-4-8-kg-cm-SL42S248A102-0524-i3422-t14804.html> [cited 16 June 2025]

³URL: <https://ns2.engineersedge.com/gears/lewis-factor.htm> [cited 20 June 2025]

10.4.1. Concept generation

Different telescopic mechanisms have been considered. Inspiration is gathered from both aerospace and non-aerospace examples. They are presented in Table 10.7.

Table 10.7: Concept generation for the telescopic hinge mechanism

Concept	Inspiration	Explanation	Outcome
Pneumatic cylinder	Crane outriggers	The design uses a gas-operated cylinder to push the wing outwards.	Unfeasible, too big
Piston linkage	Internal combustion engines	The design converts the rotational movement of an engine to linear motion using a crankshaft and a piston.	Unfeasible, too big
Spring	Blowback firearms	The spring is pre-compressed before launch; when unlocked, it pushes the outer wing outward.	Selected
Screw	Space boom deployment	A screw is turned to extend the outer wing.	Failed in trade-off
Solenoid	Locking mechanisms and valve control in cars	A coil pushes an iron/steel beam forward using the law of Lenz.	Unfeasible, electromagnetic interference with avionics
Scissor lift	Solar panel deployment	A linkage system pushes the wing forward like a scissor lift.	Failed in trade-off
Linear actuator	Sailing boats (genaker booms)	Guiding booms slide over each other, pulling a wire connected to a pulley that pulls the booms forward.	Unfeasible, too big
Rolomite	Warhead safety switch	Two rollers connected with a thin sheet rotate to push the outer wing forward.	Unfeasible, too big

10.4.2. Trade-off

As can be seen from Table 10.7, multiple designs are possible. To determine which is the best, a trade-off is conducted. The criteria used for the trade-off are:

- **Speed**, how quickly can the design be extended? (**REQ-WING-04**)
- **Serviceability**, how easy is it to perform maintenance on the mechanism? (**REQ-SYS-45**)
- **Risk**, how probable is it that the mechanism to breaks down? (**REQ-SYS-53**)
- **Attritability**, how easy is it to refurbish the system? (**REQ-SYS-34**)

Based on these criteria, the scores and weights can be established. The speed criterion was deemed the most important as it will influence how quickly the system can actively control itself. Risk also has a high weight as a failure of the mechanism to extent can give catastrophic consequences. Serviceability and attritability were given a lesser weight as the system will not have a long service life due to its attritable nature.

After the trade-off was set up, the score could be determined. The results can be found in Table 10.9. It is important to note the subjectivity of this trade-off. Due to time and resource constraints, none of the trade-off designs could be worked out enough to make the scores quantitative. The scores can be found in Table 10.8.

Table 10.8: The score justification for the telescopic wing mechanism trade-off

	Speed	Serviceability	Risk	Attritability
Screw	The design takes a long time as many rotations are needed to fully extent	The design can easily be accessed by jut screwing the wing off	There only a few parts that can break	The design can reset itself
Spring	The design can spring the outer wing quickly	The design has many parts that are difficult to access	There are many part that need to work together	The design can't reset itself
Scissor	The design can extend the outer wing reasonably quickly	The design has many parts, but they are only accessible when the wing is removed	There are many parts that need to work together, it is difficult to mitigate the risks	The design can reset itself

Table 10.9: Completed trade-off table. Criteria are given in the top row, and design options are in the first column. The actual values for the parameters are given. The colour is related to the number of points. The white circles, top right of the coloured cell, indicate the colour; G for green, B for blue, Y for yellow and R for red.

	Speed	Serviceability	Risk	Attritability	Score
Weight	43%	14%	29%	14%	
Screw	0 (R)	1 (G)	1 (G)	1 (G)	0.57
Spring	1 (G)	0.33 (Y)	0.66 (B)	0 (R)	0.66
Scissor lift	0.66 (B)	0.66 (B)	0.33 (Y)	1 (G)	0.61

10.4.3. Design Overview

After the general design concept has been selected, a more detailed design can be made. The design is presented in different extension stages in Figure 10.3. The extension sequence can be described as the following:

- **Stage 1**, The wing is in its unextended, but rotated state. The orange locking levers keep the wing in place.
- **Stage 2**, The telescopic mechanism gets a signal from the flight computer (not shown) to extend. Therefore, two actuators (not shown) pull on the cyan-blue ropes that pull the orange locking levers out of their locked state.
- **Stage 3**, The light green outer wing is now free to extend. The black spring extends and accelerates the light green outer wing. The orange locking levers are still in an unlocked state.
- **Stage 4**, The outer wing reaches its endpoint and is slowed down by a dark green spring connected to a yellow rope.
- **Stage 5**, The light green wing is locked into position by relaxing the cyan ropes to release the orange locking levers.

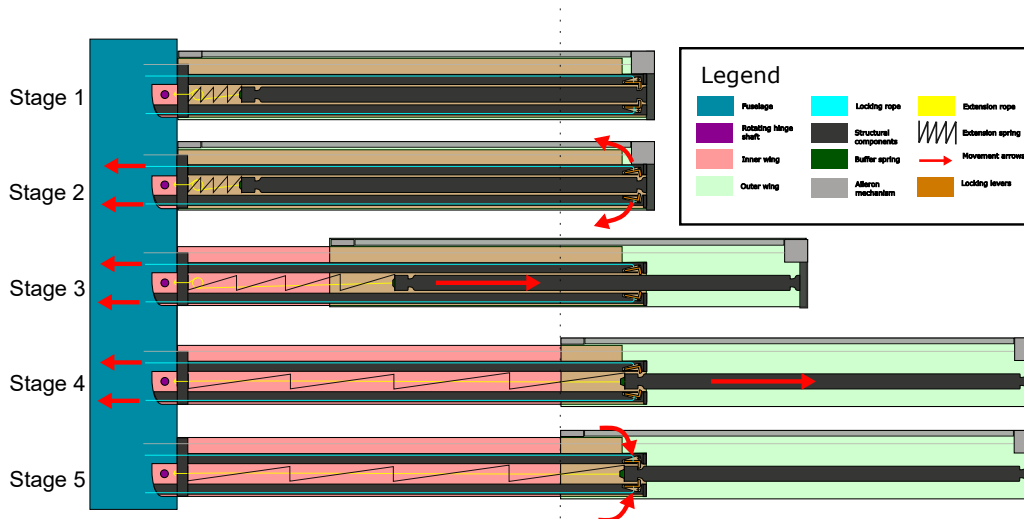


Figure 10.3: A top view of the main wing with the telescopic wing mechanism inside the wing

10.4.4. Extension Dynamics

Before a detailed analysis can be made, the dynamics of the system need to be defined. The mechanisms will move the outer wing over a distance of 440 mm in a time of 1 second. Assuming that 0.8 seconds will be used to accelerate the system and 0.2 seconds to decelerate the outer wing. According to Equation 10.2 [40], where a is the acceleration, s the distance and t the time, this means that the wing needs to be accelerated with an acceleration of at least 1.1 m/s^2 . The exact mass of the outer wing is not known yet, but a conservative estimation is to take half of the wing mass, which is 1.278 kg. Using Newton's second law, the force needed for such an acceleration is equal to 1.41 N. Of course, the spring also needs to overcome friction. Friction can come

from the rail mechanism, the guiding rod (red part in Figure 10.6) sliding over the inner wing, and the extension spring sliding over the inner wing. Exact calculation is beyond the scope of this report, but an estimation can be given. It is assumed that the four-rail mechanisms carry the weight of the outer wing over the inner wing. The mechanism uses ball bearings which have an estimated friction coefficient of 0.0015 (according to Table 11-4 in [41]). Using Equation 10.3 [40], the friction force is thus equal to 0.018 N, which means the spring needs to exert a force of 1.42 N.

$$a = \frac{2s}{t^2} \quad (10.2) \quad F_{\text{friction}} = \mu N \quad (10.3)$$

10.4.5. Detailed Analysis

Detailed analysis and sizing of all components is beyond the scope of this report. However, as the feasibility of the design needs to be proven, some components will be discussed in this subsection.

Locking Mechanism

The locking mechanism consists of two locking levers on both sides that lock the outer wing in either an extended or unextended state. The levers can be operated by either pulling on the cyan rope, raising the levers or relaxing the rope so that the lever spring (① in Figure 10.4) will push the levers down. The levers will carry the static spring load and the forces on the outer wing in the y-direction during flight. The lever rope is located in a tube (③ in Figure 10.7) on the outside of the guiding plates (blue part in Figure 10.6)

Spring Mechanism

The outer wing is pushed forward by a large slender spring (③ in Figure 10.5). This spring has a compressed length of about 60 mm and an uncompressed length of about 510 mm. The spring itself is rectangular in shape to fit inside the wing, similar to the springs used in pistol magazines. The wing is stopped by a rope connected to the inner wing structure (① in Figure 10.5) and via a buffer spring (④ in Figure 10.5) to the guiding rod (the red structure in 10.6). The purpose of the spring (④ in Figure 10.5) is to slow down the guiding rod and provide a more gentle impact of the outer wing into the structure.

The spring constant (k) of the extension spring can be calculated with Equation 10.4 [39] to be 2.56 N/m. Using Equation 10.5 [39] the thickness can be calculated if the material is assumed to be A227 steel (a common material for springs according to R. L. Mott [39]) and the spring has a minimum spring thickness (D_M) of 4 mm. The equation will yield a wire thickness (D_w) of at least 0.56 mm, which would fit in the chosen mechanism for SPARTA.

$$k = \frac{\Delta F}{\Delta L} \quad (10.4) \quad \tau = \frac{8kFD_M}{\pi D_w^3} \quad (10.5)$$

The rope will need to decelerate the mechanism with a speed of 0.88 m/s to 0 m/s in a distance of 88 mm. Using the impact energy equation (Equation 10.6 [40]), the tension force F the rope needs to resist is equal to 5.39 N. This can easily be done with, for example, a nylon fishing wire⁴.

$$F = \frac{mv^2}{2s} \quad (10.6)$$

⁴URL: <https://www.nootica.com/nylon-fishing-line-asari-pink-0-26-mm.html> [cited 16 June 2025]

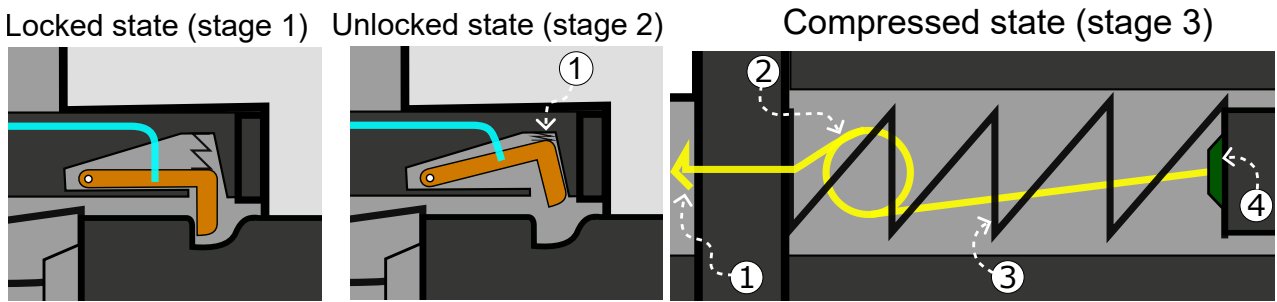


Figure 10.4: Close up of the locking lever mechanism

Figure 10.5: Close up of the spring mechanism

Structural Elements

The wings have different elements that guide the mechanism. They can be found in Figure 10.6. The red part is the guiding rod, which provides space for the locking levers to lock the wing. It does slide over the inner wing, but it does not carry any weight of the outer wing. That is carried by the rail mechanism explained later in this subsection. The green part is the spring buffer plate, and it provides a foothold for the extension spring. The magenta part is the guiding rod plate, which transfers the load of the guiding rod to the outer wing. The blue part is the guiding plates that only guide the guiding rod when it slides over the inner wing.

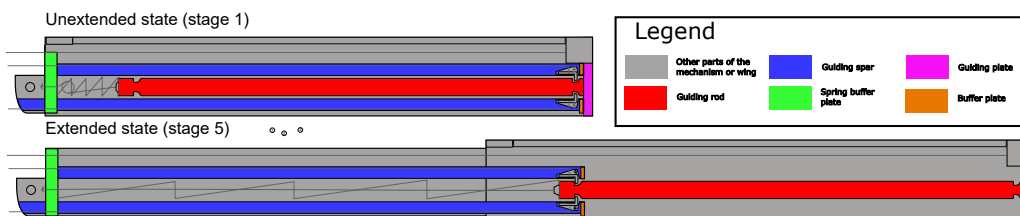


Figure 10.6: Overview of all telescopic mechanism structural elements. Note that the colour of the different elements in this figure do not correspond with any of the other figures.

Rail Mechanism

The outer wing should only translate in one direction therefore, the wing should restrict motion and rotation in all the other directions. To make sure that the system can only move in one degree of freedom, a rail mechanism needs to be designed. Designing rail mechanisms is an art, so the team looked for off-the-shelf components and found a mechanism that could work. The "C-Lube Linear Way LWL 1" is a stainless steel rolling guide that has a very small size. The mechanisms consist of two parts, a rail (lilac coloured part in Figure 10.7) which needs to be mounted along the entire length of a wing and a small carriage (ochre coloured part in Figure 10.7) that rolls over the rail. As the mechanisms should not interfere with the aerodynamics of the wings, it was decided that the rail will be mounted on the inside of the outer wing and the carriage on the outside of the inner wing at the tip of the inner wing (1 in Figure 10.7).

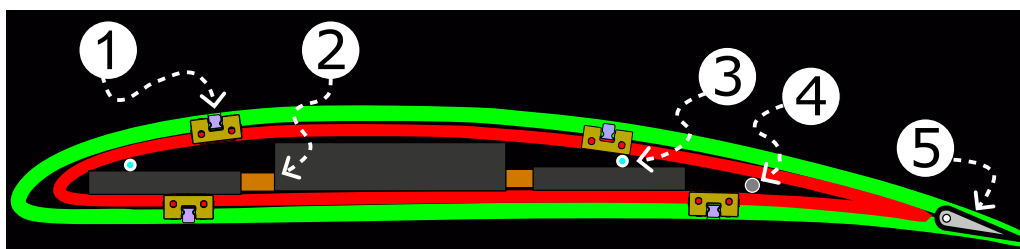


Figure 10.7: The cross-section of the tip chord of the wing in an unextended state

10.5. Aileron Mechanism

The aileron surface and mechanism are sized according to the space left inside the outer wing. The aileron surface has a maximum span of 495 mm and a chord length of 7.5 mm. Inside the outer wing, there is space allocated for the aileron mechanism with a volume of 4.2 cm³. An example of a servo that could fit and control

the mechanism is the "A2030 Ultra-Micro Analog 2.3g Linear Long Throw Offset Aircraft Servo"⁵. The servo is operated with a cable that can be fitted inside the wing (horizontal grey line in 10.3 and grey circle in ④ in Figure 10.7).

10.6. Rotating Tail And Ruddervator Mechanism

The tail wing has a rotating hinge design that is similar to the main wing hinge design. The biggest difference is the addition of a servo to rotate the ruddervator. To house this servo, the shaft is not solid but a tube with a diameter of 35 mm and a thickness of 3 mm made out of ASM-350 stainless steel. The bearings are "SKF 61807-2RZ Deep groove ball bearing with seals"⁶ from stainless steel. A servo that could fit and provide enough torque to overcome the maximum moment generated by the tail is the Spektrum "A5060 servo"⁷. This servo rotates with the tail and is connected to the tail wing further up the span. The rotating mechanism itself is rotated by a spur gear connected to a worm gear, which is connected to a stepper motor. An example of a stepper motor is the "NEMA17"⁸ motor.

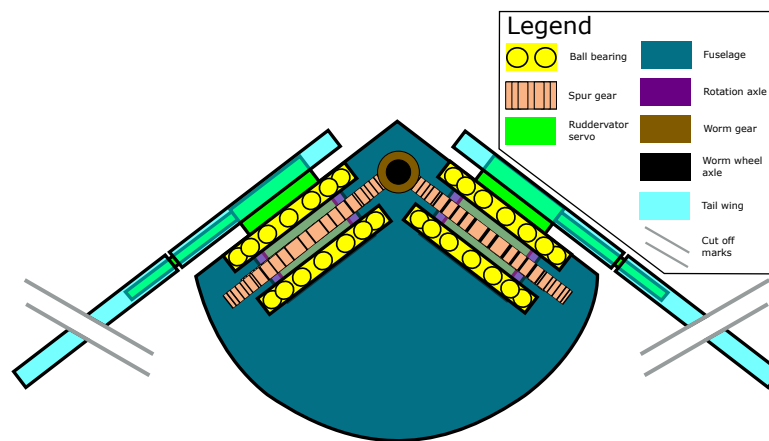


Figure 10.8: The front view of the rotating tail hinge and the ruddervator mechanism

10.7. Component List

As a summary, all components discussed in this section are tabulated in Table 10.10.

Table 10.10: Component list for all mechanisms and control surface controls

Component	Quantity	Material	Production process	Critical component	Off the shelf component	Origin of the shelf component	Total mass (g)
Rotating Wing Mechanism							
Ball bearings	4	Stainless steel	Machining	Yes	SKF W 61704-2RS	Sweden	25.2
Rotational wing axle	2	AM 350 steel	Machining	Yes	-	-	123
Wing spur gears	2	AM 350 steel	Machining	Margin	-	-	55.1
Wing worm gear	1	AM 350 steel	Machining	Margin	-	-	4.4
Stepper engine	1	Polymer, metal	Off site production	Margin	NEMA17	China	132

⁵URL: <https://www.spektrumrc.com/product/a2030-ultra-micro-analog-2.3g-linear-long-throw-offset-aircraft-servo/SPMSA2030L0.html> [cited 16-06-2025]

⁶URL: <https://www.skf.com/group/products/rolling-bearings/ball-bearings/deep-groove-ball-bearings/productid-61807-2RZ> [cited 16 June 2025]

⁷URL: <https://www.spektrumrc.com/product/a5060-mini-digital-hv-high-torque-metal-gear-aircraft-servo/SPMSA5060.html#> [cited 16 June 2025]

⁸URL: <https://www.123-3d.nl/123-3D-NEMA17-stappenmotor-1-8-graden-per-stap-48-mm-lang-4-8-kg-cm-S142S248A102-0524-i3422-t14804.html> [cited 16 June 2025]

Component	Quantity	Material	Production process	Critical component	Off the shelf component	Origin of the shelf component	Total mass (g)	
Telescopic wing mechanism							Sum	340
Guiding rod	2	7075-T6 aluminium	Stamping	No	-	-	140	
Spar guiders	4	7075-T6 aluminium	Stamping	No	-	-	140	
Spring/guiding buffer plates	4	7075-T6 aluminium	Machining	No	-	-	25.0	
Extension spring	2	A227 steel	Coiling	Margin	-	-	78.4	
Buffer spring	2	A227 steel	Machining	Margin	-	-	2.52	
Lever springs	4	A227 steel	Coiling	No	-	-	9.22	
Locking levers	4	AM 350 steel	Stamping	Margin	-	-	13.5	
Locking rope	4	Nylon	Drawing	No	Nylon fishing line Asari Pink - 0.26 mm	Japan	0.04	
Extension rope	2	Nylon	Drawing	Margin	Nylon fishing line Asari Pink - 0.26 mm	Japan	0.04	
Locking rope tube	4	7075-T6 aluminium	Extrusion	No	-	-	6.86	
Guiding rail	8	Stainless steel	Machining	Margin	C-Lube Linear Way LWL 1	Japan	74.0	
Cable pulling servo	4	Polymer	Off site production	Margin	TS90D Mini Servo	China	44	
Aileron servo	2	Polymer, metal	Off site production	Margin	SPMSA2030L	China/USA	4.6	
Rotating tail mechanism							Sum	539
Ball bearings	4	Stainless steel	Machining	Yes	SKF 61807-2RZ	Sweden	116	
Rotating tail axle	2	AM 350 steel	Machining	Margin	-	-	123	
Tail spur gears	2	AM 350 steel	Machining	Margin	-	-	79.6	
Tail worm gear	1	AM 350 steel	Machining	Margin	-	-	4.4	
Stepper engine	1	Polymer, metal	Off site production	Margin	NEMA17	China	132	
Ruddervator servo	2	Polymer, metal	Off site production	Margin	SPMSA5060	China/USA	52	
Sum							507	

10.8. Sustainability & Attritability

The system has numerous different components with different materials made with the help of different production techniques. Most of the materials are either common aerospace materials or production techniques. As the system needs to operate in a military context, these materials may not be available. As most components are not heavily loaded or not loaded to their limit, they may be replaced by weaker materials or components. These are marked with a "no" or a "margin" in the "Critical component" column in Table 10.10. The difference between the two categories is that "no" components have a negligible stress, and "margin" components have a non-negligible stress, but their stress is significantly lower than their limit stress.

With the exception of the electric components, all components can be recycled as they are made from metals or polymers. Some of the components are fixed to the wing, notably the guiding rail, guiding rod, spar guiders and buffer plates. For recyclability this will only pose a problem for the guiding rail as this is made from a different material than the wing. Therefore, the guiding rail should be mounted such that it can be removed at the end-of-life. All other components can be removed at the end of life. Except for the electrical component, no toxic or rare earth metals are used.

10.9. Risk Analysis

Below, the most critical risks associated with the mechanism structure are outlined, and mitigations are proposed.

RSK-MEC-01: The spur/worm gears teeth break

As the spur gears are heavily loaded, there might be a possibility that the teeth of the gear break. This could cause the mechanism to freely rotate and cause a partly unrotated wing. This could be mitigated by signing the gears to be safe-life by adding a larger safety factor.

RSK-MEC-02: The stepper engines break

The stepper engines are electric and can fail due to, for example, moisture or a short circuit. This can cause the wing or the tail to not fully rotate and thus be ineffective. This risk can be mitigated by sealing the motors and good quality control.

RSK-MEC-03: The extension rope breaks

If the extension rope breaks then the outer wing can fall out of the inner wing. This can cause asymmetric lift and thus failure of the vehicle. This can be mitigated with a fail-safe design by adding a second rope that is slightly longer than the original rope. This rope will not be loaded during normal operations and only be loaded if there is a need.

RSK-MEC-04: The extension rope gets tangled with the extension spring

As both the extension spring and the rope are close together, there is a risk of entanglement. This can cause the rope to restrict the extension of the wing, causing asymmetric lift. This will probably not cause catastrophic failure, but it should be considered. This risk can be mitigated by adding a rope folding procedure to the manufacturing and refurbishment manual, similar to parachute rigging manuals.

RSK-MEC-05: The locking levers fail

The locking levers hold the outer wing in place during storage and flight. If the locking levers break, they may cause unexpected extension or excess stress on the extension rope. This can cause premature extension of the outer wing which could damage the propeller and influence the initial stability of the vehicle. This can be mitigated by delaying the unfolding of the propeller until the wing is rotated. Additionally, the flight dynamics of the vehicle for premature deployment should be analysed.

RSK-MEC-06: The locking lever ropes break

If the locking levers can be pulled out of place, the wing may not extend causing asymmetric lift. The likelihood is quite low as the wires are not stressed during storage and are only weakly loaded during operation.

RSK-MEC-07: The outer wing is jammed

The outer wing needs to slide over the inner wing during extension. It can happen that due to manufacturing tolerances or temperature fluctuations, the structure can be jammed. This can be mitigated by testing for different manufacturing tolerances and tight quality control.

RSK-MEC-08: The control surfaces servos fail

The control surfaces are rotated by servos. These electrical components can fail due to moisture or a short circuit. It could cause controllability issues and make the system crash. This can be mitigated by having strict quality control during the manufacturing of the components and sealing them against moisture.

10.10. RAMS Analysis

The RAMS analysis for the mechanism is discussed in this section.

Reliability

The system needs to operate in a wide variety of environments. As specified in the requirements, it needs to operate at -70°C , 50°C , dust storms, hail storms and rain storms. For the mechanisms, it means that all mechanical components need to be sealed to protect them from ice, water and dust. For the rotating wing and tail mechanisms, this will not pose a problem. The only exposed part of these mechanisms are the axles and the ball bearings. The axles are not a problem as they are made from stainless steel and can resist the environment. The ball bearings are equipped with integral seals that, according to the manufacturer, provide

a seal against containment, water and moisture⁹. All other rotational hinge components are located inside the fuselage, therefore, they are protected by the fuselage skin panels against the environment.

When designing the telescopic wing mechanism, care has been taken to make sure that all parts are either inside the inner wing or inside the fuselage. The only components that are not are the rail mechanism and the control ropes and wire for the locking levers, and the aileron control. For the rail mechanisms, this is inevitable, as it connects the inner and outer wings to each other. To still make sure that they are protected against the elements, the rail has been mounted on the inside of the outer wing, and the carriage on the outside of the inner wing, surrounded by the outer wing. The inner and outer wings are fitted tightly, but a rubber seal can be placed to prevent any contamination from entering the mechanism.

The service life of the vehicle is quite short, only five hours of continuous operation for a minimum of twenty flights. This means that the mechanism will only experience approximately twenty cycles or 200 hours of continuous (locking) operation. According to R.L.Norton [41] that constitutes low service life of mechanical parts as it is less than 10,000 cycles. Therefore, fatigue life does not have to be considered for our system.

Availability

Most of the parts are simple metal components that should not be difficult to manufacture. The springs and the ball bearings are an exception as they have strict size and/or performance constraints. Ball bearings are standardised, thus, it might be possible to obtain ball bearings from other bearing manufacturers. The extension spring has an unusual geometry as it has a rectangular shape, which might be difficult to obtain. But this is a common spring shape in the arms industry, so in the military context, it should not be too difficult to obtain¹⁰.

The electronics are a problem for availability. As can be seen from Table 10.10, some of the actuators come from Asian or American countries. These may not be our allies in times of war. Some of the servos can be interchanged for other actuators from European countries, but as these types of electronics are often not produced in Europe, this may pose a problem. A possible solution would be to recycle servos and engines from products like cars, gardening equipment or small electric appliances.

Maintainability

During the design of the mechanism, the team considered the maintainability of the system. For the rotating wing and tail mechanism, the mechanism can be accessed and removed by removing skin panels and screwing open the hinge boxes that houses the mechanism.

The telescopic mechanism can be removed by untying the extension rope at the base of the wings. The extension rope is the only component that prevents the outer wing from fully sliding over the inner wing. After the outer wing is removed, many components can be accessed. The only components that are not maintainable are the locking mechanisms. The only way of accessing it is by destroying the wing skin. It would be possible to provide a removable skin panel, but this design has not been structurally and aerodynamically analysed.

Safety

The mechanism has many different parts that can cause harm people. Fortunately, most of the mechanisms are inside the wing, fuselage or hinge blocks. Therefore, the only parts that can cause harm are an unexpected telescopic extension or an unexpected rotation of the wing or tail. The telescopic hinge can, in theory, cause bruising, but because the speed and the weight of the outer wing is small (the maximum kinetic energy of the outer wing is in the order of 10 joules), in practice it will not cause harm. An unexpected rotation can cause a problem since the torque of the stepper engine is quite high. Therefore, it can jam fingers between the wing and the fuselage. Care should be taken that the rotating hinge mechanism cannot rotate after recovery by interrupting power to the servos and engines.

10.11. Financial Analysis

The mechanisms have approximately 68 different parts, of which 25 are unique and 17 are custom. The commercial off-the-shelf components with their associated cost can be found in Table 10.11. The cost of custom

⁹URL: <https://www.skf.com/group/products/rolling-bearings/principles-of-rolling-bearing-selection/general-bearing-knowledge/bearing-basics/components-and-materials> [cited 17 June 2025]

¹⁰URL: <https://www.springfieldspring.com/products-capabilities/magazine-springs/> [cited 16 June 2025]

parts is more difficult to determine and requires a more extensive analysis. This can be found in Section 18.1.2.

Table 10.11: The cost of the off-the-shelf parts for the mechanism

Component	Commercial name	Unit cost (€)	Quantity	Total (€)
Rail	C-Lube Linear Way LWL 1 ¹¹	21.34	32	682.88
Ball bearing	SKF W 61704-2RS ¹²	2.46	4	9.84
Ball bearing	SKF 61807-2RZ ¹³	28.32	4	113.28
Stepper engine	NEMA17 ¹⁴	16.5	2	33.00
Aileron servo	SPMSA2030L ¹⁵	22.58	2	45.16
Cable pulling servo	TS90D Mini Servo ¹⁶	4.5	4	18.00
Ruddervator	SPMSA5060 ¹⁷	70.89	2	141.78
			Sum	1043.94

10.12. Compliance Matrix

In this section, one can find the compliance matrix of the mechanisms subsystem along with its compliance with budgets. The compliance matrix can be found in Table 10.12. The budget compliance can be seen in Table 10.13. Preliminary mass and volume values contain a contingency of 20%, with the actual values using the final design contingencies of 10% and 5%, respectively. As can be seen, the hinge mechanism is three times bigger than was sized in the baseline. This is mostly due to the fact that the rotating tail hinge is not a smaller version of the rotating wing hinge. It also houses the servo needed to operate the ruddervator. The mass budget for the hinge design was met.

Table 10.12: Mechanism compliance matrix

Code	Comp.	Code	Comp.
REQ-MEC-01	G	REQ-MEC-15	G
REQ-MEC-02	G	REQ-MEC-16	G
REQ-MEC-03	G	REQ-MEC-17	G
REQ-MEC-04	G	REQ-MEC-18	G
REQ-MEC-05	G	REQ-MEC-19	G
REQ-MEC-06	G	REQ-MEC-20	G
REQ-MEC-07	G	REQ-MEC-21	G
REQ-MEC-08	G	REQ-MEC-22	G
REQ-MEC-09	G	REQ-MEC-23	G
REQ-MEC-10	G	REQ-MEC-24	G
REQ-MEC-11	G	REQ-MEC-25	G
REQ-MEC-12	G	REQ-MEC-26	G
REQ-MEC-13	G	REQ-MEC-27	G
REQ-MEC-14	G	-	-

Table 10.13: Mechanism budget adherence

Budget	Preliminary Value	Actual Value
Mass	1.00 kg	0.92 kg
Volume	0.06 L	0.18 L

10.13. Recommendations

The purpose of this chapter is to show the conceptual design of all the mechanisms, do a preliminary sizing of the different parts and prove the feasibility of the concepts. Detailed design has only been conducted on parts that are critical for the operation of the mechanism. A detailed analysis of all the parts thus still has to be conducted.

Another problem that has not yet been analysed is the temperature constraints. The gap between components needs to be small enough to provide smooth movement, but the gap should not be big enough to make the wings "unhinge" from themselves. This gap size between the inner and outer wings has not been analysed. Some of the components have different material properties and thus, for example, different expansion coefficients. The wing is made out of aluminium, but the rail mechanisms are from an unspecified stainless steel. The gap size can thus be larger or smaller than expected. A possible solution would be to make the rail mechanism in-house out of aluminium, but this has to be analysed.

Another part of the design that has been omitted is the lever rope pull mechanisms. It is currently assumed

that there are servos inside the fuselage that pull on the ropes to raise the locking levers, but it still needs to be worked out.

To accurately analyse the flight dynamics of the system, the extension of the outer wing needs to be modelled. Because the system uses an extension spring, a buffer spring and an extension rope, the extension behaviour can be tuned by modifying the spring constants of the spring and the length of the extension rope. This could provide an easier system to be analysed by the flight dynamics team.

Finally, if there are moving parts, there should be lubrication. The ball bearing, guiding rod, and locking levers all need some form of lubrication. As the system needs to work for a wide variety of environments, common viscous lubrication might not work. Therefore, they need to be analysed.

11. Propulsion Design

In this chapter, the propulsion subsystem is discussed. Firstly, functional and requirements analysis in Sections 11.1 and 11.2 is performed. Then the design and method are presented in Sections 11.4-11.7. Subsystem analysis of sustainability, risks, RAMS and financials is performed in Sections 11.4-11.10. To conclude, a compliance matrix and recommendations are provided in Sections 11.11 and 11.12.

11.1. Functional Analysis

The functional analysis of the propulsion subsystem outlines the main functions performed, and these are derived from the Functional Flow Diagram.

Table 11.1: Propulsion system functions

Code	Description	Origin
FUN-PROP-01	Deploy the propeller	FUN-SYS-5.2
FUN-PROP-02	Provide Thrust	FUN-SYS-6
FUN-PROP-02-01	Provide cruise thrust	FUN-PROP-02
FUN-PROP-02-02	Provide climb thrust	FUN-PROP-02
FUN-PROP-02-03	Provide descent thrust	FUN-PROP-02
FUN-PROP-03	Minimise Noise emissions	FUN-SYS-7.3.4

11.2. Requirement Analysis

Having obtained the required functions, they can be combined with existing system, and subsystem requirements to derive a list of requirements for the propulsion system to comply with and guide its design. They can be found in Table 11.2.

Table 11.2: Propulsion system requirements

Code	Description	Origin
REQ-PROP-01	The propulsion systems shall provide thrust	FUN-PROP-02
REQ-PROP-01-01	The propulsion systems shall provide a thrust of X N in Cruise	REQ-PROP-01
REQ-PROP-01-02	The propulsion systems shall provide a thrust of X N in Climb	REQ-PROP-01
REQ-PROP-01-03	The propulsion systems shall provide a thrust of X N in Descent	REQ-PROP-01
REQ-PROP-02	The propulsion system shall weigh less than 510 g	REQ-SYS-23
REQ-PROP-03	The propulsion system shall require less than 25,000 Rotation Per Minute (RPM) in any condition	FUN-PROP-02
REQ-PROP-04	The propulsion system shall require less than 1.5 Nm	FUN-PROP-02
REQ-PROP-05	The propulsion system shall require less than 1 kW of peak power from the engine	FUN-PROP-02
REQ-PROP-06	The propulsion system shall have a propeller efficiency in cruise of 0.8 or greater	[7]
REQ-PROP-07	The propulsion system shall have a volume of less than 0.83 L	Volume budget Table 5.4
REQ-PROP-08	The propulsion system shall have a maximum folded diameter of 123.9 mm	REQ-SYS-34-02

Code	Description	Origin
REQ-PROP-09	The propulsion system shall have a maximum folded depth of 78 mm	From fuselage design Chapter 8
REQ-PROP-10	The Propulsion system shall have a maximum folded diameter of 82 mm	From fuselage design Chapter 8

11.3. Trade-off Setup

To properly evaluate propeller performance, the following criteria are considered most important:

Propeller mass, due to the requirement that the propulsion system weigh less than 510 grams (**REQ-PROP-02**). This is measured on a linear quantitative scale, where a value of 1 corresponds to the lowest recorded mass, and 0 represents double that value. This wide range reflects the significant variation in propeller masses.

Propeller efficiency in cruise, to meet the requirement of a propulsive efficiency, must be greater than 0.8 (**REQ-PROP-06**). This is evaluated using a linear scale, where 0 corresponds to a value 10% below the highest-performing propeller. The tighter range accounts for the relatively small differences in cruise efficiency.

Propeller chord at the hinge location, since folding requires a hinge. Chord length serves as a proxy for hinge installation ease. This is scored using a linear scale with a standard 25% margin, where a value of 1 reflects the most suitable configuration.

Performance degradation due to necessary modifications, as adding an unfolding mechanism, requires replacing the inner portion of the blade with a folding lug. This causes some thrust loss and may reduce the accuracy of the manufacturer's data. This criterion is assessed on a linear scale based on the percentage of thrust lost, using the standard 25% margin. A schematic overview is shown in Figure 11.1.

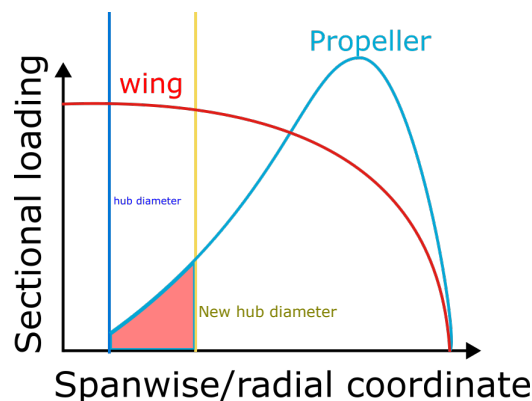


Figure 11.1: Schematic distribution of the lift over a propeller, the red area shows what is removed to make the prop foldable.

The criteria are weighted using the AHP method, resulting in the following matrix.

Table 11.3: AHP pairwise comparison values and their resulting normalised weights for skin trade-off

Criteria	Efficiency	Degradation	Mass	Root Chord	Computed Weight	Rounded Weight
Efficiency	1.00	0.50	1.50	0.50	0.1795	0.2
Degradation	2.00	1.00	3.00	2.00	0.4103	0.4
Mass	0.67	0.33	1.00	0.50	0.1282	0.1
Root Chord	2.00	0.50	2.00	1.00	0.2821	0.3

11.4. Propeller Design

In this section, the design of the propeller is discussed. It is deemed unnecessary to design a proprietary propeller within this preliminary design stage. The decision is made to select an off-the-shelf solution for this stage of the design. For this, the propeller database of manufacturer APC—known for its extensive catalogue—is used¹. To

¹URL:<https://www.apcprop.com/technical-information/file-downloads/?v=796834e7a283>[18 June 2025]

narrow down the vast database to a subset of propellers that may satisfy the system requirements, a data analysis is carried out.

First, the data is filtered based on propellers that meet the following conditions: a propulsive efficiency of 0.8 or higher at a cruise velocity of 40.33 m/s, a rotational speed below 25,000 RPM, and a power delivery of 208.691 W. Since the dataset is discrete, a 10% error margin is applied to all these values. Furthermore, any propeller with a diameter smaller than twice the minimum allowable folded diameter of 82 mm is removed, as such propellers would require excessive modification and have a probable cause to fail to generate sufficient thrust. Given that the maximum allowable folded depth is 78 mm, the largest permissible total diameter is 238 mm (twice the folded depth plus minimum diameter). Any propeller exceeding this diameter is also eliminated. Together, these constraints form the initial filter.

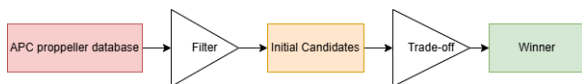


Figure 11.2: Filtering process

Table 11.4: Search criteria used for filtering APC propellers

Parameter	Value ($\pm 10\%$)
Cruise velocity	40.33 m/s
Efficiency	≥ 0.8
Maximum RPM	$\leq 25,000$
Power delivered	208.691 W
Minimum diameter	≥ 164 mm
Maximum diameter	≤ 238 mm

From the filtered APC dataset, values such as efficiency, mass, and root chord length are extracted. However, evaluating the performance degradation due to necessary propeller modifications requires a more involved approach. First, the original geometry of the propeller (including chord, thickness, and pitch) is entered into the JavaProp software, and the resulting thrust is recorded. The hub diameter is then increased to simulate the modification, and the new thrust is calculated. The percentage reduction in thrust represents the degradation in performance.

Although this method yields intuitively sound results, it is subject to several limitations. JavaProp, while trusted and validated, is a relatively simple tool². Not all airfoils in the APC dataset are available within the software, so the closest available approximations are used. Moreover, airfoil data within JavaProp is limited to specific Reynolds numbers (e.g., 50,000; 100,000; 500,000), which may not align exactly with the operating conditions specified by APC. In all cases, the nearest available match is selected to maintain consistency in the analysis.

11.5. Trade-off Results

Table 11.5 presents the results of the propeller trade-off. Based on the evaluated criteria, the propeller with a diameter of nine inches and a pitch of ten inches achieves the highest overall score and is therefore selected for use in the propulsion subsystem.

Table 11.5: Completed trade-off table. Criteria are given in the top row, and design options are in the first column. The actual values for the parameters are given. The colour is related to the number of points. The white circles, top right of the coloured cell, indicate the colour; G for green, B for blue, Y for yellow and R for red.

	Efficiency	Performance	Weight	Root Chord	Score
Weight	20%	40%	10%	30%	100%
8x10	0.81 G	95.0% G	18.99 B	17.18 R	0.60
9x10	0.82 G	97.4% G	22.11 Y	17.31 Y	0.74
7x9E	0.81 G	86.5% R	9.92 G	18.76 G	0.55

A supplier for customizable electric motors is Plettenberg Elektromotoren GmbH & Co. KG³. This supplier is based in Germany, which is essential to comply with the requirement that excludes the use of non-European

²A conversation was had with experts from the NLR regarding this method and, they believe it is suitable

³URL: <https://plettenbergmotors.com/> [cited 28 May 2025]

components (**REQ-SYS-31**). Their Orbit 1 family is customizable to match the RPM required by the propeller. It has a weight of 260 grams⁴. This motor can be powered by a compatible Electronic Speed Controller (ESC) from Plettenberg: the MST 35-45⁵.

11.6. Unfolding Mechanism Design

In this section, the unfolding mechanism is designed. The designed unfolding mechanism functions as follows: the propeller folds along the sides of the fuselage and is held in place by torsional springs. In the stowed position, it is prevented from unfolding by two small lips (stage 1 in Figure 11.3). When the engine starts and the propeller begins to spin, it automatically unfolds (stage 2 and 3 in Figure 11.3). This design has one important implication for the rest of the propeller: the inner folded diameter, which consists of a lug, does not contribute to thrust generation. The detailed design and sizing of the individual components fall outside the scope of this initial design phase and are left for future development.

However, using the values from the chosen propeller, a rough conservative estimate is made for the mass of the lug by assuming the root chord (17.31 mm) and maximum thickness (2.96 mm) of the propeller, multiplied by a factor of 2, and applying the density of AL 7075-T6 (2.7 g/cm³). This results in an estimated mass of 47.22 grams. The unfolding procedure is graphically shown in Figure 11.3.

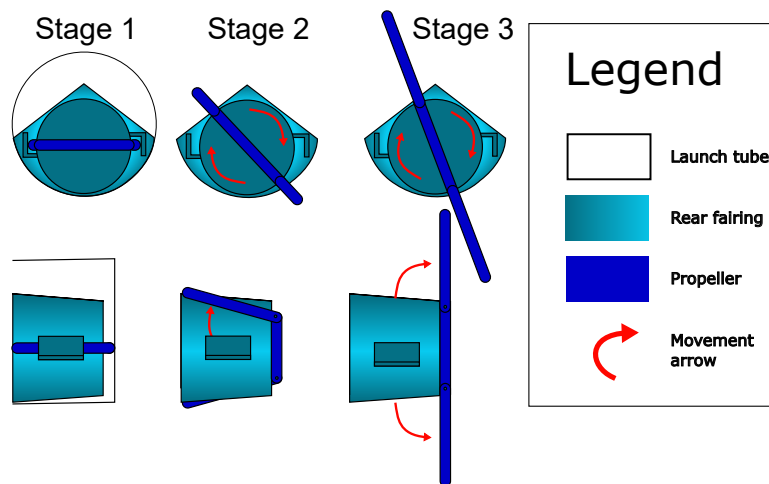


Figure 11.3: The propeller unfolding procedure

11.7. Sustainability & Attritability

In this section, the attritability of the propulsion system is briefly discussed. The attritability of the propulsion subsystem is expected to be highly dependent on the availability of the engine. Unlike the propeller, it is a custom-made high-cost component. If Plettenberg is unable to ramp up production, it might become a production bottleneck. Time should be invested in potentially finding another company for a second engine option and to recycle engines from SPARTA's that have reached their 20 mission EOL.

11.8. Risk Analysis

Below, the most critical risks associated with the propulsion system are outlined, and mitigations are proposed.

RSK-PROP-01: The propeller vibrates free

The propeller vibrates loose due to vehicle transport vibrations, causing it to partially unfold and potentially be damaged during launch. To mitigate this, the lip design should incorporate a passive mechanism with a neutral point positioned away from the edge.

RSK-PROP-02: The propeller modifications cause it to fail

Modifications required for the propeller to be able to unfold lead to its failure, rendering it unsuitable for use.

⁴URL: <https://plettenbergmotors.com/wp-content/uploads/2022/03/ORBIT-1-25-with-fan.pdf> [cited 23 June 2025]

⁵URL: <https://plettenbergmotors.com/wp-content/uploads/2023/02/MST-35-45.pdf> [cited 23 June 2025]

To prevent this, reinforcement of the propeller or the design of a custom propeller is necessary.

RSK-PROP-03: The propeller is damaged on recovery

During recovery, the propeller is permanently damaged. Rendering it unusable for future missions. In order to mitigate this, the propeller should be designed to be easily replaceable.

11.9. RAMS Analysis

In this section, the reliability, availability, maintainability and safety analysis can be found in this section.

Reliability

The reliability of the propulsion system is expected to be reasonable, provided that standard operating conditions are maintained and the unfolding mechanism functions as intended. The components involved are mechanically simple, reducing the likelihood of failure. However, if failure were to occur, this would likely result in the catastrophic loss of the system.

Availability

The system's availability is high, as both the propeller and lug are straightforward to manufacture or procure in volume. Their simplicity and lack of complex geometries make production and sourcing relatively easy. While the electric engine might suffer from availability issues. Electric motors are widely available parts and there is high confidence that a suitable replacement could be found in the case of an availability problem

Maintainability

Maintainability is limited due to the propeller's reliance on precise shape and balance for optimal performance. As a result, repairs are not recommended. If damage is detected during post-mission inspection, the propeller should be replaced rather than repaired to ensure system integrity.

Safety

Safety considerations are few; only that care must be taken to disconnect the engine from its power supply if performing maintenance on it to reduce the chances of a lethal shock. In the cabling, design, care should be taken to make this cable accessible.

11.10. Financial Analysis

This section aims to estimate the cost per SPARTA unit for the propulsion system. The APC propeller costs \$2.83⁶. The engine cost is estimated by quintupling the price of a comparable off-the-shelf motor to account for the customizable performance of the Plettenberg ORBIT 1, which can be tuned according to customer specifications and is therefore more complex than the average electric motor⁷.

11.11. Compliance Matrix

The compliance matrix of the design is shown in Table 11.6, and the propulsion subsystem's total budget is shown in Table 11.7.

⁶<https://www.apcprop.com/technical-information/file-downloads/?v=796834e7a283> [cited 18 June 2025]

⁷<https://plettenbergmotors.com/product/orbit-1-en/> [cited 18 June 2025]

Table 11.6: Propulsion System compliance matrix

Code	Comp.	Code	Comp.
REQ-PROP-01	G	REQ-PROP-06	G
REQ-PROP-02	G	REQ-PROP-07	G
REQ-PROP-03	G	REQ-PROP-08	G
REQ-PROP-04	G	REQ-PROP-09	G
REQ-PROP-05	G	REQ-PROP-10	G

Table 11.7: Propulsion System Component Overview

Type	Name	Weight [kg]	Volume [L]	Origin Country
Engine	Orbit1	0.260	0.038	Germany
ESC	MST 35-45	0.070	0.027	Germany
Propeller	APC prop	0.022	0.008	American design
Lug	Custom	0.047	0.017	local
Total	262.63 W	0.399	0.104	-

11.12. Recommendations

For future development of the propulsion subsystem, it is recommended to pursue the design of a custom-made propeller. Although this approach may lead to a slight increase in cost, it enables improved performance and seamless integration with the unfolding mechanism, eliminating the need for post-manufacture modification. Additionally, it reduces reliance on an American-designed propeller, which better aligns with the intended design autonomy. A custom propeller would also allow targeted optimisation of the minimum noise function (**FUN-PROP-03**), which is currently not specifically addressed and only assessed in Section 15.3.

The rear diameter of the fairing in the current design was selected somewhat arbitrarily, as no comprehensive analysis of the flow over the rear fuselage was conducted. Future iterations should include a more rigorous trade-off analysis, adjusting the rear fuselage diameter in conjunction with the propeller under evaluation to achieve improved aerodynamic performance.

Moreover, detailed design of the lug should be carried out to facilitate easy replacement of the propeller, as discussed in Section 11.8. This would enhance maintainability and support the modularity of the propulsion system.

12. Communication System

In this chapter, the communication subsystem will be selected for SPARTA. Firstly, a functional analysis is performed in Section 12.1, followed by the requirements in Section 12.2. Analysis is performed in Section 12.3 and components collected in Section 12.4. Next, sustainability, risk, financial and RAMS analyses are performed in Sections 12.5, 12.6, 12.7 and 12.8, respectively. Finally, compliance with the requirements is checked in Section 12.9 and recommendations given in Section 12.10.

12.1. Functional Analysis

The communication system has as primary function to transmit and receive data to and from the operator. Below in Table 12.1, the functions of the communication system are addressed.

Table 12.1: Functions of the communication system

Code	Description	Origin
FUN-COM-01	Collect all data from information sources	FUN-SYS-4.4.1, FUN-SYS-7.2.1, FUN-SYS-7.5.1
FUN-COM-02	Encode the data	FUN-SYS-4.4.1
FUN-COM-03	Encrypt the data	FUN-SYS-4.4.1
FUN-COM-04	Modulate the data	FUN-SYS-4.4.1
FUN-COM-05	Transmit the data	FUN-SYS-4.4.1
FUN-COM-06	Receive the data	FUN-SYS-4.4.2
FUN-COM-07	De-modulate the data	FUN-SYS-4.4.2

Code	Description	Origin
FUN-COM-08	Decrypt the data	FUN-SYS-4.4.2
FUN-COM-09	Decode the data	FUN-SYS-4.4.2
FUN-COM-10	Visualise all received data	FUN-SYS-4.4.2
FUN-COM-11	Store all collected data	FUN-SYS-6.3.3

12.2. Requirement Analysis

Having obtained the required functions, they can be combined with existing system and subsystem requirements to derive a list of requirements for the fuselage structure to comply with and guide its design. They can be found in Table 12.2.

Table 12.2: Communication system requirements

Code	Description	Origin
REQ-COM-01	The communication system shall transmit essential telemetry data to ground and launch vehicle at a range of minimum 100 km.	REQ-SYS-04
REQ-COM-02	The communication system shall transmit full HD video at a range of a minimum of 100 km.	REQ-SYS-08, -09
REQ-COM-03	All transmitted data shall be encrypted using at least the AES128 algorithm.	REQ-SYS-20
REQ-COM-04	Radio communication shall switch between frequencies in a pseudorandom manner.	REQ-SYS-08, -09
REQ-COM-05	The Encoder shall apply H.265 HEVC encoding to video data.	REQ-SYS-04
REQ-COM-06	The communication system shall transmit a telemetry datastream of a minimum of 12.48 kbps.	REQ-SYS-31
REQ-COM-07	No components shall originate from outside Europe.	REQ-SYS-31
REQ-COM-08	SPARTA shall store all collected data internally.	REQ-SYS-23
REQ-COM-09	The mass of the communication system will be not more than 0.450 kilogram (excluding contingency).	EQ-SYS-22
REQ-COM-10	The volume of the communication system will be no more than 0.56 litre (excluding contingency).	

12.3. Analysis

This section covers the different parts of the architecture of the communication system. Figure 12.1 shows the communication architecture from Barnhart et al.[42], with some modifications to reflect the functions of SPARTA’s communication system.

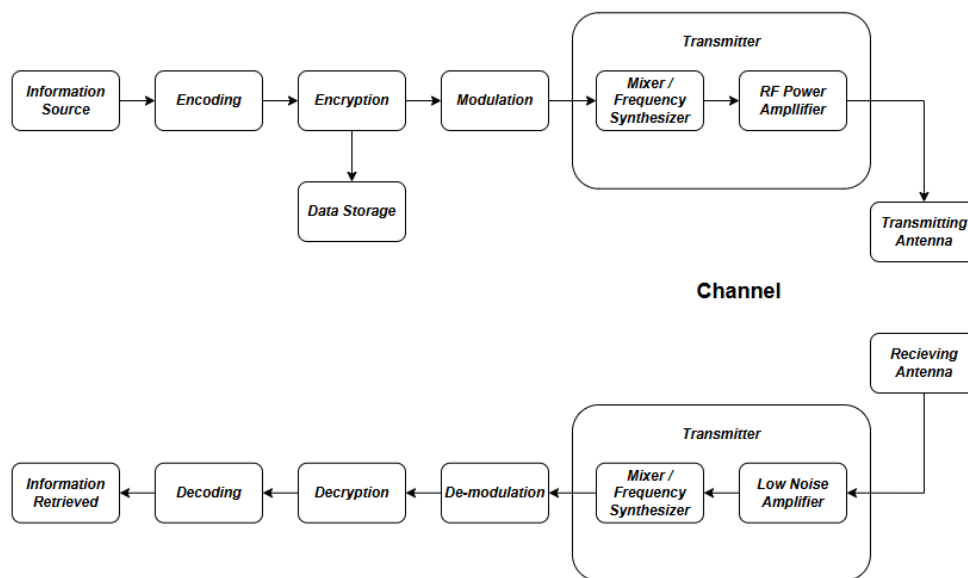


Figure 12.1: Communications Architecture [42]

12.3.1. Information Source

The transmitted information consists of two main aspects. The live video stream, and the telemetry and mission variables. The live video is in full HD resolution with a frame rate of 30 Frames Per Second (FPS). The MAVLink Protocol is used to structure the telemetry data. The telemetry data consists of the data as listed in Table 12.3. Using the MAVLink protocol data types, the bit size for a single timestamp sums up to 312 bits. With a rate of 40 packages a second, a data rate of at least 12.48 kbps is needed to transfer all telemetry data.

Table 12.3: Telemetry data mapped to MAVLink protocol

Data type	Example	MAVLink Type	Bit size
Flight Status & Navigation			
Ground Speed [m/s]	46.2	float	32
Vertical Speed [m/s]	2.1	float	32
Heading [°]	12.1	uint16_t (degrees×100)	16
Longitude Position [°]	51.5074000	int32_t (degrees×1E7)	32
Latitude Position [°]	10.3012000	int32_t (degrees×1E7)	32
Altitude AMSL [m]	120.40	int32_t (mm)	32
System Health			
Battery [%]	64	uint8_t	8
CPU Temperature [°C]	41.20	int16_t (×100)	16
RC Signal Strength [%]	87	uint8_t	8
Mission Parameters			
Waypoint Progress [%]	79	uint8_t	8
Distance to waypoint [m]	243.70	float	32
Target Altitude [m]	120.00	float	32
Timestamp [ms since boot]	12,340,000	uint32_t	32

12.3.2. Encoding

Encoding is done to reduce the bitrate of the data that is transmitted. Advanced compression techniques can be used to decrease the data rate of both the video transmission and the state and mission variables. For video transmission encoding, a widely used encoding protocol is the High Efficiency Video Coding (HEVC) standard, which is also known as H.265 [43]. Using this protocol, the bitrate of the Full HD video as discussed in Subsection 12.3.1 can be reduced and still deliver good quality at 8 Mbps [44].

12.3.3. Encryption

To encrypt the data, a common protocol used is the Advanced Encryption Standard (AES). The protocol is based on the Rijndael algorithm and established by the National Institute of Standards and Technology of The United States (NIST). This is a publicly available and royalty-free algorithm that works efficiently for all kinds of data encryption. It relies on data blocks of 128 bits which can be encrypted with a 128, 192, or 256 bit key depending on the encryption security required. A higher key bit size does come at the cost of more encryption latency and computational power required. As SPARTA requires live transmission and no highly sensitive information is transferred, a 128 bit key will be sufficient. This will suffice in preventing break-ins in the live information stream and ensure quick encryption using as low as possible computational power [45].

12.4. Chosen Components

The XVTR transmitter, in combination with the XBOOST24G8W video booster, offers an all-in-one solution for encoding, encryption, modulation, and transmission. This system is developed by Digital Micro Devices, a company specialised in UAV communication systems, based in Spain¹.

The XVTR system supports H.265 (HEVC) video encoding, and integrates AES128 encryption. It is also capable of handling Full HD video transmission. Moreover, the system accommodates telemetry and mission-data transmission at the required rate, and provides point-to-point range of up to 150 km for Full HD video, and up to

¹URL: https://d3.xlrs.eu/wp-content/uploads/2023/11/XVHD-SAT_Datasheet_01.pdf [cited 13 June 2025]

250 km for telemetry data. Frequency-Hopping Spread-Spectrum (FHSS) capabilities reduce tracking possibilities and improve stealth as explained in Section 15.3. All encrypted data will be stored locally on an Universal Serial Bus (USB) flash drive². Key specifications of the XVTR + XBOOST24G8W are listed in Table 12.4.

Table 12.4: Key specifications of the XVTR + XBOOST24G8W setup

Parameter	Specification	Parameter	Specification
Video input	Full HD (1080p) supported via HDMI	Encoding standard	H.265 (HEVC)
Encryption	AES128 hardware encryption	Transmission range	Video: 150 km ; Telemetry: 250 km
Operating frequency	2.4 GHz ISM band	Size	111×72×34 mm
Data support	MAVLink-compatible telemetry channel	Weight	Transmitter: 165 g; booster: 120 g
Temperature range	-20°C to +60°C	Power requirements	Max 19 W

To accompany the chosen transmitter, a ground control and launch vehicle control receiver and interface is selected. All components are also developed by Digital Micro Devices and are compatible with the XVTR transmitter.

For the ground station, the data can be received by the SATPROV2³, which is a tracking antenna and is able to receive video streams from up to 150 km and telemetry data from up to 250 km. It is also capable of transmitting potential mission updates from the ground controller back to the UAV. The GCSD5 DUAL⁴ provides a convenient control interface where video and telemetry data can be observed and analysed, any mission updates can be initiated and the interface allows for connection to two UAV's at the same time.

For an operator on a launch vehicle, the SATPROV2 receiver can only be used if it is possible to install it on the launch vehicle. This depends on the architecture of the launch vehicle and environment. If it is not used, the compact RXLRS⁵ receiver can be used to receive telemetry data on board on the launch vehicle. This device does not allow for a bidirectional telemetry link. All data received can be observed and analysed by the operator, using the XPAD5⁶, which is a portable control station.

The XVTR and XBOOST24G8W, in combination with the selected receivers and control stations, meet the communication requirements set out in Section 12.2. Using these off the shelf components minimizes integration complexity and simplifies certification and testing due to the commercial availability and reliability in other UAV applications.

Figure 12.2 visualises the data rates and volumes that are expected to be handled by the system. Here, the avionics and autopilot system that is selected in Chapter 13 and its data rates are included. It is important to note that although the autopilot takes inputs from the communication system, it can operate without them in case the communication is lost. The system operator will not be able to make any changes to the mission objective and the autopilot will perform the mission according to the last updates.

²URL: https://www.intenso.de/wp-content/uploads/2024/02/de_usb_high_speed_line.pdf [cited 13 June 2025]

³URL: <https://d3.xlrs.eu/satpro/> [cited 23 June 2025]

⁴URL: <https://d3.xlrs.eu/gcsd4dual/> [cited 23 June 2025]

⁵URL: <https://d3.xlrs.eu/product/rxlr-professional-rx-radio-control-mavlink-telemetry-transparent-data-link-aes128-encryption-8ch-sppm-rcb-sma-f-usb/> [cited 23 June 2025]

⁶URL: <https://d3.xlrs.eu/product/xpad5-all-in-one-portable-ground-control-station-d5/> [cited 23 June 2025]

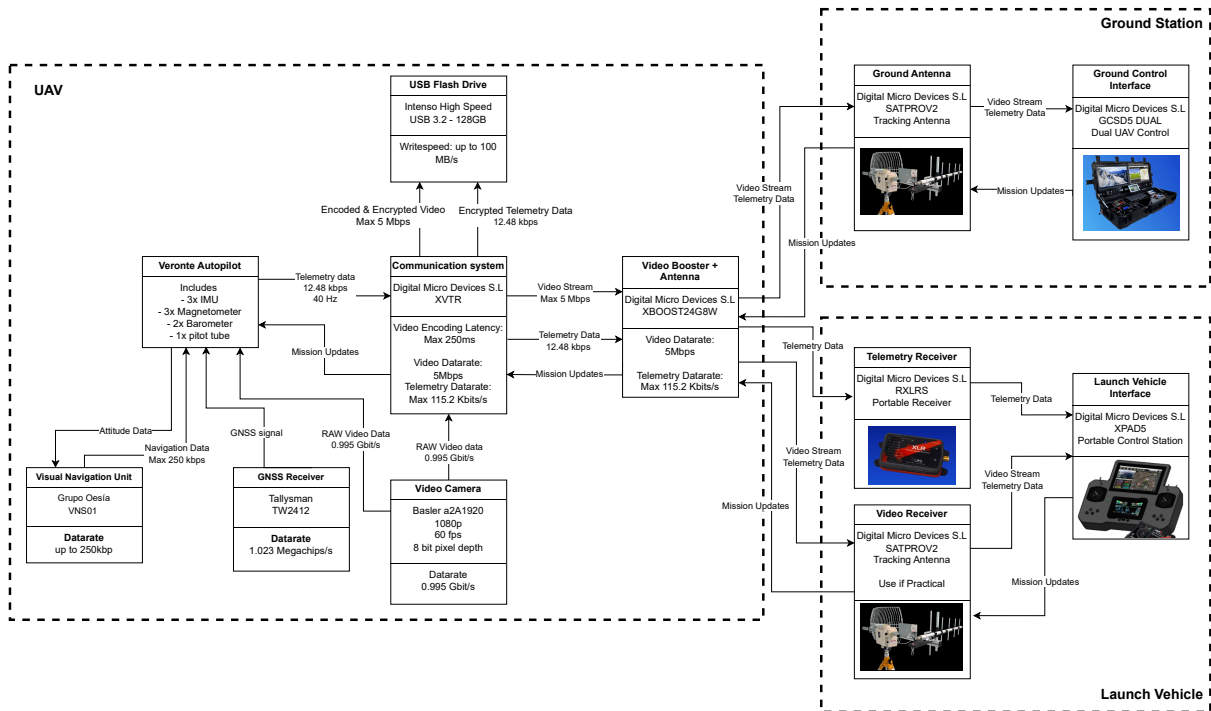


Figure 12.2: Data handling and Communication flow diagram

12.5. Sustainability & Attritability

In this section, the sustainability and attritability of the communication system are discussed. Since the components used by ground stations and on the launch vehicle can be reused many times, the focus will be on the parts within the UAV. The XVTR and XBOOST24G8W do not require rare materials for production and can be reused in new SPARTA units if system failures are caused by other components. However, since all parts used in the communication system are produced by external suppliers, this could pose challenges to its attritability. If mass production is required, Digital Micro Devices may not be able to meet demand. If the financial situation permits, SPARTA may need to consider acquiring the company to get full control over the production process.

12.6. Risk Analysis

Below, the most critical risks associated with the communication system are outlined, and mitigations are proposed.

RSK-COM-01: Communication system does not meet the provided performance specifications.

It could be the case that the performance specifications tests performed by Digital Micro Devices were performed under idealised operating conditions, and that SPARTA is not able to match these during operations. To mitigate this risk, SPARTA's team should be in close contact with the systems provider to adapt any changes that could make the system more suitable for the mission. Think of changes in Modulation techniques or frequency bands that are used.

RSK-COM-02: Communication system components are not delivered on time during production.

As explained in Section 12.5, delays in the supply chain could lead to setbacks in the production timeline, since all components of the communication system are sourced from one external supplier. This risk can be mitigated by establishing contacts with alternative suppliers of similar systems and switching suppliers when supply is limited. In addition to that, SPARTA needs to investigate the possibility to produce their own communication system, or alternatively pursue the acquisition of Digital Micro Devices.

RSK-COM-03: Communication system is jammed or intercepted.

Although the FHSS technology is used, it could occur that communication is lost. For example, if broadband jamming systems are used. To allow for correct operation after a data-link is lost, the autopilot system should be

able to operate independent of the communication. Additionally, mission updates should always be encrypted to ensure that the mission objectives can only be changed by allied operators.

12.7. RAMS Analysis

This section will cover the RAMS analysis for the communications subsystem.

Reliability

The communication system is a reliable subsystem, SPARTA uses components from one manufacturer which are all compatible with each other. Furthermore, the components are widely used and tested in other UAV applications.

Availability

The availability of the system depends on the operating conditions. During operations in military situations, the communication channels could be jammed by broadband jamming systems. During this period, the transmitted data will not be available. However, since the system is autonomous and all data is stored internally, all data will be available upon recovery or when data-links are re-established.

Maintainability

In the short term, the communication system is very maintainable, because maintenance procedures are designed and documented already, which allows easy implementation. In the long term, there are some negative impacts on maintainability because using off-the-shelf components gives limited customization and integration possibilities.

Safety

A main concern regarding safety is the cybersecurity of the system. In case the FHSS sequence or the encryption algorithm are compromised, the data transferred to and from the UAV are available to opponent forces. This could impose dangers for system operators as sensitive mission data might be compromised.

12.8. Financial Analysis

Regarding the costs of the communication system that, a quote has been requested from Digital Micro Devices. Since the quote has not been received yet, the costs will be estimated. The main costs will be in the ground station setup, which will not be lost as often as the UAV. Based on prices of similar communication systems, the price of the transmitter and booster are estimated to be €8,000 and the ground station and control interface are €12,000⁷. Maintenance will consist of system checks and software updates, this will cost one system operator approximately 2 hours a week.

12.9. Compliance Matrix

Table 12.5: Communication system compliance matrix







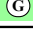
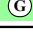
Code	Comp.	Code	Comp.
REQ-COM-01		REQ-COM-05	
REQ-COM-02		REQ-COM-06	
REQ-COM-03		REQ-COM-07	
REQ-COM-04		REQ-COM-08	

Table 12.6: Communication System margin adherence

Budget	Preliminary Value	Actual Value
Mass	0.450 kg	0.285 kg
Volume	0.56 L	0.28 L

⁷URL: https://store.foxtech.com/accessory/datavideo-link/?srsltid=AfmB0ooUh-75KW5D5LD8wAbTLRn2u5_t5zmd6eDzp5pBcz9QTH9tz7hW [cited 13 June 2025]

12.10. Recommendations

This section covers the next steps to be taken to achieve a more detailed and suitable design of the communication system. First of all, specifications provided by the manufacturer should be validated by conducting performance tests. If the tests do not satisfy the requirements of the communication system, a different supplier must be selected or the communication can be custom made. In addition to that, to provide a better mitigation for **RSK-COM-03**, it can be investigated if it is possible to transmit the data on more exotic frequency bands to prevent jamming and interception of communication signals.

13. Avionics

In this chapter, the avionics will be selected for SPARTA. Firstly, a functional analysis is performed in Section 13.1, followed by the requirements in Section 13.2. Analysis is performed in Section 13.3 and components collected in Section 13.4. Next, risk, financial and RAMS analysis are performed in Sections 13.5, 13.6 and 13.7 respectively. Finally, compliance with the requirements is checked in Section 13.8, after which recommendations are given in 13.9.

13.1. Functional Analysis

The functional analysis for the avionics subsystem is performed in this section in Table 13.2.

Table 13.1: Requirements or functions

Code	Description	Origin
FUN-AVI-01	Determine Flight Conditions	FUN-SYS-3.4.2
FUN-AVI-02	Determine Current Location	FUN-SYS-3.3.3
FUN-AVI-03	Measure Current State	FUN-SYS-4.6
FUN-AVI-03-01	Measure Velocities	FUN-AVI-03, FUN-SYS-4.6.1
FUN-AVI-03-02	Measure Rates	FUN-AVI-03, FUN-SYS-4.6.2
FUN-AVI-03-03	Measure Angles	FUN-AVI-03, FUN-SYS-4.6.3
FUN-AVI-03-04	Measure Position	FUN-AVI-03, FUN-SYS-4.6.4

13.2. Requirement Analysis

The functions identified previously are converted to requirements for the avionics subsystem. They can be found in Table 13.2.

Table 13.2: Avionics system requirements

Code	Description	Origin
REQ-AVI-01	The avionics system shall determine flight conditions in real-time	FUN-AVI-01
REQ-AVI-02	The avionics system shall determine FUN-AVI-02	
REQ-AVI-03	The avionics system shall measure the current flight state FUN-AVI-03	
REQ-AVI-03-01	The avionics shall measure pitch angle θ	FUN-AVI-03-03
REQ-AVI-03-02	The avionics shall measure roll angle ϕ	FUN-AVI-03-03
REQ-AVI-03-03	The avionics shall measure sideslip angle β	FUN-AVI-03-03
REQ-AVI-03-04	The avionics shall measure angle of attack α	FUN-AVI-03-03
REQ-AVI-03-05	The avionics shall measure pitch rate	FUN-AVI-03-02
REQ-AVI-03-06	The avionics shall measure roll rate	FUN-AVI-03-02
REQ-AVI-03-07	The avionics shall measure yaw rate	FUN-AVI-03-02
REQ-AVI-03-08	The avionics shall measure position	FUN-AVI-03-04
REQ-AVI-03-09	The avionics shall measure ground speed	FUN-AVI-03-01
REQ-AVI-03-10	The avionics shall measure airspeed	FUN-AVI-03-01
REQ-AVI-03-11	The avionics shall measure altitude	FUN-AVI-03-04
REQ-AVI-04	The avionics shall provide position in GNSS-denied environments	FUN-AVI-02
REQ-AVI-05	The avionics shall provide backup navigation	FUN-AVI-02

13.3. Analysis

The avionics of a drone consist of several distinct components. A schematic of the general layout of the avionics subsystem is shown in Figure 13.1.

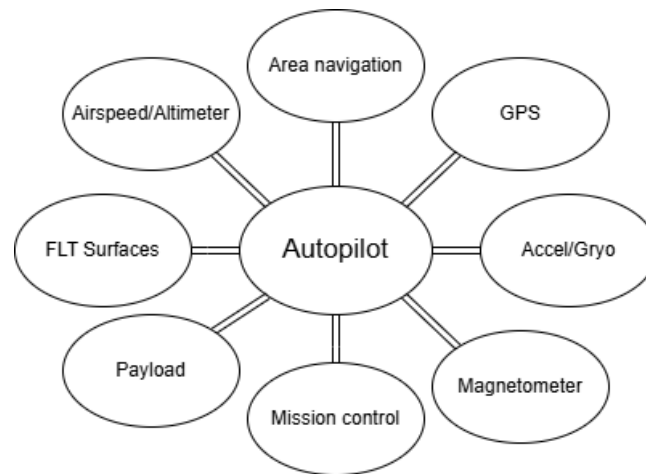


Figure 13.1: General Avionics Layout for UAS
[42]

The autopilot collects data from various sensors and makes real-time decisions to execute the programmed mission. It controls the aircraft by actuating the flight control surfaces.

To determine the aircraft's heading, the autopilot uses magnetometers, which detect the Earth's magnetic field. These sensors typically measure all three axes and assist in determining attitude. Because they rely on the local magnetic environment, they require calibration before operation [42].

Orientation and rotational rates come from the Inertial Measurement Unit (IMU), which includes accelerometers to measure lateral, longitudinal, and vertical acceleration, and gyroscopes to determine roll, pitch, and yaw rates. Due to their compact size, IMUs tend to accumulate error over time, making them less reliable for long-distance navigation. However, they remain useful for short-term dead reckoning in emergencies [42].

A Global Positioning System (GPS) or GNSS receiver uses satellite signals to calculate the aircraft's position, altitude, and velocity. While highly accurate and compact, GNSS systems are vulnerable to jamming and spoofing, making them unreliable in contested environments.

Since SPARTA may operate in areas without GNSS access, a secondary navigation method is necessary. Terrain-based navigation is a widely used alternative. This method captures video of the ground and uses either preloaded maps or onboard memory to determine location. Its primary advantage is independence from external signals, making it immune to jamming. However, it requires visual contact with the ground, limiting the drone to altitudes below the cloud layer. Given SPARTA's reconnaissance mission, this constraint is acceptable.

Airspeed is commonly determined using a pitot tube, whereas ground speed can be calculated using GNSS data or terrain-based navigation. Since neither method directly measures wind speed, a specialized instrument is necessary for measuring airspeed. A pitot tube, when paired with a static pressure port, accomplishes this by gauging the disparity between static pressure and dynamic pressure, leveraging Bernoulli's principle.

By integrating data from these systems, the autopilot adjusts the control surfaces to maintain and modify

SPARTA's heading and orientation.

13.4. Chosen Components

The Veronte Autopilot 1x is a robust, reliable flight controller featuring both physical and logical redundancy. It remains operational even after individual sensor failures, maintaining accurate estimates of attitude and position. Key onboard sensors include:

- 3 IMUs
- 3 Magnetometers
- 2 Barometers

It supports external inputs from a pitot tube and a GNSS receiver. Designed for aircraft and drones, it is STANAG-compliant, compatible with terrain-avoidance cameras, fully programmable, and capable of controlling up to 32 actuators. The unit is compact and lightweight, measuring 40×64×75 mm and weighing 198 grams. Power consumption ranges between 5–15 W, depending on system activity. A picture of the unit is shown in Figure 13.2.

The Visual Navigation System (VNS) is a Spanish-made terrain navigation system that uses an onboard camera to track ground features and estimate heading, speed, and position through a combination of odometry and terrain recognition. The product is called VNS01 and weighs 100 grams, consumes 5 W, and has dimensions of 24×80×77 mm. An image of the system appears in Figure 13.3.

The Septentrio Mosaic-G5 P3H is a Belgium-made, military-grade GNSS receiver designed for high precision and low signal noise. It operates across a wide range of bandwidths and remains reliable in harsh environments. The receiver consumes negligible power, weighs 2.2 grams, and has dimensions of 21×16×2 mm. A picture is included in Figure 13.4.



Figure 13.2: Veronte autopilot
[2]



Figure 13.3: VNS01 Visual Navigation System
[3]

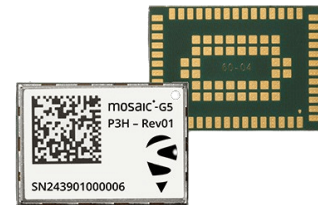


Figure 13.4: Mosaic-G5 P3H
[4]

Overview of avionics system components (not to scale)

Figure 13.5 shows the internal software diagram of the Veronte autopilot, where inputs and output connections are visualised with arrows. Most software modules are supplied by Veronte and customisable to our system. For

¹URL: <https://www.sbg-systems.com/wp-content/uploads/SBG-Pulse-40-MK012EN.pdf> [cited 18 June 2025]

²URL: <https://www.sbg-systems.com/wp-content/uploads/SBG-Ellipse-Micro-Series-MK008EN.pdf> [cited 18 June 2025]

³URL: <https://support.sbg-systems.com/sc/el/latest/ellipse-documentation> [cited 18 June 2025]

⁴URL: https://www.vectornav.com/docs/default-source/product-brief/vn-100-product-brief.pdf?sfvrsn=a2a5ae5f_2 [cited 18 June 2025]

⁵URL: <https://www.sbg-systems.com/ins/ellipse-e/documentation> [cited 18 June 2025]

⁶URL: <https://www.swiss-airdata.com/products/flow-vanes/smv-1> [cited 18 June 2025]

⁷URL: <https://www.uavnavigation.com/products/autopilots/vector-400> [cited 18 June 2025]

⁸URL: https://content.u-blox.com/sites/default/files/documents/ZED-F9P-05B_DataSheet_UBXDOC-9638021-14-12824.pdf [cited 18 June 2025]

example, the mission progress and flight plan control can be adjusted for ISTAR mission profiles. However, the use of morphing structures makes our case unique. Therefore, the morphing mechanisms module must be fully engineered in future design steps. Here, it is important that the lifting devices are only deployed when the system is in its safe operating envelope, which shall be determined using the attitude and environment conditions of the aircraft after launch.

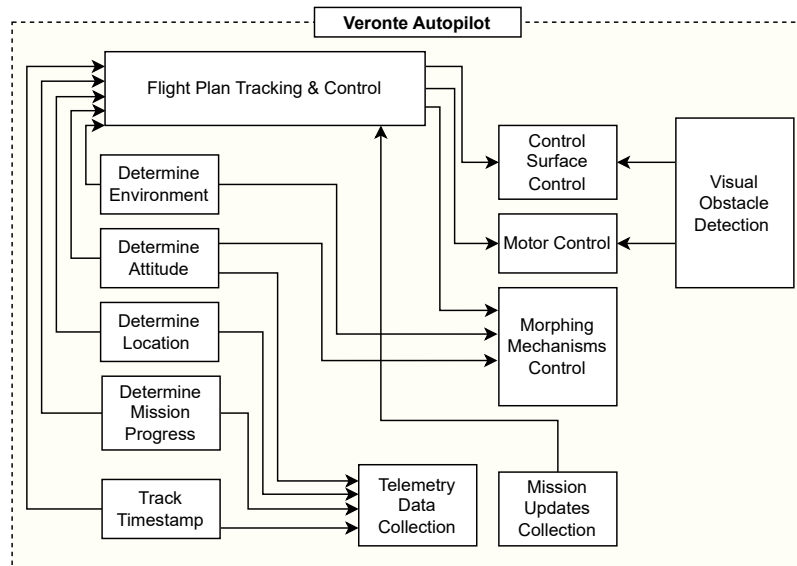


Figure 13.5: Software Diagram Veronte Autopilot

13.5. Risk Analysis

Below, the most critical risk associated with the Avionics is outlined, and a mitigation is proposed.

RSK-AVI-01: A lack of supply of chosen components

Due to being unable to meet the demand of one of the avionics components, there is a bottleneck in the production of the avionics subsystem. To mitigate this risk, backup components should be selected. For the autopilot, the vector 400 could be a viable alternative¹ for the GNSS Helix Antenna could be used². An alternative for the visual navigation system will still need to be found and selected.

13.6. Financial Analysis

For the financial analysis of the avionics, it is important to look at the price of the selected components. For the Veronte autopilot and the GNSS antenna, these prices are €6,150 and €67.91 [2] [4]. But for the visual navigation system, a quotation request would have to be sent regarding the price of the component.

13.7. RAMS Analysis

The RAMS analysis for the Avionics is discussed in this section.

Reliability

The reliability of the avionics is expected to be good. Most chosen components offer a degree of reliability regarding their sensors. However, there are still components with single points of failure, namely the flight computer, visual navigation system and pitot tube. Of these, only the loss of the flight computer would cause an immediate catastrophic loss of the UAV but given the size, power and cost increase required to accommodate a redundant flight computer, this was not deemed worth it.

¹URL:<https://www.uavnavigation.com/products/autopilots/vector-400>,[cited:18-06-2025]

²URL:<https://www.gpsworld.com/mil-spec-gps-gnss-antennas-released-by-pasternack/>,[cited:18-06-2025]

Maintainability

The maintainability of the Avionics is relatively mixed. While the high accessibility of the components through removing a skin panel should make them easy to swap in case of a failure. Due to the components being made by external parties, it may not be possible to repair the components without their help. Detailed discussion should be had with the chosen companies regarding these matters.

Availability

As discussed in section 13.5, availability is deemed to be the biggest risk facing the Avionics subsystem. As mentioned, there are alternatives selected in order to mitigate this risk.

Safety

The Safety risk posed by the Avionics to both the system and the operator is not deemed to be high. The low expected lifetime of the system at 20 missions means the risk of failure of one of the few non-redundant components is low and should be safe as long as the operator depowers the components before working on them.

13.8. Compliance Matrix

The compliance matrix of the avionics Subsystem is shown in Table 13.3, and the propulsion subsystem's total budget is shown in Table 13.4.

Table 13.3: Avionics System Compliance Matrix

Code	Comp.	Code	Comp.	Code	Comp.
REQ-AVI-01	G	REQ-AVI-02	G	REQ-AVI-03	G
REQ-AVI-03-01	G	REQ-AVI-03-02	G	REQ-AVI-03-03	G
REQ-AVI-03-04	G	REQ-AVI-03-05	G	REQ-AVI-03-06	G
REQ-AVI-03-07	G	REQ-AVI-03-08	G	REQ-AVI-03-09	G
REQ-AVI-03-10	G	REQ-AVI-03-11	G	REQ-AVI-04	G
REQ-AVI-05	G				

Table 13.4: Avionics System Component Overview

Type	Name	Weight (kg)	Volume (L)	Origin Country
GNSS receiver	Mosaic-G5 P3H	0.002	0.000	Belgium
Auto-Pilot	Veronte 1x	0.198	0.192	Spain
Visual Navigation System	VNS-01	0.148	0.008	Spain
Total	-	0.348	0.200	-

13.9. Recommendations

For future development of the Avionics subsystem, a more detailed analysis and trade-off study can be conducted on various components, evaluating their advantages and disadvantages once the exact system requirements become clearer. Enquiries should be sent to the selected companies to gather information on production capacity, bulk discounts, and pricing. The system should be designed to support the use of multiple options for each component, allowing for greater scalability and redundancy. Additionally, potential interoperability issues between the various components should be investigated to ensure seamless integration.

14. Recovery

In this chapter, the recovery method will be selected for SPARTA. Firstly, a functional analysis is performed in Section 14.1, followed by the requirements in Section 14.2. A trade-off is performed in Section 14.3. Next, sustainability, risk and RAMS analysis are performed in Sections 14.4, 14.5 and 14.6 respectively. Next a financial analysis is performed in Section 14.7, to get a first estimate of the costs of the recovery system. Finally, compliance with the requirements is checked in Section 14.8, after which recommendations are given in 14.9.

14.1. Functional Analysis

As the recovery is the final part of the active mission, its purpose is to get the system from being airborne to the ground. Below in Table 14.1, the functions of the communication system are addressed.

Table 14.1: Functions of the recovery system

Code	Description	Origin
FUN-REC-01	Navigate to recovery area	FUN-SYS-7.1
FUN-REC-02	Prepare net	FUN-SYS-7.2.1
FUN-REC-03	Line up for approach	FUN-SYS-7.2.4
FUN-REC-04	Bring the system to a stop	FUN-SYS-7.4.1
FUN-REC-05	Secure the system	FUN-SYS-7.4.2
FUN-REC-06	Await rescue	FUN-SYS-7.5.2

14.2. Requirement Analysis

The functions obtained and their corresponding requirements are listed in Table 14.2, as shown below.

Table 14.2: Communication system requirements

Code	Description	Origin
REQ-REC-01	The structure shall carry recovery loads.	REQ-SYS-53-10
REQ-REC-02	The UAS shall maintain structural integrity during flight.	REQ-SYS-53
REQ-REC-03	The structure shall not plastically deform when limit loads are applied	REQ-SYS-36-12
REQ-REC-04	The structure shall not rupture when ultimate loads are applied	REQ-SYS-36-13
REQ-REC-05	Safety factor shall be 1.3 for critical design areas	REQ-SYS-53-01
REQ-REC-06	The UAS shall withstand the loads during landing.	REQ-SYS-53-06
REQ-REC-07	The recovery system shall weigh less than 3 kg.	REQ-SYS-23
REQ-REC-08	The recovery system shall have a volume of less than 1.5L.	REQ-SYS-22

14.3. Trade-off

As many options are viable for recovery, this section highlights the most realistic ones and selects the method with the most potential.

14.3.1. Trade-off Criteria and Weights

Given the mission's requirement for a recovery system, SPARTA must decelerate from approximately stall speed to a complete stop. These deceleration forces are substantial, particularly at the operational speeds previously identified in Chapter 5. Accordingly, the airframe must be capable of withstanding the resulting structural loads, making recovery-induced loading a critical trade-off criterion. These loads directly influence the probability of structural damage, which in turn affects material consumption and increases system turnaround time due to necessary repairs or component replacements.

Furthermore, as established in the midterm report, internal volume is a limiting factor. Most of the internal space is allocated to battery systems, necessary for achieving the desired endurance [7]. As the design is still in the conceptual phase, there is some flexibility in sizing. However, the remaining available volume is limited and must be shared among all subsystems. Consequently, system compactness becomes a significant design criterion to ensure all components exist in harmony in SPARTA.

Risk is a critical consideration in system design, as early identification enables more effective mitigation strategies. In this context, the introduction of additional components is particularly relevant, as each new mechanism may contribute further risk. This criterion, therefore, assesses the number and nature of risks introduced by the recovery mechanism itself, acknowledging that mechanically complex systems inherently tend to carry higher risk profiles.

Moreover, the adoption of a more sophisticated empennage for improved UAS control introduces additional challenges for the control system. To manage overall system complexity, recovery methods that require lower precision are preferred. Such approaches reduce dependency on highly sensitive control inputs, allowing for a

more robust control system. This, in turn, helps with manufacturing tolerances and avoids the need for high-precision components or advanced control technologies, which are often costly.

The weighting of the trade-off criteria is established using the AHP through pairwise comparison. The results of this analysis are presented in Table 14.3. Due to the conceptual nature of the current design phase, all evaluations are qualitative; assigning precise quantitative values to each criterion would require detailed simulations and testing, which fall outside the scope of this study. Nevertheless, preliminary estimations are provided where feasible. For instance, an initial approximation of system size can be derived from literature-based sizing methods. However, for controllability, a reliable assessment depends on factors such as the UAS's approach speed and the dimensions of the recovery target, which are not yet fully defined at this stage.

Table 14.3: AHP pairwise comparison values and their resulting normalised weights for recovery trade-off

Criteria	Loads	Size	Complexity	Control	Total Weight	Normalised Weight
Loads	1	0.5	4	3	8.5	0.34
Size	2	1	6	1.5	10.5	0.42
Complexity	0.25	0.17	1	0.5	1.92	0.08
Control	0.33	0.67	2	1	4	0.16

14.3.2. Recovery Options

To analyse the most feasible recovery system, several options need to be analysed. For this, the different designs that will be taken into account are: landing gear, parachute, net catch, wire catch and belly landing.

The landing gear is a conventional method widely used in aviation. It is a mature technology with high attributability, as it can absorb significant landing forces [46]. However, landing gear occupies valuable internal space, which may be a constraint for SPARTA due to its limited internal volume.

A parachute system can safely decelerate the UAS without requiring additional infrastructure, allowing for recovery in diverse terrains. The most optimal deployment occurs from the front or rear of the airframe. However, it also presents sizing problems, given that most of the size is already taken up by the other subsystems. Additionally, a deployment mechanism must be developed to ensure that the parachute avoids interference with the propeller system¹.

The net catch uses an external net to bring the UAS to a stop. It requires a ground-based recovery team to set up the system beforehand. The main benefit is the elimination of internal components within SPARTA for the recovery, conserving internal space. Moreover, net-based recovery does not require a runway, increasing operational flexibility. However, it imposes substantial loads on the wings during impact, demanding robust structural reinforcement [46].

Similar to the net catch system, the wire catch method requires SPARTA to collide with a single wire, demanding high-precision flight control [46]. The system must include a dedicated mechanism for housing and deploying the wire, increasing mechanical and control system complexity. The advantage lies in reduced structural loads during impact, as the wire catch induces its loads on the already strong fuselage, compared to the long, slender wings.

Finally, the last method that will be considered is the belly landing. In a belly landing, the aircraft lands without landing gear. Unlike traditional landings where wheels absorb impact, the aircraft's structure must bear the impact forces. This requires reinforcement of the airframe's lower surfaces and typically results in abrasions or structural damage, especially at the front. This method demands very low landing speeds and generally results in longer turnaround times due to necessary repairs². Additionally, due to the inverted tail and propeller, SPARTA will make first contact on its tail and propeller. Further increasing turnaround times.

¹URL: <https://chutes.nl/ed1-tech/descent/parachutes.html> [cited 12 June 2025]

²URL: <https://pilotinstitute.com/belly-landing/> [cited 12 June 2025]

14.3.3. Trade-Off Results

The outcomes of the trade-off analysis are presented in Table 14.4. Based on this analysis, the net catch configuration was selected due to its advantageous size and complexity. A sensitivity study was conducted, confirming that this design outperforms the alternatives in 97% of the evaluated scenarios.

Table 14.4: Completed trade-off table. Criteria are given in the top row, and design options are in the first column. The actual values for the parameters are given. The colour is related to the number of points. The white circles, top right of the coloured cell, indicate the colour; G for green, B for blue, Y for yellow and R for red.

	Loads	Size	Complexity	Control	Score
Weight	34%	42%	8%	16%	100%
Landing Gear	0.66 (B)	0 (R)	0.33 (Y)	0.66 (B)	0.36
Parachute	0.33 (Y)	0.33 (Y)	0.33 (Y)	1.00 (G)	0.44
Net Catch	0.33 (Y)	1.00 (G)	1.00 (G)	0.33 (Y)	0.67
Wire Catch	0.66 (B)	0.66 (B)	0.66 (B)	0 (R)	0.56
Belly landing	0 (R)	1.00 (G)	1.00 (G)	0.66 (B)	0.61

14.4. Sustainability & Attritability

A key attribute of the recovery system is its emphasis on attritability. The net serves to reduce the damage sustained by the UAV during recovery, thereby preserving its operational integrity. Unlike recovery methods that rely on complex onboard recovery mechanisms, this approach minimises the number of internal components required for the recovery process.

Furthermore, the passive nature of the recovery method supports flexibility in mission planning. It opens up the possibility for drone interception scenarios where the recovery platform gets carried by separate drones. This additional method increases the options for recovery, therefore leading to a decrease in reliance on a single system being operational.

14.5. Risk Analysis

The net capture system, while offering a practical and compact method of UAV recovery, is not without risks of its own.

RSK-REC-01: Unforeseen motion on landing

A primary concern is the unpredictable behaviour of the UAV upon impact. The aircraft could twist or rotate in unforeseen ways, resulting in deviations from the intended flight path. This causes a redistribution of the force, from an expected frontal load to unexpected upward or downward components, that complicates the structural load predictions. To account for these uncertainties, the structural design includes an additional conservative safety margin to accommodate for variations in force direction and magnitude.

RSK-REC-02: Failure of net

Such failure may result from user error during setup or from undetected wear and tear after repeated use. The first issue can be mitigated by implementing a standardised checklist to ensure correct deployment procedures. The latter presents an additional challenge. Frequent inspections or replacements of the net components are necessary to ensure safety, but these increase operational costs and jeopardise the system's intended affordability and attritability.

RSK-REC-03: Recovery impossible

Another identified risk is the inability of the UAV to reach the designated recovery location, often due to a malfunction in the control system. In such cases, a contingency plan is required. If the UAV cannot complete its programmed approach to the net, a belly landing will be executed as an alternative recovery method.

14.6. RAMS Analysis

This section discusses the RAMS characteristics of the recovery system.

Reliability

The reliability of the recovery system is significantly influenced by the performance of the UAV's control system. The system must support not only autonomous functionality but also manual control by ground personnel when within range. This redundancy increases the reliability of the recovery operation.

Availability

The availability of the net may be constrained due to its large structure, which is necessary to ensure the retrieval of the drone. This can be worked around by utilising the drone's extended range and manoeuvring to a region where the net is available. Furthermore, deploying multiple smaller nets in series can enhance deceleration, improving the overall success rate of the capture process.

Maintainability

Maintenance of the recovery system involves routine inspection and handling of the net. In addition, the UAS itself has to be serviced to return to its retracted state. As noted in Section 14.5, any damage incurred during the mission must be identified and remedied. Having a replacement tube available, together with all components being designed for manual handling, helps the turnaround time. Consequently, field personnel can perform recovery and maintenance without the need for complex tools or equipment, assuming the mission proceeds without major complications.

Safety

The safety of the system also needs to consider that of the ground team. For this, the net can be set up during a time that is safe for the ground team and the same for the recovery of the drone itself. Now, for the safety of the drone itself, the net will enable the drone to use a long distance to slow down. Also as a net can be set up anywhere, also in a forest has the possibility to be connected to trees to use as setup poles.

14.7. Financial Analysis

This section aims to provide insight into the costs of the recovery system. Here, the main cost that will be considered is that of the net itself; for this, the costs will be split up over its mission. The net will last longer than the lifetime of SPARTA. Now the cost of fabricating a single net will amount to approximately €6,000³. This net will be used for multiple lifetimes of SPARTA. The net is able to perform about 100 cycles before replacement has to take place. Therefore, the cost per unit comes down to €1,000. Now in addition, there are also labour costs associated with setting up the net, these are shown in more detail in Section 18.1.

14.8. Compliance Matrix

For the requirements presented in Section 14.2, it shall be confirmed that with the methods used, they are all met. This is visualised in Table 14.5.

Table 14.5: Requirement compliance matrix for the airfoil selection

Code	Compliance	Code	Compliance
REQ-REC-01	G	REQ-REC-05	G
REQ-REC-02	G	REQ-REC-06	G
REQ-REC-03	G	REQ-REC-07	G
REQ-REC-04	G		

14.9. Recommendations

For future development of the recovery, it can be looked into using energy methods to estimate the impact energy and determine the loads on the structure with those methods. Furthermore, it could be looked into including the fuselage forces in the updated internal force diagrams as the fuselage will experience more forces from the net. If time allows there can also be investigated different types of net systems to extend the distance that SPARTA can travel before coming to a standstill. In addition, there can be a look into using air intercept or using a net gun

³URL: <https://www.embention.com/drones-unmanned-vehicles/drone-recovery-net/> [cited 14 June 2025]

for feasibility. Finally, a dynamic analysis can be conducted, simulating the impact on the net and the change of forces over time. This will provide additional insight into the impact.

15. System Overview

This chapter aims to look at the SPARTA system as a whole and evaluate how design decisions made throughout the subsystem design Chapters 7-14. Section 15.1 presents the internal architecture. Section 15.2 discusses resource allocation after the end of this design phase. Followed by Sections 15.3 and 15.4 which evaluate the system's signature and stability. Then Section 15.5 performs a variety of sensitivity analyses on the design. Section 15.6 discusses the impact of the decisions made during this design phase on the performance. Finally, Section 15.7 outlines the verification coverage of the utilised models.

15.1. Architecture

The aim of this section is to describe the internal architecture of the SPARTA system. This is done by presenting the hardware diagrams in Subsection 15.1.1 and electrical diagrams in Section 15.1.2.

15.1.1. Hardware Architecture

This section presents the internal layout of the SPARTA system in the form of a hardware diagram in Figure 15.1 and in the form of internal layout diagram in Figure 15.2. The hardware diagram shows all the electrical wiring, data cabling and ropes.

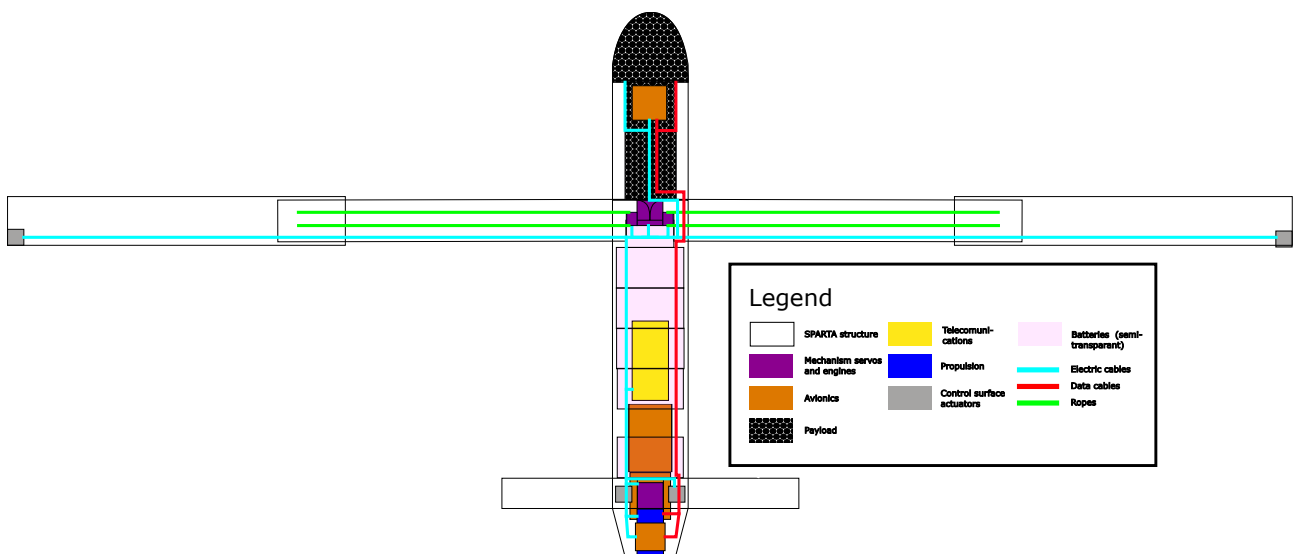


Figure 15.1: The hardware diagram of the system

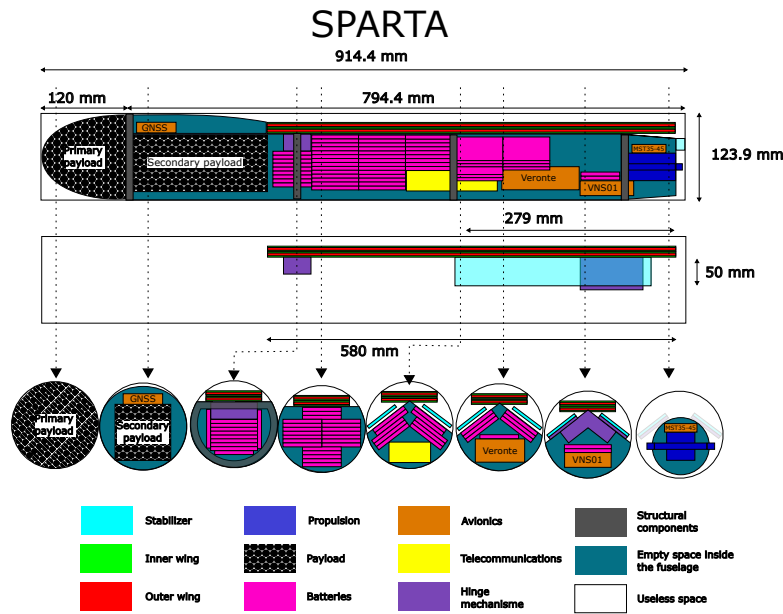


Figure 15.2: The internal layout of the system

15.1.2. Electrical architecture

In this section, a description of the electrical architecture is provided. First, to establish the total power required by all the various components, a table is produced. This table can be seen in Table 15.1.

Table 15.1: Power Requirements for Key Components

Component Name	Power [W]	Voltage [V]	Current [A]	Source	Special Notes
Wing rotation mechanism	4.2	4.2	1.00	Chapter 10	ESC required, operates once
Telescopic mechanism x4	16.0	4.2	1.00	Chapter 10	ESC required, operates once
Tail rotation mechanism	4.2	4.2	1.00	Chapter 10	ESC required
Aileron control mechanism 2x	7.72	4.2	0.80	Chapter 10	ESC required
Ruddervator control mechanism 2x	13.44	8.4	0.80	Chapter 10	ESC required
Veronte autopilot	15.0	15.0	1.00	Chapter 13	-
Visual navigation system	5.0	15.0	0.333	Chapter 13	-
Telecommunications	19	1.27	15.0	Chapter 12	-
Orbit 1 Engine	262.63	50.0	5.25	Chapter 13	ESC
Payload	15.0	15.0	1.00	[7]	-
Total Power	342.55				
Peak Power	362.77				

The design assumes that unfolding actuators draw power only during their active unfolding phase, while control mechanisms consume negligible or no power during standard operation. All other components are presumed to draw their maximum rated power continuously, except for the engine, which is the primary and constant power consumer. This simplification is considered reasonable because, in practice, it is unlikely that all secondary components will simultaneously operate at peak power.

To manage power more efficiently, the electrical system is divided into two distinct buses. A high-power bus dedicated solely to the engine, which is the dominant power consumer and a low-power bus which services all other components, which are further subdivided across three different voltage levels depending on their operational requirements. Two Direct Converters (DC) are implemented within the low-power bus to step down the battery voltage to the appropriate levels for each group of components. This ensures optimal voltage matching and minimises conversion losses across the system.

Electronic Speed Controllers (ESCs) are required for both the engine and all actuators to regulate their power and speed accurately. These controllers are critical for ensuring smooth operation and protecting sensitive subsystems from overload or abrupt current surges. Power Isolation and Protection Systems (PIPS) are installed on each set of battery packs, as well as on the VNS, telecommunications unit, and payload systems. These are selected due to their natural redundancy; a short out in one of these systems will not bring the whole system down, so isolation makes the system safer.

The BASQUEVOLT batteries are organised in six packs; four of 20 cells and two of six cells. This is done to ensure the correct voltage and current can be delivered. All battery packs are equipped with temperature sensors. These sensors continuously monitor the thermal condition of each battery to prevent thermal runaway and detect early signs of failure. In the event of an emergency, the pack can be disconnected using the PIPS. The electrical diagram can be seen in Figure 15.3.

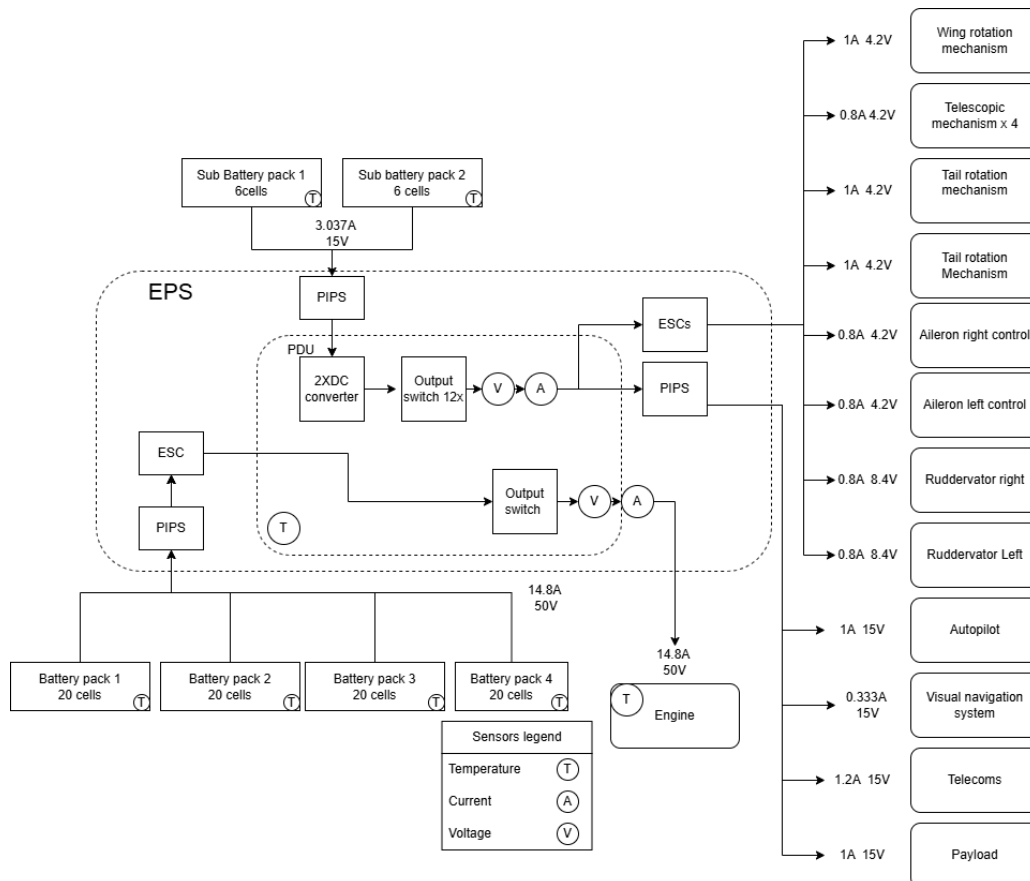


Figure 15.3: Complete electrical diagram of SPARTA

15.2. Resource Allocation

During the Baseline phase [6], contingency management and resource allocation were visited for the first time. The volume, mass and power budgets were established along with the contingencies for each design phase. Below, one can find the budget breakdowns for the volume, mass and power. The preliminary values from the Midterm Report [7] are reported along with the values obtained through analysis in this report, design values, and the final values with contingencies.

Volume

The final internal layout is presented in Subsection 15.1.1. For this configuration, the volume allocation budgets are presented in Table 15.2. It can be seen that the system shrank as contingencies were reduced and the definition increased. The only subsystems that increased in volume are all structural components, the wing, mechanisms and fuselage, but considering the decreases in other subsystems, this is considered an acceptable trade.

Table 15.2: Volume Resource Allocation

Budget	Preliminary Value [L]	Design Value [L]	Contingency [%]	Final Value [L]
Wing	0.81	0.84	2	0.86
Tail	0.33	0.17	5	0.18
Battery	2.54	2.05	5	2.54
Fuselage Structure	0.46	0.47	5	0.49
Propulsion	0.83	0.12	10	0.14
Wing Mechanisms	0.06	0.18	5	0.19
Payload	2.86	2.86	0	2.86
Telecommunication	0.56	0.27	3	0.28
Avionics	0.36	0.20	3	0.21
Useless	0.34	0.4	5	0.42
Leftover	1.86			2.54

Mass

The mass budget breakdown is in Table 15.3. The overall mass has decreased through the design work of this report. The most significant weight decrease occurred in the wing structure, which was originally likely overestimated by the use of a Class II weight estimation method intended for UAVs of much larger dimensions. The only subsystem that has increased in weight is the avionics subsystem due to a wider range of necessary instruments being needed.

Table 15.3: Mass Resource Allocation

Budget	Preliminary Value [kg]	Design Value [kg]	Contingency [%]	Final Value [kg]
Wing	1.56	0.88	10	0.97
Tail ¹	0.80	0.67	10	0.74
Battery	4.14	3.76	10	4.14
Fuselage Structure	1.39	1.08	10	1.19
Propulsion	0.51	0.43	10	0.47
Wing Mechanisms	1.00	0.88	5	0.92
Payload	3.50	3.50	0	3.50
Telecommunication	0.45	0.29	5	0.30
Avionics	0.35	0.35	5	0.37
Other	0.6	0.5	5	0.53
Total	14.29			13.12

Power

In the original estimations, the power budget did not account for mechanisms or telecommunications at all and instead presented a single avionics budget. By choosing exact components in Chapters 11, 12, and 13, a new power draw is established and presented in Table 15.4. It can be seen that the design stays well within budgets, with total power draw dropping lower and enabling the group to reassess the performance.

Table 15.4: Power resource allocation during cruise with contingency

Category	Preliminary Value [W]	Design Value [W]	Contingency [%]	Final Value [W]
Mechanisms	0	25.56	5	26.838
Telecommunications	0	19	5	19.95
Avionics	50	20	5	21
Engine	319.10	262.63	5	275.76
Total	369.10			342.55

¹Including its mechanism

15.3. Signature Assessment

The ability of SPARTA to remain undetected during operation is crucial for mission success. For SPARTA, minimising its detectability across multiple sensor domains is essential for both survivability and operational effectiveness. This chapter presents a preliminary assessment of SPARTA's signature in three primary domains: radar, acoustic, and infrared.

15.3.1. Radar Signature

Radar Cross Section (RCS) is a key performance parameter when assessing the radar signature of airborne systems. It quantifies how detectable an object is by radar and is expressed in square meters. It represents the area that would scatter radar energy back to the source as if the object were a perfectly reflective sphere. This subsection focuses on providing a first-order estimate of the RCS for SPARTA in cruise configuration. The estimation relies on analytical expressions derived from electromagnetic scattering theory.

Knott et al. established seven main mechanisms of scattering mechanisms that usually make up the net scattering from a target [47]. For this estimation, the two most important and applicable factors are taken into account. These are:

- "Specular scattering from planar, singly curved, and doubly curved surfaces when their surface normals point back toward the radar (for backscatter); the specular mechanism is the bright flash return"
- "Multiple bounce dihedral or trihedral corner reflectors with only a few bounces or cavity-like returns with many bounces"

For the RCS estimation, the specular scattering from planar, singly curved and doubly curved surfaces is considered. It is important to note that specular scattering methods become invalid when the target size is approximately equal to the wavelength of the radar signal. Also, the chosen configuration of an inverted V-tail gives a dihedral reflection contribution of this part. Although the tail is at a 105° angle and not on a right angle, this still gives a significant contribution to the RCS of SPARTA. Therefore, the tail configuration is assumed to be a dihedral structure in the RSC estimations.

Specular backscatter ($\sigma_{specular}$) occurs when the surface normal points back toward the radar. The magnitude is due to that region or area of the surface for which the surface currents add in phase to create the scattered EM field:

$$\sigma_{specular} = 4\pi \frac{(A_{effective})^2}{\lambda^2} \quad (15.1)$$

Here, λ is the wavelength. To estimate the effective specular area for a curved surface, the area where the phase varies by no more than $\frac{\lambda}{12}$ is considered. Where λ is the wavelength of the radar signal that is used to detect SPARTA. Using this, the following equations were derived by Knott et al. [47].

For a cylinder, with cross section A , length L , and with $A \gg \lambda$, we have:

$$A_{effective} = \sqrt{\frac{A\lambda}{2}} L \quad (15.2)$$

For a flat plate, with length a and width b , the effective area is equal to the physical area:

$$A_{effective} = A_{physical} = ab \quad (15.3)$$

To estimate the contribution of a dihedral structure, where a and b are the lengths of a single plate contributing to the dihedral, we use the following equation:

$$A_{effective} = 2(ab) \quad (15.4)$$

To estimate the radar cross section of SPARTA, the system in cruise configuration can be divided into three parts: a cylindrical fuselage, the main wings as flat plates, and the inverted V-tail as a dihedral structure. Hence, substituting the effective areas into Equation (15.1), radar cross sections for the different components can be estimated with the following equations:

$$\sigma_{\text{fuselage}} = 4\pi \frac{1}{\lambda^2} \left(\sqrt{\frac{R_{\text{fuselage}} \lambda}{2}} l_{\text{fuselage}} \right)^2 \quad (15.5)$$

$$\sigma_{\text{wing}} = 4\pi \frac{1}{\lambda^2} (MAC_{\text{wing}} b_{\text{wing}})^2 \quad (15.6)$$

$$\sigma_{\text{tail}} = 4\pi \frac{1}{\lambda^2} \left(2 \frac{b_{\text{tail}}}{2} MAC_{\text{tail}} \right)^2. \quad (15.7)$$

Assuming there is no radar interaction between the different components, the total specular radar cross section can be estimated for SPARTA in cruise configuration as the sum of the cross sections of the different parts:

$$\sigma_{\text{total}} = 4\pi \frac{1}{\lambda^2} \left[\left(\sqrt{\frac{R_{\text{fuselage}} \lambda}{2}} l_{\text{fuselage}} \right)^2 + (MAC_{\text{wing}} b_{\text{wing}})^2 + \left(2 \frac{b_{\text{tail}}}{2} MAC_{\text{tail}} \right)^2 \right]. \quad (15.8)$$

Considering that typical radar detection system radio frequencies are the S-, C-, and X-band. These are in the range of 2-12 GHz. [47, p. 27]. Using the geometric parameters as listed in Table 5.4, we can plot the RCS for different radar frequency bands. This is shown in Figure 15.4

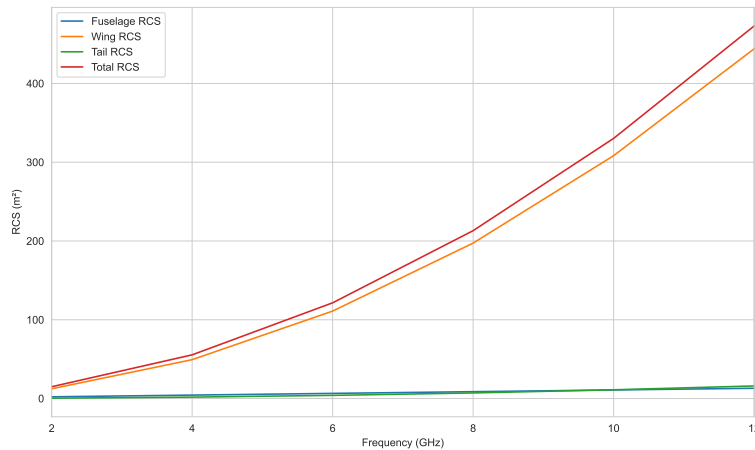


Figure 15.4: RCS for S-, C-, and X-band Frequencies

From Figure 15.4, it can be seen that the total RCS for a frequency from 2-12 GHz varies between 15 m² and 470 m². The values shown are a first-order estimate of the RCS by summing the cross sections of three primary components: the cylindrical fuselage, the flat-plate-like wings, and the dihedral tail structure. It assumes each contributes independently and that the radar illumination is oriented such that the incoming waves are normal to the reflecting surfaces, and reflected right back at the source.

As such, this estimation gives an upper-bound approximation for the worst case. In a realistic scenario, the wings will not reflect right back to the radar source as if it is attempted to detect SPARTA during approach, a more inclined view of all components will be reflected back to the radar detection station. Therefore, the actual radar cross section, especially of the wing, will be a lot lower in a practical scenario. However, Equation (15.1) provides an estimation of the maximum RCS during the operation of SPARTA and can be used in future design iterations to decrease the radar signature by evaluating the effect of geometry changes on the radar signature. Design considerations based on the results of the estimations are discussed in Subsection 15.3.4.

For more accurate RCS predictions in future design iterations, or for evaluation of radar cross sections at different angles of incidence, full-wave numerical methods such as Method of Moments, Physical Optics, or Finite-Difference Time-Domain could be employed [47]. In addition to that, radar sources can be detected and miti-

gated by doing measurements on prototype versions in the next phases of the project.

15.3.2. Noise Signature

A first-order estimation will be done of the noise levels of SPARTA. Primary noise sources include propeller, engine, and airframe noise. From these sources, the propeller will be the main contributor. This is because the relatively low cruise velocity drastically reduces airframe noise, and we are using an electric engine which typically has low noise levels [48]. Consequently, this preliminary assessment will concentrate on estimating the propeller's acoustic output to provide insight into SPARTA's noise footprint and its detectability in operational environments.

There are multiple factors that contribute to the noise produced by the propeller. They are divided into tonal or broadband noises. Tonal noises are noises on discrete frequencies and generated by the blade's periodic motion. Broadband noises are noises on a wider spectrum range. Tonal noises are the main contributors to the noise signature of UAV. Due to their generally higher signal-to-noise ratio, they can be noticed more easily than broadband noises, which tend to spread out and blend with background noises more quickly. In addition to that, for SPARTA, the intensity of tonal noises is higher than broadband noises. Tonal noises of a propeller are caused by thickness noise, which is the periodic displacement of air by blade volume [49].

So, to calculate the noise signature of SPARTA, we will assess the tonal noises caused by the thickness noise of the propeller. To estimate this, a semi-analytical model, developed by Gutin, can be used, which provides a suitable estimate of the total noise of the rotating propeller [49]:

$$p_m = \frac{169.3 mBRM_t}{SA} \left[\frac{0.76 P_h}{M_t^2} - T \cos \theta \right] J_{mB}(x) \quad (15.9)$$

Table ?? summarises the parameters, for which values were determined in the propulsion design in Chapter 11.

Symbol	Unit	Value	Description
p_m	dyne/cm ²	—	RMS sound pressure level
m	—	1	Harmonic order
B	—	2	Number of blades
R	ft	0.417	Propeller radius (5")
M_t	—	0.31	Tip Mach number
S	ft	3280	Distance from prop hub to observer (cruise altitude)
A	ft ²	0.546	Propeller disk area (πR^2)
P_h	hp	0.347	Absorbed power
T	lbf	1.16	Thrust
θ	°	90	Observer angle relative to prop axis
$J_{mB}(x)$	—	0.0467	Bessel function of order mB at argument x

Table 15.5: Definition of symbols, units, and example values for propeller noise estimate

To calculate $J_{mB}(x)$, the `scipy.special` library was used in python². Assuming the observer is located at a 90° angle from the propeller axis, and SPARTA is flying at its cruise altitude, the sound pressure level of the primary harmonic at the observer is 0.0031 dyne/cm², which corresponds to 43.86 dB. To verify these results, an alternative empirical equation from Simons and Snellen was used to evaluate the sound pressure level of the tonal propeller noise [48]. Using the same parameters, this equation gave a noise strength of 37.98 dB for a distance to the observer of the cruise altitude. To compare, this sound level of these results is approximately equal to a refrigerator hum or quiet office noises³. This would mean that, when flying at cruise altitude, SPARTA could only be detected by humans or microphones in extremely low-noise environments. Also, the location of

²URL: <https://docs.scipy.org/doc/scipy/reference/special.html>

³URL: <https://www.mdhearingaid.com/blog/decibel-chart> [cited 11 June 2025]

SPARTA can still not be detected. To detect directionality of acoustic noise sources, an acoustic array with beam forming algorithms must be used [50].

15.3.3. Infrared Signature

Another aspect of the signature assessment is the infrared signature. This includes the infrared power emission from various components of the UAV that may be detected by thermal imaging systems used on infrared-guided missiles. The primary source of heat in SPARTA consists of power losses in electric components. The relevant parameter to assess infrared detectability is the radiative contrast between the UAV surface and the ambient background, which can be expressed in terms of irradiance difference:

$$\Delta E = \frac{\varepsilon \sigma A \cos(\theta) (T^4 - T_{\text{env}}^4)}{r^2} \quad (15.10)$$

where ΔE is the excess irradiance above background (W/m^2), ε is the surface emissivity, σ is the Stefan–Boltzmann constant, A is the projected area presented to the sensor, θ is the angle between the surface normal and line of sight, T is the UAV surface temperature, T_{env} is the ambient temperature, and r is the distance to the sensor.

A detector requires a minimum contrast ΔE_{min} to register a target. This contrast threshold depends on the sensor sensitivity of the detection system. In many practical scenarios, differences in surface temperatures of more than 5–10 K are needed before a small UAV like SPARTA at its cruise altitude becomes readily detectable at operational ranges.

Electric propulsion and onboard electronics generate heat primarily through conduction to the airframe. Assuming that this heat is uniformly distributed, the steady-state skin temperature rise can be estimated from its internal heat dissipation:

$$Q_{\text{gen}} = P_{\text{in}}(1 - \eta), \quad T_{\text{skin}} \approx T_{\text{amb}} + \frac{Q_{\text{gen}} d}{kA} \quad (15.11)$$

where P_{in} is electrical input power, η is system efficiency, d is skin thickness, k is thermal conductivity, A is surface area, and T_{amb} is ambient temperature. To calculate the temperature difference, we have 37.5 Watts lost in the ESC and electric motor, a fuselage skin is made of Al7075-T6 and has a thickness of 1 mm, and an aluminium surface area of 0.2262 m^2 . Using Equation (15.11), the resulting skin temperature rise is 0.00128 K above ambient for SPARTA. Such small deltas produce a contrast ΔE well below sensor thresholds, especially at significant distances. For comparison, measurements conducted by Barela et al. reported a minimum Noise Equivalent Temperature Difference (NETD) of 0.00168 K for the most sensitive infrared camera, indicating the smallest detectable temperature difference. This means that no matter the distance, the cameras they tested would not be able to detect SPARTA [51].

To conclude, if heat is distributed over large areas, without producing localised hot spots or exhaust plumes, there is no infrared emission that would stand out in any detection or tracking systems. In practical situations, hot spots can not be avoided. However, the preliminary calculations performed in this section show that infrared emissions can be neglected if energy from hot spots are properly distributed over the fuselage.

15.3.4. Design Considerations

To reduce the radar cross-section of SPARTA, several design considerations regarding geometry, material choice, and communication systems should be incorporated in the next stage of the development process.

One critical factor is the avoidance of dihedral and trihedral structures, which are known to produce strong radar returns due to multiple internal reflections. These corner-like configurations act as efficient reflectors, directing radar energy back toward the source for all angles of incidence. To mitigate this, surfaces and mechanisms should be designed to prevent the formation of right-angled corners, and wherever possible, transitions between components should be smooth to scatter radar energy away from the incoming angle. Additionally, exposed cavities should be minimised, as these can resonate and create significant RCS spikes. Overall, a good design

philosophy is that the external shape of SPARTA should be designed to redirect incident radar waves away from their origin rather than reflecting them directly back. Such as designing a wing with a flat bottom, which is already taken into account for the airfoil trade-off performed in Chapter 6.

The materials used also play a role in minimising radar cross-section. Materials with low radar reflectivity, such as Radar-Absorbent Materials (RAM), can significantly reduce the amount of energy reflected back to a radar source by converting the energy to heat. When more sophisticated RCS estimation techniques are used or measurements have been performed on a prototype, RAM could provide solutions for regions of SPARTA that are identified as radar reflection sources.

To maintain stealth characteristics, the communication system should employ FHSS techniques. Frequency hopping involves rapidly switching the carrier frequency among many distinct channels in a pseudorandom sequence known to both transmitter and receiver. This approach reduces the probability of interception and detection by enemy radar. Since the transmission does not remain on a single frequency for long, it becomes more difficult for adversaries to detect and locate the signal.

15.4. Dynamic Stability Analysis

This section focuses on the analysis of the dynamic stability of the UAS in cruise conditions. Subsection 15.4.1 introduces the Equations of Motion (EoMs), which describe the UAS's motion numerically. Then, in Subsection 15.4.2, the eigenvalues obtained from EoMs are analysed to determine the UAS's dynamic stability.

15.4.1. Equations of Motion

An aircraft's motion can be described using EoMs. There are two sets: symmetric and asymmetric. The symmetric EoMs describe the aircraft's longitudinal dynamics, while the asymmetric EoMs describe the lateral dynamics. For a dynamic model, the EoMs must be converted to the state-space form. Using the steps described by Mulder et al. [28] (with the trim tab contribution omitted due to no trim tab in the UAS), both EoMs can be written in the form,

$$\mathbf{P}\dot{\mathbf{x}} = \mathbf{P}\frac{d\mathbf{x}}{dt} = \mathbf{Q}\mathbf{x} + \mathbf{R}u \quad (15.12)$$

with,

$$\mathbf{P} = \begin{bmatrix} -2\mu_c \frac{\bar{c}}{\bar{V}} & 0 & 0 & 0 \\ 0 & (C_{Z\dot{\alpha}} - 2\mu_c) \frac{\bar{c}}{\bar{V}} & 0 & 0 \\ 0 & 0 & -\frac{\bar{c}}{\bar{V}} & 0 \\ 0 & C_{m\dot{\alpha}} \frac{\bar{c}}{\bar{V}} & 0 & -2\mu_c K_Y^2 \frac{\bar{c}}{\bar{V}} \end{bmatrix}$$

$$\mathbf{Q} = \begin{bmatrix} -C_{X_u} & -C_{X_\alpha} & -C_{Z_0} & -C_{X_q} \\ -C_{Z_u} & -C_{Z_\alpha} & -C_{X_0} & -(C_{Z_q} + 2\mu_c) \\ 0 & 0 & 0 & -1 \\ -C_{m_u} & -C_{m_\alpha} & 0 & -C_{m_q} \end{bmatrix}$$

$$\mathbf{R} = \begin{bmatrix} -C_{X\delta_e} \\ -C_{Z\delta_e} \\ 0 \\ -C_{m\delta_e} \end{bmatrix}$$

for the symmetric case, and

$$\mathbf{P} = \begin{bmatrix} (C_{Y\dot{\beta}} - 2\mu_b) \frac{b}{\bar{V}} & 0 & 0 & 0 \\ 0 & -\frac{1}{2} \frac{b}{\bar{V}} & 0 & 0 \\ 0 & 0 & -4\mu_b K_X^2 \frac{b}{\bar{V}} & 4\mu_b K_{XZ} \frac{b}{\bar{V}} \\ C_{n\dot{\beta}} \frac{b}{\bar{V}} & 0 & 4\mu_b K_{XZ} \frac{b}{\bar{V}} & -4\mu_b K_Z^2 \frac{b}{\bar{V}} \end{bmatrix}$$

$$\mathbf{Q} = \begin{bmatrix} -C_{Y\beta} & -C_L & -C_{Yp} & -(C_{Yr} - 4\mu_b) \\ 0 & 0 & -1 & 0 \\ -C_{l\beta} & 0 & -C_{lp} & -C_{lr} \\ -C_{n\beta} & 0 & -C_{np} & -C_{nr} \end{bmatrix}$$

$$\mathbf{R} = \begin{bmatrix} -C_{Y\delta_a} & -C_{Y\delta_r} \\ 0 & 0 \\ -C_{l\delta_a} & -C_{l\delta_r} \\ -C_{n\delta_a} & -C_{n\delta_r} \end{bmatrix}$$

for the asymmetric case. Now, the final state-space form is defined as such,

$$\dot{\mathbf{x}} = \mathbf{P}^{-1}\mathbf{Q}\mathbf{x} + \mathbf{P}^{-1}\mathbf{R}\mathbf{u} = \mathbf{A}\mathbf{x} + \mathbf{B}\mathbf{u}, \tag{15.13}$$

which yields $\mathbf{A} = \mathbf{P}^{-1}\mathbf{Q}$ and $\mathbf{B} = \mathbf{P}^{-1}\mathbf{R}$.

The variables used are listed in Table 15.6, with the stability and control derivatives defined as $C_{\text{force/moment}_{\text{parameter}}}$ (which indicates a "force/moment" derivative with respect to the "parameter") and listed in Tables 15.7 and 15.8.

Table 15.6: Variables for Equations of Motion (in order of appearance)

Variable	Description	Variable	Description
\mathbf{P} [-]	Descriptor matrix	$\dot{\beta}$ [rad/s]	Sideslip angle rate
$\dot{\mathbf{x}}$ [-]	Time derivative of the state vector	μ_b [-]	Non-dimensional mass
\mathbf{x} [-]	State vector	b [m]	Wing span
\mathbf{Q} [-]	State coefficient matrix	K_X^2 [-]	Non-dimensional product of inertia around x-axis
\mathbf{R} [-]	Input coefficient matrix	K_{XZ} [-]	Non-dimensional product of inertia around x- and z-axes
μ_c [-]	Non-dimensional mass	n [N/m]	Yawing moment
\bar{c} [m]	Mean aerodynamic chord	K_Z^2 [-]	Non-dimensional product of inertia around z-axis
V [m/s]	Velocity	β [rad]	Sideslip angle
Z [N]	Normal force	C_L [-]	Lift coefficient
m [N/m]	Pitching moment	p [rad/s]	Roll rate
$\dot{\alpha}$ [rad/s]	Angle of attack rate	r [rad/s]	Yaw rate
K_Y^2 [-]	Non-dimensional product of inertia around y-axis	l [N/m]	Rolling moment
X [N]	Axial force	δ_a [rad]	Deflection angle of the aileron
u [m/s]	Forward velocity	δ_r [rad]	Deflection angle of the rudder
α [rad]	Angle of attack	\mathbf{A} [-]	System matrix
q [rad/s]	Pitch rate	\mathbf{B} [-]	Input matrix
δ_e [rad]	Deflection angle of the elevator		
Y [N]	Side force		

Table 15.7: Stability and control derivatives - Symmetric Motions

Symbol	Value	Source
Stability derivatives		
C_{X_u}	-0.183	Etkin & Reid [52]
C_{Z_u}	-1.909	Etkin & Reid [52]
C_{m_u}	0.235	Etkin & Reid [52]
C_{X_α}	1.321	Etkin & Reid [52]
C_{Z_α}	-6.214	Etkin & Reid [52]
C_{m_α}	-1.146	XFLR5 simulation
$C_{Z_{\dot{\alpha}}}$	-1.906	Etkin & Reid [52]
$C_{m_{\dot{\alpha}}}$	-4.169	Etkin & Reid [52]
C_{X_q}	0.000	Cook [53]
C_{Z_q}	-0.759	Etkin & Reid [52]
C_{m_q}	-4.338	Etkin & Reid [52]
Control derivatives		
$C_{X_{\delta_e}}$	-0.023	XFLR5 simulation
$C_{Z_{\delta_e}}$	-0.573	XFLR5 simulation
$C_{m_{\delta_e}}$	-2.865	XFLR5 simulation

Table 15.8: Stability and control derivatives - Asymmetric Motions

Symbol	Value	Source
Stability derivatives		
C_{Y_β}	-0.321	XFLR5 simulation
C_{l_β}	-0.072	XFLR5 simulation
C_{n_β}	0.057	XFLR5 simulation
$C_{Y_{\dot{\beta}}}$	0.000	DATCOM method [54]
$C_{n_{\dot{\beta}}}$	0.000	DATCOM method [54]
C_{Y_p}	0.135	DATCOM method [54]
C_{l_p}	-1.121	DATCOM method [54]
C_{n_p}	-0.168	DATCOM method [54]
C_{Y_r}	0.579	DATCOM method [54]
C_{l_r}	0.018	DATCOM method [54]
C_{n_r}	-0.126	DATCOM method [54]
Control derivatives		
$C_{Y_{\delta_a}}$	-0.004	XFLR5 simulation
$C_{l_{\delta_a}}$	-0.322	XFLR5 simulation
$C_{n_{\delta_a}}$	0.001	XFLR5 simulation
$C_{Y_{\delta_r}}$	0.358	XFLR5 simulation
$C_{l_{\delta_r}}$	-0.069	XFLR5 simulation
$C_{n_{\delta_r}}$	-0.076	XFLR5 simulation

The derivatives shown in Tables 15.7 and 15.8 have a couple of different entries in the "Source" columns. The DATCOM method [54] is a method that, among other things, describes how to derive stability and control derivatives for an aircraft. It was the main method used; however, for some derivatives, it was not relevant for this UAS, and some derivatives were not covered at all. For those cases, other methods were used. Etkin & Reid [52] explain methods for some derivatives that are relevant in the case of this UAS. Cook [53] stated that C_{X_q} is negligibly small and can be assumed to be 0. The XFLR5 simulation was utilized for all possible derivatives, as it was more accurate than both the DATCOM method and Etkin & Reid. Since the DATCOM and Etkin & Reid methods are numerical and not case specific, and the XFLR5 simulation does not take into account the fuselage effects, it is recommended to use CFD with the UAS precisely modelled, or a set of wind tunnel experiments to attain accurate values for the derivatives.

15.4.2. Eigenvalue Analysis

Now that the EoMs are described and converted to the state-space form, the dynamic stability can be analysed. The eigenvalues of the **A** matrix, for both symmetric and asymmetric, are computed using the `numpy.linalg.eigvals()` function. The results are shown on a plot in Figure 15.5, with the values in Table 15.9.

Table 15.9: Eigenvalue analysis

No.	Eigenmode	Value	Damping Ratio	Stability
Symmetric modes				
1, 2	Short Period	$-0.9935 \pm 5.0013j$	0.195	Stable
3, 4	Phugoid	$-0.0014 \pm 0.4422j$	0.003	Stable
Asymmetric modes				
1, 2	Dutch Roll	$-0.8177 \pm 5.9788j$	0.136	Stable
3	A-periodic Roll	-105.382	-	Stable
4	Spiral	-0.0254	-	Stable

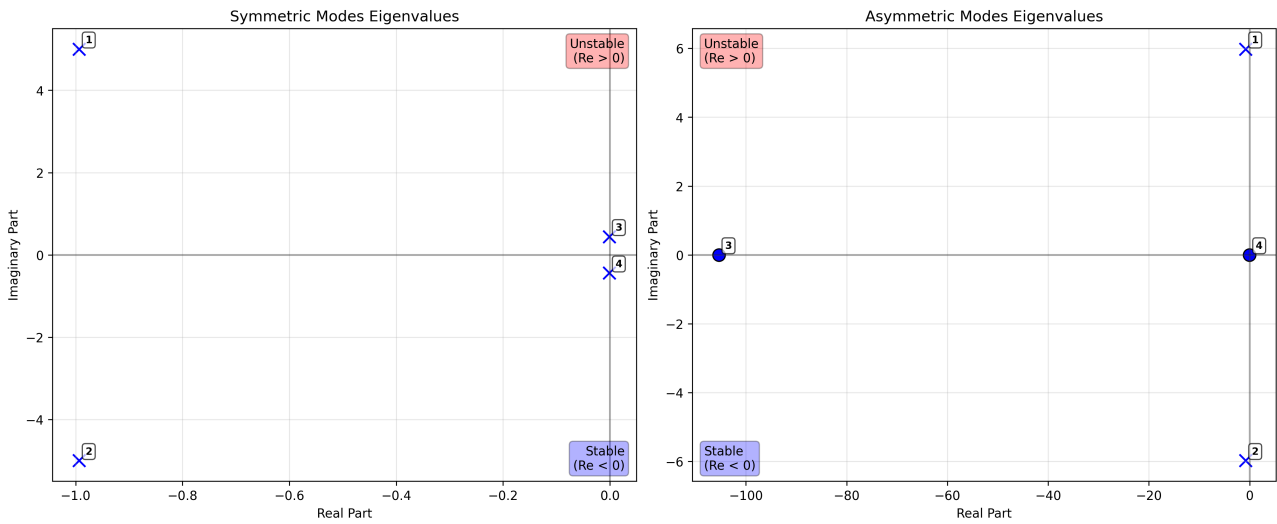


Figure 15.5: The location of the eigenvalues for the symmetric and asymmetric motions

After analysing the eigenvalues from Table 15.9 and Figure 15.5, it can be deduced that all modes are stable since the real part of each eigenvalue is negative. Furthermore, looking at the damping ratios for the damped eigenmodes, the short period and Dutch roll both have moderate damping ratios, which indicates a fairly quick convergence and moderate damping. Nevertheless, phugoid has a very low damping ratio, which implies that a lightly damped long-period oscillation occurs. Now, let’s take a look at the a-periodic roll and spiral modes. They have no imaginary part (no oscillation); however, the real part can still say a lot about the behaviour. In particular, a-periodic roll has a very large negative real part, which indicates a very fast and stable convergence. On the other hand, the spiral has a very small negative real part, which implies a very slow response. While this case is technically stable, it is so low that any modelling inaccuracies could make it marginally unstable in practice. This is expected and not problematic, as instability would imply a slow divergence that allows for easy responses to prevent deeper spirals.

15.5. Sensitivity Analysis

In this section, the analysis of the sensitivity of the UAS design to a change in major system parameters is shown. Namely, there are three changes: the battery used, the required endurance, and the secondary payload mass.

How these changes influenced the most relevant parameters is shown in the Tables 15.10, 15.11, and 15.12, respectively. In each table, the rows for which the initial parameters were changed are highlighted in yellow. Also, there are three cases for static stability: the most forward case (a case where secondary payload CG is in its most possible forward position), the general case (a case where secondary payload CG is at its centre, meaning no change in the design), and the most aft case (a case where secondary payload mass is set to 0 kg). These cases are also explained in Section 5.2. Furthermore, each table has a "Base Case" column, which shows the parameters for the design with no change. On the other hand, "Sensitive Case" columns differ throughout the tables. Namely, in Table 15.10, the "Sensitive Case" column shows parameters for the design with the changed battery. Next, in Table 15.11, "Sensitive Case 1" and "Sensitive Case 2" columns show parameters for the design with the required endurance of 4 hours and 6 hours, respectively. Lastly, in Table 15.12, "Sensitive Case 1" and "Sensitive Case 2" columns show parameters for the design with the secondary payload mass of 0 kg and 4 kg, respectively.

Table 15.10: Parameters for a battery change

Parameter	Base Case	Sensitive Case
ρ_m [Wh/kg]	450	196.8
ρ_V [Wh/L]	1000	437
v_{stall} [m/s]	31.02	34.43
v_{cruise} [m/s]	40.33	44.76
b_t [m]	0.56	0.60

Parameter	Base Case	Sensitive Case
m [kg]	14.29	17.59
R [km]	725.97	452.23
E [h]	5	2.81
P_r [W]	211	276.1
Static Stability		
Most forward case	Stable	Unstable
General case	Stable	Unstable
Most aft case	Stable	Unstable

Table 15.11: Parameters for a change in endurance

Parameter	Base Case	Sensitive Case 1	Sensitive Case 2
v_{stall} [m/s]	31.02	29.46	33.24
v_{cruise} [m/s]	40.33	38.30	43.21
b_t [m]	0.56	0.36	0.60
m [kg]	14.29	12.57	16.43
R [km]	725.97	551.51	933.36
E [h]	5	4	6
P_r [W]	211.0	176.8	252.6
Static Stability			
Most forward case	Stable	Stable	Stable
General case	Stable	Stable	Stable
Most aft case	Stable	Stable	Unstable

Table 15.12: Parameters for a change in secondary payload mass

Parameter	Base Case	Sensitive Case 1	Sensitive Case 2
v_{stall} [m/s]	31.02	26.26	35.55
v_{cruise} [m/s]	40.33	34.14	46.22
b_t [m]	0.56	0.28	0.60
m [kg]	14.29	9.90	18.73
$m_{\text{payload},2}$ [kg]	2	0	4
R [km]	725.97	614.5	831.92
E [h]	5	5	5
P_r [W]	211.0	130.9	299.1
Static Stability			
Most forward case	Stable	Stable	Stable
General case	Stable	Stable	Stable
Most aft case	Stable	Stable	Unstable

Now, to determine how sensitive the UAS design is, one should analyse whether the sensitive cases still meet the requirements. The case for a changed battery does not satisfy both requirements, **REQ-SYS-01** and **REQ-SYS-02**. The maximum achievable endurance of the battery is 2.807 hours, which is less than the required 5 hours. Additionally, the maximum range is 452.228 km, falling short of the required 500 km. Secondly, the case for a required endurance of 4 hours does not technically meet the **REQ-SYS-02** requirement; however, for this case, the requirement would be lowered to 4 hours. In such a case, it would meet all the other requirements. On the other hand, the case for a required endurance of 6 hours meets all requirements without any changes. Thirdly, the case for a secondary payload mass of 0 kg does not technically meet the **REQ-SYS-06** requirement; however, for this case, the requirement would be omitted. With that, it would meet all the remaining requirements. Lastly, the case for a secondary payload mass of 4 kg meets all requirements without any changes. It is important to note that there are no requirements regarding static stability; however, it is undesired since it would require more work from the pilot or the autonomous control software to maintain a stable flight.

15.6. Performance Changes

In the previous section, a new mass and power required is established. As concluded in Section 15.2, the system budgets have been met and more performance-favourable results obtained. Since the mass and power draw decreased in this stage, more performance can be obtained without modifying the design. This, in turn, means that to comply with requirements, the design can be further simplified in upcoming iterations. When using the new power draw, including contingency to calculate endurance, the total flight time comes to 5.43 hours.

The fact that the total weight of SPARTA has decreased means that endurance actually increases further, as the system's weight is directly tied to drag and, therefore, to the power required. With the new weight of 13.18 kg, and assuming the lift-to-drag ratio from Chapter 5 remains valid, the new power requirement, including consistency margins, is 322 W. This results in an endurance of 5.78 hours. A portion of the battery can therefore be removed, amounting to 0.558 kg. This reduction in mass causes a further decrease in power required and overall weight. The design can then be iterated, freeing up internal volume for a cleaner and more efficient configuration.

Table 15.13 shows the key parameters that changed after performing the iteration.

Table 15.13: Parameters obtained after new iteration

Parameter	Old Value	New Value
v_{stall} [m/s]	31.02	28.57
v_{cruise} [m/s]	40.33	37.14
b_t [m]	0.56	0.38
m [kg]	14.29	11.85
m_{batt} [kg]	4.14	2.99
R [km]	725.97	668.55
E [h]	5	5

15.7. Model Verification

All models used during this design project need to be verified before use. The models and other computer tools created by the group are first unit tested to ensure the correct functioning of individual components. The total coverage obtained is 86%. To ensure larger systems work as expected, a series of system tests is performed as well. These check the expected behaviour of systems and the physicality of models but comparing against laws of physics, hand calculations and available examples. They have been documented alongside the models in each of the design chapters.

16. Sustainability & Attritability

Natural resources are limited globally, but even more so in Europe. Therefore, they have to be used responsibly. To make the most of a given system, the resources used should be minimised. To make sustainability relevant in the military context, this system will be used and thus this section will focus on attritability.

16.1. Wing, Control Surfaces and Fuselage

The wing, control surfaces and the structural part of the fuselage will be made out of AL7075-T6, and aerodynamic fairings out of polycarbonate. The metal parts are planned to be made by extrusion and bending, with milling where unavoidable, and joined together by welding or with screws, while plastic will be injection moulded. The manufacturing is to be done in-house, with enough slack capacity to ramp up production if needed.

16.2. Mechanisms

The mechanisms that enable wing movement and actuate control surfaces come in three groups: the (metal) parts to be made in-house, generic parts to be bought off the shelf, and uncommon parts. Only a few parts (small servos) are in the uncommon category and should be stockpiled to avoid bottlenecks.

16.3. Avionics and Propulsion

This group represents the most complex parts, which will have to be sourced from other outside companies. Some of them, such as the trans-receiver, are made by a single company in Europe. This could represent a bottleneck in the manufacturing process. Therefore, it would be recommended to stockpile the parts in case of shortage.

All of the parts, with the exception of the battery, are designed to withstand way more than the 20 required missions, and thus can be fully reused in case of system retirement after the minimum number of required missions. The battery is singled out because it has considerable degradation with each cycle, and is expected to be the first to be replaced.

16.4. Flight Environment

As the attritability inherently relies on the response of the enemy, there is a need to revisit where the system is most likely to fly.

SPARTA has a communication range of at least 100 km and a range of more than 700 km. This makes it most suited for calling artillery fire and enabling deep strikes. Taking the Ukraine war as an example, most of the air defence is concentrated within a 20 km zone around the frontline¹. Additionally, the air defence usually consists of Surface to Air Missiles (SAM), Short Range Air Defence (SHORAD), Electric Warfare (EW), small arms fire and drone hunters.

SAM missiles cost in the range of millions, SHORAD missiles' cost is in the €100k range, with the cannon costing around €560 per round², and drone hunters entail either a man in a "crop duster" with a shotgun or a dedicated UAV system. Of those, EW is countered by the autonomous capability of SPARTA, and small arms are not an issue as our operational height is 1000 m (See Chapter 4)

The main dangers with negative value trade are the drone hunters, SHORAD cannons and missiles. It is assumed that a SHORAD cannon takes €22,400 (40 rounds with €560 each), a SHORAD missile €80,000, and the drone hunters cost €5,000. Additionally, the ratio of the systems varies wildly based on the theatre in which the system will be deployed and the object it is observing.

Unfortunately, the casualty rate of specific types of drones is closely guarded information among militaries, . To make the LCA possible, the cannon is assumed to be the cause of death 60% of the time, a missile 10% and hunters the remaining 30%. It is expected that the system, on average, will survive 15 missions before being shot down, comparing it to a similar system used in Ukraine war³

16.5. Operations

The operations induce more cost, beyond the initial investment, but they also return value in the form of intelligence. The ground segment requires at least one operator to monitor the video feed and the equipment to monitor the drone. Assuming they will monitor at least 3 drones on average and that a salary plus monitoring system would cost €120 per hour for 5 hours of operational time, per mission operational cost per drone is €200. According to Subsection 18.1.3, O&R cost is €675, therefore recovery costs €475. The maintenance also includes the cost of the drone is shot down. The cost of maintenance per mission becomes:

$$\text{COST} = \frac{14}{15} \cdot 475 + \frac{1}{15} \cdot 150,000 = \text{€}10,400 \quad (16.1)$$

16.6. Social Sustainability

When developing a dual-use UAV such as SPARTA, it is crucial to address ethical considerations and social sustainability. Although SPARTA is not designed to directly cause harm, its capabilities, such as locating or laser-

¹URL:<https://press.armywarcollege.edu/cgi/viewcontent.cgi?article=3257&context=parameters> [cited 18 June 2025]

²URL: <https://www.grosswald.org/germany-35mm-cram/> [cited 18 June 2025]

³URL: <https://kyivindependent.com/opinion-a-look-at-the-drone-arsenal-russia-uses-against-ukraine/> [Cited on 22 June, 2025]

designating targets, necessitate a clear framework of accountability. Ensuring that a human operator remains in the decision-making loop is vital to maintaining ethical oversight, particularly in high-risk scenarios. Moreover, robust export controls should be established to prevent the system from being acquired by actors who do not adhere to the ethical standards upheld by the European Union⁴. Importantly, SPARTA also offers significant potential for civilian use, including scientific research, humanitarian assistance, and disaster response, thereby contributing positively to society.

16.7. Life Cycle Assessment

The Life Cycle Assessment (LCA) will be value-based, measured in euros. The LCA assumes 20 missions. Manufacturing is based on the shelf price, logistics consist of transport and storage cost, operation includes the supporting infrastructure cost and the value extracted from the ISTAR data, and retirement considers what can be recovered from the loss. For the last part, considering the dangerous environment the system will fly in, retirement was assumed to mean being taken down by the enemy.

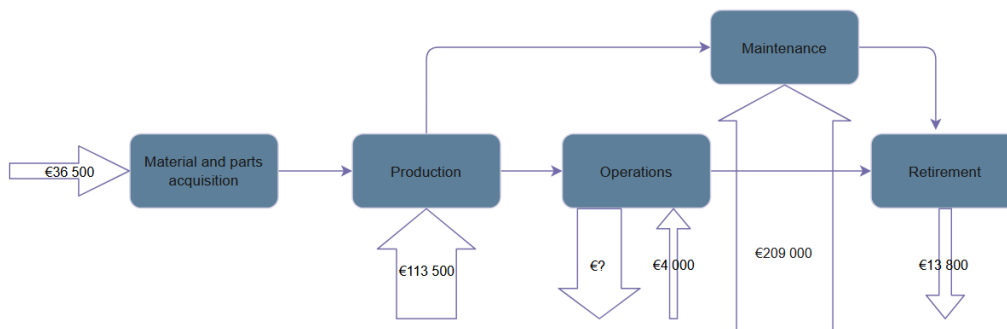


Figure 16.1: The life cycle assessment based on the product cost

In Figure 16.1, showing the LCA, the arrows that go inward symbolise cost, and arrows outward show value extracted. The value of the ISTAR data is fully based on the mission profile of a given operation. Although considering the other costs, it could be tuned to provide maximum value per Euro invested. To break even one would need to gain €8,000 worth of information per mission.

17. Risk Analysis

This chapter presents the risks associated with UAS design at the system level, which is divided into development and operational ones. The subsystem risks are treated in their respective chapter, so they are not included in this chapter. Firstly, the system risks are identified and split between the development and operational risks, in Section 17.1. Then the established risks are assessed in Section 17.2 and mitigated in Section 17.3.

17.1. System Risks

The development of complex systems is inherently subject to a range of technical, logistical, and operational uncertainties. This section identifies and evaluates potential risk events that could impact the progress, cost, or success of the project. Table 17.1 lists the development risks identified for this project. In Section 17.2, the likelihoods and severities of the development risks are assessed.

Table 17.1: Identified development risk events

ID	Risk Event
RSK-DEV-01	Overly ambitious requirements.
RSK-DEV-02	Invalid assumptions are used in the design process.
RSK-DEV-03	Licences to essential software revoked or expired.
RSK-DEV-04	Parts can not be properly integrated in the tube.

⁴URL: https://www.eeas.europa.eu/_en [cited 20 June 2025]

RSK-DEV-05	Prototype assembly errors occur.
RSK-DEV-06	Unavailability of testing facilities.
RSK-DEV-07	Aerodynamic performance overestimated.
RSK-DEV-08	Unexpected certification delays occur.
RSK-DEV-09	Delays or discontinuation in supply of key components.
RSK-DEV-10	Accidents causing injuries to manufacturing operators.
RSK-DEV-11	The main client cancels the planned purchases.

The system that is being designed has multiple subsystems and components performing functions that have been defined in the Chapter 2. However, each function has a risk of failure, which endangers the completion of the mission or significantly impacts performance. Most of the risks that can be derived from the functional analysis are on the subsystem level and are thus treated in their respective chapter. For each risk event, the severity and likelihood must be assessed. In Section 17.2, the likelihoods and severities of the development risks are assessed.

Table 17.2: Identified operational risks

ID	Risk Event
RSK-OPS-01	The UAS is detected and shot down by the enemy.
RSK-OPS-02	Due to slow reaction time, the UAS crashes into an obstacle.
RSK-OPS-03	The UAS enters a spin manoeuvre.

17.2. Risk Assessment

The scoring criteria of the likelihood and severity are shown in Figure 17.3 and 17.4, respectively. To visualise their scores, all risks are placed on a risk map, as shown in Figure 17.1. Here, green boxes resemble acceptable risks, orange boxes show critical risks, and red boxes show unacceptable risks for the design. It was decided that risks that have a likelihood of 3 or higher in combination with a severity of 3 or higher are considered unacceptable and require effort to be mitigated. Risks are listed in the boxes, where risks listed in bold letters are different for different designs.

Table 17.3: Likelihood of risks

Likelihood	Score	Probability Range
Rare	1	Less than once per 1000 projects/missions
Unlikely	2	Less than once per 100 projects/missions
Moderate	3	Less than once per 10 projects/missions
Likely	4	Once per project/mission
Almost certain	5	Multiple times per project/mission

Table 17.4: Severity of risks

Severity	Score	Description
Negligible	1	Barely impacts the project/mission.
Marginal	2	Manageable impact on the project/mission.
Critical	3	Significant impact on the project/mission.
Catastrophic	4	Failure of the project/mission.

		Likelihood				
		1	2	3	4	5
Severity	4	DEV-10	DEV-07	DEV-11 OPS-01 OPS-02		
	3		DEV-04	OPS-03		
	2		DEV-08 DEV-09	DEV-01 DEV-02 DEV-03 DEV-06	DEV-05	
	1					

Figure 17.1: The system level risk map

17.3. Risk Mitigation

The unacceptable risks need to be mitigated in order to design a product without any unacceptable risks. Therefore, in this risk mitigation section, we will assess all development and operational risks that were assessed to be unacceptable. The mitigated system risks are shown in Figure 17.2.

DEV-11: The main client cancels the planned purchases.

To mitigate this risk, multiple aspects need to be considered. The likelihood of this event can be reduced by carefully managing the expectations of our clients, adjusting needs and requirements where necessary. In addition, to reduce the severity of this event, other clients and partners should be identified and contacted to establish a relationship. In this way, it is ensured that there are available alternative clients who would be willing to purchase the product, even if the main client is not interested anymore.

OPS-01: The UAS is detected and shot down by the enemy.

Since SPARTA is expected to operate in the enemy territory, it is susceptible to being shot down by advanced defence systems. Therefore, to prevent detection, the aircraft has to be built with stealth technology that minimises the chances of detection. SPARTA is restricted by mass and size, such that it is unlikely that it is feasible to equip the system with countermeasures such as flares. Consequently, if detected, the chances of being shot down are extremely high. If equipped with stealth technology, the likelihood of detection reduces.

OPS-02: Due to slow reaction time, the UAS crashes into an obstacle.

During the ISTAR mission or when avoiding detection, SPARTA needs to fly quite low, so it is crucial to ensure that it does not collide with the terrain. In order to do that, the system must be able to make rapid adjustments to its trajectory. One part of this is that it should detect the obstacles, but maybe a more important part is that these obstacles can be avoided. If the aircraft can avoid the obstacles with agile manoeuvres, the likelihood of collision is significantly reduced.

OPS-03: The UAS enters a spin manoeuvre.

The cruise speed for the designs is very close to their stall speed. Therefore, it could happen that SPARTA enters a spin manoeuvre by asymmetrically stalling the wings. To recover from a spin manoeuvre, a combination of rudder and elevator controls must be used to counteract the spin and to pitch down to stop the stall. So, to reduce the severity of the system being in a spin manoeuvre, the system must have enough pitch and rudder control to get out of it easily.

		Likelihood				
		1	2	3	4	5
Severity	4	DEV-10	DEV-07 OPS-01 OPS-02			
	3		DEV-04 DEV-11 OPS-03			
	2		DEV-08 DEV-09	DEV-01 DEV-02 DEV-03 DEV-06	DEV-05	
	1					

Figure 17.2: The system level mitigated risk map

18. Financial Analysis

This chapter aims to assess the overall profitability of the project by evaluating its cost structure and expected returns. The cost analysis (Section 18.1) is divided into three main categories: Research and Development (R&D) costs, which include activities such as detailed design, modelling, prototyping, and testing of the system; Production & Assembly costs, representing the expenses associated with manufacturing and assembling each unit; and Operational and Maintenance costs, which account for user expense during its deployment. Based on this cost breakdown, key financial indicators such as Return on Investment (ROI) are used to evaluate the project's business performance and potential (Section 18.2). In the end, a compliance matrix is provided (Section 18.3).

18.1. Cost Breakdown

This section explores the project's cost breakdown through three essential components: Non-Recurring Development Costs (Subsection 18.1.1), which will analyse the structuring of the budget for each of the project phases. Next, the Production and Assembly Costs (Subsection 18.1.2) will summarise the expenses associated with manufacturing and assembling the UAS. Finally, the Operations and Maintenance Costs will focus on the expenses related to the product's deployment and the ongoing support for the clients.

18.1.1. Non-Recurring Development Costs

Considering the **REQ-SYS-25** from Chapter 4 regarding the cost of UASs, it can be stated that it needs to cost approximately €300,000. The overall budget of this project is set at 300 million euros, including the production of the first 50 UASs. Based on these values, it can be estimated that the non-manufacturing budget requirement is 285 million euros. To account for any unforeseen costs, a contingency factor will be included in the project management & systems engineering part of the financial breakdown. This percentage is intended to help manage unexpected expenses. Project has a relatively high complexity as well as a large likelihood to underestimate the cost, therefore it has been decided that the contingency factor will be set at 10%, as recommended in this source¹. This budget can be divided into the following parts:

- **Conceptual design** This phase involves overall project planning, requirement analysis, as well as initial design. The cost for this phase will be estimated by calculating the total number of hours worked by the group, with an hourly rate of €150. Resulting in a total cost of €540,000.
- **Detailed design** Further design requires engineering drawings, subsystem integration, and detailed performance characteristics. This project plans to allocate almost 20% of the budget to cover the hiring and salaries of senior engineers, rental of a headquarters, and further development of this project into a fully operating and professional enterprise.

¹URL: <https://www.e-a-a.com/what-is-a-standard-percentage-for-contingency/> [cited 29 April 2025]

- **Prototyping** This phase will involve the fabrication of a model to evaluate its performance in real-world conditions. It can reveal design flaws, thus extending the implementation process. In such a case the it will lead to additional expenses related to redesigning. This stage will be assigned 20% of the total budget.
- **Testing & Validation** This section includes ground tests, flight tests, and deployment tests, which are especially important for this project. It also needs to meet rigorous and expensive military certification and reliability standards². This part will account for a total of 30% of the overall cost.
- **Tooling & Manufacturing** This element includes the investment in the production line and the necessary machinery. It will account for 10% of the total budget as suggested in the following source³.
- **Project management & Systems engineering** This has been identified as a critical part of the project since it addresses neglects and oversights. It will involve risk management, and integration between each phase, and will use the remaining 20% of the resources.

Table 18.1: Financial budget breakdown

Cost Category	% of Total	Budget
Conceptual Design	0.2%	€540,000
Detailed Design	19.8%	€56,460,000
Prototyping	20%	€57,000,000
Testing & Validation	30%	€85,500,000
Tooling & Manufacturing Setup	10%	€28,500,000
Project Management & Systems Engineering	20%	€57,000,000
Total	100%	€285,000,000

18.1.2. Production & Assembly

To assess the project's success in the market, an analysis of costs needs to be performed. Table 18.2 provides a preliminary cost breakdown of the product. This table is still in the early stages because many components have yet to be estimated, and in many cases, detailed pricing has not been provided by manufacturers. For example, in the case of telecommunications systems, or an engine that will be custom-made to meet the project's specific requirements, it is essential to obtain a quote from the sales team to determine an accurate price. Additionally, the chosen battery manufacturer has not yet produced the batteries, so a price for them is currently unavailable.

Since there are large uncertainties in the final price values, it was decided to incorporate the safety factors. First element to use this factor is an engine using a value of five. It was chosen based on the engineering judgement to reflect the need for a custom-made engine, which will probably significantly increase the cost. The base price was estimated using similar engines from this specific manufacturer. It is important to note that these prices are based on data from 2016, implying they may have changed considerably over the last nine years, which has also been accounted for when choosing an appropriate factor.

A similar factor of three has been applied for the batteries. As previously mentioned, since the batteries have not yet been produced, there is no price available. To estimate the cost, a comparable battery was selected. Given its lower performance, a factor of three was chosen to account for the expected higher price resulting from the more advanced technology that the selected manufacturer is going to provide.

When estimating the SPARTA price, one of the key factors was the estimation of labour hours for each employee. Due to the relatively small size of the team, it was assumed that the following specialists would be needed: two technicians, an electrical technician, a CNC specialist, a software engineer, a quality control inspector, and a logistics and support person. Additionally, an average pay rate of €50.00 per hour was chosen. Since there is not enough data to accurately estimate the time required to manufacture a UAS, a total of 250 hours for the entire team was used as an estimate. This value should be updated once more data becomes available to allow for a more precise estimation of the workforce needed.

²URL: https://militarysphere.com/uav-production-cost/#Testing_and_Quality_Assurance_Expenses [cited 29 April 2025]

³URL: <https://businessplan-templates.com/blogs/running-costs/uav-production> [cited 29 April 2025]

Price is a crucial factor in driving demand for the product and being competitive. An estimated price of around 55,000 euros provides a significant margin between the manufacturing cost and the requirement of 300,000 euros. Therefore, it was decided to further improve the product's appeal by decreasing its price.

As a result, it can be anticipated that the total return on investment will be lower. However, a reduced price may accelerate the process of establishing the company in the market and conquering the military drone sector. Therefore, the decision has been made to lower the price to 150,000 euros. This price point still allows for profit margins while enhancing competitiveness.

Table 18.2: Production and assembly cost breakdown table

Category	Cost in €
Propulsion	
Engine	1,088
Propellers	3
Batteries	13,050
Avionics	
Antenna	68
Autopilot	6,150
Telecommunications	20,000
Hinge Mechanisms	1,050
Materials	
Wing	4
Tail	3
Fuselage	12
Labour	12,500
Recovery	1,000
Total	€54,928

18.1.3. Operations & Maintenance

At this stage of the project, it is very difficult to estimate the Operational & Support costs. For an accurate values, certain parameters need to be known like: the lifespan of components, the failure rates of critical parts, the impact of the cold and hot environments, and the hourly rates for the technicians or operators performing maintenance. Additionally, the cost of the tube-launch system must be accounted for, as it can differ depending on whether it is a helicopter, aircraft, or ground-based system. Since this information is currently unavailable, this section will analyse available data on the maintenance and operational costs of similar military drones that are in use.

The analysis will begin by examining the relationship between Operations and Support (O&S) costs and the acquisition cost of the UAS. It can be estimated that the annual O&S costs would account for approximately 10% of the acquisition cost [55], resulting in an estimated value of around 15,000 euros per year based on the cost explained in Subsection 18.1.2.

The estimation of the average cost per mission requires a value for the number of missions being flown each year. This value will be based on the data from the most commonly used drone. Such an example is Reaper MQ-9, which typically flies an average of once to twice a week [56]. Since the Reaper drone is one of the most used drones by the military, a more conservative estimate for SPARTA will be used of two flights per month. This results in a total of 24 flights per year

With these values, the average cost per mission can be calculated to approximately 625 euros per flight. Having estimated this number, it can be concluded that the requirement **REQ-SYS-26** about the maximum maintenance cost per mission is met. It should be noted that this value does not account for variations in flight duration or the specific deployment conditions. Therefore, it should be treated as an initial approximation and should be further refined once more details are available.

18.2. Return of Investment

To estimate the potential return on investment, several market assumptions have been established. Key features, such as the tube-launch system and European-based manufacturing, further explained in Chapter 3, align with current geopolitical trends and the European ReArm project. Therefore, it is expected that most sales will occur within the European market. The product is not limited to Europe and is also expected that the project will gather attention in other regions. However, this financial analysis will only focus on the European market as it will be the dominating customer.

Based on these factors, it is estimated that over the next three years, the SPARTA project could capture approximately 3% of the European military drone market. It is expected that gaining this market share will not be

straightforward and constant, which is the reason why this projection will consider three years. The project is likely to yield low returns in the first year, followed by an increase in the second and third years as the company establishes its reputation and secures contracts. Therefore, a conservative average of 2% market share over these three years will be used. These figures will serve as indicators for assessing potential return on investment.

Based on the figures outlined in Chapter 3, the projected annual military drone market volume in Europe is approximately €45 billion, including up to €0.9 billion per year for the drone sector. This would account for a total of €2.7 billion over the three years. Given an initial cost of €150,000 per unit, this means a potential sales volume of approximately 18,000 units during that period.

Having the initial cost of an investment of 300 million euros, the cost of manufacturing outlined in Section 18.1 as well as an approximated number of units sold, a potential Return on Investment can be calculated using the following formula:




$$ROI = \frac{(\text{Profit per Unit} \cdot \text{Number of Units}) - \text{Total Investment}}{\text{Total Investment}} \cdot 100\% \quad (18.1)$$

Inputting all the values, the ROI is calculated to be 470%, which indicates a remarkably high return on the initial investment. For every €1 invested, the project is expected to generate €4.7 in profit. Such a substantial return strongly suggests that the venture has great potential for profitability. Additionally, this result should be viewed as a very positive indicator of the project's financial viability and a great opportunity for success.

18.3. Compliance Matrix

This section outlines compliance with financial budget limitations, shown in Table 18.3.

Table 18.3: Financial analysis compliance matrix

Code	Compliance
REQ-SYS-24	
REQ-SYS-25	
REQ-SYS-26	

19. Project Design and Development Logic

Ten weeks and 3600 man-hours of work are but a drop in the bucket in the grand scheme of getting an aerospace engineering system from the idea on the back of a napkin to a functioning and operating system that brings value to the world. This means that there are further years of work on a system that need to be planned and executed, from design work to decommissioning. This chapter aims to outline a definite plan for the rest of the SPARTA project. Sections 19.1-19.6 outline the six design stages of SPARTA, starting with the Design Synthesis and ending with Operations.

19.1. Stage I: Design Synthesis

Stage I of the project took place during the 2025 summer Design Synthesis Exercise over the period of 10 weeks and involved the vast majority of the commonly defined conceptual and preliminary phases of engineering design, with slight ventures into subsystem detailed design.

During these phases, the hazy image of the SPARTA system was gradually refined, starting from a sheet of user requirements, previously presented in Chapter 4. Initially, project planning was performed and through market, stakeholder and functional analyses, enough definition was obtained to draft a range of feasible concepts through the use of design option trees.

The concepts were then developed to a sufficient resolution using iterative Class I and Class II methods, so that a trade-off could be made. A recapitulation of this process can be found in Chapter 5. With a concrete

concept in hand, preliminary studies were conducted on the most important subsystems: structure, mechanisms, communications, control surfaces, propulsion, avionics, and recovery. During this stage, a jaunt was made into the financials, risks and the future development and operations of the system. Thus, enough resolution was achieved to hand the design off to new hands to continue with Detailed Design.

19.2. Stage II: Detailed Engineering Design

In the second phase, estimated to last about six months, the preliminary design of SPARTA and its subsystems will be flashed out in its entirety to bring the engineering design of the system to a close. During this stage, complete computer models will be created to facilitate simulation and upcoming prototyping and production. The goal is to satisfy all of the system requirements set out by the customer and the Design Synthesis group in the first stage.

To this end, the compliance matrix of the design coming out of stage I has to be analysed so that focus areas can be identified. This is done in Subsection 19.2.1. Additionally, through simulation, subsystem and system prototyping and review, the requirements will need to be verified and validated to prove to the customer that the correct product was developed. For this, a preliminary verification plan is presented in Subsection 19.2.2.

19.2.1. Compliance Matrix

Below, the compliance matrix for the system requirements is presented in Table 19.1. As can be seen from the table, some system requirements are still To Be Determined (TBD). These will be further discussed, to make sure they will be met in the future.

Table 19.1: System compliance matrix of SPARTA

Code	Compliance	Reference	Code	Compliance	Reference
REQ-SYS-01	G	Chapter 15	REQ-SYS-34	G	Chapter 8 and 10
REQ-SYS-02	G	Chapter 15	REQ-SYS-34-01	G	Chapter 8 and 10
REQ-SYS-03	G	Chapter 15	REQ-SYS-34-02	G	Chapter 10 and 11
REQ-SYS-36-17	G	Chapter 5	REQ-SYS-19	G	Chapter 19
REQ-SYS-04	Y	TBD	REQ-SYS-20	G	Chapter 15
REQ-SYS-05	G	Chapter 15	REQ-SYS-21	G	Chapter 7 and 8
REQ-SYS-06	G	Chapter 15	REQ-SYS-22	G	Chapter 15
REQ-SYS-07	G	Chapter 8	REQ-SYS-23	G	Chapter 15
REQ-SYS-08	G	Chapter 12	REQ-SYS-24	G	Chapter 18
REQ-SYS-09	G	Chapter 12	REQ-SYS-25	G	Chapter 18
REQ-SYS-10	G	Chapter 7	REQ-SYS-26	G	Chapter 18
REQ-SYS-11	G ¹	Chapter 7	REQ-SYS-27	G	Chapter 19
REQ-SYS-12	G	Chapter 7	REQ-SYS-28	G	Chapter 19
REQ-SYS-45	G	Holds for all designed components	REQ-SYS-29	G	Chapter 19
REQ-SYS-52	G	Chapter 19	REQ-SYS-30	G	Chapter 19
REQ-SYS-53	G	Chapters 7 and 8	REQ-SYS-31	G ²	Chapter 12, 13 and 10
REQ-SYS-38	G	Chapter 12	REQ-SYS-32	G	Chapter 7 and 8
REQ-SYS-13	Y	TBD	REQ-SYS-41	G	Chapter 12, 13 and 10
REQ-SYS-14	G	Chapter 7	REQ-SYS-54	G	Chapter 19
REQ-SYS-15	Y	TBD	REQ-SYS-35	Y	TBD
REQ-SYS-16	Y	TBD	REQ-SYS-36	G	Designed towards
REQ-SYS-17	Y	TBD	REQ-SYS-43	G	Holds for all designed components
REQ-SYS-18	G	Chapter 7 and 8	REQ-SYS-47	Y	TBD
REQ-SYS-33	Y	TBD			

Firstly, **REQ-SYS-04** has not yet been fully covered. It covers the autonomy level of the UAS, however requires software integration; a software architecture is not yet made. The diagram shall be created following the guidelines of Clough. Next, the failure rate of the mission (**REQ-SYS-13**) not exceeding 1% can not yet be

¹Further analysis can be done to accurately simulate the downwash, mentioned in Section 7.14.

²See Chapter 10, Section 10.10, and Chapter 13, Section 13.4 for clarification

confirmed and requires further analysis for the entire system. **REQ-SYS-15** covers the collision probability of the aircraft, however the exact launching procedure is not yet established and requires further analysis.

REQ-SYS-16 and **REQ-SYS-17** are related to the temperature range of the UAS. The structures design in Chapter 7 and 8 can sustain these temperature ranges, however some of the components selected for the avionics and communications cannot sustain these temperature ranges. Further analysis is required on active heating and cooling to fulfil this requirement.

Next, **REQ-SYS-33** states that materials from outside Europe shall not exceed 5%. The subsystem design has been done to comply with this requirement, however no exact overview has been created to confirm that this requirement is met. This also holds for the regulatory system requirements **REQ-SYS-33**, **REQ-SYS-35** and **REQ-SYS-47**.

19.2.2. Requirement Verification

This section aims to present the planned verification and validation procedures, ensuring that the system meets the requirements set out for it. In Table 19.2, each system requirement is assigned a verification method (test, analysis, simulation, review or similarity) with a more detailed description of the procedure.

Table 19.2: Requirement verification strategies for the system

Code	Method	Procedure
Performance Requirements		
REQ-SYS-01	Analysis	Using expected power required and power draw values, evaluate the range in ideal conditions.
REQ-SYS-02	Analysis or Test	Using expected power required and power draw values, evaluate the endurance in ideal conditions. Can be tested by running a prototype on a test bench until battery exhaustion.
REQ-SYS-03	Simulation	Evaluation of expected drag using CFD. From the engine power, evaluate the speed.
REQ-SYS-36-17	Analysis	Inspection of excess power.
REQ-SYS-04	Review	Check if it was implemented.
REQ-SYS-05	Review	Check if sufficient space is present.
REQ-SYS-06	Review	Check if sufficient space is present.
REQ-SYS-07	Test	Measure the time required to replace the payloads.
REQ-SYS-08	Review	Review of specification sheet of the transmitter and antenna.
REQ-SYS-09	Review	Review of specification sheet of the transmitter and antenna
REQ-SYS-10	Simulation	Simulate the loads on the structure and stability during launch using a coupled aerodynamics, flight dynamics and structural model.
REQ-SYS-11	Simulation	Simulate the loads on the structure and stability during launch using a coupled aerodynamics, flight dynamics and structural model.
REQ-SYS-12	Simulation	Simulate the loads on the structure and stability during launch using a coupled aerodynamics, flight dynamics and structural model.
REQ-SYS-45	Review	Check if it has been designed with repairability in mind.
REQ-SYS-52	Review	Check if it has been designed to do so.
REQ-SYS-53	Simulation or Test	Simulate aerodynamic loads and structural stresses. Test for limit expected loads using whiffletree bending, compressive and tensile testing.
REQ-SYS-38	Review	Check if it is there.
REQ-SYS-37	Review	Check if it is there.
Safety and Reliability Requirements		
REQ-SYS-13	Review and Simulation	Review the reliability of the components. Perform one test flight for maximum endurance. Evaluate the degradation of parts and components and simulate this behaviour to see the degradation of the parts.
REQ-SYS-14	Review	Check if provided.
REQ-SYS-15	Simulation	Run a flight dynamics simulation with varying launch and environmental parameters to evaluate the likelihood of impact.
REQ-SYS-16	Review or Test	Review specification sheets of materials and parts. Test using cold and hot chambers for the whole design.
REQ-SYS-17	Review or Test	Review specification sheets of materials and parts. Test using cold and hot chambers for the whole design.
REQ-SYS-18	Review or Test	Review specification sheets of materials and parts. Test water, dust and other types of resistance.

Code	Method	Procedure
REQ-SYS-34	Test	Have a skilled operator refurbish the design.
REQ-SYS-34-01	Review	Check if it was designed for it.
REQ-SYS-34-02	Review	Check if it has been designed for it.
Sustainability Requirements		
REQ-SYS-19	Review	Check if it was performed.
REQ-SYS-20	Review	Check if it was performed.
REQ-SYS-21	Review	Review the bill of materials.
Engineering Budget Requirements		
REQ-SYS-22	Test	Measure a unit.
REQ-SYS-23	Test	Weigh a unit.
Financial Requirements		
REQ-SYS-24	Analysis	Evaluation of the costs associated with development and production
REQ-SYS-25	Analysis	Evaluation of the costs associated with production
REQ-SYS-26	Analysis	Evaluation of the costs associated with maintenance.
Timeline and Resource Requirements		
REQ-SYS-27	Review	Check the timeline.
REQ-SYS-28	Review	Check the timeline.
REQ-SYS-29	Review	Check production capacity plans.
REQ-SYS-30	Review	Check production capacity plans.
REQ-SYS-31	Review	Check bill of materials and components, supply chain analysis.
REQ-SYS-32	Review	Check bill of materials and components, supply chain analysis.
REQ-SYS-33	Review	Check the bill of materials and components.
REQ-SYS-41	Review and Analysis	Review lifespan of components, analyse the decay of batteries and other components.
REQ-SYS-54	Review	Review production capacity and slack.
Regulatory Requirements		
REQ-SYS-35	Review	Compare documentation with the regulations.
REQ-SYS-36	Review and Test	Compare documentation with the regulations. Demonstrate using a test whenever required.
REQ-SYS-43	Review	Compare the bill of materials with the regulations. Review manufacturing procedures.
REQ-SYS-47	Review	Check compliance of logistics and operations.

19.3. Stage III: Manufacturing, Assembly & Integration

The third stage of the design involves the manufacture, assembly and integration of the entire air segment of the SPARTA system. The procedure is devised to manufacture both the prototypes used for testing and certification, and, with modifications revealed by the testing campaign, for serial production.

19.3.1. Manufacturing

The SPARTA system uses various off-the-shelf components and custom-made parts. The manufacturing process is captured in a manufacturing plan flow chart that can be found Figure 19.1 and 19.2. The raw materials, and mechanical and electrical component list can be found in Table 19.3. This list does not include the propulsion system, avionics, telecommunication, battery and payload. They can be found in Tables 11.7, 13.4, 12.4 respectively.

Table 19.3: Raw material and mechanical components list

Raw materials	Quantity	Material	Origin	Mechanical components	Quantity	Material	Origin
Beam (20x20x2 mm)	10	7075-T6 Aluminium	Europe	Screw (M3, Phillips head shaft length 10 mm)	100	Stainless steel	Europe
Sheet (1 mm thick)	8	7075-T6 Aluminium	Europe	SKF 61807-2RZ Bearing	4	Stainless steel	Sweden
Sheet (1.5 mm thick)	15	7075-T6 Aluminium	Europe	SKF 61807-2RZ Bearing	4	Stainless steel	Sweden
Rod (diameter of 7 mm)	1	AM-350 steel	Europe	C-Lube Linear Way LWL 1 Rail	32	Stainless steel	Japan
Rod (diameter of 12 mm)	1	AM-350 steel	Europe				
Rod (diameter of 20 mm)	2	AM-350 steel	Europe				
Rod (diameter of 30 mm)	2	AM-350 steel	Europe				
Rod (diameter of 45 mm)	2	AM-350 steel	Europe				
Tube (diameter of 35 mm, thickness of 5 mm)	2	AM-350 steel	Europe				
Block (67x25x23 mm)	1	7075-T6 Aluminium	Europe				
Block (80x10x10 mm)	6	7075-T6 Aluminium	Europe				
Block (20x20x20 mm)	2	A227 Steel	Europe				
Block (70x50x40 mm)	1	7075-T6 Aluminium	Europe				
Wire (diameter of 0.6 mm)	6	A227 Steel	Europe				
Wire (diameter of 0.5 mm)	4	Nylon	Europe				
Pellets	189 grams	Polycarbonate	Europe				
				Electrical components	Quantity	Material	Origin
				NEMA17 Stepper motor	2	Polymer, metal	China
				SPMSA2030L Servo	2	Polymer, metal	China/USA
				TS90D Mini Servo	4	Polymer, metal	China
				SPMSA5060 HV Servo	2	Polymer, metal	China/USA

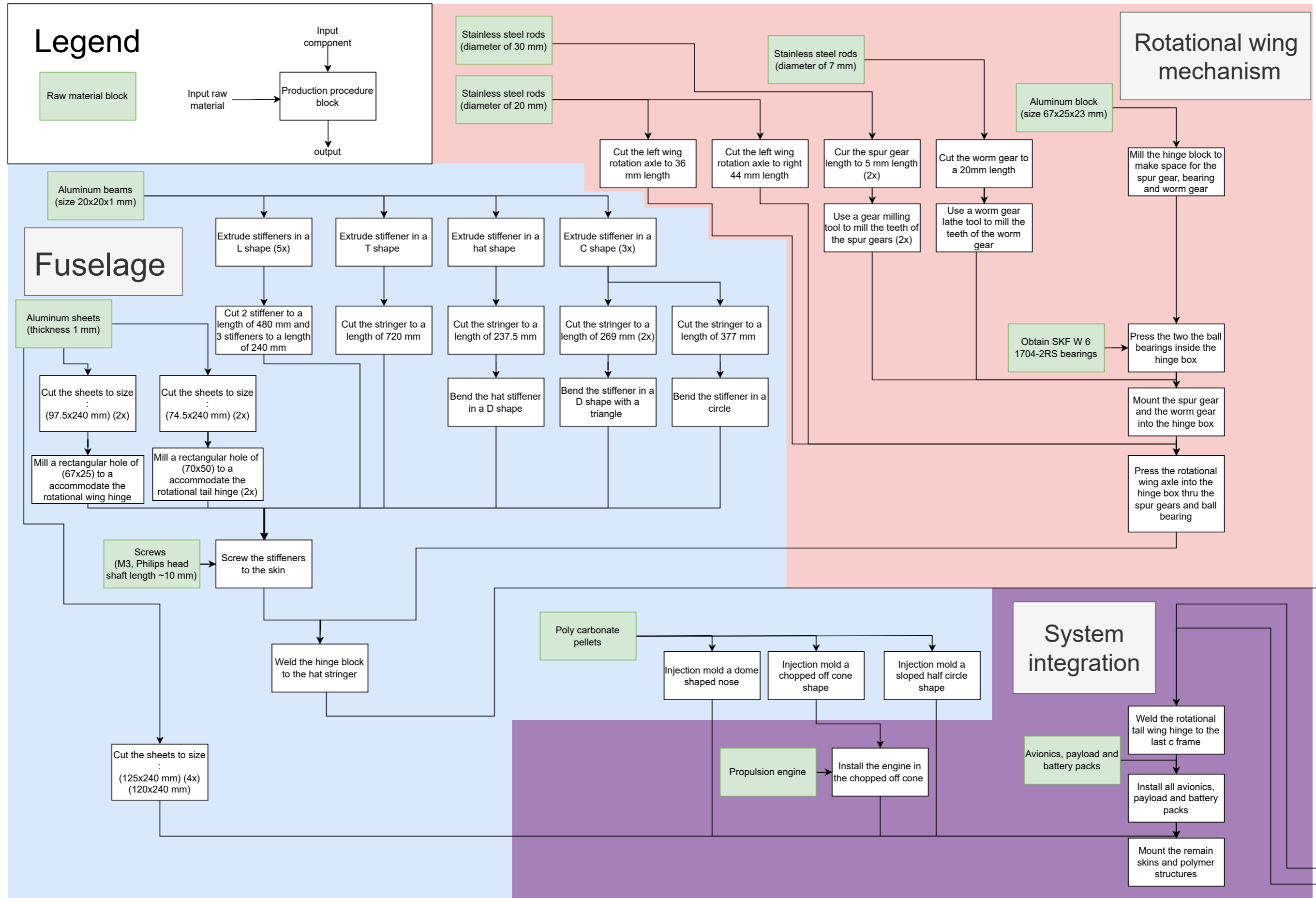


Figure 19.1: The manufacturing plan for first SPARTA drone

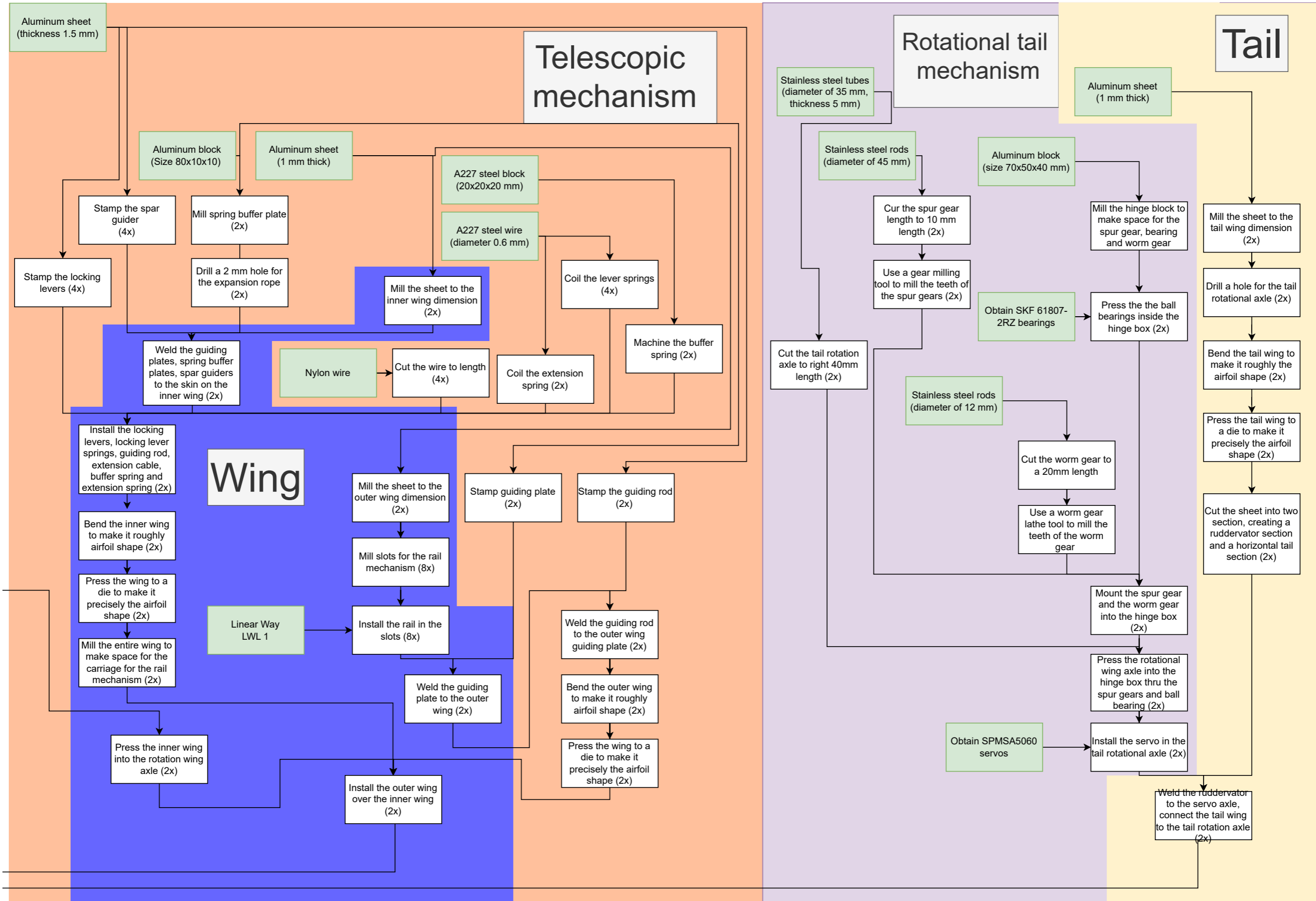


Figure 19.2: The manufacturing plan for first SPARTA drone

19.4. Stage IV: Testing

With the manufacturing, assembly and integration finished, SPARTA has its first prototype created. This prototype can be used to test, verify and validate the functions of the system. This design stage is, however, the main reason for delays in the production of SPARTA, since some of the facilities have to be booked well in advance, special crews are needed to carry out the tests, and the results from the tests need to be reviewed. If any anomalies or failure modes are identified, redesign could be required, which would further delay the production of SPARTA. Therefore, this stage has a reserved time of about nine months. Below, a list of system tests is presented to verify and validate SPARTA.

- **TST-SYS-01: Verify software functionality and integration across all modules**

This test ensures that the software performs all its intended functions as defined in the system and subsystem requirements. It verifies correct operation between different software modules via data flow and communication between components. Furthermore, it can be checked that when activating the system, all components receive their required power. Simulation-based testing can be performed via Software-In-the-Loop (SIL) simulations, which feed the software realistic inputs and observe the outputs.

The test requires no special facilities, but does require a simulation environment and real-time interface tools.

- **TST-SYS-02: Verify structural integrity under mechanical and environmental loads**

This test ensures that the fully integrated UAS can maintain structural integrity and operational readiness when exposed to both mechanical and environmental loading conditions. The system will undergo static load testing, applying loads simultaneously to all subsystems. Additionally, dynamic load testing can be performed, simulating the recovery of the system and vibrational loads to check resilience to aeroelastic effects. Furthermore, the system will undergo environmental testing that includes exposure to extreme temperatures and shock loads. Post-testing inspections and data will confirm the verification.

These tests can be performed in the Delft Aerospace Structures and Materials Laboratory (DASML) at TU Delft, which contains large hydraulic actuators and multi-axis load frames that can apply controlled static, dynamic and environmental loads.

- **TST-SYS-03: Verify system response through all launch procedures**

This test ensures that the system can be launched from all three intended launch platforms. It checks if the system correctly activates itself, unfolds to the final configuration and obtains stable flight. Simultaneously, the structural integrity of the system is tested during launch. The test will analyse the timing and sequence of deployment mechanisms, the ability of the system to establish communication with the ground station, and the initial control responses to stabilise the system. Post-testing inspections and data will confirm the verification.

To perform this test, a military air base such as Air Base Gilze-Rijen can be used, which must be requested and coordinated with the Royal Netherlands Air Force (RNLAf). It provides all necessities for the test: a working ground station infrastructure, a controlled airspace and access to military aircraft and helicopters capable of performing aerial launch. Furthermore, it is open, such that visual tracking of SPARTA is possible. Note that possession of a size A sonobuoy is also required, likely not available at this facility.

- **TST-SYS-04: Verify that the system can be recovered without severe damage**

This test ensures that the system can be safely recovered at the end of the mission without structural damage. The system will be flown at cruise conditions and navigated towards the recovery area, where a controlled net catch is performed. This will test the accuracy of the trajectory and the system's ability to land in the net. Post-catch inspection and data will analyse the structural integrity and health of the system, and check the functioning of all the components. Additionally, the same test will be performed for the back-up method of belly landing on a suitable surface to analyse the damage to the system.

To perform this test, an open area with a vehicle can suffice if the net can be installed and a portable ground station is used. Note that the possession of a size A sonobuoy is again required to take the system to its flying conditions. A belly landing can also be performed on a grassy surface in an open field. Although this would suffice, performing the test at a military air base would simplify the testing procedure.

- **TST-SYS-05: Verify performance and functionality during flight operations**

This test verifies the ability of the system to perform all flight-related functions under real operational conditions. The system will be flown through a representative mission profile that includes navigation and loitering. The test assesses subsystem functionality during flight, such as payload performance, power consumption. Furthermore, the test assesses system functionality, i.e. checking stable flight characteristics, continuous communication with the ground station and correct navigation along its flight path. The ground station will also perform some checks; commands will be sent from the ground station to the system to analyse its response and behaviour, and radar, noise and infrared signatures can be assessed. Post-testing inspections on the flight data logs and the system health will be conducted to confirm the verification.

To perform this test, an open area with a vehicle can suffice if a portable ground station is used. Again, a military air base would simplify the testing procedure.

- **TST-SYS-06: Validate capability to perform a full ISTAR mission**

This test will validate the entire system of fulfilling a full ISTAR mission. From the system functional analysis in Chapter 2, this test will cover **FUN-SYS-2** through **FUN-SYS-8**, which encompasses preparation, launch, flight operations, mission execution, recovery and refurbishment. The system will be launched from the air. The ISTAR mission will require the system to stream real-time full HD video footage of a military vehicle, stationary at a distance of 90 kilometres from the ground station. Once the vehicle is tracked by SPARTA, it shall drive towards a distance of 105 kilometres from the ground station and then return to its original position. Throughout the mission, performance and data handling will be checked. Furthermore, the effectiveness of the mission will be analysed for correctness and usefulness of the data. After the mission, the system is instructed to fly back to its launch location, where it will be recovered. After recovery, refurbishment and post-flight inspection will be performed on the flight data logs and the system health.

To perform this test, a military air base such as Air Base Gilze-Rijen must be used, for the aforementioned reasons. Note that possession of a size A sonobuoy and the recovery net installation is also required, likely not available at this facility. Finally, a military vehicle can be positioned at the Veluwe, which is open and thus allows for easy tracking, covering a distance of slightly less than 100 kilometres.

If no anomalies or failure modes are identified throughout the tests, SPARTA is verified, validated and operationally ready, capable of meeting its mission objectives. If testing goes smoothly and is completed within nine months, more extensive flight tests can be done. These can focus on more extreme operational conditions, such as adverse weather, rural areas and on the boundaries of the flight envelope of SPARTA. Furthermore, flight tests can be performed with malfunctioning subsystems with back-up systems present, to analyse their impact on the system and verify their functioning.

19.5. Stage V: Production

With a validated design, it is key to set up the production process to be able to produce the system more quickly and more efficiently. The production process must be designed towards meeting the requirement of a lead time of less than six weeks and a production rate of 50 systems per month from 2029 (**REQ-SYS-29**, **REQ-SYS-30**).

19.5.1. Production Facilities

Firstly, the production facilities that are needed can be identified. To reduce lead time and improve efficiency, all parts of the system can be produced in the same building. However, it is important to separate the production facility into sections to be able to adapt the equipment to the specific step. For SPARTA, the main production facility can be divided into departments for the production of the airframe and mechanisms, assembly of electrical components, development of flight and control software, and a quality control department. Each department must be tailored to facilitate an efficient working environment. For example, the department for the electrical components needs to have grounded systems and benches. The software development department needs good cybersecurity to prevent data leaks. In the airframe and wing department, personnel must wear additional personal protective equipment to prevent injuries. More department-specific measures will be identified in the design of the production facility.

Then, a suitable location for the production facilities can be identified. For military production facilities, it is primarily influenced by tactical considerations. For example, the facility must preferably not be located in border territory. Also, due to the attributable nature of the system, the facility must have good access to the supply of materials and parts. Additionally, the facilities must preferably be located near industrial hubs or research centres as the development and production of SPARTA requires a skilled workforce and engineers. Within the Netherlands, a location near the port of Rotterdam is suitable. This place is situated inland of the Netherlands, has good access to resources and components through the port, and is close to the industrial hub of Rotterdam and the Delft University of Technology.

19.5.2. Ramp-up Plan

Secondly, to be able to produce 50 systems per month from 2029 onwards, the production must be carefully ramped up. A ramp-up strategy is needed to verify production processes, train and certify workforces, and gather useful process improvement data. The production ramp-up will be divided into three parts: Pilot production, scale-up production and full-rate production. The pilot production can start immediately after the detailed design stage and run in parallel to the certification process. It will take a maximum of six months. Only 1-5 units of SPARTA will be produced each month in this phase of the design. During the production, all facilities, machines, and tools are tested and verified. Also, the workforce will be trained to use and operate the production systems during the pilot production phase. Then, during the scale-up production phase, which will cover four more months, the production rate will be ramped up to 20-30 units per month by partially implementing automation solutions. These solutions are constantly identified and implemented by process engineers. In the scale-up phase, supply chains will be stress-tested to identify potential weaknesses. Any problems regarding suppliers of materials and components can be solved in this phase by selecting different materials or finding alternative suppliers. After a total of ten months, the production process will run at full rate. Using the full implementation of automations in the production process, 50 units will be produced each month. Applicable Key Performance Indicators (KPI) should be monitored. For example, the first-pass yield assesses how many of the produced units pass the quality control tests without rework. The cycle time per unit needs to be monitored to assess the average lead time [57].

19.5.3. Quality Control

Using an automated production process can decrease cycle time per unit and increase production rate. However, it can come at the cost of quality. To ensure that all delivered units of SPARTA conform to the specifications and requirements, quality control must be performed. Quality control must be performed on incoming materials and components, the production process and the final product. The incoming materials must be checked for certification and performance. This can involve visual checks or simple performance tests. During the production process, the quality of different machining systems needs to be checked. Especially the internal structures need to be checked since they will be harder to inspect once the product is complete. Once the final product is produced, a thorough visual inspection should be conducted to check for any abnormalities. After that, the main functionality of the unfolding and telescopic mechanisms needs to be checked to ensure there are no jams. Additionally, it is tested that the control surfaces and the engine work as intended. During ramp-up, it might be necessary to check flight performance on the final product to verify performance. To reduce production costs, flight tests may be omitted or conducted randomly during later production stages, provided there is sufficient confidence in the product's performance.

19.6. Stage VI: Operations

This section describes the operations and logistics of the SPARTA system. This includes everything from leaving the factory to retirement. First, RAMS of the system will be introduced in Subsection 19.6.1 followed by the operations and logistics plan itself in Subsection 19.6.2.

19.6.1. RAMS Analysis

This subsection investigates the reliability, accessibility, maintainability and safety of the SPARTA system.

Reliability

The reliability of the SPARTA system is mostly characterised by its mission profile. The technical aspects of the design itself can be considered quite reliable. The structures and mechanisms have considerable margins of safety, both as mandated by regulations (NATO STANAG 4703 [11]) and due to manufacturing limits leading to the structure being overdesigned. Other internal subsystems are also considered reliable, even without maintenance, during the minimum required unit life span of 20 missions.

Main reliability concerns come from external factors. As SPARTA is operating in hostile environments, both man-made and natural, it faces the threat of external intervention. While the frequency and severity of these are largely out of the control of the designers, some steps have been taken to address these. SPARTA is designed to operate in a wide range of temperatures from -70 to 50 ° C and with harsh environments in mind, addressing reliability in natural environments. The signature of SPARTA is addressed in Section 15.3, and design choices have been taken to keep detectability low. This includes focusing on airfoils with flatter bottoms and using electric engines, reducing radar reflection and infrared signature, respectively.

The launch is a critical stage in terms of reliability, as failure to stabilise, deploy or clear the launcher could lead to mission failure. As simple mechanisms are used for the wing and tail with parts rated for up to 10,000 deployments, it is expected that reliability will be high. The launcher is also cleared quickly at a relative velocity of at least 40 m/s, making the chance of impact low, barring severe weather conditions. Lastly, the net used in recovery is rated for a 40 kg UAV, as discussed in Chapter 14, meaning SPARTA is unlikely to break it by delivering excessive kinetic energy. In case recovery is impossible, SPARTA will attempt a belly landing at a suitable location. This will likely lead to damage to the externals, but keep the system reusable after maintenance.

Availability

As a reusable surveillance UAV capable of rapid deployment, availability needs to be high. An important aspect is that materials and components are available in Europe. Europe is, for the SPARTA project, defined as the European Political Community³.

All structural materials can be sourced in Europe and close trade partners. They mostly consist of aluminium, with some components made of stainless steel and polycarbonate. For aluminium, most in Europe is derived from aluminium scrap⁴, of which there is enough. For steel and virgin aluminium, Turkish production can be used [58, 59], therefore, its supply is considered safe.

A suitable battery manufacturer in Europe is difficult to find. Many companies import and resell products from China⁵ or have insolvency issues^{6, 7, 8, 9}. In the end, BASQUEVOLT was chosen as the primary provider. They have a high-performance solid-state battery that will be mass-produced in 2027¹⁰ in time for the launch of SPARTA. In case BASQUEVOLT fails, SOLiTHOR is expected to make similar batteries in terms of specific volume¹¹. In the worst case, the most stable backup is conventional lithium-ion batteries from VARTA, but the volumetric performance would drop to 420 Wh/l¹². This option is investigated in the sensitivity study in Section 15.5.

³URL: <https://www.consilium.europa.eu/en/meetings/international-summit/2025/05/16/> [cited 23 June 2025]

⁴URL: <https://european-aluminium.eu/about-aluminium/aluminium-industry/> [cited 18 June 2025]

⁵URL: <https://www.rrc-ps.com/en/battery-packs/standard-battery-packs/products/RRC2140> [cited 18 June 2025]

⁶URL: <https://customcells.com/customcells-files-for-insolvency-proceedings-for-key-operating-entities/> [cited 18 June 2025]

⁷URL: <https://en.wikipedia.org/wiki/VARTA> [cited 18 June 2025]

⁸URL: <https://www.politico.eu/article/britishvolt-bankruptcy-uk-britain-battery-bluff/> [cited 18 June 2025]

⁹URL: <https://insideevs.com/news/509878/oxis-faces-bankruptcy/> [cited 18 June 2025]

¹⁰URL: <https://www.elcorreo.com/economia/crisis-coche-electrico-frena-desarrollo-fabrica-vasca-20250203004008-nt.html> [cited 18 June 2025]

¹¹URL: <https://www.prnewswire.com/news-releases/solihor-reaches-1000-charging-cycles-with-over-80-c capacity-retention-a-key-milestone-in-its-development-of-solid-state-batteries-for-the-aviation-and-maritime-sectors-302288699.html> [cited 18 June 2025]

¹²URL: <https://www.elektronik.ropla.eu/pdf/stock/vmb/plf503562.pdf> [cited 18 June 2025]

For the avionics and other electronics, mostly Spanish components are used; however, their supply chains are unclear and could potentially be cut off. Alternatives are identified in Chapter 13, but as they could face similar restrictions, it is necessary to ensure that a stockpile is maintained if global tension increases. An exception is made for the GNSS receiver, which is Canadian as Canada has recently committed to joining a European defence initiative as a formal partner¹³.

The time fraction in which the system will be available (A_0) can be estimated. This is defined as the ratio between the time the drone can be in the air and the total time of an operational cycle. It can be calculated using Equation (19.1).

$$A_0 = \frac{t_{\text{operation}}}{t_{\text{operation}} + t_{\text{charging}} + t_{\text{refurbishment}} + t_{\text{preparation}} + t_{\text{launch}}} \quad (19.1)$$

$t_{\text{operation}}$ is five hours following **REQ-SYS-02**, $t_{\text{refurbishment}}$ is four hours following **REQ-SYS-34**. As the batteries are hot swappable, 15 minutes is accounted for t_{charging} . The launch time is estimated to be between five minutes and up to one hour, depending on the method of launch, with A-400 taking the longest and ground launch the shortest. Preparation is taken to be around 15 minutes, which includes mission loading and putting it in the tube. So, the availability determined range of A_0 is 0.47-0.52. In case spare batteries are not available, recharging is assumed to take the same as the discharge time, five hours, lowering availability to 0.32 in the worst case.

Maintainability

The SPARTA system is designed with maintainability in mind due to its reusability requirements. All fairings and skin panels are fully removable as they are attached with standard Phillips-head screws and can thus be removed even in the field by an operator. After removing all skin panels, all components of the UAV are accessible and removable using standard tools. Batteries are contained in six packs, which can be hot-swapped, decreasing maintenance time and load, and increasing life span. Wings, tail and propeller are fully detachable and can be easily replaced in case of damage during recovery.

The complex mechanisms can mostly be disassembled; however, they are rated for 10,000 uses, so over the required minimal life span of SPARTA of 20 flights, it is unlikely that it would need to be inspected. Likewise, the backbone structure of the fuselage is integrally welded together and cannot be easily maintained without compromising the structure, but can be inspected with NDT methods.

Safety

The safety aspects of SPARTA connect to both its refurbishment and manufacturing on the ground as well as the mission phase in flight. SPARTA is built up from thin, sharp aluminium sheets, which can cause bodily harm if handled incorrectly. The electrical systems also need to be paid attention to, as they can shock the maintenance crew and can be damaged by incorrect manipulation. The moving parts of SPARTA, hinges, wings and tail, and propeller, may damage themselves or their surroundings if activated outside of their intended launch scenario or controlled testing. The batteries powering SPARTA are sensitive to temperature and could pose a fire hazard if heated to or stored at a temperature above 50°C. Prolonged exposure to both high (above 50°C) and sub-zero temperatures severely harms battery health.

The highest safety risk phase occurs during air launch. A collision with the carrier could have catastrophic consequences. While SPARTA clears the space around the launcher quickly at a speed of 40 m/s, above the speed of the carrier, it can still be deviated from its flight path by strong atmospheric phenomena. Therefore, air launch should be avoided during adverse weather and severe turbulence to maintain the crew's safety.

As SPARTA will operate in hostile airspace, there exists the inherent risk of the system being compromised or taken down. To ensure the safety of the system and the ground operations team, SPARTA's autonomous control will avoid collisions and execute a controlled descent to an identified safe location in the case of critical system failure or encounter with enemy fire.

¹³<https://www.cbc.ca/news/politics/canada-signing-onto-european-rearmment-deal-eu-canada-summit-1.7560891>[cited 18 June 2025]

SPARTA continually assesses its own state and mission status, and has the power to either request mission alterations or abort the mission on its own, depending on the preset selected by the operator. This ensures optimal survivability without limiting operator options. In the case that there is a chance of loss in hostile territory, SPARTA can be equipped with a small explosive charge that will be activated by a mission abort signal. Alternatively, the drone can be left to be captured after the system self-scrambles all on-board data.

Finally, during recovery, SPARTA decelerates from approach speed to standstill in a net. During this process, it will experience a large deceleration, refer to Chapter 14, and cover a significant distance. Therefore, significant space behind the net needs to be cleared to reduce the safety risk to the UAV and its operators. Despite the measures, some parts like the tail, propeller and nose might be damaged by the landing.

19.6.2. Logistics & Operations

In this subsection, the logistics and operations of Sparta are discussed during its operational life. First, the preflight inspections are discussed, then the mission operation is covered, and subsequently, both the post-mission refurbishment and battery hotswap are covered. Finally, the storage and EOL protocols are described.

Preflight inspections

Before SPARTA is deployed, a series of pre-flight inspections is conducted to ensure system integrity and readiness. The inspection process begins with a thorough check of the ailerons for any defects or irregularities, as detailed in Chapter 9.

Following mechanical checks, the Veronte autopilot system is powered on remotely. A full system health check is then initiated to verify that all onboard subsystems are operating within nominal parameters. This includes verification of aileron movement, wing unfolding, and tail unfolding and articulation in a flight control check. During this stage, it is critical to inspect the entire drone for any visible signs of wear, loose connections, or damage that could affect flight performance.

Next, the propeller must be examined to confirm that it unfolds correctly. Once this functionality is verified, the propeller should be stowed securely in its folded position to prevent damage or interference during transport and deployment.

Once all pre-flight inspections are completed and the system passes all functional checks, SPARTA is carefully stowed in its launch tube, ready for deployment.

This procedure must be formalised in a pre-flight checklist that the operator is required to complete before every SPARTA flight operation.

Mission Operation

During operations, the drone is transported by one of the three designated launch vehicles: **REQ-SYS-10**, **REQ-SYS-11**, or **REQ-SYS-12**. While in transit, an initial version of the mission plan is wirelessly uploaded to the Veronte 1x autopilot using the system's telecommunications interface. This flight plan consists of a sequence of waypoints that the drone will navigate to autonomously.

Since the drone is battery-operated and remains in an idle state during transit, it slowly consumes battery power. To maximise endurance, the time spent in this state must be minimised.

Upon arrival at the selected launch site, the system operator must verify that the launch vehicle is within SPARTA's defined launch envelope (see Chapter 7). Once confirmed, the drone is launched and automatically unfolds into its cruise configuration. It then begins autonomous navigation toward the first waypoint in its mission plan. This process can be seen in Figure 19.3

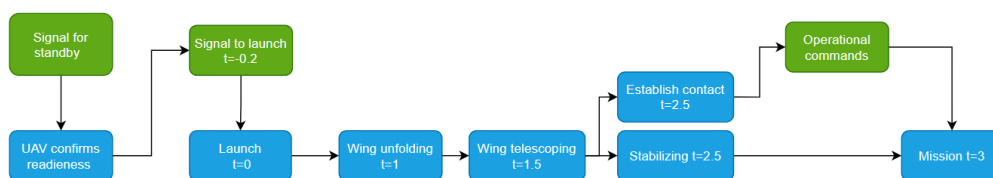


Figure 19.3: Launch procedure, (t is time in seconds, green is the operator, blue is the system)

If the drone operates in a GNSS-denied environment, it relies on the Veronte 1x's IMU and the onboard visual navigation system to acquire and maintain its position. In the event of overcast weather conditions, as discussed in Chapter 13, SPARTA must descend below the cloud layer to maintain reliable visual navigation.

During this operational phase, the drone continuously transmits its health status, telemetry data, and Full HD video feed via the onboard communication system (see Chapter 12). As outlined in the communications architecture, these data streams are received by either the Digital Micro Devices SL XPad5 portable control station or the Digital Micro Devices S.: Dual UAV Control System, depending on whether it is controlled from the launch vehicle or a ground station.

During this phase, the drone is either attrited due to enemy action or system failure, or it completes its mission. If the mission is completed, the drone proceeds to the designated recovery area, where a recovery team, consisting of at least three personnel, has pre-positioned and set up the RN86 recovery net. SPARTA then autonomously manoeuvres into the net and is safely recovered.

Following recovery, both the drone and net shall be rapidly stowed to facilitate a swift extraction. This phase is the most vulnerable period for the operator in a military context. Therefore, the recovery net must be designed for rapid deployment and takedown, and the operators shall be well trained in the setup procedure, minimising the time the operator remains stationary and exposed. Careful planning and efficient execution during this stage are required to ensure operational security and mission success.

Post mission refurbishment

After recovery, the system must be inspected for any damage that it might have incurred during landing or the operation. In this section, damage to the wing, fuselage and electronics is explored.

The wing is made of two distinct parts: inner and outer portions. If any of the outer portion of the wing is damaged, the whole outer wing will be replaced, including the aileron. The same holds for the inner wing.

The fuselage is the aerodynamic fairings and the structural components. The structure is unlikely to fail, but if it does, the failed panels need to be replaced. Fairings can also be replaced individually.

Finally, the electronics, power and avionics subsystems are unlikely to need refurbishment, as if the guidance systems, engine, actuators or central unit fail, SPARTA is not coming back. Also, these systems are unlikely to fail during landing as they do not experience higher-g loads than during launch. Still, after a mission, the health of each component has to be inspected and swapped if needed. The propeller likely needs to be replaced after each landing.

Battery Hotswap

If immediate redeployment is required following post-mission checks and any necessary repairs, the batteries can be hot-swapped. As discussed in Chapter 8, the skin panels are unscrewed to access and replace the batteries, allowing for rapid turnaround and quick reuse of the system.

Storage protocol

During storage, protocols have to be followed so that the health of the system is maintained and the safety of the storage facility and personnel is ensured. The UAV may be stored outside for short periods, hours or a few days, if it is sheltered, and cleaned and inspected before returning to service. If the UAV is stored for periods longer than one month or in locations with extreme temperatures (below 0°C and above 50°C), the battery shall be removed and stored separately in a facility with the correct storage temperature. This stems from the safety

aspects of the design discussed in Subsection 19.6.1. For short periods, SPARTA may be stowed both in its tube and on its own, but for periods longer than one month, it must be stored outside of a tube in a dry environment.

If the UAV is desired for service after an extended storage period, it needs to be tested. This testing procedure involves cleaning and inspecting the structure, testing the functionality of electronics, reinstalling the battery, and testing the folding and unfolding procedure. This procedure is estimated to take 6 hours. As per the requirements, SPARTA can be stored and restored to service even after ten years of storage.

End-of-Life

If, during post-mission inspections, it is determined that sufficient wear has accumulated such that the system can no longer be refurbished and thus has reached its EOL, SPARTA is disassembled into its individual components. Any parts that remain usable are sent back to the factory for potential reuse. In particular, the telecommunications and avionics systems are salvaged, as they are the most expensive and complex components to manufacture.

19.7. Project Gantt Chart

The stages presented in this chapter have been planned in time and are visualised with a Gantt Chart shown in Figure 19.4. If this planning is followed, we will have the first version of SPARTA operational by the end of 2027, according to **REQ-SYS-27**. We will run at full-rate production at a rate of 50 units per month by the start of 2029, according to **REQ-SYS-28, -29**. The sixth stage is performed continuously during the lifespan of the produced systems; therefore, it spans from the production of the first system until the end of the project.

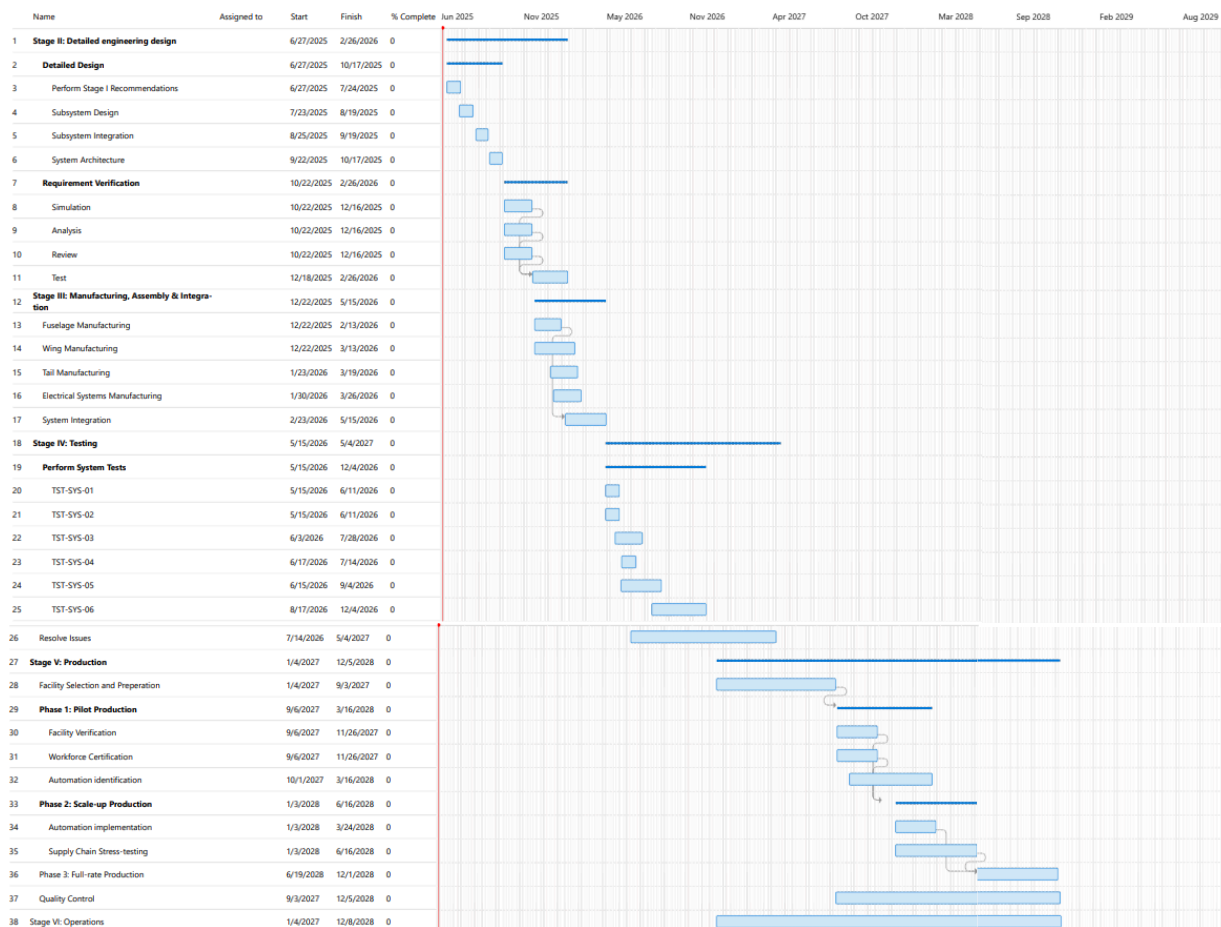


Figure 19.4: Project Design Timeline

20. Conclusion

This project began when Europe was in a precarious situation. Due to the uncertain security guarantees and an aggressor in the east, there was a need for a domestically produced attritable tube-launched unmanned reusable system capable of ISTAR. The team's objective was to design such a system with 10 students in 10 weeks. Now, the team is proud to present a design that meets all the requirements and achieves all its goals.

The SPARTA (Surveillance Platform for Attritable Reconnaissance and Target Acquisition) system is a high-wing morphing drone with an inverted V-tail. It can be launched from an Airbus A400m aircraft, an Apache helicopter or from the ground. The system operator just needs to press a button, and it will launch automatically from the tube and provide an HD video feed to the system operator over the mission area. It can fly to targets at least 725 km away or loiter for 5 hours around the target at speeds between 31 m/s and 55 m/s, depending on the mission. After the mission, it can be recovered by catching SPARTA in a net. When the system is back on the ground, it can be inspected, maintained and folded to fit inside the tube within four hours, so it to fly again.

SPARTA features a telescopic extending wing that maximises the wing area. The wing is thus split into an inner wing and an outer wing. The base airfoil of the wing is the SG6043 airfoil, which provides high aerodynamic performance while still having a somewhat rectangular inner space. The outer wing follows this profile while the inner wing uses a slightly stretched profile to maximise the inner volume for the telescope mechanism. The wing extends using a spring-operated system that locks into place before and after the extension. The wing and tail itself use a spur and worm wheel system that rotates and locks the wing into place. The tail rotational mechanism also houses the ruddervator actuators, which rotate the outer part of the tail surface to provide more than sufficient controllability for the drone to operate in hostile environments. The ailerons are also sized accordingly and fit on the trailing edge of the outer wing. Fitting the propeller and propulsion system initially raised concerns, but the team found a solution and modified an existing propeller that can be folded during storage and launch.

The fuselage of the structure uses a semi-monocoque structure with load-bearing frames and stringers. The skin is not essential for load-carrying and can thus be removed for easy access to the system internals, payload and batteries. The structure of the fuselage and wings is sized to cope with 89g of launch load corresponding to a launch speed of 40 m/s. The flight envelopes during launch have been evaluated to investigate if stability or controllability issues would arise. This investigation found that the system is stable for all relevant launch cases except for the aircraft launch, but the team is confident that they can be mitigated with active control inputs.

As the world is heating up, sustainability forms a core part of our design. The wing, fuselage and some of the mechanism components are made from recyclable metal and polymer parts. The system uses a low-emission electric engine that makes shooting down the drone difficult, thus prolonging the life of the drone. Most of the components are sourced from European manufacturers or can be made in a metal and polymer workshop somewhere in Europe. The team aspired to make sure that all electronics systems are sourced from Europe. For mission-critical components like the telecommunication, battery, propulsion and navigational equipment, this is indeed the case. For the actuators, it was decided that they could be recycled from existing products in times of war.

Limitations & Recommendations

Even though the team is confident in the design of the vehicle, there are still some possibilities for further research, analysis and design. The stall behaviour is for example not fully understood due to limitation of the XFOIL software. Also during launch, the helicopter downwash was not taken into account and complex flow phenomena like downwash and turbulence were neglected. A full CFD simulation or wind tunnel test can give a better understanding of these effects. For the structural analysis, the buckling of the wing skin has not been given the proper detailed analysis it deserves. The thermal control has also not given enough attention.

Acknowledgements

Finally, this project would not have been possible with the help of our tutor, Sam van Elsloo and our coaches Imran Khan and George Popi. Without their guidance, feedback and sometimes emotional support, this project would not have been possible. We also would like to thank our contacted experts: Ash Hamraz, Raphael Dekkers and their team from the Nationaal Lucht- en Ruimtevaartlaboratorium for helping finding weak points in our design and helping the aerodynamic analysis, aeroelasticity analysis and propeller design; Saullo Castro for providing guidance to the mechanical design of the mechanism and Mark Voskuyl for helping with the signature assessment and the operational context of drones; Tomas Sinnige for his help on the propeller design; Jan Eek for helping with the LCA analysis and provide advice on polymer design and last but not least Jurij Sodja on helping the aeroelasticity analysis.

Bibliography

- [1] Industries, A., “ALTIUS Air Launched Effects Demonstrated Advanced Teaming at US Army Project Edge 2022,” Anduril Blog, 2022.
- [2] Embention, “Veronte autopilot 1x,” 2025. URL https://www.embention.com/wp-content/uploads/2024/01/Veronte-Autopilot-1x-ENG-Datasheet_LR_Web.pdf.
- [3] UAV Navigation Oesia Group, “Visual Navigation System - VNS01,” 2023. URL https://www.uavnavigation.com/sites/default/files/docs/2023-08/UAV%20Navigation_VNS01_Brochure_0.pdf.
- [4] Tallysman, “TW2410/TW2412 Magnetic Mount GPS/GLONASS Antenna,” 2011. URL <https://www.farnell.com/data-sheets/2860198.pdf>.
- [5] Group 31, “Project Plan: ATLAS - Design of an Attritable Tube-Launched Unmanned Aerial System,” Project plan, Delft University of Technology, Faculty of Aerospace Engineering, 2025. Design Synthesis Exercise. Tutors: Sam van Elsloo, Imran Khan, and George Popi.
- [6] Group 31, “Baseline Report: ATLAS - Design of an Attritable Tube-Launched Unmanned Aerial System,” Baseline report, Delft University of Technology, Faculty of Aerospace Engineering, 2025. Design Synthesis Exercise, Tutors: Sam van Elsloo, Imran Khan, and George Popi.
- [7] Group 31, “Midterm report: SPARTA - Design of an Surveillance Platform for Attritable, Reconnaissance and Target Acquisition,” Midterm report, Delft University of Technology, Faculty of Aerospace Engineering, 2025. Design Synthesis Exercise, Tutors: Sam van Elsloo, Imran Khan, and George Popi.
- [8] European Defence Agency, “European Defence Data 2023-2024,” March 2024. URL <https://eda.europa.eu/docs/default-source/brochures/eda---defence-data-23-24---web---final.pdf>.
- [9] European Commission, “Questions and answers on ReArm Europe Plan Readiness 2030,” 2025. URL https://ec.europa.eu/commission/presscorner/detail/en/qanda_25_790.
- [10] European Commission and European External Action Service and European Defence Agency, “European Defence – Readiness 2030,” Tech. rep., European Commission, 03 2025.
- [11] NATO Standardization Agency, “Light Unmanned Aircraft Systems Airworthiness Requirements,” Article, 2014. [cited 30 April 2025].
- [12] Williams, A. P., and Scharre, P. D., “Autonomous Systems: Issues for Defence Policymakers,” *Center for a New American Security (CNAS) report*, Vol. 2, 2015, pp. 41–44.
- [13] “COUNCIL DECISION (CFSP) 2017/2315 of 11 December 2017 establishing permanent structured cooperation (PESCO) and determining the list of participating Member States,” *Official Journal of the European Union*, 2017.
- [14] The European Parliament and The Council of the European Union, “Regulation (EU) 2021/821 of the European Parliament and of the Council of 20 May 2021 setting up a Union regime for the control of exports, brokering, technical assistance, transit and transfer of dual-use items (recast),” 5 2021.
- [15] Oliviero, F., “Requirement Analysis and Design principles for A/C stability control (Part 1),” AE3211-I Systems Engineering and Aerospace Design, 2025.
- [16] Oliviero, F., “Requirement Analysis and Design principles for A/C stability control (Part 2),” AE3211-I Systems Engineering and Aerospace Design, 2025.
- [17] Saaty, R., “The Analytical Hierarchy Process - What It Is and How It Is Used,” *Pergamon Journals*, Vol. 9, 1987, pp. 161–176.
- [18] Anderson, J., *Fundamentals of Aerodynamics*, McGraw-Hill Education, 2023.
- [19] Sforza, P., “Chapter 5 - Wing Design,” *Commercial Airplane Design Principles*, edited by P. Sforza, Butterworth-Heinemann, Boston, 2014, pp. 119–212. doi:10.1016/B978-0-12-419953-8.00005-X.
- [20] Megson, T., *Aircraft Structures for Engineering Students*, Elsevier, 2007.
- [21] Panagiotopoulos, I., Sakellariou, L., and Hatziefremidis, A., “Design, Construction, and Flight Performance of an Electrically Operated Fixed-Wing UAV,” *Drones*, Vol. 8, 2024, p. 217. doi:10.3390/drones8060217.
- [22] Kapoulas, I. K., C. Statharas, J. C., Hatziefremidis, A., and Baldoukas, A. K., “Fast Airfoil Selection Methodology for Small Unmanned Aerial Vehicles,” *Applied Sciences*, Vol. 12, 2022, p. 9328. doi:10.3390/app12189328.
- [23] A. Williamson, G., D. McGranahan, B., A. Broughton, B., W. Deters, R., B. Brandt, J., and S. Selig, M., “Summary of Low-Speed Airfoil Data,” Vol. 5, 2012.
- [24] Hoang Duy, V., Trong Dao, T., Zelinka, I., Choi, H.-S., and Chadli, M., “AETA 2015: Recent Advances in Electrical Engineering and Related Sciences,” *Lecture Notes in Electrical Engineering*, Vol. 371, 2015. doi:10.1007/978-3-319-27247-4.
- [25] Shin, P., and Kim, K., “Aerodynamic Performance Prediction of SG6043 Airfoil for a horizontal-axis Small Wind Turbine,” *Journal of Physics: Conference Series*, Vol. 1452, 2020, p. 012018. doi:10.1088/1742-6596/1452/1/012018.

- [26] Ashby, M. F., Shercliff, H., and Cebon, D., *Materials: Engineering, Science, Processing and Design*, 4th ed., Elsevier, 2019.
- [27] Hamm, K., Price, D., Imtiaz, K., and Raju, I., "Revisiting Building-Block Approaches for Structures," , Januari 2022.
- [28] Mulder, J., van Staveren, W., van der Vaart, J., de Weerd, E., de Visser, C., in 't Veld, A., and Mooij, E., "Flight Dynamics Lecture Notes," , 2013.
- [29] Yue, T., Zhanga, X., and L. Wanga, J. A., "Flight dynamic modeling and control for a telescopic wing morphing aircraft via asymmetric wing morphing," *Aerospace Science and Technology*, Vol. 70, 2017, pp. 328–338.
- [30] Hibbeler, R. C., *Engineering Mechanics Dynamics*, 14th ed., Pearson, Harlow, England, 2017.
- [31] Theodorsen, T., and Garrick, I. E., "A Theoretical and Experimental Investigation of the Flutter Problem," Tech. rep., NACA, 1940.
- [32] Dimitriadis, G., *Introduction to Nonlinear Aeroelasticity*, John Wiley Sons Ltd, 2017. Appendix 2 and Section 5.2.
- [33] NAVEDTRA, *Welding Costs*, NAVEDTRA 14251A STEELWORKER ADVANCED, 1996, Vol. 2.
- [34] Wang, C., *Applied Elasticity*, McGraw-Hill, 1953.
- [35] Gerard, G., and Becker, H., *Handbook of Structural Stability Part III - Buckling of Curved Plates and Shells*, NACA, 1957.
- [36] "Fuselage Structural Analysis Volume III - Frames, Bulkheads And Fittings," Tech. rep., General Electric Advanced Engine and Technology Department, 2 1964.
- [37] Nieto, J. T., "Feature Based Costing of Extruded Parts," Ph.D. thesis, University of Illinois at Urbana-Champaign, 2010.
- [38] Raymer, D. P., *Aircraft Design: a Conceptual Approach.*, Amer Institute of Aeronautics, 2019.
- [39] Mott, R. L., *Machine Element in Mechanical Design*, 3rd ed., Prentice Hall, Upper Saddle River, New Jersey, 1999.
- [40] Hibbeler, R., *Engineering Mechanics Dynamics*, fourteenth ed., Pearson, 2017. SI Edition.
- [41] Norton, R. L., *MACHINE DESIGN An Integrated Approach*, 4th ed., Prentice Hall, 2011.
- [42] Barnhart, K., Marshall, D. M., and Shappee, E., *Introduction to Unmanned Aircraft Systems*, 3rd ed., CRC Press, Boca Raton, FL, 2021.
- [43] Sullivan, G. J., Ohm, J.-R., Han, W.-J., and Wiegand, T., "Overview of the High Efficiency Video Coding (HEVC) Standard," *IEEE Transactions on Circuits and Systems for Video Technology*, Vol. 22, No. 12, 2012, pp. 1649–1668. doi:10.1109/TCSVT.2012.2221191.
- [44] Sze, V., Budagavi, M., and Sullivan, G. J. (eds.), *High Efficiency Video Coding (HEVC): Algorithms and Architectures*, Integrated Circuits and Systems, Springer, Cham, Switzerland, 2014. doi:10.1007/978-3-319-06895-4.
- [45] Nechvatal, J., Barker, E., Bassham, L., Burr, W., Dworkin, M., Foti, J., and Roback, E., "Report on the Development of the Advanced Encryption Standard (AES)," *Journal of Research of the National Institute of Standards and Technology*, Vol. 106, No. 3, 2001, pp. 511–577. doi:10.6028/jres.106.023.
- [46] JinHui Ge, R. Z., "Research on the Launch and Recovery Methods of UAVs," *Eurasia Journal of Science and Technology*, 2024.
- [47] Knott, E. F., Schaeffer, J. F., and Tuley, M. T., *Radar Cross Section*, 2nd ed., SciTech Publishing, Raleigh, NC, 2004.
- [48] Simons, D., and Snellen, M., *Aircraft Noise: An introduction to general acoustics and aircraft noise*, Delft, The Netherlands, 2023. Lecture notes for course AE4431-23, Faculty of Aerospace Engineering, Delft University of Technology.
- [49] Gutin, L., and Magliozzi, B., "Aerodynamic Noise from Propellers in Axial Flow," Tech. Rep. NASA TR R-99, NASA, 1970.
- [50] Dumitrescu, C., Minea, M., Costea, I. M., Chiva, I. C., and Semenescu, A., "Development of an Acoustic System for UAV Detection," *Sensors*, Vol. 20, No. 17, 2020, p. 4870. doi:10.3390/s20174870.
- [51] Barela, J., Firmanty, K., and Kastek, M., "Measurement and Analysis of the Parameters of Modern Long-Range Thermal Imaging Cameras," *Sensors*, Vol. 21, No. 17, 2021, p. 5700. doi:10.3390/s21175700.
- [52] Etkin, B., and Reid, L. D., *Dynamics of Flight: Stability and Control*, John Wiley & Sons, 1995.
- [53] Cook, M. V., *Flight Dynamics Principles: A Linear Systems Approach to Aircraft Stability and Control*, Butterworth-Heinemann, 2012.
- [54] Hoak, D. E., and Finck, R. D., *USAF Stability and Control Datcom*, National Technical Information Service, 1975.
- [55] R. Everly, C. M., D. Limmer, *Cost-Effectiveness Analysis of Autonomous Aerial Platforms and Communication Payloads*, Iowa State university, 2015.
- [56] Wheeler, W., "Keeping Track of the Drones," *Time*, 2012.
- [57] Peterson, E. T., *The Big Book of Key Performance Indicators*, Web Analytics Demystified, Portland, OR, 2006. Available at: <https://www.webanalyticsdemystified.com/kpi/>.
- [58] "Economic and Steel Market Outlook, 2025-2026 Q1," Tech. rep., EUROFER, 2025.
- [59] Hanilci, N., *Bauxite Deposits of Turkey*, Nurullah, 2019. doi:10.1007/978-3-030-02950-0_15.